

ПРИМЉЕНО:		12. 10. 2021	
Рад.јед.	број	Архивифра	Прилог
0801	844/1		

Научном већу Института за физику у Београду

Београд, 11. 10. 2021.

Предмет: Молба за покретање поступка за избор у звање истраживач сарадник

Молим Научно веће Института за физику у Београду да у складу са Правилником о поступку и начину вредновања и квантитативном исказивању научно-истраживачких резултата истраживача покрене поступак за мој избор у звање истраживач сарадник.

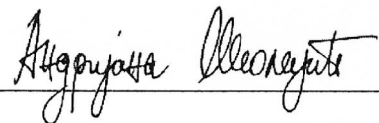
У прилогу достављам:

1. Мишљење руководиоца лабораторије са предлогом чланова комисије за избор у звање
2. Стручну биографију
3. Преглед научне активности
4. Списак публикација и њихове копије
5. Копије диплома основних и мастер студија
6. Потврда о уписаним докторским студијама
7. Списак положених испита на докторским студијама
8. Уверење о прихваћеној теми докторске дисертације

С поштовањем,

Андријана Шолајић,

Истраживач приправник



Научном већу Института за физику у Београду

Београд, 11.10.2021.


Предмет: Мишљење руководиоца лабораторије о избору Андријане Шолајић у звање истраживач сарадник

Андријана Шолајић је студент докторских студија физике, а тезу ради под менторством др Јелене Пешић. Запослена је од децембра 2018. године у Лабораторији за 2Д материјале у Центру за физику чврстог стања и нове материјале, Института за физику у Београду. Бави се проучавањем нових хетероструктура на бази хексагоналног бор нитрида и монохалкогенида IIIa групе и примене различитих спољашњих сила као што је напрезање у циљу прецизног подешавања жељених електронских и оптичких својстава. Такође је учесник је на ПРОМИС пројекту "StrainedFeSC - Strain effects in iron chalcogenide superconductors" под руководством др Ненада Лазаревића. С обзиром да испуњава све предвиђене услове у складу са Правилником о поступку, начину вредновања и квантитативном исказивању научноистраживачких резултата истраживача МПНТР, сагласни смо са покретањем поступка за избор Андријане Шолајић у звање истраживач сарадник.

За састав комисије за избор у звање Андријане Шолајић у звање истраживач сарадник предлажемо:

1. др Јелена Пешић, научни сарадник Института за физику у Београду,
2. Др Ненад Лазаревић, виши научни сарадник Института за физику у Београду,
3. Др Божидар Николић, ванредни професор Физичког факултета Универзитета у Београду

Др Ивана Милошевић,
научни сарадник Института за Физику у Београду,
Руководилац лабораторије за 2Д материјале



Стручна биографија Андријане Шолајић

Андријана Шолајић је рођена 1991. године у Београду, где је завршила Математичку гимназију 2010. године. Дипломирала је на одсеку за Физичку електронику на Електротехничком факултету Универзитета у Београду, на смеру Наноелектроника, оптоелектроника и ласерска техника, са просеком 8.26. Дипломски рад под називом „Електронска структура напрегнутих графенских нанотачака“ одбранила је са оценом 10 у јуну 2016. године.

Исте године уписује мастер студије на Електротехничком факултету Универзитета у Београду, на модулу Наноелектроника и фотоника. У септембру 2017. године одбранила је мастер тезу под називом “Одређивање електронских и фононских својстава графена допираног стронцијумом и итербијумом ДФТ методом”, чиме завршава мастер студије са просечном оценом 10.0. Мастер рад је комплетно урађен у Центру за физику чврстог стања и нове материјале, Института за физику у Београду, у лабораторији за 2Д материјале, под менторством др Јелене Пешић.

У октобру 2017. године уписује докторске студије из Физике кондензоване материје и статистичке физике, на Физичком факултету Универзитета у Београду, од када волонтира у Центру за физику чврстог стања и нове материјале, Института за Физику Београд, у Лабораторији за 2Д материјале. Од децембра 2018. године запослена је у истој групи.

У оквиру свог доктората, Андријана се бави истраживањем особина нових хетероструктура базираних на хексагоналном бор нитриду (hBN) и монохалкогенидима IIIa групе помоћу теорије функционала густине. Примарно циљ истраживања је утицај различитих спољашњих сила на овакве структуре, првенствено примене напрезања, у циљу испитивања могућности прецизне контроле одређених својстава, као што су ширина енергијског процепа и оптичке особине. На колегијуму докторских студија Физичког факултета одржаног 01.12.2021. одобрена јој је израда докторске дисертације под темом под називом “Испитивање утицаја напрезања на особине хетероструктура дводимензионалних монохалкогенида IIIa групе *ab-initio* методама”. Од августа 2020. године учесник је ПРОМИС пројекта “StrainedFeSC - Strain effects in iron chalcogenide superconductors” под руководством др Ненада Лазаревића, задужена за нумеричке прорачуне.

До сада је аутор на 10 радова у међународним часописима, као и учесник на неколико међународних конференција. У септембру 2019 године учествовала је на ДФТ школи у Љубљани “Summer School on Advanced Materials and Molecular Modelling” као учесник и татор на практичним вежбама. Рецензент је два рада у међународним часописима. У октобру 2019. године била је члан организационог одбора конференције Симпозијум физике кондензоване материје у Београду.

Преглед научне активности Андријане Шолајић

Андријана Шолајић се у свом научном раду бави истраживањем особина нових слојевитих и 2Д материјала као и хетероструктура базираних на њима. У свом истраживању користи ab-initio прорачуне, базиране на теорији функционала густине. Теорија функционала густине је данас једна од најпопуларнијих умеричких метода за моделирање материјала, заснована на законима квантне механике. Резултати добијени овим методом се углавном добро слажу са експерименталним резултатима, и користе се како за објашњење и потврду експерименталних резултата, тако и за предвиђање нових материјала и њихових својстава.

- **Хетероструктуре на бази хексагоналног бор нитрида (hBN) и монохалкогенида IIIa групе**

Моделовање и испитивање хетероструктура на бази једнослојног хексагоналног бор нитрида (hBN) и једнослојних монохалкогенида IIIa групе (InTe, GaTe) помоћу теорије функционала густине. Анализиране су електронска структура и оптичке особине оваквих хетероструктура, као и утицај hBN-а на својства монохалкогенида у циљу механичке заштите осетљивих монослојева монохалкогенида подложних оксидацији при изложености ваздуху. Уочена је повећана оптичка апсорпција у UV делу спектра приликом формирања хетероструктуре, у поређењу са монослојевима InTe и GaTe. Резултати истраживања су тренутно на рецензији у међународном часопису.

Наставак истраживања базиран је на даљем испитивању ових и сличних хетероструктура, тј. могућности примене различитих спољашњих сила на овакве системе у циљу прецизне контроле жељених својстава материјала. Конкретно у фокусу је тренутно испитивање примене униформног напрезања на хетероструктуре у циљу контроле ширине енергијског процепа као и оптичких својстава, као истраживање и боље познавање фундаменталних процеса у њима – међуслојног спрезања, трансфера наелектрисања

- **Изучавање утицаја спин-орбитне интеракције на електронске дисперзије 2Д материјала одређених типова симетрије**

Према истраживањима колеге Владимира Дамљановића и колега са Физичког факултета, симетријска анализа даје индикације да ниско-енергијски спектар материјала одређених типова симетрије може бити интересантнији од Дираковог или квадратног спектра. Систематски анализирајући ефективне Хамилтонијане и дисперзије у тачкама високе симетрије са четвороструком зонском дегенерацијом, откривене су нове врсте електронских дисперзија, такозване “porru flower” дисперзије (облик подсећа на цвет мака). Овакви типови дисперзија постоје у немагнетним дводимензионим материјалима са спин-орбитном интеракцијом који поседују неку од десет предложених 10 симетријских група. Међу

материјалима који су као ексфолирани у монослој кандидати за овакав тип дисперзије, налази се и слојевити BiIO_4 , који постоји као тродимензиони кристал и ексфолира се у стабилни монослој симетрије $pb21a$. Методом теорије функционала густине, потврђена је стабилност једнослојног BiIO_4 и изучавана су електронска својства овог материјала, која потврђују присуство тзв. Fortune Teller фермиона у тачкама високе симетрије електронске дисперзије.

Резултати овог истраживања објављени су у истакнутом међународном часопису:

Damljanović, V., Lazić, N., **Šolajić, A.**, Pešić, J., Nikolić, B. and Damjanović, M., 2020. Peculiar symmetry-protected electronic dispersions in two-dimensional materials. *Journal of Physics: Condensed Matter*, 32(48), p.485501.

- **Истраживање електрон-фонон интеракције у допираном графену и његових оптичких и механичких особина**

Настављено је истраживање особина једнослојног графена допираног металним адатомима. Претходни резултати анализе електронских и фононских особина оваквих система индиковали су могућу појаву суперпроводности у слоју графена допираног различитим адатомима. Ови закључци мотивисали су на даља истраживања својстава допираног графена. Анализирани су особине једнослојног графена допираног стронцијумом, као и прелазним металима итријумом и скандијумом. Методом теорије функционала густине рачуната је електрон-фонон интеракција оваквих система. Показано је да монослој графена допираног стронцијумом има појачану електрон-фонон интеракцију са параметром $\lambda=0.38$ и испољава суперпроводност испод $T_c = 0.9$ К, а слични резултати очекивани су и за преостале две структуре услед повећања густине стања на Ферми нивоу.

Даље, како овакви материјали могу наћи различите примене у многим областима, испитиване су њихова механичка и оптичка својства. Рачунате и анализирани су еластичне константе свих структура. Резултати показују да се допирањем еластичне константе смањују за око 50% у односу на чист једнослојни графен, што их и даље чини супериорним у поређењу са многим сличним 2Д материјалима. Израчуната диелектрична функција, тј. њен имагинарни део, не показује било какве значајне промене које би довеле до смањеног квалитета оптичких особина повољних у графену.

Резултати овог истраживања објављени су у истакнутом међународном часопису (M22):

Šolajić, A., Pešić, J. & Gajić, R. Optical and mechanical properties and electron-phonon interaction in graphene doped with metal atoms. *Opt Quant Electron* 52, 182 (2020). <https://doi.org/10.1007/s11082-020-02300-0>

- **Истраживање вибрационих и својстава слојевитих квази 2Д материјала**

- **Испитивање електронских и фононских својстава VI3**

Испитиване су електронска структура и рачунати Раман спектри за различите фазе структуре VI3, комплементарно са Раман мерењима колега из Центра за физику чврстог стања и нове материјале. Рад који сумира све резултате истраживања објављен је у међународном часопису изузетних вредности (M21a):

Djurdjić Mijin S, Abeykoon AMM, **Šolajić A**, Milosavljević A, Pešić J, Liu Y, Petrovic C, Popović ZV, Lazarević N. Short-Range Order in VI3. Inorganic Chemistry, 2020. doi:10.1021/acs.inorgchem.0c02060.

- **Прорачуни Раман спектра CrSi0.8Ge0.1Te3**

Рачунати су Раман спектри и анализирана динамика решетке CrSi0.8Ge0.1Te3 у циљу бољег разумевања експерименталних резултата. Резултати истраживања су публиковани у раду у истакнутом међународном часопису (M22):

Milosavljević, **A. Šolajić**, A, Višić, B, et al. Vacancies and spin-phonon coupling in CrSi0.8Ge0.1Te3. Journal of Raman Spectroscopy, 2020; 1– 8. <https://doi.org/10.1002/jrs.5962>

- **Прорачуни електронских и фононских особина квази-2Д трихалкогенида и емиксена**

Испитиване су вибрационе особине Ti3C2 и TiC2 методом теорије функционала густине, у циљу бољег разумевања експерименталних резултата карактеризације Ti3C2/PMMA нанокмозита. Рад који сумира резултате истраживања послат је у међународни часопис и очекује се скорашња публикација.

- **Динамика решетке слојевитог Fe_{3-x}GeTe₂**

Прорачуни раман спектра и вибрационих својстава слојевитог Fe_{3-x}GeTe₂ комплементарно експерименталним резултатима, у циљу анализе динамике решетке и фазних прелаза овог материјала. Резултати истраживања публиковани су у врхунском међународном часопису (M21):

A. Milosavljević, **A. Šolajić**, S. Djurdjić-Mijin, J. Pešić, B. Višić, Yu Liu, C. Petrovic, N. Lazarević, and Z. V. Popović. "Lattice dynamics and phase transitions in Fe 3– x GeTe 2." Physical Review B 99, no. 21: 214304. (2019)

- **Учешће на пројектима у овом периоду:**

2020 - : Фонд за науку републике Србије: Промис пројекат под бројем 6062656 – “StrainedFeSC - Strain effects in iron chalcogenide superconductors”

2018 – 2020: Физика уређених наноструктура и нових материјала у фотоници ОИ171005, Министарство просвете, науке и технолошког развоја

2018 – 2020: Наноструктурни мултифункционални материјали и нанокомпозити ИИИ450018, Министарство просвете, науке и технолошког развоја

2018 – 2020: Modelling and measuring phase transitions and optical properties for perovskites, Билатерални пројекат са Johannes Kepler Универзитетом, Linz Austria

- **Рецензије радова у међународним часописима:**

Децембар 2019 – Physica E: Low dimensional Systems and Nanostructures, Elsevier

Септембар 2020 – Electronic Structure, IOP publishing

Списак публикација Андријане Шолајић

РАДОВИ У МЕЂУНАРОДНИМ ЧАСОПИСИМА ИЗУЗЕТНИХ ВРЕДНОСТИ (M21a):

1. S. Djurdjic Mijin, A. M. M. Abeykoon, **A. Šolajić**, A. Milosavljević, J. Pešić, Y. Liu, C. Petrovic, Z. V. Popović, N. Lazarević, Short-Range Order in VI₃, Inorganic Chemistry, vol. 59, no. 22, pp. 16265 - 16271, doi: 10.1021/acs.inorgchem.0c02060, (2020).

РАДОВИ У ВРХУНСКИМ МЕЂУНАРОДНИМ ЧАСОПИСИМА (M21):

1. S. Djurdjić-Mijin, **A. Šolajić**, J. Pešić, M. Šćepanović, Y. Liu, A. Baum, C. Petrovic, N. Lazarević, Z.V. Popović, "Lattice dynamics and phase transition in CrI₃ single crystals", Physical Review B 98 (10), 104307 (2018)

2. A. Milosavljević, **A. Šolajić**, J. Pešić, Yu Liu, C. Petrovic, N. Lazarević, Z.V. Popović, "Evidence of spin-phonon coupling in CrSiTe₃", Physical Review B 98 (10), 104306 (2018)

3. A. Milosavljević, **A. Šolajić**, B. Višić, M. Opačić, J. Pešić, Y. Liu, C. Petrovic, Z. V. Popović, N. Lazarević, Vacancies and spin-phonon coupling in CrSi_{0.8}Ge_{0.1}Te₃, Journal of Raman Spectroscopy, Wiley, 51, 11, 0377-0486, 10.1002/jrs.5962, (2020).

4. S. Djurdjic-Mijin., A. Baum, J. Bekaert, **A. Šolajić**, J. Pešić, Y. Liu, ... & N. Lazarević, "Probing charge density wave phases and the Mott transition in 1 T- TaS₂ by inelastic light scattering", Physical Review B, 103(24), 245133. (2021)

5. A. Milosavljević, **A. Šolajić**, S. Djurdjić-Mijin, J. Pešić, B. Višić, Yu Liu, C. Petrovic, N. Lazarević, and Z. V. Popović. "Lattice dynamics and phase transitions in Fe_{3-x}GeTe₂." Physical Review B 99, no. 21: 214304. (2019)

РАДОВИ У ИСТАКНУТИМ МЕЂУНАРОДНИМ ЧАСОПИСИМА (M22):

1. **A. Šolajić**, J. Pešić, R. Gajić, "Ab-initio calculations of electronic and vibrational properties of Sr and Yb intercalated graphene", Optical and Quantum Electronics 50 (7), 276 (2018)

2. **A. Solajic**, J. Pesic, R. Gajic, "Optical and mechanical properties and electron-phonon interaction in graphene doped with metal atoms", Optical and Quantum Electronics, vol. 52, no. 3, issn: 0306-8919, doi: 10.1007/s11082-020-02300-0 (2020).

3. V. Damljanović, N. Lazić, A. Šolajić, J. Pešić, B. Nikolić, & M. Damjanović. "Peculiar symmetry-protected electronic dispersions in two-dimensional materials". Journal of Physics: Condensed Matter, 32(48), 485501. (2020)

РАДОВИ У НОВИМ ЧАСОПИСИМА БЕЗ КАТЕГОРИЈЕ:

1. J. Pešić, I. Popov, **A. Šolajić**, V. Damljanović, K. Hingerl, M. Belić, & R. Gajić (2019). Ab initio study of the electronic, vibrational, and mechanical properties of the magnesium diboride monolayer. Condensed Matter, 4(2), 37. (2019)

САОПШТЕЊЕ СА МЕЂУНАРОДНОГ СКУПА ШТАМПАНО У ИЗВОДУ М34:

1. **A. Šolajić**, J. Pešić, R. Gajić, "Ab-initio calculations of electronic and vibrational properties of Sr and Yb-intercalated graphene", VI International School and Conference on Photonics - PHOTONICA 2017, 28.8 - 1.9.2017, Beograd, Srbija, ISBN 978-86-82441-46-5
2. **A. Šolajić**, J. Pešić, R. Gajić, "First principle study of Yb and Sr doped monolayer graphene", Program and the Book of Abstracts / Sixteenth Young Researchers' Conference Materials Sciences and Engineering, December 6-8, 2017, Beograd, Srbija, str 27., ISBN 978-86-80321-33-2
3. J. Pešić, **A. Šolajić**, Electron-Phonon Interaction in Monolayer MgB₂ from the First Principles, School on Electron-Phonon Physics from First Principles, International Centre for Theoretical Physics (ICTP), Trieste, Italy, 19. - 23. Mar, 2018
4. J. Pesic, **A. Solajic**, R. Gajic, Strain effects on vibrational properties in hexagonal 2D materials from the first principles – doped graphene and MgB₂- monolayer study, Knjiga Abstrakata - Simpozijum Fizike Kondenzovane Materije, pp. 69 - 69, Beograd, Srbija, 7. - 11. Oct, 2019
5. **A. Šolajić**, J. Pešić, R. Gajić, Optical and mechanical properties and electron-phonon interaction in graphene doped with metal atoms, PHOTONICA2019: The Seventh International School and Conference on Photonics, 26 August – 30 August 2019, Belgrade, Serbia, Vinča Institute of Nuclear Sciences, pp. 106 - 106, isbn: 978-86-7306-153-5, Београд, 26. Aug - 30. Sep, 2019
6. A. Milosavljević, **A. Šolajić**, S. Djurdjić Mijin, J. Pešić, B. Višić, Y. Liu, C. Petrovic, N. Lazarević, Z. V. Popović, Lattice dynamics and phase transitions in Fe_{3-x}GeTe₂, The 20th Symposium on Condensed Matter Physics BOOK OF ABSTRACTS, pp. 84 - 84, Београд, 7. - 11. Oct, 2019
7. **A. Šolajić**, J. Pesic, Electron-phonon interaction and superconductivity in graphene doped with metal atoms, BOOK OF ABSTRACTS: Quantum ESPRESSO Summer School on Advanced Materials and Molecular Modelling, Jožef Stefan Institute, Jamova 39, Ljubljana, Slovenia, pp. 16 - 16, isbn: 978-961-264-154-2, Љубљана, 15. - 20. Sep, 2019
8. J. Pesic, **A. Solajic**, Computational study of vibrational properties of chemically exfoliated titanium carbide MXenes - Ti₃C₂ and TiC₂, BOOK OF ABSTRACTS: Quantum ESPRESSO Summer School on Advanced Materials and Molecular Modelling, Jožef Stefan Institute, Jamova 39, Ljubljana, Slovenia, vol. 1, no. 1, pp. 16 - 16, issn: 301641728, isbn: 978-961-264-154-2, Ljubljana, Slovenia, 15. - 20. Sep, 2019
9. J. Pesic, **A. Šolajić**, Strain effects on vibrational properties in hexagonal 2D materials from the first principles – doped graphene and MgB₂- monolayer, Book of abstracts – Mauterndorf 2020, 21st International Winterschool, New Developments in Solid State Physics, Mauterndorf, Mauterndorf, Salzburg, Austria, 23. - 28. Feb, 2020
10. **Andrijana Solajic** and Jelena Pesic, Novel hBN/In(Ga)Te Heterostructures For Wide Spectrum Light Absorbers, Book of Abstracts - International Symposium on Nanoscale Research, 20-21th Sep 2021, Leoben



Република Србија

УБ

Универзитет у Београду
Електротехнички факултет, Београд



Оснивач: Република Србија

Дозволу за рад број 612-00-02666/2010-04 од 10. децембра 2010.
године је издало Министарство просвете и науке Републике Србије

Диплома

Андријана, Слободан, Шолајић

рођена 5. маја 1991. године у Београду, Савски венац, Република Србија, уписана
школске 2010/2011. године, а дана 3. јуна 2016. године завршила је основне академске
студије, првог степена, на студијском програму Електротехника и рачунарство,
обима 240 (двеста четрдесет) бодова ЕСПБ са просечном оценом 8,26 (осам и 26/100).

На основу тога издаје јој се ова диплома о стеченом високом образовању и стручном називу
дипломирани инжењер електротехнике и рачунарства

Број: 5860500

У Београду, 31. октобра 2016. године

Декан
Проф. др Зоран Јовановић

Ректор
Проф. др Владимир Бумбаширевић

00058647



Република Србија

УБ

Универзитет у Београду
Електротехнички факултет, Београд



Оснивач: Република Србија
Дозволу за рад број 612-00-02666/2010-04 од 10. децембра 2010.
године је издало Министарство просвете и науке Републике Србије

Диплома

Андријана, Слободан, Шолајић

рођена 5. маја 1991. године у Београду, Савски венац, Република Србија, уписана
школске 2016/2017. године, а дана 7. септембра 2017. године завршила је мастер
академске студије, другој степена, на студијском програму Електротехника и
рачунарство, обима 60 (шездесет) бодова ЕСПБ са просечном оценом 10,00 (десет и 0/100).

На основу тога издаје јој се ова диплома о стеченом високом образовању и академском називу
мастер инжењер електротехнике и рачунарства

Број: 7575300

У Београду, 25. децембра 2017. године

в.д. Декан

Проф. др Мило Томашевић

Ректор

Проф. др Владимир Бумбаширевић

00076086



Република Србија
Универзитет у Београду
Физички факултет
Д.Бр.2017/8005
Датум: 08.10.2021. године

На основу члана 161 Закона о општем управном поступку и службене евиденције издаје се

УВЕРЕЊЕ

Шолајић (Слободан) Андријана, бр. индекса 2017/8005, рођена 05.05.1991. године, Београд, Савски венац, Република Србија, уписана школске 2020/2021. године, у статусу: самофинансирање; тип студија: докторске академске студије; студијски програм: Физика.

Према Статуту факултета студије трају (број година): три.
Рок за завршетак студија: у двоструком трајању студија.

Ово се уверење може употребити за регулисање војне обавезе, издавање визе, права на дечији додатак, породичне пензије, инвалидског додатка, добијања здравствене књижице, легитимације за повлашћену возњу и стипендије.



Овлашћено лице факултета

[Signature]



Република Србија
Универзитет у Београду
Физички факултет
Д.Бр.2017/8005
Датум: 08.10.2021. године

На основу члана 161 Закона о општем управном поступку и службене евиденције издаје се

УВЕРЕЊЕ

Шолајић (Слободан) Андријана, бр. индекса 2017/8005, рођена 05.05.1991. године, Београд, Савски венац, Република Србија, уписана школске 2020/2021. године, у статусу: самофинансирање; тип студија: докторске академске студије; студијски програм: Физика.

Према Статуту факултета студије трају (број година): три.
Рок за завршетак студија: у двоструком трајању студија.

Ово се уверење може употребити за регулисање војне обавезе, издавање визе, права на дечији додатак, породичне пензије, инвалидског додатка, добијања здравствене књижице, легитимације за повлашћену возњу и стипендије.



Овлашћено лице факултета

[Signature]



Република Србија
Универзитет у Београду
Физички факултет
Број индекса: 2017/8005
Датум: 08.10.2021.

На основу члана 29. Закона о општем управном поступку и службене евиденције издаје се

УВЕРЕЊЕ О ПОЛОЖЕНИМ ИСПИТИМА

Андријана Шолајић, име једног родитеља Слободан, рођена 05.05.1991. године, Београд, Савски венац, Република Србија, уписана школске 2017/2018. године на докторске академске студије, школске 2020/2021. године уписана на статус самофинансирање, студијски програм Физика, током студија положила је испите из следећих предмета:

Р.бр.	Шифра	Назив предмета	Оцена	ЕСПБ	Фонд часова**	Датум
1.	ДС15КМ16	Компјутерско моделовање структурних и електронских особина материјала	10 (десет)	15	I:(8+0+0)	21.08.2018.
2.	ДС15КМ17	Скенирајућа атомска микроскопија чврстих тела	10 (десет)	15	II:(8+0+0)	24.08.2018.
3.	ДС15ФРНД1	Рад на докторату 1. део	П.	30	I:(0+0+12) II:(0+0+12)	
4.	ДС15КМ1	Спектроскопске технике у физици кондензоване материје	10 (десет)	15	III:(8+0+0)	10.09.2019.
5.	ДС15ФРНД2	Рад на докторату 2. део	П.	30	III:(0+0+12) IV:(0+0+12)	
6.	ДС15ВО2	Монте Карло симулације у физици	10 (десет)	15	III:(8+0+0)	30.09.2019.
7.	ДС15ФРНД3	Рад на докторату 3. део	П.	15	V:(0+0+20)	

* - еквивалентан/признат испит.

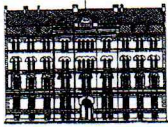
** - Фонд часова је у формату (предавања+вежбе+остало).

Општи успех: 10,00 (десет и 00/100), по годинама студија (10,00, 10,00, /).



Одговорно лице факултета

[Handwritten signature]



ДОКТОРСКЕ СТУДИЈЕ

ПРЕДЛОГ ТЕМЕ ДОКТОРСКЕ ДИСЕРТАЦИЈЕ
КОЛЕГИЈУМУ ДОКТОРСКИХ СТУДИЈА

Школска година
2021/2022

Подаци о студенту

Име

Андријана

Презиме

Шолајић

Број индекса

2017/8005

Научна област дисертације

Физика кондензоване материје и
статистичка физика

Подаци о ментору докторске дисертације

Име

Јелена

Презиме

Пешић

Научна област

Физика кондензоване материје

Звање

Научни сарадник

Институција

Институт за Физику у Београду

Предлог теме докторске дисертације

Наслов

Испитивање утицаја напрезања на особине хетероструктура дводимензионалних монохалкогенида IIIa групе *ab-initio* методама

Уз пријаву теме докторске дисертације Колегијуму докторских студија, потребно је приложити следећа документа:

1. Семинарски рад (дужине до 10 страница)
2. Кратку стручну биографију писану у трећем лицу јединине
3. Фотокопију индекса са докторских студија

Потпис ментора

Потпис студента

Датум

Мишљење Колегијума докторских студија

Након образложења теме докторске дисертације Колегијум докторских студија је тему

прихватио није прихватио

Датум

Продекан за науку Физичког факултета

Probing charge density wave phases and the Mott transition in 1T-TaS₂ by inelastic light scatteringS. Djurdjic Mijin,¹ A. Baum,² J. Bekaert,³ A. Šolajić,¹ J. Pešić,¹ Y. Liu,^{4,*} Ge He,² M. V. Milošević,³ C. Petrovic,⁴ Z. V. Popović,^{1,5} R. Hackl,² and N. Lazarević¹¹Center for Solid State Physics and New Materials, Institute of Physics Belgrade, University of Belgrade, Pregrevica 118, RS-11080 Belgrade, Serbia²Walther Meissner Institut, Bayerische Akademie der Wissenschaften, D-85748 Garching, Germany³Department of Physics, University of Antwerp, Groenenborgerlaan 171, B-2020 Antwerp, Belgium⁴Condensed Matter Physics and Materials Science Department, Brookhaven National Laboratory, Upton, New York 11973-5000, USA⁵Serbian Academy of Sciences and Arts, Knez Mihailova 35, RS-11000 Belgrade, Serbia

(Received 10 March 2021; revised 14 June 2021; accepted 16 June 2021; published 22 June 2021)

We present a polarization-resolved, high-resolution Raman scattering study of the three consecutive charge density wave (CDW) regimes in 1T-TaS₂ single crystals, supported by *ab initio* calculations. Our analysis of the spectra within the low-temperature commensurate (C-CDW) regime shows $P\bar{3}$ symmetry of the system, thus excluding the previously proposed triclinic stacking of the “star-of-David” structure, and promoting trigonal or hexagonal stacking instead. The spectra of the high-temperature incommensurate (IC-CDW) phase directly project the phonon density of states due to the breaking of the translational invariance, supplemented by sizable electron-phonon coupling. Between 200 and 352 K, our Raman spectra show contributions from both the IC-CDW and the C-CDW phases, indicating their coexistence in the so-called nearly commensurate (NC-CDW) phase. The temperature dependence of the symmetry-resolved Raman conductivity indicates the stepwise reduction of the density of states in the CDW phases, followed by a Mott transition within the C-CDW phase. We determine the size of the Mott gap to be $\Omega_{\text{gap}} \approx 170\text{--}190$ meV, and track its temperature dependence.

DOI: [10.1103/PhysRevB.103.245133](https://doi.org/10.1103/PhysRevB.103.245133)**I. INTRODUCTION**

Quasi-two-dimensional transition metal dichalcogenides (TMDs), such as the various structures of TaSe₂ and TaS₂, have been in the focus of various scientific investigations over the last 30 years, mostly due to the plethora of charge density wave (CDW) phases [1,2]. Among all TMD compounds 1T-TaS₂ stands out because of its unique and rich electronic phase diagram [3–6]. It experiences phase transitions at relatively high temperatures, making it easily accessible for investigation and, mainly for the hysteresis effects, attractive for potential applications such as data storage [7], information processing [8], or voltage-controlled oscillators [9].

The cascade of phase transitions as a function of temperature includes the transition from the normal metallic to the incommensurate CDW (IC-CDW) phase, the nearly commensurate CDW (NC-CDW) phase, and the commensurate CDW (C-CDW) phase occurring at around $T_{\text{IC}} = 554$ K, $T_{\text{NC}} = 355$ K, and in the temperature range from $T_{\text{C}\downarrow} = 180$ K to $T_{\text{C}\uparrow} = 230$ K, respectively. Recent studies indicate the possibility of yet another phase transition in 1T-TaS₂ at $T_H = 80$ K, named the hidden CDW state [10–12]. This discovery led to a new boost in attention for 1T-TaS₂.

Upon lowering the temperature to $T_{\text{IC}} = 554$ K, the normal metallic state structure, described by the space group $P\bar{3}m1$ (D_{3d}^d) [13], transforms into the IC-CDW state. As will be

demonstrated here, the IC-CDW domains shrink upon further temperature reduction until they gradually disappear, giving place to the C-CDW ordered state. This region in the phase diagram between 554 and roughly 200 K is characterized by the coexistence of the IC-CDW and C-CDW phases and is often referred to as NC-CDW. At the transition temperature T_C , IC-CDW domains completely vanish [14] and a new lattice symmetry is established. There is a general consensus about the formation of “star-of-David” clusters with in-plane $\sqrt{13}a \times \sqrt{13}a$ lattice reconstruction, whereby 12 Ta atoms are grouped around the 13th Ta atom [15,16]. In the absence of any external strain fields, this can be achieved in two equivalent ways (by either clockwise or counterclockwise rotations) thus yielding domains [17]. Despite extensive investigations, both experimental and theoretical, it remains an open question whether the stacking of star-of-David clusters is triclinic, trigonal, hexagonal, or a combination thereof [15,16,18–20]. The C-CDW phase is believed to be an insulator [3,21–23] with a gap of around 100 meV [13]. Very recent theoretical studies based on density-functional theory (DFT) find an additional ordering pattern along the crystallographic c axis. The related gap has a width of approximately 0.5 eV along k_z and becomes gapped at the Fermi energy E_F in the C-CDW phase [24,25].

Nearly all of the previously reported results for optical phonons in 1T-TaS₂ are based on Raman spectroscopy on the C-CDW phase and on temperature-dependent measurements in a narrow range around the NC-CDW to C-CDW phase transition [13,15,18–20]. In this paper we present temperature-dependent polarization-resolved Raman

*Present address: Los Alamos National Laboratory, Los Alamos, New Mexico 87545, USA.

measurements in the temperature range from 4 to 370 K covering all three CDW regimes of 1T-TaS₂. Our analysis of the C-CDW phase confirms the symmetry to be $P\bar{3}$, while the NC-CDW phase is confirmed as a mixed regime of commensurate and incommensurate domains. The Raman spectra of the IC-CDW phase mainly project the phonon density of states due to the breaking of translation invariance and sizable electron-phonon coupling. The growth of the CDW gap upon cooling, followed by the opening of the Mott gap, is traced via the initial slope of the symmetry-resolved spectra. The size of 170–190 meV and the temperature dependence of the Mott gap are directly determined from high-energy Raman data.

II. EXPERIMENTAL AND NUMERICAL METHODS

The preparation of the studied 1T-TaS₂ single crystals is described elsewhere [26–29]. Calibrated customized Raman scattering equipment was used to obtain the spectra. Temperature-dependent measurements were performed with the sample attached to the cold finger of a He-flow cryostat. The sample was cooled down to the lowest temperature and then heated. In either case the rates were less than ± 1 K/min. All measurements were performed in a high vacuum of approximately 5×10^{-5} Pa.

The 575-nm laser line of a diode-pumped Coherent GENESIS MX-SLM solid state laser was used as an excitation source. Additional measurements with the 458- and 514-nm laser lines were performed with a Coherent Innova 304C argon ion laser. The absorbed power was set at 4 mW. All spectra shown are corrected for the sensitivity of the instrument and the Bose factor, yielding the imaginary part of the Raman susceptibility $R\chi''$, where R is an experimental constant. An angle of incidence of $\Theta_i = 66.0 \pm 0.4^\circ$ and atomically flat cleaved surfaces enable us to measure at energies as low as 5 cm^{-1} without a detectable contribution from the laser line since the directly reflected light does not reach the spectrometer. The corresponding laser spot has an area of roughly $50 \times 100 \mu\text{m}^2$ which prevents us from observing the possible emergence of the domains [17,30]. The inelastically scattered light is collected along the surface normal (crystallographic c axis) with an objective lens having a numerical aperture of 0.25. In the experiments presented here, the linear polarizations of the incident and scattered light are denoted as \mathbf{e}_i and \mathbf{e}_s , respectively. For \mathbf{e}_i horizontal to the plane of incidence there is no projection on the crystallographic c axis. For the low numerical aperture of the collection optics \mathbf{e}_s is always perpendicular to the c axis. Low-energy data up to 550 cm^{-1} were acquired in steps of $\Delta\Omega = 1 \text{ cm}^{-1}$ with a resolution of $\sigma \approx 3 \text{ cm}^{-1}$. The symmetric phonon lines were modeled using Voigt profiles where the width of the Gaussian part is given by σ . For spectra up to higher energies the step width and resolution were set at $\Delta\Omega = 50 \text{ cm}^{-1}$ and $\sigma \approx 20 \text{ cm}^{-1}$, respectively. The Raman tensors for the D_{3d} point group are given in Table I. Accordingly, parallel linear polarizations project both A_{1g} and E_g symmetries, while crossed linear polarizations only project E_g . The pure A_{1g} response then can be extracted by subtraction.

We have performed DFT calculations as implemented in the ABINIT package [31]. We have used the Perdew-Burke-Ernzerhof (PBE) functional, an energy cutoff of 50 Ha for the

TABLE I. Raman tensors for trigonal systems (point group D_{3d}).

$$A_{1g} = \begin{pmatrix} a & 0 & 0 \\ 0 & a & 0 \\ 0 & 0 & b \end{pmatrix} \quad {}^1E_g = \begin{pmatrix} c & 0 & 0 \\ 0 & -c & d \\ 0 & d & 0 \end{pmatrix} \quad {}^2E_g = \begin{pmatrix} 0 & -c & -d \\ -c & 0 & 0 \\ -d & 0 & 0 \end{pmatrix}$$

plane-wave basis, and we have included spin-orbit coupling by means of fully relativistic Goedecker pseudopotentials [32,33], where Ta- $5d^36s^2$ and S- $3s^23p^4$ states are treated as valence electrons. The crystal structure was relaxed so that forces on each atom were below $10 \mu\text{eV}/\text{\AA}$ and the total stress on the unit cell below 1 bar, yielding lattice parameters $a = 3.44 \text{ \AA}$ and $c = 6.83 \text{ \AA}$. Subsequently, the phonons and the electron-phonon coupling (EPC) were obtained from density-functional perturbation theory (DFPT) calculations, also within ABINIT [34]. Here, we have used an $18 \times 18 \times 12$ \mathbf{k} -point grid for the electron wave vectors and a $6 \times 6 \times 4$ \mathbf{q} -point grid for the phonon wave vectors. For the electronic occupation we employed Fermi-Dirac smearing with broadening factor $\sigma_{\text{FD}} = 0.01$ Ha, which is sufficiently high to avoid unstable phonon modes related to the CDW phases.

III. RESULTS AND DISCUSSION

A. Lattice dynamics of the charge-density wave regimes

Temperature-dependent symmetry-resolved Raman spectra of 1T-TaS₂ are presented in Fig. 1. It is obvious that their evolution with temperature is divided into three distinct ranges (IC-CDW, NC-CDW, and C-CDW) as indicated. The lattice dynamics for each of these ranges will be treated separately in the first part of the section. In the second part we address the electron dynamics.

1. C-CDW phase

At the lowest temperatures 1T-TaS₂ exists in the commensurate C-CDW phase. Here, the atoms form so-called star-of-David clusters. Different studies report either triclinic stacking of these clusters leading to $P\bar{1}$ unit cell symmetry [16], or trigonal or hexagonal stacking and $P\bar{3}$ unit cell symmetry [15,18–20]. A factor group analysis predicts 57 A_g Raman-active modes with an identical polarization dependence for $P\bar{1}$ unit cell symmetry, and alternatively 19 $A_g + 19 E_g$ Raman-active modes for $P\bar{3}$ unit cell symmetry [13]. Our polarized Raman scattering measurements at $T = 4$ K, measured in two scattering channels, together with the corresponding cumulative fits are shown in Fig. 2. As it can be seen, we have observed modes of two different symmetries in the related scattering channels. This result indicates trigonal or hexagonal stacking of the star-of-David clusters. The symmetric phonon lines can be described by Voigt profiles, the best fit of which is shown as blue (for parallel light polarizations) and red (crossed polarizations) lines. After fitting Voigt profiles to the Raman spectra, 38 phonon modes were singled out. Following the selection rules for A_g and E_g symmetry modes, 19 were assigned as A_g and 19 as E_g symmetry, meaning all expected modes could be identified. The contribution from each mode to the cumulative fit is presented in Fig. 2 as green

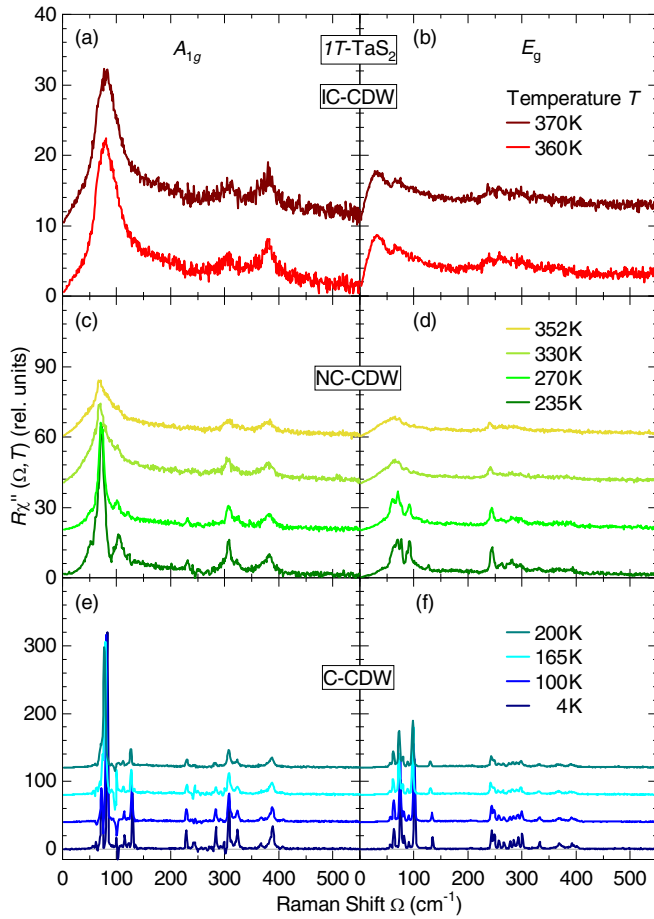


FIG. 1. Symmetry-resolved Raman spectra of $1T$ -TaS₂ at temperatures as indicated. Both C-CDW (blue lines) and IC-CDW (red lines) domains yield significant contributions to the Raman spectra of the NC-CDW phase (green lines).

TABLE II. A_{1g} and E_g Raman mode energies experimentally obtained at $T = 4$ K.

n_o	ω_{A_g} (cm ⁻¹)	ω_{E_g} (cm ⁻¹)
1	62.6	56.5
2	73.3	63.3
3	83.4	75.3
4	114.9	82.0
5	121.9	90.5
6	129.5	101.1
7	228.7	134.8
8	244.1	244.0
9	271.9	248.9
10	284.2	257.5
11	298.6	266.6
12	307.2	278.3
13	308.2	285.0
14	313.0	292.9
15	321.2	300.5
16	324.2	332.7
17	332.0	369.2
18	367.2	392.6
19	388.4	397.7

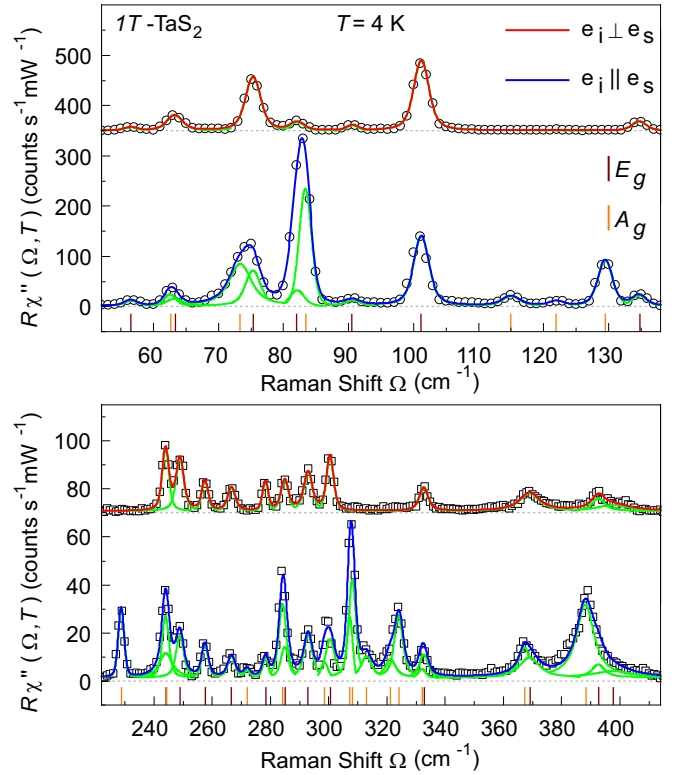


FIG. 2. Raman spectra at $T = 4$ K, i.e., in the C-CDW phase, for parallel and crossed light polarizations. Red and blue solid lines represent fits of the experimental data using Voigt profiles. Spectra are offset for clarity. The short vertical lines depict central frequencies obtained from the data analysis. The exact energy values are presented in Table II.

lines, whereas the complete list of the corresponding phonon energies can be found in Table II.

2. IC-CDW phase

At the highest experimentally accessible temperatures $1T$ -TaS₂ adopts the IC-CDW phase. Data collected by Raman scattering at $T = 370$ K, containing all symmetries, are shown as a blue solid line in Fig. 3. As $1T$ -TaS₂ is metallic in this phase [25] we expect the phonon lines to be superimposed on a continuum of electron-hole excitations which we approximate using a Drude spectrum shown as a dashed line [35,36].

Since the IC-CDW phase arises from the normal metallic phase, described by space group $P\bar{3}m1$ [13,37], it is interesting to compare our Raman results on the IC-CDW phase to an *ab initio* calculation of the phonon dispersion in the normal phase, shown as an inset in Fig. 3. Four different optical modes were obtained at Γ : E_u at 189 cm⁻¹ (double degenerate), E_g at 247 cm⁻¹ (double degenerate), A_{2u} at 342 cm⁻¹, and A_{1g} at 346 cm⁻¹. A factor group analysis shows that two of these are Raman active, namely E_g and A_{1g} [13].

We observe that the calculated phonon eigenvalues of the simple metallic phase at Γ do not closely match the observed peaks in the experimental spectra of the IC-CDW phase. Rather, these correspond better to the calculated phonon density of states (PDOS), depicted in Fig. 3. There are essentially three different ways to project the PDOS in a Raman

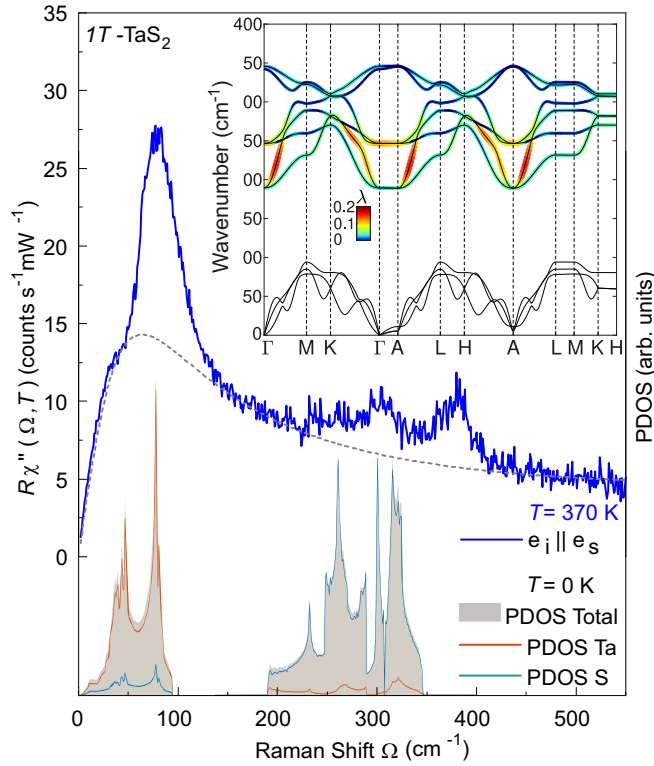


FIG. 3. Raman response for parallel light polarizations in the IC-CDW phase at 370 K (blue line). The dashed line depicts the possible electronic continuum. The contributions of the Ta (dark brown) and S atoms (light brown) to the calculated PDOS (gray area) are shown below. The inset shows the calculated phonon dispersion of 1T-TaS₂ in the simple metallic phase, with the electron-phonon coupling (λ) of the optical branches indicated through the color scale.

experiment and to overcome the $q \approx 0$ selection given by the small momentum of visible light: (i) scattering on impurities [38], (ii) enhanced electron-phonon coupling [39], and (iii) breaking of the translational symmetry in the IC-CDW phase. (i) We rule out chemical impurity scattering, expected to exist at all temperatures, as the low-temperature spectra (Fig. 2) show no signs thereof. (ii) The additional scattering channel may come from the electron-phonon coupling (EPC). The calculated EPC, λ , in the optical modes (inset of Fig. 3) is limited, yet not negligible, reaching maxima of ~ 0.2 in the lower optical branches around the Brillouin zone (BZ) points Γ and A. The calculated atom-resolved PDOS shows the acoustic modes to be predominantly due to Ta and the optical modes due to S, as a result of their difference in atomic mass. The acoustic modes display several dips that are signatures of the latent CDW phases, for which the EPC cannot be reliably determined. Significant EPC in the optical modes of 1T-TaS₂ is furthermore supported by experimental results linking a sharp increase in the resistivity above the IC-CDW transition temperature to the EPC [37]. It also corroborates calculated [14] and experimentally obtained [13] values of the CDW gap, which correspond to intermediate to strong EPC [37]. (iii) Although EPC certainly contributes we believe that the majority of the additional scattering channels can be traced back to the incommensurate breaking of the translational in-

variance upon entering IC-CDW. Thus the “weighted” PDOS is projected into the Raman spectrum [see Figs. 1(a) and 1(b)]. These “weighting” factors depend on the specific symmetries along the phonon branches as well as the “new periodicity” and go well beyond the scope of this paper.

3. NC-CDW phase

The nearly commensurate phase is seen as a mixed phase consisting of regions of commensurate and incommensurate CDWs [40,41]. This coexistence of high- and low-temperature phases is observable in our temperature-dependent data as shown in Fig. 1. The spectra for the IC-CDW (red curves) and C-CDW phase (blue curves) are distinctly different, as also visible in the data shown above (Figs. 2 and 3). The spectra of the NC-CDW phase ($235 \text{ K} < T < 352 \text{ K}$) comprise contributions from both phases. As 352 K is the highest temperature at which the contributions from the C-CDW phase can be observed in the spectra, we suggest that the phase transition temperature from IC-CDW to NC-CDW phase is somewhere in between 352 and 360 K. This conclusion is in good agreement with experimental results regarding this transition [4–6].

B. Gap evolution

The opening of a typically momentum-dependent gap in the electronic excitation spectrum is a fundamental property of CDW systems which has also been observed in 1T-TaS₂ [13,37,42]. Here, in addition to the CDW, a Mott transition at the onset of the C-CDW phase leads to an additional gap opening in the bands close to the Γ point [21,43]. Symmetry-resolved Raman spectroscopy can provide additional information here using the momentum resolution provided by the selection rules. To this end, we look at the initial slopes of the electronic part of the spectra.

As shown in Figs. 4(a)–4(c), different symmetries project individual parts of the BZ [36,44]. The vertices given by the hexagonal symmetry of 1T-TaS₂ are derived in Appendix C. The A_{1g} vertex mainly highlights the area around the Γ point while the E_g vertices predominantly project the BZ boundaries. The opening of a gap at the Fermi level reduces N_F , leading to an increase of the resistivity in the case of 1T-TaS₂. This reduction of N_F manifests itself also in the Raman spectra which, to zeroth order, are proportional to N_F [35,44]. As a result, the initial slope changes as shown Figs. 4(d) and 4(e), which zoom in on the low-energy region of the spectra from Fig. 1. The initial slope of the Raman response is $R \lim_{\Omega \rightarrow 0} \frac{\partial \chi''}{\partial \Omega} \propto N_F \tau_0$, where R incorporates only experimental factors [44]. The electronic relaxation $\Gamma_0^* \propto (N_F \tau_0)^{-1}$ is proportional to the dc resistivity $\rho(T)$ [45]. If a gap opens up there is vanishing intensity at $T = 0$ below the gap edge for an isotropic gap. At finite temperature there are thermally excited quasiparticles which scatter. Thus, there is a linear increase at low energies [35]. The black lines in Figs. 4(d)–4(g) represent the initial slopes and their temperature dependences. The lines comprise carrier relaxation and gap effects, and we focus only on the relative changes.

Starting in the IC-CDW phase at $T = 370 \text{ K}$ [Fig. 4(d)] the initial slope is higher for the E_g spectrum than for A_{1g} symmetry. While the CDW gap started to open already at

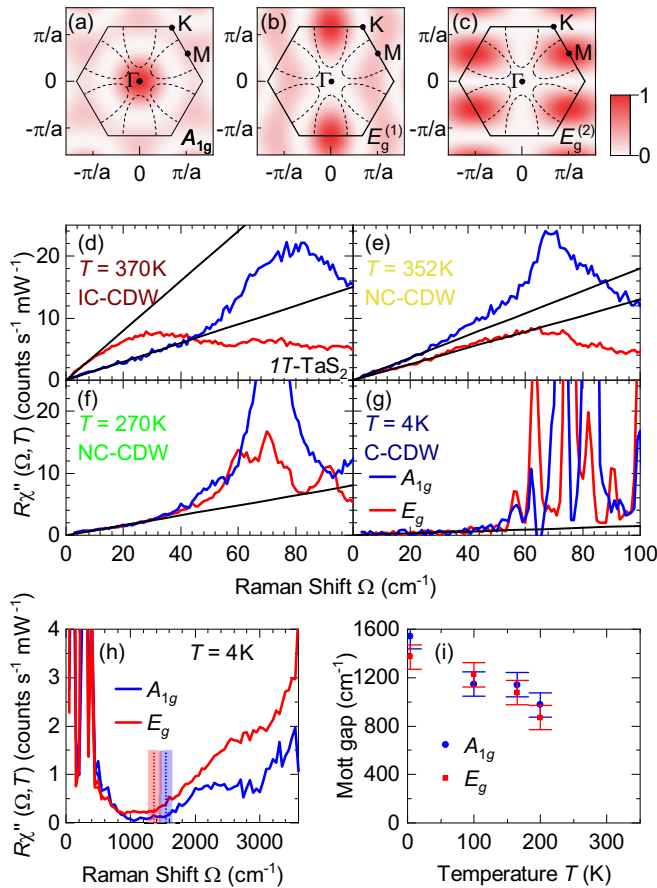


FIG. 4. Evolution of the gaps. (a)–(c) Squared Raman vertices and Fermi surface of $1T\text{-TaS}_2$ for the indicated symmetries in the normal phase above T_C . The derivation of Raman vertices is presented in Appendix C. (d)–(g) Low-energy Raman spectra for A_{1g} symmetry (blue) and E_g symmetries (red) at temperatures as indicated. The spectra shown are zooms on the data shown in Fig. 1. The black lines highlight the initial slope of the spectra. (h) High-energy spectra at 4 K. Vertical dashed lines and colored bars indicate the approximate size and error bars of the Mott gap for the correspondingly colored spectrum. (i) Temperature dependence of the Mott gap Δ_μ ($\mu = A_{1g}, E_g$).

554 K around the M points [43], which are highlighted by the E_g vertex, the Fermi surface projected by the E_g vertex continues to exist. Thus, we may interpret the different slopes as a manifestation of a momentum-dependent gap in the IC-CDW phase and assume overall intensity effects to be symmetry independent for all temperatures. At $T = 352$ K [Fig. 4(e)] the slope for E_g symmetry is substantially reduced to below the A_{1g} slope due to a strong increase of the CDW gap in the commensurate regions [43] which emerge upon entering the NC-CDW phase. Further cooling also decreases the slope for the A_{1g} spectrum, as the Mott gap around the Γ point starts to open within the continuously growing C-CDW domains [40,41]. Below $T = 270$ K the initial slopes are identical for both symmetries and decrease with temperature. Apparently, the Mott gap opens up on the entire Fermi surface in direct correspondence with the increase of the resistivity by approximately an order of magnitude [3]. Finally, at the lowest temperature close to 4 K the initial slopes drop to almost zero

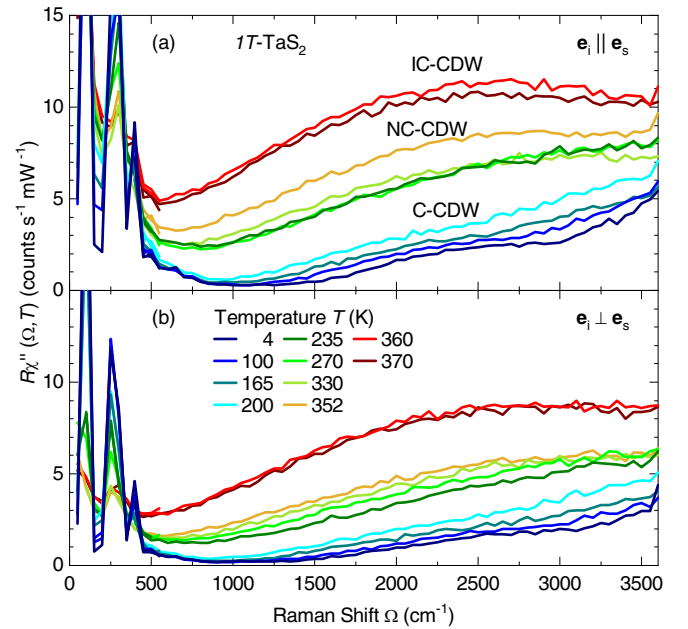


FIG. 5. Raman spectra up to high energies for (a) parallel and (b) crossed polarizations of the incident and scattered light at temperatures as given in the legend.

[Fig. 4(g)], indicating vanishing conductivity or fully gapped bands in the entire BZ.

Concomitantly, and actually more intuitive for the opening of a gap, we observe the loss of intensity in the Raman spectra below a threshold at an energy Ω_{gap} . Below 30 cm^{-1} the intensity is smaller than $0.2 \text{ counts}(\text{mW s})^{-1}$ [Fig. 4(g)] and still smaller than $0.3 \text{ counts}(\text{mW s})^{-1}$ up to 1500 cm^{-1} [Fig. 4(h)]. For a superconductor or a CDW system the threshold is given by 2Δ , where Δ is the single-particle gap, and a pileup of intensity for higher energies, $\Omega > 2\Delta$ [44]. A pileup of intensity cannot be observed here. Rather, the overall intensity is further reduced with decreasing temperature as shown in Figs. 5 and 6 in Appendixes A and B. In particular, the reduction occurs in distinct steps between the phases and continuous inside the phases with the strongest effect in the C-CDW phase below approximately 210 K (Fig. 5). In a system as clean as $1T\text{-TaS}_2$ the missing pileup in the C-CDW phase is surprising and argues for an alternative interpretation.

In a Mott system, the gap persists to be observable but the pileup is not a coherence phenomenon and has not been observed yet. In fact, the physics is quite different, and the conduction band is split symmetrically about the Fermi energy E_F into a lower and an upper Hubbard band. Thus in the case of Mott-Hubbard physics the experimental signatures are more such as those expected for an insulator or semiconductor having a small gap, where at $T = 0$ there is a range without intensity and an interband onset with a band-dependent shape. At finite temperature there are thermal excitations inside the gap. For $1T\text{-TaS}_2$ at the lowest accessible temperature, both symmetries exhibit a flat, nearly vanishing electronic continuum below a slightly symmetry-dependent threshold (superposed by the phonon lines at low energies). Above the threshold a weakly structured increase is observed. We interpret this onset as the distance of the lower

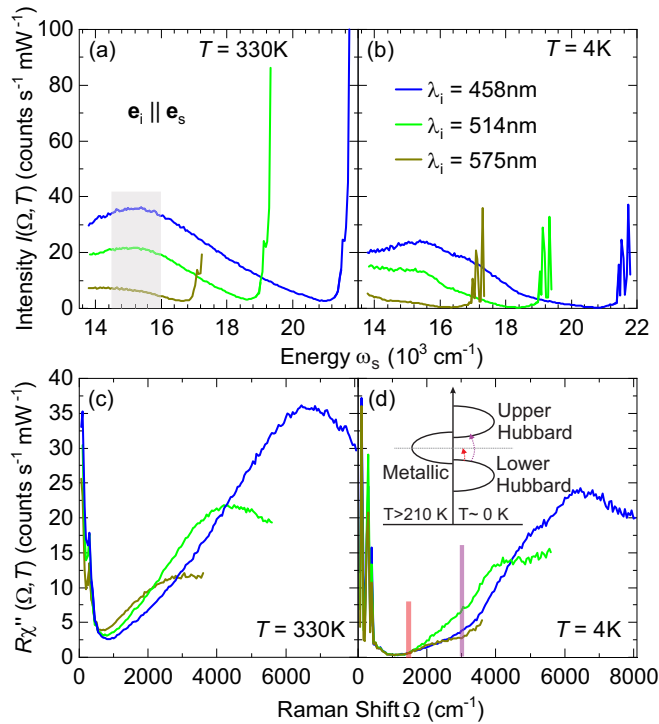


FIG. 6. Luminescence contribution to the Raman data. (a), (b) Intensity as a function of the absolute frequency for (a) $T = 330$ K and (b) $T = 4$ K. The approximate peak maximum of the contribution attributed to luminescence is highlighted by the gray shaded area. (c), (d) Raman susceptibility calculated from (a) and (b), respectively, shown as a function of frequency (Raman) shift. The luminescence peak appears at different Raman shifts depending on the wavelength of the laser light. At $T = 4$ K the spectra are identical up to 1600 cm^{-1} for all laser light wavelengths.

Hubbard band from the Fermi energy E_F or half of the distance between the lower and the upper Hubbard band, shown as vertical dashed lines at 1350 – 1550 $\text{cm}^{-1} \equiv 170$ – 190 meV [Fig. 4(h)]. The energy is in good agreement with gap obtained from the in-plane angle-resolved photoemission spectroscopy (ARPES) [43], scanning tunneling spectroscopy [46], and infrared spectroscopy [13] which may be compared directly with our Raman results measured with in-plane polarizations. Upon increasing the temperature the size of the gap shrinks uniformly in both symmetries [Fig. 4(i)] and may point to an onset above the C-CDW phase transition, consistent with the result indicated by the initial slope. However, we cannot track the development of the gap into the NC-CDW phase as an increasing contribution of luminescence (see Appendix B) overlaps with the Raman data.

Recently, it was proposed on the basis of DFT calculations that $1T$ -TaS₂ orders also along the c axis perpendicular to the planes in the C-CDW state [24,25]. This quasi-one-dimensional (1D) coupling is unexpectedly strong and the resulting metallic band is predicted to have a width of approximately 0.5 eV. For specific relative ordering of the star of David patterns along the c axis this band develops a gap of 0.15 eV at E_F [25], which is intriguingly close to the various experimental observations. However, since our light polarizations are strictly in plane, we have to conclude that the gap

observed here (and presumably in the other experiments) is an in-plane gap. Our experiment cannot detect an out-of-plane gap. Thus, neither a quasimetallic dispersion along the c axis nor a gap in this band along k_z may be excluded in the C-CDW phase. However, there is compelling evidence for a Mott-like gap in the layers rather than a CDW gap.

IV. CONCLUSIONS

We have presented a study of the various charge density wave regimes in $1T$ -TaS₂ by inelastic light scattering, supported by *ab initio* calculations. The spectra of lattice excitations in the commensurate CDW (C-CDW) phase determine the unit cell symmetry to be $P\bar{3}$, indicating trigonal or hexagonal stacking of the “star-of-David” structure. The high-temperature spectra of the incommensurate CDW (IC-CDW) state are dominated by a projection of the phonon density of states caused by either a significant electron-phonon coupling or, more likely, the superstructure. The intermediate nearly commensurate (NC-CDW) phase is confirmed to be a mixed regime of commensurate and incommensurate regions contributing to the phonon spectra below an onset temperature $T_{\text{NC}} \approx 352$ – 360 K, in good agreement with previously reported values. At the lowest measured temperatures, the observation of a virtually clean gap without a redistribution of spectral weight from low to high energies below T_C argues for the existence of a Mott metal-insulator transition at a temperature of order 100 K. The magnitude of the gap is found to be $\Omega_{\text{gap}} \approx 170$ – 190 meV and has little symmetry, thus momentum, dependence, in agreement with earlier ARPES results [37]. At 200 K, on the high-temperature end of the C-CDW phase, the gap shrinks to $\sim 60\%$ of its low-temperature value. Additionally, the progressive filling of the CDW gaps by thermal excitations is tracked via the initial slope of the spectra, and indicates that the Mott gap opens primarily on the parts of the Fermi surface closest to the Γ point.

Our results demonstrate the potential of using inelastic light scattering to probe the momentum dependence and energy scale of changes in the electronic structure driven by low-temperature collective quantum phenomena. This opens perspectives to investigate the effect of hybridization on collective quantum phenomena in heterostructures composed of different 2D materials, e.g., alternating T and H monolayers as in the $4Hb$ -TaS₂ phase [47].

ACKNOWLEDGMENTS

The authors acknowledge funding provided by the Institute of Physics Belgrade through the grant by the Ministry of Education, Science and Technological Development of the Republic of Serbia. The work was supported by the Science Fund of the Republic of Serbia, PROMIS, No. 6062656, StrainedFeSC, and by Research Foundation-Flanders (FWO). J.B. acknowledges support of a postdoctoral fellowship of the FWO, and of the Erasmus + program for staff mobility and training (KA107, 2018) for a research stay at the Institute of Physics Belgrade, during which part of the work was carried out. The computational resources and services used for the first-principles calculations in this work were provided by the VSC (Flemish Supercomputer Center), funded by the

FWO and the Flemish Government – department EWI. Work at Brookhaven is supported by the U.S. DOE under Contract No. DESC0012704. A.B. and R.H. acknowledge support by the German research foundation (DFG) via Projects No. Ha2071/12-1 and No. 107745057 – TRR 80 and by the DAAD via the project-related personal exchange program PPP with Serbia Grant No. 57449106.

APPENDIX A: RAW DATA

Figure 5 shows Raman spectra at temperatures ranging from $T = 4$ to 370 K for parallel [Fig. 5(a)] and crossed [Fig. 5(b)] in-plane light polarizations. The spectra were measured in steps of $\Delta\Omega = 50 \text{ cm}^{-1}$ and a resolution of $\sigma \approx 20 \text{ cm}^{-1}$. Therefore neither the shapes nor the positions of the phonon lines below 500 cm^{-1} may be resolved. All spectra reach a minimum in the range from 500 to 1600 cm^{-1} . At energies above 500 cm^{-1} the overall intensities are strongly temperature dependent and decreasing with decreasing temperature. Three clusters of spectra are well separated according to the phases they belong to.

In the C-CDW phase ($T \leq 200 \text{ K}$, blue lines) the spectra start to develop substructures at 1500 and 3000 cm^{-1} . The spectra at 200 K increase almost linearly with energy. The spectra of the NC- and IC-CDW phases exhibit a broad maximum centered in the region of $2200\text{--}3200 \text{ cm}^{-1}$ which may be attributed to luminescence (see Appendix B). For clarification we measured a few spectra with various laser lines for excitation.

APPENDIX B: LUMINESCENCE

Figure 6 shows Raman spectra measured with parallel light polarizations for three different wavelengths λ_i of the incident laser light. Figures 6(a) and 6(b) depict the measured intensity I (without the Bose factor) as a function of the absolute frequency $\tilde{\nu}$ of the scattered light.

At high temperature [$T = 330 \text{ K}$, Fig. 6(a)] a broad peak can be seen for all λ_i which is centered at a fixed frequency of $15\,200 \text{ cm}^{-1}$ of the scattered photons (gray shaded area). The peak intensity decreases for increasing λ_i (decreasing energy). Correspondingly, this peak's center depends on the laser wavelength in the spectra shown as a function of the Raman shift [Fig. 6(c)]. This behavior indicates that the origin of this excitation is likely to be luminescence where transitions at fixed absolute final frequencies are expected.

At low temperature [Fig. 6(b)] we can no longer find a structure at a fixed absolute energy. Rather, as already indicated in the main part, the spectra develop additional, yet weak, structures which are observable in all spectra but are particularly pronounced for blue excitation. For green and yellow excitation the spectral range of the spectrometer, limited to 732 nm, is not wide enough for a deeper insight into the luminescence contributions (at energies different from those at high temperature) and no maximum common to all three spectra is observed. If these spectra are plotted as a function of the Raman shift, the changes in slope at 1500 and 3000 cm^{-1} are found to be in the same position for all λ_i , values thus arguing for inelastic scattering rather than luminescence. Since we do currently not have the appropriate experimental

tools for an in-depth study, our interpretation is preliminary although supported by the observations in Fig. 6(d).

As shown in the inset of Fig. 6(d) we propose a scenario on the basis of Mott physics. In the C-CDW phase the reduced bandwidth is no longer the largest energy and the Coulomb repulsion U becomes relevant [22] and splits the conduction band into a lower and upper Hubbard band. We assume that the onset of scattering at 1500 cm^{-1} corresponds to the distance of the highest energy of the lower Hubbard band to the Fermi energy E_F . The second onset corresponds then to the distance between the highest energy of the lower Hubbard band and the lowest energy of the upper Hubbard band. An important question needs to be answered: Into which unoccupied states right above E_F does the first process scatter electrons? We may speculate that some DOS is provided by the metallic band dispersing along k_z or by the metallic domain walls between the different types of ordering patterns along the c axis observed recently by tunneling spectroscopy [46]. These quasi-1D domain walls would provide the states required for the onset of scattering at high energy but are topologically too small for providing enough density of states for a measurable intensity at low energy [Fig. 4(g)] in a location-integrated experiment such as Raman scattering.

APPENDIX C: DERIVATION OF THE RAMAN VERTICES

Phenomenologically, the Raman vertices can be derived based on lattice symmetry, which are proportional to the Brillouin zone harmonics. They are a set of functions that exhibit the symmetry and periodicity of the lattice structure proposed by Allen [48]. These functions make the k -space sums and energy integrals more convenient than that of the Cartesian basis or the spherical harmonics basis, especially for those materials who have anisotropic and/or multiple Fermi pockets. The three Cartesian components of the Fermi velocity v_k are recommended to generate this set of functions since they inherit the symmetry and periodicity of the crystal lattice naturally. However, in most cases, we do not know the details of band dispersion. A phenomenological method is needed to construct such a set of basis functions. Here, we demonstrate a method based on the group theory. The Brillouin zone harmonics can be obtained by the projection operation on specific trial functions.

For a certain group G with symmetry elements R and symmetry operators \hat{P}_R , it can be described by several irreducible representations Γ_n , where n labels the representation. For each irreducible representation, there are corresponding basis functions $\Phi_{\Gamma_n}^j$ that can be used to generate representation matrices for a particular symmetry. Here, j labels the component or partner of the representations. For an arbitrary function F , we have

$$F = \sum_{\Gamma_n} \sum_j f_j^{\Gamma_n} \Phi_{\Gamma_n}^j. \quad (\text{C1})$$

According to the group theory, we can always define a projection operator by the relation [49]

$$\hat{P}^{\Gamma_n} = \frac{d}{N} \sum_R \chi^{\Gamma_n}(R) * \hat{P}_R, \quad (\text{C2})$$

TABLE III. Symmetry operations \hat{P}_R and corresponding character table of the D_{3d} point group.

\hat{P}_R	x'	y'	z'	$\chi^{\Gamma_n}(R)$	
				A_{1g}	E_g
E	x	y	z	1	2
C_3^1	$-\frac{1}{2}x + \frac{\sqrt{3}}{2}y$	$-\frac{\sqrt{3}}{2}x - \frac{1}{2}y$	z	1	-1
C_3^{-1}	$-\frac{1}{2}x - \frac{\sqrt{3}}{2}y$	$\frac{\sqrt{3}}{2}x - \frac{1}{2}y$	z	1	-1
C_2'	x	$-y$	$-z$	1	0
C_2''	$-\frac{1}{2}x + \frac{\sqrt{3}}{2}y$	$\frac{\sqrt{3}}{2}x + \frac{1}{2}y$	$-z$	1	0
C_2'''	$-\frac{1}{2}x - \frac{\sqrt{3}}{2}y$	$-\frac{\sqrt{3}}{2}x + \frac{1}{2}y$	$-z$	1	0
I	$-x$	$-y$	$-z$	1	2
S_6^1	$\frac{1}{2}x - \frac{\sqrt{3}}{2}y$	$\frac{\sqrt{3}}{2}x + \frac{1}{2}y$	$-z$	1	-1
S_6^{-1}	$\frac{1}{2}x + \frac{\sqrt{3}}{2}y$	$-\frac{\sqrt{3}}{2}x + \frac{1}{2}y$	$-z$	1	-1
σ_v'	$-x$	y	z	1	0
σ_v''	$\frac{1}{2}x - \frac{\sqrt{3}}{2}y$	$-\frac{\sqrt{3}}{2}x - \frac{1}{2}y$	z	1	0
σ_v'''	$\frac{1}{2}x + \frac{\sqrt{3}}{2}y$	$\frac{\sqrt{3}}{2}x - \frac{1}{2}y$	z	1	0

that satisfies the relation

$$\hat{P}^{\Gamma_n} F = \sum_j f_j^{\Gamma_n} \Phi_{\Gamma_n}^j, \quad (C3)$$

where d is the dimensionality of the irreducible representation Γ_n , N is the number of symmetry operators in the group, and $\chi^{\Gamma_n}(R)$ is the character of the matrix of symmetry operator R in irreducible representation Γ_n . By projection operation on a certain irreducible representation Γ_n , we can directly get its basis functions $\Phi_{\Gamma_n}^j$.

The basis functions are not unique. In specific physical problems, it is useful to use physical insight to guess an appropriate arbitrary function to find the basis functions for specific

problems. $1T$ -TaS₂ belongs to the D_{3d} point group. There are 12 symmetry operators in this group, i.e., E , C_3^1 , C_3^{-1} , C_2' , C_2'' , C_2''' , I , S_6^1 , S_6^{-1} , σ_v' , σ_v'' , σ_v''' . The coordinate transformations after symmetry operations and the corresponding character table are listed in Table III.

In order to simulate the periodicity of the Brillouin zone, trigonometric functions are used as trial functions. According to the parity of the irreducible representations, we can choose an appropriate trigonometric function, e.g., a sine function for odd parity representation and cosine function for even parity representation. The combinations of them are also available.

Here, we use $F = \cos(k_x a)$ as a trial function, where a is the in-plane crystal constant. The basis function of A_{1g} can be derived as

$$\Phi_{A_{1g}}(\mathbf{k}) = \frac{1}{3} \left[\cos(k_x a) + 2 \cos\left(\frac{1}{2}k_x a\right) \cos\left(\frac{\sqrt{3}}{2}k_y a\right) \right]. \quad (C4)$$

With the same method, we obtain a basis function of E_g as

$$\Phi_{E_g^1}(\mathbf{k}) = \frac{2}{3} \left[\cos(k_x a) - \cos\left(\frac{1}{2}k_x a\right) \cos\left(\frac{\sqrt{3}}{2}k_y a\right) \right]. \quad (C5)$$

Since the E_g is a two-dimensional representation, the projection operation provides only one of the two basis functions of the corresponding subspace. The second function is found based on the subspace invariance under the symmetry operations (e.g., if we operate $\Phi_{E_g^1}$ with C_3^1 symmetry, the result can be presented as a linear combination of $\Phi_{E_g^1}$ and $\Phi_{E_g^2}$). Thus we obtain

$$\Phi_{E_g^2}(\mathbf{k}) = 2 \sin\left(\frac{1}{2}k_x a\right) \sin\left(\frac{\sqrt{3}}{2}k_y a\right). \quad (C6)$$

- [1] J. C. Tsang, J. E. Smith, M. W. Shafer, and S. F. Meyer, Raman spectroscopy of the charge-density-wave state in $1T$ - and $2H$ -TaSe₂, *Phys. Rev. B* **16**, 4239 (1977).
- [2] C. J. Sayers, H. Hedayat, A. Ceraso, F. Musser, M. Cattelan, L. S. Hart, L. S. Farrar, S. Dal Conte, G. Cerullo, C. Dallera, E. Da Como, and E. Carpena, Coherent phonons and the interplay between charge density wave and Mott phases in $1T$ -TaSe₂, *Phys. Rev. B* **102**, 161105(R) (2020).
- [3] A. J. Wilson, J. F. D. Salvo, and S. Mahajan, Charge-density waves and superlattices in the metallic layered transition metal dichalcogenides, *Adv. Phys.* **24**, 117 (1975).
- [4] C. B. Scruby, P. M. Williams, and G. S. Parry, The role of charge density waves in structural transformations of $1T$ -TaS₂, *Philos. Mag.* **31**, 255 (1975).
- [5] R. E. Thomson, B. Burk, A. Zettl, and J. Clarke, Scanning tunneling microscopy of the charge-density-wave structure in $1T$ -TaS₂, *Phys. Rev. B* **49**, 16899 (1994).
- [6] W. Wen, C. Dang, and L. Xie, Photoinduced phase transitions in two-dimensional charge-density-wave $1T$ -TaS₂, *Chin. Phys. B* **28**, 058504 (2019).
- [7] D. Svetin, I. Vaskivskiy, S. Brazovskii, Mertelj, and D. Mihailovic, Three-dimensional resistivity and switching between correlated electronic states in $1T$ -TaS₂, *Sci. Rep.* **7**, 46048 (2017).
- [8] D. Svetin, I. Vaskivskiy, P. Sutar, E. Goresnik, J. Gospodaric, T. Mertelj, and D. Mihailovic, Transitions between photoinduced macroscopic quantum states in $1T$ -TaS₂ controlled by substrate strain, *Appl. Phys. Express* **7**, 103201 (2014).
- [9] G. Liu, B. Debnath, T. R. Pope, T. T. Salguero, R. K. Lake, and A. A. Balandin, A charge-density wave oscillator based on an integrated tantalum disulfide-boron nitride-graphene device operating at room temperature, *Nat. Nanotechnol.* **11**, 845 (2016).
- [10] R. Salgado, A. Mohammadzadeh, F. Kargar, A. Geremew, C.-Y. Huang, M. A. Bloodgood, S. Romyantsev, T. T. Salguero, and A. A. Balandin, Low-frequency noise spectroscopy of charge-density-wave phase transitions in vertical quasi-2D $1T$ -TaS₂ devices, *Appl. Phys. Express* **12**, 037001 (2019).
- [11] Z. X. Wang, Q. M. Liu, L. Y. Shi, S. J. Zhang, T. Lin, T. Dong, D. Wu, and N. L. Wang, Photoinduced hidden CDW state and relaxation dynamics of $1T$ -TaS₂ probed by time-resolved terahertz spectroscopy, *arXiv:1906.01500*.
- [12] L. Stojchevska, I. Vaskivskiy, T. Mertelj, P. Kusar, D. Svetin, S. Brazovskii, and D. Mihailovic, Ultrafast switching to a stable

- hidden quantum state in an electronic crystal, *Science* **344**, 177 (2014).
- [13] L. V. Gasparov, K. G. Brown, A. C. Wint, D. B. Tanner, H. Berger, G. Margaritondo, R. Gaál, and L. Forró, Phonon anomaly at the charge ordering transition in $1T$ -TaS₂, *Phys. Rev. B* **66**, 094301 (2002).
- [14] O. R. Albertini, R. Zhao, R. L. McCann, S. Feng, M. Terrones, J. K. Freericks, J. A. Robinson, and A. Y. Liu, Zone-center phonons of bulk, few-layer, and monolayer $1T$ -TaS₂: Detection of commensurate charge density wave phase through Raman scattering, *Phys. Rev. B* **93**, 214109 (2016).
- [15] S. Uchida and S. Sugai, Infrared and raman studies on a commensurate CDW states in transition metal dichalcogenides, *Physica B+C* **105**, 393 (1981).
- [16] R. Brouwer and F. Jellinek, The low-temperature superstructures of $1T$ -TaSe₂ and $2H$ -TaSe₂, *Physica B+C* **99**, 51 (1980).
- [17] A. Zong, X. Shen, A. Kogar, L. Ye, C. Marks, D. Chowdhury, T. Rohwer, B. Freelon, S. Weathersby, R. Li, J. Yang, J. Checkelsky, X. Wang, and N. Gedik, Ultrafast manipulation of mirror domain walls in a charge density wave, *Sci. Adv.* **4**, eaau5501 (2018).
- [18] J. R. Duffay and R. D. Kirby, Raman scattering from $1T$ -TaS₂, *Solid State Commun.* **20**, 617 (1976).
- [19] T. Hirata and F. S. Ohuchi, Temperature dependence of the Raman spectra of $1T$ -TaS₂, *Solid State Commun.* **117**, 361 (2001).
- [20] S. L. L. M. Ramos, R. Plumadore, J. Boddison-Chouinard, S. W. Hla, J. R. Guest, D. J. Gosztola, M. A. Pimenta, and A. Luican-Mayer, Suppression of the commensurate charge density wave phase in ultrathin $1T$ -TaS₂ evidenced by Raman hyperspectral analysis, *Phys. Rev. B* **100**, 165414 (2019).
- [21] B. Sipos, A. F. Kusmartseva, A. Akrap, H. Berger, L. Forró, and E. Tutis, From Mott state to superconductivity in $1T$ -TaS₂, *Nat. Mater.* **7**, 960 (2008).
- [22] P. Fazekas and E. Tosatti, Electrical, structural and magnetic properties of pure and doped $1T$ -TaS₂, *Philos. Mag. B* **39**, 229 (1979).
- [23] E. Martino, A. Pisoni, L. Ćirić, A. Arakcheeva, H. Berger, A. Akrap, C. Putzke, P. J. W. Moll, I. Batistić, E. Tutiš, L. Forró, and K., Preferential out-of-plane conduction and quasi-one-dimensional electronic states in layered $1T$ -TaS₂, *npj 2D Mater. Appl.* **4**, 7 (2020).
- [24] P. Darancet, A. J. Millis, and C. A. Marianetti, Three-dimensional metallic and two-dimensional insulating behavior in octahedral tantalum dichalcogenides, *Phys. Rev. B* **90**, 045134 (2014).
- [25] S.-H. Lee, J. S. Goh, and D. Cho, Origin of the Insulating Phase and First-Order Metal-Insulator Transition in $1T$ -TaS₂, *Phys. Rev. Lett.* **122**, 106404 (2019).
- [26] Y. Ma, Y. Hou, C. Lu, L. Li, and C. Petrovic, Possible origin of nonlinear conductivity and large dielectric constant in the commensurate charge-density-wave phase of $1T$ -TaS₂, *Phys. Rev. B* **97**, 195117 (2018).
- [27] L. J. Li, W. J. Lu, X. D. Zhu, L. S. Ling, Z. Qu, and Y. P. Sun, Fe-doping induced superconductivity in the charge-density-wave system $1T$ -TaS₂, *Europhys. Lett.* **98**, 29902 (2012).
- [28] Y. Liu, R. Ang, W. J. Lu, W. H. Song, L. J. Li, and Y. P. Sun, Superconductivity induced by Se-doping in layered charge-density-wave system $1T$ -TaS_{2-x}Se_x, *Appl. Phys. Lett.* **102**, 192602 (2013).
- [29] R. Ang, Y. Miyata, E. Ieki, K. Nakayama, T. Sato, Y. Liu, W. J. Lu, Y. P. Sun, and T. Takahashi, Superconductivity and bandwidth-controlled Mott metal-insulator transition in $1T$ -TaS_{2-x}Se_x, *Phys. Rev. B* **88**, 115145 (2013).
- [30] M. Bovet, D. Popović, F. Clerc, C. Koitzsch, U. Probst, E. Bucher, H. Berger, D. Naumović, and P. Aebi, Pseudogapped Fermi surfaces of $1T$ -TaS₂ and $1T$ -TaSe₂: A charge density wave effect, *Phys. Rev. B* **69**, 125117 (2004).
- [31] X. Gonze, B. Amadon, P.-M. Anglade, J.-M. Beuken, F. Bottin, P. Boulanger, F. Bruneval, D. Caliste, R. Caracas, M. Côté, T. Deutsch, L. Genovese, P. Ghosez, M. Giantomassi, S. Goedecker, D. Hamann, P. Hermet, F. Jollet, G. Jomard, S. Leroux *et al.*, ABINIT: First-principles approach to material and nanosystem properties, *Comput. Phys. Commun.* **180**, 2582 (2009).
- [32] S. Goedecker, M. Teter, and J. Hutter, Separable dual-space Gaussian pseudopotentials, *Phys. Rev. B* **54**, 1703 (1996).
- [33] M. Krack, Pseudopotentials for H to Kr optimized for gradient-corrected exchange-correlation functionals, *Theor. Chem. Acc.* **114**, 145 (2005).
- [34] X. Gonze, D. C. Allan, and M. P. Teter, Dielectric Tensor, Effective Charges, and Phonons in α -Quartz by Variational Density-Functional Perturbation Theory, *Phys. Rev. Lett.* **68**, 3603 (1992).
- [35] A. Zawadowski and M. Cardona, Theory of Raman scattering on normal metals with impurities, *Phys. Rev. B* **42**, 10732 (1990).
- [36] N. Lazarević and R. Hackl, Fluctuations and pairing in Fe-based superconductors: Light scattering experiments, *J. Phys.: Condens. Matter* **32**, 413001 (2020).
- [37] K. Rossnagel, On the origin of charge-density waves in select layered transition-metal dichalcogenides, *J. Phys.: Condens. Matter* **23**, 213001 (2011).
- [38] R. Shuker and R. W. Gammon, Raman-Scattering Selection-Rule Breaking and the Density of States in Amorphous Materials, *Phys. Rev. Lett.* **25**, 222 (1970).
- [39] A. Baum, A. Milosavljević, N. Lazarević, M. M. Radonjić, B. Nikolić, M. Mitschek, Z. I. Maranloo, M. Šćepanović, M. Grujić-Brojčin, N. Stojilović, M. Opel, A. Wang, C. Petrovic, Z. V. Popović, and R. Hackl, Phonon anomalies in FeS, *Phys. Rev. B* **97**, 054306 (2018).
- [40] A. Spijkerman, J. L. de Boer, A. Meetsma, G. A. Wiegers, and S. van Smaalen, X-ray crystal-structure refinement of the nearly commensurate phase of $1T$ -TaS₂ in (3 + 2)-dimensional superspace, *Phys. Rev. B* **56**, 13757 (1997).
- [41] R. He, J. Okamoto, Z. Ye, G. Ye, H. Anderson, X. Dai, X. Wu, J. Hu, Y. Liu, W. Lu, Y. Sun, A. N. Pasupathy, and A. W. Tsen, Distinct surface and bulk charge density waves in ultrathin $1T$ -TaS₂, *Phys. Rev. B* **94**, 201108(R) (2016).
- [42] G. Grüner, The dynamics of charge-density waves, *Rev. Mod. Phys.* **60**, 1129 (1988).
- [43] C. Sohrt, A. Stange, M. Bauer, and K. Rossnagel, How fast can a Peierls–Mott insulator be melted?, *Faraday Discuss.* **171**, 243 (2014).
- [44] T. P. Devereaux and R. Hackl, Inelastic light scattering from correlated electrons, *Rev. Mod. Phys.* **79**, 175 (2007).
- [45] M. Opel, R. Nemetschek, C. Hoffmann, R. Philipp, P. F. Müller, R. Hackl, I. Tüttő, A. Erb, B. Revaz, E. Walker, H. Berger, and L. Forró, Carrier relaxation, pseudogap, and superconducting

- gap in high- T_c cuprates: A Raman scattering study, *Phys. Rev. B* **61**, 9752 (2000).
- [46] J. Skolimowski, Y. Gerasimenko, and R. Žitko, Mottness Collapse without Metallization in the Domain Wall of the Triangular-Lattice Mott Insulator $1T$ -TaS₂, *Phys. Rev. Lett.* **122**, 036802 (2019).
- [47] A. Ribak, R. M. Skiff, M. Mograbi, P. K. Rout, M. H. Fischer, J. Ruhman, K. Chashka, Y. Dagan, and A. Kanigel, Chiral superconductivity in the alternate stacking compound $4Hb$ -TaS₂, *Sci. Adv.* **6**, eaax9480 (2020).
- [48] P. B. Allen, Fermi-surface harmonics: A general method for nonspherical problems. Application to Boltzmann and Eliashberg equations, *Phys. Rev. B* **13**, 1416 (1976).
- [49] M. S. Dresselhaus, G. Dresselhaus, and A. Jorio, *Group Theory* (Springer, Berlin, 2008).

Short-Range Order in VI_3

Sanja Djurdjic Mijin, A. M. Milinda Abeykoon, Andrijana Šolajić, Ana Milosavljević, Jelena Pešić, Yu Liu, Cedimir Petrovic, Zoran V. Popović, and Nenad Lazarević*

Cite This: *Inorg. Chem.* 2020, 59, 16265–16271

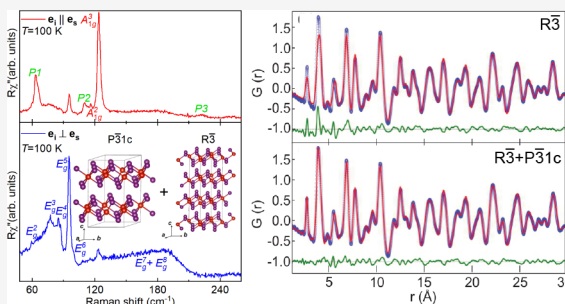
Read Online

ACCESS |

Metrics & More

Article Recommendations

ABSTRACT: We present a detailed investigation of the crystal structure of VI_3 , a two-dimensional van der Waals material of interest for studies of low-dimensional magnetism. As opposed to the average crystal structure that features $R\bar{3}$ symmetry of the unit cell, our Raman scattering and X-ray atomic pair distribution function analysis supported by density functional theory calculations point to the coexistence of short-range ordered $P\bar{3}1c$ and long-range ordered $R\bar{3}$ phases. The highest-intensity peak, A_{1g} , exhibits a moderate asymmetry that might be traced back to the spin–phonon interactions, as in the case of CrI_3 .



INTRODUCTION

A well-known family of transition metal trihalides (TMTs) MX_3 ($X = \text{Cr}, \text{B}, \text{or I}$) have received a great deal of attention due to potential existence of two-dimensional (2D) ferromagnetism,^{1–6} which has been confirmed in CrI_3 .^{7,8} The similar crystal structure and magnetic properties of CrI_3 and VI_3 fostered a belief that the same might be found in the latter. In fact, magnetization measurements revealed the 2D ferromagnetic nature of VI_3 with a Currie temperature (T_c) of around 50 K.^{9,10} Contrary to a layer-dependent ferromagnetism in CrI_3 ,¹¹ the first-principles calculations predict that ferromagnetism in VI_3 persists down to a single layer,⁹ making it a suitable candidate for engineering 2D spintronic devices. Resistivity measurements showed VI_3 is an insulator with an optical band gap of ~ 0.6 eV.^{9,12}

Whereas laboratory X-ray diffraction studies reported three possible high-temperature VI_3 unit cell symmetries,^{9,12–14} high-resolution synchrotron X-ray diffraction confirmed a rhombohedral $R\bar{3}$ space group.¹⁰ A very recently published Raman spectroscopy study indicated that the VI_3 crystal structure can be described within the C_{2h} point group.¹⁵ All results agree on the existence of a phase transition at a temperature of 79 K. However, the subtle¹² structural changes below 79 K are still under debate.

The long-range magnetic order in ultrathin 2D van der Waals (vdW) crystals stems from strong uniaxial anisotropy, in contrast to materials with isotropic exchange interactions where order parameters are forbidden.^{16–18} 2D vdW magnetic materials are of interest both as examples of exotic magnetic order¹⁹ and for potential applications in spintronic technology.^{2,4,20,21}

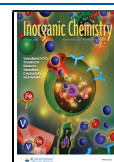
Atomically thin flakes of CrCl_3 have a magnetic transition temperature that is different from that of bulk crystals possibly

due to the different crystal structure of the monolayer and ultrathin crystals when compared to bulk.^{22,23} Similar observations were made on CrI_3 monolayers.^{22,24,25} It has been proposed²³ that the second anomaly in heat capacity in bulk CrCl_3 arises due to regions close to the surface that host a different crystal structure when compared to bulk;^{26,27} however, due to the substantial mass fraction detected in heat capacity measurements, this could also reflect differences between the short-range order and long-range crystallographic order of Bragg planes. The short-range order is determined by the space group that is energetically favorable for a monolayer or a few layers, whereas the long-range crystallographic order is established over large packing lengths.

In this paper, we present an experimental Raman scattering study of the bulk VI_3 high-temperature structure, supported by density functional theory (DFT) calculations and the X-ray atomic pair distribution function (PDF) analysis. The comparison between the Raman experiment and DFT calculations for each of the previously reported space groups suggested that the high-temperature lattice vibrations of bulk VI_3 are consistent with a $P\bar{3}1c$ trigonal structure. Nine ($2A_{1g} + 7E_g$) of 12 observed peaks were assigned on the basis of factor group analysis (FGA) and DFT calculations. The PDF analysis indicated the coexistence of two crystallographic phases at two different interatomic distances, short-range ordered $P\bar{3}1c$ and

Received: July 12, 2020

Published: October 23, 2020



long-range ordered $R\bar{3}$, as two segregated phases and/or as randomly distributed short-range ordered $P\bar{3}1c$ domains in the long-range ordered $R\bar{3}$ lattice. Raman data displayed a moderate asymmetry of the A_{1g}^3 phonon line. This behavior was attributed to the spin–phonon interaction, similar to the case for CrI_3 . The additional peaks in our spectra obey A_g selection rules and can be described in terms of overtones, as well as the A_{2g} silent modes “activated” by the symmetry breaking.

EXPERIMENTAL AND COMPUTATIONAL DETAILS

The preparation of single-crystal VI_3 samples used in this study is presented elsewhere.¹⁰ For the Raman scattering experiment, a Tri Vista 557 spectrometer was used in the backscattering micro-Raman configuration with a 1800/1800/2400 grooves/mm diffraction grating combination. A Coherent Ar^+/Kr^+ ion laser with a 514 nm line was used as an excitation source. Laser beam focusing was achieved through the microscope objective with 50 \times magnification. The direction of the incident (scattered) light coincides with the crystallographic c axis. The sample, cleaved in open air, was held inside a KONTI CryoVac continuous helium flow cryostat with a 0.5 mm thick window. Raman scattering measurements were performed under high vacuum (10^{-6} mbar). All of the obtained Raman spectra were corrected by the Bose factor. The spectrometer resolution is comparable to the Gaussian width of 1 cm^{-1} .

PDF and wide-angle X-ray scattering measurements were carried out in capillary transmission geometry using a PerkinElmer amorphous silicon area detector placed 206 and 983 mm downstream from the sample, respectively, at beamline 28-ID-1 (PDF) of National Synchrotron Light Source II at Brookhaven National Laboratory. The setup utilized a 74.3 keV ($\lambda = 0.1668\text{ \AA}$) X-ray beam.

Two-dimensional diffraction data were integrated using the Fit2D software package.²⁸ Data reduction was performed to obtain experimental PDFs ($Q_{\text{max}} = 26\text{ \AA}^{-1}$) using the xPDFsuite software package.²⁹ The Rietveld and PDF analyses were carried out using GSAS-II³⁰ and PDFgui³¹ software packages, respectively.

Density functional theory calculations were performed using the Quantum Espresso software package,³² employing the PBE exchange–correlation functional³³ and PAW pseudopotentials.^{34,35} All calculations are spin-polarized. The cutoff for wave functions and the charge density were set to 48 and 650 Ry, respectively. The k -points were sampled using the Monkhorst–Pack scheme, on a $6 \times 6 \times 6$ Γ -centered grid for $R\bar{3}$ and $C2/m$ structures and a $12 \times 12 \times 8$ grid for the $P\bar{3}1c$ structure. Optimization of the lattice parameters and atomic positions in the unit cell was performed until the interatomic forces were $<10^{-6}$ Ry/ \AA . To obtain more accurate lattice parameters, treatment of the van der Waals interactions is included using the Grimme-D2 correction. The correlation effects are treated with the Hubbard U correction (LDA+ U), using a rotationally invariant formulation implemented in QE,³⁶ where $U = 3.68\text{ eV}$. Band structure plots are calculated at 800 k -points on the chosen path over high-symmetry points. Phonon frequencies were calculated with the linear response method, as implemented in the -homon part of Quantum Espresso.

RESULTS AND DISCUSSION

The first reported results for VI_3 , dating from the 1950s,^{37–39} indicated that VI_3 adopts a honeycomb layer-type BiI_3 structure described with space group $R\bar{3}$, which is a structure common in TMTs, also found in the low-temperature phase of CrI_3 .^{6,40}

There have been several proposed unit cell symmetries for VI_3 in the literature: $R\bar{3}$,^{12,13} $C2/m$,¹⁴ and $P\bar{3}1c$.⁹ Schematic representations of the $P\bar{3}1c$, $R\bar{3}$, and $C2/m$ crystal structures are depicted in Figure 1. The corresponding crystallographic unit cell parameters, previously reported, are listed in Table 1.

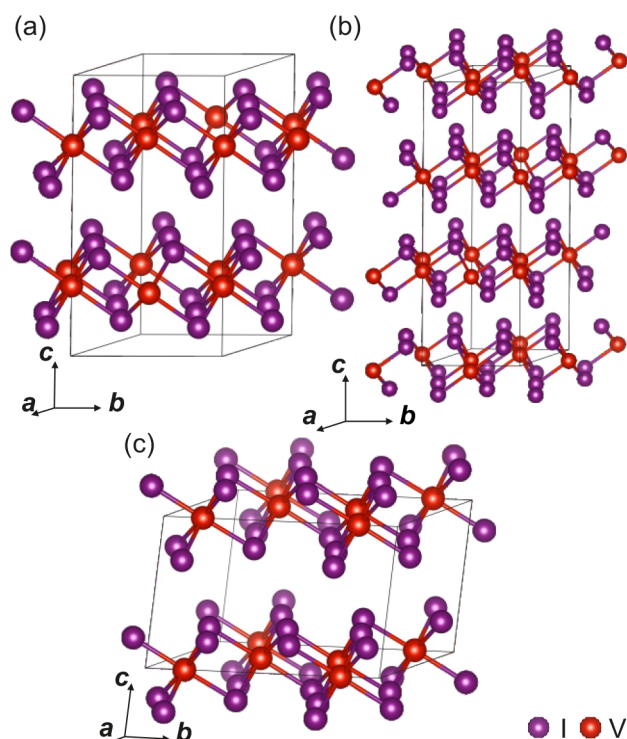


Figure 1. Schematic representation of the high-temperature (a) $P\bar{3}1c$, (b) $R\bar{3}$, and (c) $C2/m$ structures of VI_3 . Black solid lines represent unit cells.

Each of the suggested symmetries implies a different distribution of Raman active modes.

According to FGA, eight ($4A_g + 4E_g$), 11 ($3A_{1g} + 8E_g$), and 12 ($6A_g + 6B_g$) Raman active modes are expected to be observed in the light scattering experiment for $R\bar{3}$, $P\bar{3}1c$, and $C2/m$ crystal structures, respectively. Wyckoff positions, irreducible representations, and corresponding tensors of Raman active modes for each space group are listed in Table 2.

The first step in determining the crystal symmetry from the light scattering experiment is to compare the expected and observed Raman active modes, shown in Figure 2. The red solid line represents the spectrum measured in the parallel polarization configuration, whereas the blue line corresponds to the cross polarization configuration. Five of 12 observed peaks emerge only in parallel, whereas five peaks and a broad peak-like structure can be observed for both polarization configurations. The emergence of the 123.4 cm^{-1} peak in the cross polarization can be understood as a “leakage” of the A_{1g}^3 mode due to a possible finite c axis projection and/or the presence of defects.

Now the peaks that appear only for the parallel polarization configuration can be assigned as either A_{1g} or A_g symmetry modes, assuming the light polarization direction along the main crystal axis of the $C2/m$ structure for the later. On the basis of the FGA for possible symmetry group candidates, the remaining Raman active modes can be either of E_g or B_g symmetry. The selection rules (Table 2) do not allow observation of the B_g symmetry modes for the parallel polarization configuration. Consequently, the peaks that can be observed in both scattering channels were recognized as E_g modes. The absence of B_g modes in the Raman spectra rules out the possibility of the AlCl_3 type of structure (space group $C2/m$). Two possible remaining crystal symmetries ($R\bar{3}$ and

Table 1. Previously Reported Experimental and Calculated Unit Cell Parameters for $\bar{P}31c$, $\bar{R}3$, and $C2/m$ Structures of VI_3

	$\bar{P}31c$		$\bar{R}3$		$C2/m$	
	calcd	exp. ⁹	calcd	exp. ¹²	calcd	exp. ¹⁴
<i>a</i> (Å)	6.87	6.89(10)	6.69	6.89(3)	7.01	6.84(3)
<i>b</i> (Å)	6.87	6.89(10)	6.69	6.89(3)	12.14	11.83(6)
<i>c</i> (Å)	13.224	13.289(1)	19.81	19.81(9)	7.01	6.95(4)
α (deg)	90	90	90	90	90	90
β (deg)	90	90	90	90	109.05	108.68
γ (deg)	120	120	120	120	90	90
cell volume (Å ³)	559.62	547.74(10)	767.71	814.09(8)	563.33	533.66(36)

Table 2. Wyckoff Positions of Atoms and Their Contributions to the Γ -Point Phonons for the $\bar{R}3$, $C2/m$, and $\bar{P}31c$ Structures and the Raman Tensors for the Corresponding Space Groups

space group $\bar{P}31c$		space group $\bar{R}3$		space group $C2/m$	
atom	irreducible representation	atom	irreducible representation	atom	irreducible representation
V (2a)	$A_{2g} + A_{2u} + E_g + E_u$	V (3a)	$A_g + A_u + E_g + E_u$	V (4g)	$A_g + A_u + 2B_g + 2B_u$
V (2c)	$A_{2g} + A_{2u} + E_g + E_u$	V (6c)	$A_g + A_u + E_g + E_u$	I (4i)	$2A_g + A_u + B_g + 2B_u$
I (12i)	$3A_{1g} + 3A_{1u} + 3A_{2g} + 3A_{2u} + 6E_g + 6E_u$	I (18f)	$3A_g + 3A_u + 3E_g + 3E_u$	I (8j)	$3A_g + 3A_u + 3B_g + 3B_u$

$A_{1g} = \begin{pmatrix} a & a & b \end{pmatrix}$	$A_g = \begin{pmatrix} a & a & b \end{pmatrix}$	$A_g = \begin{pmatrix} a & d \\ c & b \end{pmatrix}$
${}^1E_g = \begin{pmatrix} c & d \\ -c & d \end{pmatrix} {}^2E_g = \begin{pmatrix} -c & -d \\ d & c \end{pmatrix}$	${}^1E_g = \begin{pmatrix} c & d & e \\ d & -c & f \\ e & f & e \end{pmatrix} {}^2E_g = \begin{pmatrix} d & -c & -f \\ -c & -d & e \\ -f & e & e \end{pmatrix}$	$B_g = \begin{pmatrix} e & f \\ e & f \end{pmatrix}$

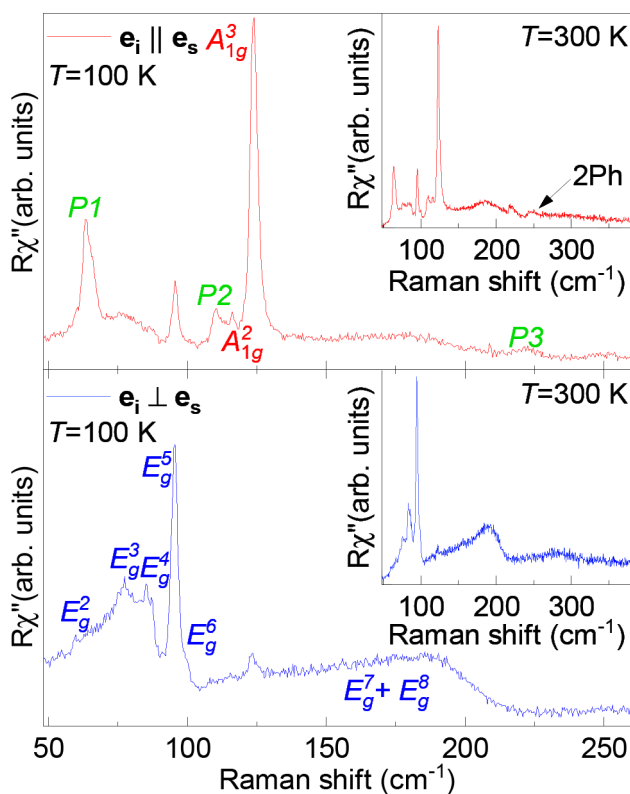


Figure 2. Raman spectra of the high-temperature VI_3 single-crystal structure measured in parallel (red solid line) and cross (blue solid line) polarization configurations at 100 K. Peaks observed in both spectra were identified as E_g modes, whereas peaks observed only in the red spectrum were assigned as A_{1g} modes. Additional peaks that obey pure A_{1g} symmetry are marked as $P1$ – $P3$.

$\bar{P}31c$) are difficult to single out on the basis of the Raman data symmetry analysis alone. To overcome this obstacle, the DFT method was applied for each of the suggested structures.

It was reported in the literature that $\bar{P}31c$ VI_3 can have two possible electronic states^{9,14,41–43} that both can be obtained using DFT+U calculations by varying the smearing and mixing parameters. This approach resulted in a Mott-insulator state having a lower energy making it the electronic ground state of VI_3 . However, the total energy difference of these two states is small and will not be mentioned further because it is outside of the scope of our analysis. For the sake of completeness, both sets of phonon energies obtained through DFT calculations for these electronic states of the $\bar{P}31c$ structure are listed in Table 3 together with the results for the $\bar{R}3$ and $C2/m$ space groups as well as the experimental results measured at 100 K.

Now one can see that, even though the Raman mode symmetries for the case of the $\bar{R}3$ crystal structure can describe our Raman spectra, there is a stronger mismatch in calculated and experimentally determined phonon energies when compared to the results obtained for the $\bar{P}31c$ structure. The deviation is largest for the calculated A_g^1 mode. The closest mode in energy, which obeys the same symmetry rules as the calculated A_g^1 , is a peak at ~ 64.1 cm^{-1} , yielding a deviation of $\sim 30\%$. Also, the calculated energy of the A_g^4 mode could not be identified within our spectrum, with the closest experimental A_g peaks being within 20%. Such deviation in theory and experiment, $>20\%$, indicates that the room-temperature phonon vibrations in VI_3 do not originate predominantly from the BiI_3 structure type either, leaving $\bar{P}31c$ as the only candidate. This indication is further reinforced by the inability to connect the experimentally observed E_g modes at ~ 77 and ~ 86 cm^{-1} with the $\bar{R}3$ -calculated modes.

Our experimental data (Table 3) are mostly supported by the phonon energies obtained for possible electronic states of

Table 3. Comparison between Calculated Values of Raman Active Phonon Energies for Insulating and Half-Metallic States of the $P\bar{3}1c$ Structure and Experimentally Obtained Values (left)^a and Phonon Symmetries and Calculated Phonon Energies for the $R\bar{3}$ and $C2/m$ Structures of VI_3 ^b

space group $P\bar{3}1c$				space group $R\bar{3}$		space group $C2/m$	
symmetry	calcd (cm ⁻¹)	calcd (cm ⁻¹)	exp. (cm ⁻¹)	symmetry	calcd (cm ⁻¹)	symmetry	calcd (cm ⁻¹)
E_g^1	17.2	15.2	–	E_g^1	45.2	A_g^1	58.1
A_{2g}^1 (silent)	35.0	56.8		E_g^2	69.9	B_g^1	60.0
E_g^2	62.2	61.6	59.8	A_g^1	99.3	A_g^2	82.7
A_{2g}^2 (silent)	69.4	72.3		E_g^3	99.8	B_g^2	82.9
E_g^3	74.1	75.9	77.2	A_g^2	105.1	A_g^3	85.7
A_{1g}^1	83.3	84.2	–	A_g^3	135.5	B_g^3	88.9
E_g^4	84.9	86.6	86.7	A_g^4	167.9	A_g^4	99.3
E_g^5	91.5	98.4	95.2	E_g^4	176.8	B_g^4	99.3
A_{2g}^3 (silent)	92.2	96.3				A_g^5	122.3
E_g^6	97.4	108.3	100.4			B_g^5	149.9
A_{1g}^2	113.2	119.3	116.8			B_g^6	161.0
A_{1g}^3	117.1	123.9	123.4			A_g^6	164.0
A_{2g}^4 (silent)	121.3	147.8					
E_g^7	132.2	151.9	<i>c</i>				
E_g^8	149.4	166.9	<i>c</i>				
A_{2g}^5 (silent)	185.9	212.1					

^aThe experimental values were determined at 100 K. The experimental uncertainty is 0.3 cm⁻¹. ^bAll calculations were performed at 0 K. ^cSee the text for an explanation.

the $P\bar{3}1c$ trigonal structure with deviations of around 10% and 15%. Nine of 11 Raman modes were singled out and identified, with E_g^1 being not observable in our experimental setup due to its low energy. The A_{1g}^1 mode might be missing due to its low intensity and/or the finite spectrometer resolution. The most striking was the observation of the broad feature at ~ 180 cm⁻¹, persisting up to 300 K in both scattering channels. Whereas its line shape resembles those of the two-magnon type of excitation, we believe that scenario is unlikely for a ferromagnetic material. The energy region where the feature was observed may also suggest the possibility of a two-phonon type of excitation. However, their scattering cross sections are usually small and dominated by overtones, thus mostly observed for the parallel scattering configuration.⁴⁵ For example, such an excitation was observed at ~ 250 cm⁻¹ (Figure 2). Finally, the observed feature also falls into the energy region where, as suggested by the numerical calculations, observation of the E_g^7 and E_g^8 modes is expected. We believe that it is actually a complex structure comprising E_g^7 and E_g^8 Raman modes, significantly broadened by the spin-phonon interaction, that is particularly strong on these phonon branches. The proximity of the two very broad, presumably asymmetric peaks hampers their precise assignment.

Closer inspection of other Raman peaks revealed that some of them also exhibit an asymmetric line shape. To further demonstrate this virtue, we have quantitatively analyzed the highest-intensity peak, A_{1g}^3 , using the symmetric Voigt line shape and convolution of a Fano profile and a Gaussian.^{44–46} The asymmetric line shape (with a Fano parameter of $|q| = 12.3$) gives a slightly better agreement with the experimental data, as depicted in Figure 3. Considering that the observed asymmetry in similar materials was shown to reflect the spin-phonon interaction,^{46,47} we propose it as a possible scenario in VI_3 , as well.

Our findings, based on the inelastic light scattering experiments, at first glance differ from those presented in ref 10. To resolve this discrepancy, we used synchrotron X-ray Rietveld and PDF analysis. Typically, the short-range order

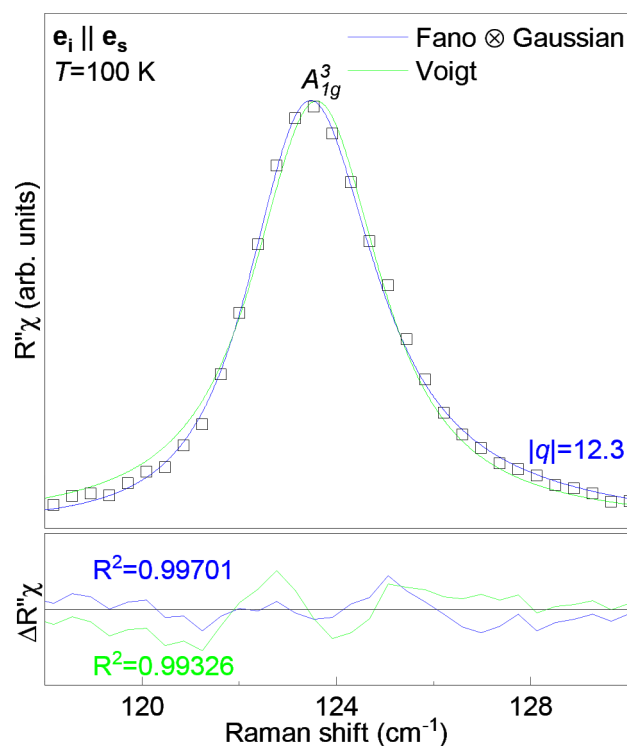


Figure 3. Quantitative analysis of the A_{1g}^3 mode. The blue solid line represents the line shape obtained as a convolution of the Fano line shape and the Gaussian, whereas the green one represents a Voigt profile fitted to experimental data (\square). For details, see refs 44 and 45.

(SRO) contributes to diffuse scattering under the long-range order (LRO) Bragg peaks when they coexist. Because the diffuse scattering is subtracted as part of the background in the Rietveld refinement, this method is more sensitive to the average structure of materials. In contrast, PDF analysis is performed on the sine Fourier transform of the properly corrected diffraction pattern, including both Bragg and diffuse

components. PDF is a real space function that provides a histogram of interatomic distances, which contain information regarding all length scales.^{48–51} The 1–10 and 11–30 Å PDF length scales are more sensitive to SRO and LRO, respectively. For the VI_3 system, the best Rietveld fit was obtained using the $R\bar{3}$ space group (Figure 4a), in agreement with that previously

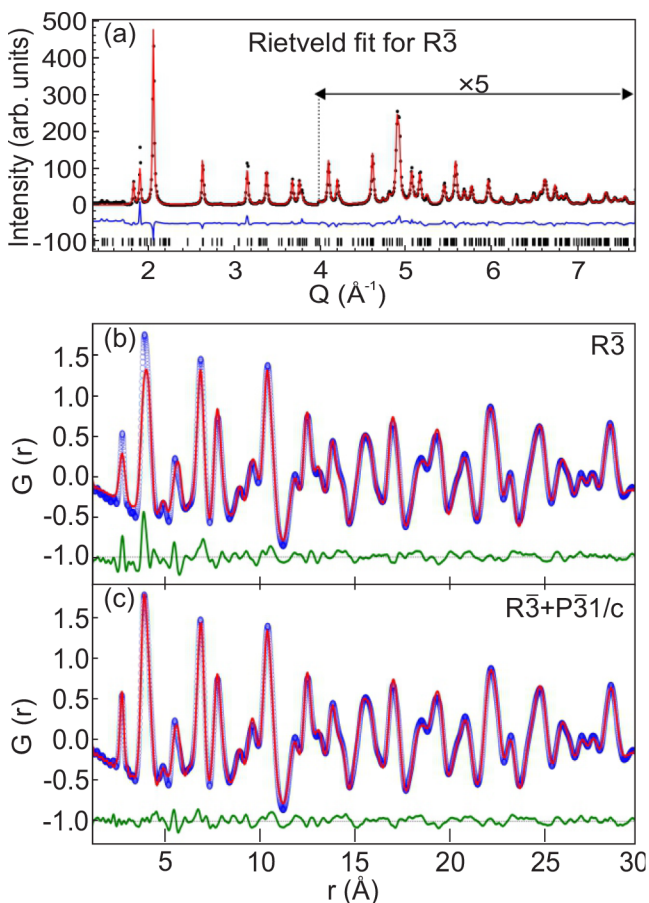


Figure 4. Best structural model fits to diffraction data. (a) Rietveld fit using the $R\bar{3}$ space group with black vertical bars indicating calculated peak positions. (b) PDF fit using the $R\bar{3}$ space group. (c) Two-phase PDF fit using $R\bar{3}$ and $P\bar{3}1c$ space groups to fit LRO and SRO, respectively. Black dots (XRD) and blue dots (PDF) represent experimental data, and red solid lines represent the model-based fits. The fit residues are shown at the bottom of each plot.

observed.¹⁰ Not surprisingly, LRO obtained from the Rietveld refinement showed a good agreement on the PDF length scale of 10–30 Å. However, the $R\bar{3}$ space group gave a poor fit on the length scale of 1.5–15 Å with refined $\delta 1$ to account for correlated motion (Figure 4b). In contrast, $P\bar{3}1c$ gave a better fit to SRO, but a poor fit to LRO. The best PDF fits were obtained by refining a weighted two-phase structural model containing ~ 25 wt % SRO $P\bar{3}1c$ and ~ 75 wt % LRO $R\bar{3}$ phases. The refined correlation length of the SRO is ~ 15 – 20 Å (Figure 4c). These results suggest two possible scenarios: (1) coexistence of two segregated phases, LRO $R\bar{3}$ and SRO $P\bar{3}1c$, and (2) randomly distributed short-range ordered $P\bar{3}1c$ domains in the long-range ordered $R\bar{3}$ lattice. A detailed structural analysis is required to pinpoint scenario 1 and/or 2, which is beyond the scope of this work.

In addition to the peaks already assigned to Γ -point Raman active phonons of the $P\bar{3}1c$ crystal structure (Table 2), three

additional peaks at 64.2 cm^{-1} (P_1), 110.1 cm^{-1} (P_2), and 220.6 cm^{-1} (P_3) are observed (see Figure 2). According to the results of DFT, energies of these modes correspond well to those calculated for silent A_{2g}^2 , A_{2g}^3 , and A_{2g}^5 modes. Their observability in Raman data may come from the release of the symmetry selection rules by breaking of the (translation) symmetry as suggested by the PDF in both scenarios.^{52–55} However, as previously discussed, these peaks obey A_{1g} selection rules, indicating the possibility for them to be overtones in nature. In this less likely scenario, the phonon–phonon coupling is enhanced by the spin–phonon interaction and/or by the structural imperfections, thus enhancing the Raman scattering rate for the two-phonon processes.⁴⁵ Hence, the observed Raman modes reflect the symmetry of phonon vibrations related to the SRO.^{56,57} It is interesting to note that, besides a possible short-range crystallography that is different from the average, VI_3 might also feature short-range magnetic order above 79 K.¹⁴

CONCLUSION

In summary, room-temperature phonon vibrations of VI_3 stem from the $P\bar{3}1c$ symmetry of the unit cell. The PDF analysis suggested the coexistence of two phases, short-range ordered $P\bar{3}1c$ and long-range ordered $R\bar{3}$, as two segregated phases and/or as randomly distributed short-range ordered $P\bar{3}1c$ domains in the long-range ordered $R\bar{3}$ lattice. Nine of 12 observed peaks in the Raman spectra were assigned in agreement with $P\bar{3}1c$ symmetry calculations. Three additional peaks, which obey A_{1g} symmetry rules, could be explained as either overtones or as activated A_{2g} silent modes caused by a symmetry breaking. The asymmetry of one of the A_{1g} phonon modes, together with the anomalous behavior of E_g^7 and E_g^8 , indicates strong spin–phonon coupling, which has already been reported in similar 2D materials.^{46,58}

AUTHOR INFORMATION

Corresponding Author

Nenad Lazarević – Institute of Physics Belgrade, University of Belgrade, 11080 Belgrade, Serbia; orcid.org/0000-0001-6310-9511; Email: nenadl@ipb.ac.rs

Authors

Sanja Djurdjić Mijin – Institute of Physics Belgrade, University of Belgrade, 11080 Belgrade, Serbia

A. M. Milinda Abeykoon – National Synchrotron Light Source II, Brookhaven National Laboratory, Upton, New York 11973, United States

Andrijana Solajić – Institute of Physics Belgrade, University of Belgrade, 11080 Belgrade, Serbia

Ana Milosavljević – Institute of Physics Belgrade, University of Belgrade, 11080 Belgrade, Serbia

Jelena Pešić – Institute of Physics Belgrade, University of Belgrade, 11080 Belgrade, Serbia

Yu Liu – Condensed Matter Physics and Materials Science Department, Brookhaven National Laboratory, Upton, New York 11973-5000, United States; orcid.org/0000-0001-8886-2876

Cedomir Petrović – Condensed Matter Physics and Materials Science Department, Brookhaven National Laboratory, Upton, New York 11973-5000, United States; orcid.org/0000-0001-6063-1881

Zoran V. Popović – Institute of Physics Belgrade, University of Belgrade, 11080 Belgrade, Serbia; Serbian Academy of Sciences and Arts, 11000 Belgrade, Serbia

Complete contact information is available at:
<https://pubs.acs.org/10.1021/acs.inorgchem.0c02060>

Notes

The authors declare no competing financial interest.

ACKNOWLEDGMENTS

The authors acknowledge funding provided by the Institute of Physics Belgrade, through a grant from the Ministry of Education, Science and Technological Development of the Republic of Serbia, Project F-134 of the Serbian Academy of Sciences and Arts, and the Science Fund of the Republic of Serbia, PROMIS, 6062656, StrainedFeSC. DFT calculations were performed using computational resources at Johannes Kepler University (Linz, Austria). Materials synthesis was supported by the U.S. DOE-BES, Division of Materials Science and Engineering, under Contract DE-SC0012704 (BNL). This research used beamline 28-ID-1 of National Synchrotron Light Source II, a U.S. DOE Office of Science User Facility operated for the DOE Office of Science by Brookhaven National Laboratory under Contract DE-S.




REFERENCES

- (1) Seyler, K. L.; Zhong, D.; Klein, D. R.; et al. Ligand-field helical luminescence in a 2D ferromagnetic insulator. *Nat. Phys.* **2018**, *14*, 277–281.
- (2) Klein, D. R.; MacNeill, D.; Lado, J. L.; Soriano, D.; Navarro-Moratalla, E.; Watanabe, K.; et al. Probing magnetism in 2D van der Waals crystalline insulators via electron tunneling. *Science* **2018**, *360*, 1218–1222.
- (3) Huang, B.; Clark, G.; Klein, D. R.; MacNeill, D.; Navarro-Moratalla, E.; Seyler, K. L.; et al. Electrical control of 2D magnetism in bilayer CrI₃. *Nat. Nanotechnol.* **2018**, *13*, 544–548.
- (4) Jiang, S.; Li, L.; Wang, Z.; Mak, K. F.; Shan, J. Controlling magnetism in 2D CrI₃ by electrostatic doping. *Nat. Nanotechnol.* **2018**, *13*, 549–553.
- (5) McGuire, M. A.; Clark, G.; KC, S.; Chance, W. M.; Jellison, G. E.; Cooper, V. R.; Xu, X.; Sales, B. C. Magnetic behavior and spin-lattice coupling in cleavable van der Waals layered CrCl₃ crystals. *Phys. Rev. Materials* **2017**, *1*, 014001.
- (6) Djurdjic-Mijin, S. D.; Solajić, A.; Pešić, J.; Šćepanović, M.; Liu, Y.; Baum, A.; et al. Lattice dynamics and phase transition in CrI₃ single crystals. *Phys. Rev. B: Condens. Matter Mater. Phys.* **2018**, *98*, 104307.
- (7) Thiel, L.; Wang, Z.; Tschudin, M.; Rohner, D.; Gutierrez-Lezama, I. G.; Ubrig, N.; et al. Probing magnetism in 2D materials at the nanoscale with single-spin microscopy. *Science* **2019**, *364*, 973–976.
- (8) Lin, G. T.; Luo, X.; Chen, F. C.; Yan, J.; Gao, J. J.; Sun, Y.; et al. Critical behavior of two-dimensional intrinsically ferromagnetic semiconductor CrI₃. *Appl. Phys. Lett.* **2018**, *112*, 072405.
- (9) Son, S.; Coak, M. J.; Lee, N.; Kim, J.; Kim, T. Y.; Hamidov, H.; et al. Bulk properties of the van der Waals hard ferromagnet VI₃. *Phys. Rev. B: Condens. Matter Mater. Phys.* **2019**, *99*, 041402.
- (10) Liu, Y.; Abeykoon, M.; Petrovic, C. Critical behavior and magnetocaloric effect in VI₃. *Phys. Rev. Research* **2020**, *2*, 013013.
- (11) Huang, B.; Clark, G.; Navarro-Moratalla, E.; Klein, D. R.; Cheng, R.; Seyler, K. L.; et al. Layer-dependent ferromagnetism in a van der Waals crystal down to the monolayer limit. *Nature* **2017**, *546*, 270–273.
- (12) Kong, T.; Stolze, K.; Timmons, E. I.; Tao, J.; Ni, D.; Guo, S.; et al. VI₃ – a New Layered Ferromagnetic Semiconductor. *Adv. Mater.* **2019**, *31*, 1808074.
- (13) Doležal, P.; Kratochvílová, M.; Holý, V.; Čermak, P.; Sechovský, V.; Dušek, M.; et al. Crystal structures and phase transitions of the van der Waals ferromagnet VI₃. *Phys. Rev. Materials* **2019**, *3*, 121401.
- (14) Tian, S.; Zhang, J.-F.; Li, C.; Ying, T.; Li, S.; Zhang, X.; et al. Ferromagnetic van der Waals Crystal VI₃. *J. Am. Chem. Soc.* **2019**, *141*, 5326–5333.
- (15) Wang, Y.-M.; Tian, S.-J.; Li, C.-H.; Jin, F.; Ji, J.-T.; Lei, H.-C.; Zhang, Q.-M. Raman scattering study of two-dimensional magnetic van der Waals compound VI₃. *Chin. Phys. B* **2020**, *29*, 056301.
- (16) Lee, I.; Utermohlen, F. G.; Weber, D.; Hwang, K.; Zhang, C.; van Tol, J.; Goldberger, J. E.; Trivedi, N.; Hammel, P. C. Fundamental Spin Interactions Underlying the Magnetic Anisotropy in the Kitaev Ferromagnet CrI₃. *Phys. Rev. Lett.* **2020**, *124*, 017201.
- (17) Xu, C.; Feng, J.; Xiang, H.; Bellaiche, L. Interplay between Kitaev interaction and single ion anisotropy in ferromagnetic CrI₃ and CrGeTe₃ monolayers. *npj Comput. Mater.* **2018**, *4*, 57.
- (18) Mermin, N. D.; Wagner, H. Absence of Ferromagnetism or Antiferromagnetism in One- or Two-Dimensional Isotropic Heisenberg Models. *Phys. Rev. Lett.* **1966**, *17*, 1133–1136.
- (19) Pershoguba, S. S.; Banerjee, S.; Lashley, J. C.; Park, J.; Ågren, H.; Aeppli, G.; Balatsky, A. V. Dirac Magnons in Honeycomb Ferromagnets. *Phys. Rev. X* **2018**, *8*, 011010.
- (20) Liu, J.; Shi, M.; Mo, P.; Lu, J. Electrical-field-induced magnetic Skyrmion ground state in a two-dimensional chromium tri-iodide ferromagnetic monolayer. *AIP Adv.* **2018**, *8*, 055316.
- (21) Jiang, S.; Li, L.; Wang, Z.; Shan, J.; Mak, K. Spin tunnel field-effect transistors based on two-dimensional van der Waals heterostructures. *Nature Electronics* **2019**, *2*, 159.
- (22) Klein, D. R.; MacNeill, D.; Song, Q.; Larson, D. T.; Fang, S.; Xu, M.; Ribeiro, R. A.; Canfield, P. C.; Kaxiras, E.; Comin, R.; Jarillo-Herrero, P. Enhancement of interlayer exchange in an ultrathin two-dimensional magnet. *Nat. Phys.* **2019**, *15*, 1255–1260.
- (23) Wang, Z.; Gibertini, M.; Dumcenco, D.; Taniguchi, T.; Watanabe, K.; Giannini, E.; Morpurgo, A. Determining the phase diagram of atomically thin layered antiferromagnet CrCl₃. *Nat. Nanotechnol.* **2019**, *14*, 1116.
- (24) Ubrig, N.; Wang, Z.; Teyssier, J.; Taniguchi, T.; Watanabe, K.; Giannini, E.; Morpurgo, A. F.; Gibertini, M. Low-temperature monoclinic layer stacking in atomically thin CrI₃ crystals. *2D Mater.* **2020**, *7*, 015007.
- (25) Sun, Z.; et al. Giant nonreciprocal second-harmonic generation from antiferromagnetic bilayer CrI₃. *Nature* **2019**, *572*, 497–501.
- (26) McGuire, M. A.; Clark, G.; KC, S.; Chance, W. M.; Jellison, G. E.; Cooper, V. R.; Xu, X.; Sales, B. C. Magnetic behavior and spin-lattice coupling in cleavable van der Waals layered CrCl₃ crystals. *Phys. Rev. Materials* **2017**, *1*, 014001.
- (27) Kuhlów, B. Magnetic Ordering in CrCl₃ at the Phase Transition. *physica status solidi (a)* **1982**, *72*, 161–168.
- (28) Hammersley, A. P.; Svensson, S. O.; Hanfland, M.; Fitch, A. N.; Hausermann, D. Two-dimensional detector software: From real detector to idealised image or two-theta scan. *High Pressure Res.* **1996**, *14*, 235–248.
- (29) Yang, X.; Juhas, P.; Farrow, C. L.; Billinge, S. J. L. *xPDFsuite: an end-to-end software solution for high throughput pair distribution function transformation, visualization and analysis*; 2014.
- (30) Toby, B. H.; Von Dreele, R. B. GSAS-II: the genesis of a modern open-source all purpose crystallography software package. *J. Appl. Crystallogr.* **2013**, *46*, 544–549.
- (31) Farrow, C. L.; Juhas, P.; Liu, J. W.; Bryndin, D.; Božin, E. S.; Bloch, J.; Proffen, T.; Billinge, S. J. L. PDFfit2 and PDFgui: computer programs for studying nanostructure in crystals. *J. Phys.: Condens. Matter* **2007**, *19*, 335219.
- (32) Giannozzi, P.; et al. QUANTUM ESPRESSO: a modular and open-source software project for quantum simulations of materials. *J. Phys.: Condens. Matter* **2009**, *21*, 395502.
- (33) Perdew, J. P.; Burke, K.; Ernzerhof, M. Generalized Gradient Approximation Made Simple. *Phys. Rev. Lett.* **1996**, *77*, 3865–3868.

- (34) Blöchl, P. E. Projector augmented-wave method. *Phys. Rev. B: Condens. Matter Mater. Phys.* **1994**, *50*, 17953–17979.
- (35) Kresse, G.; Joubert, D. From ultrasoft pseudopotentials to the projector augmented-wave method. *Phys. Rev. B: Condens. Matter Mater. Phys.* **1999**, *59*, 1758–1775.
- (36) Cococcioni, M.; de Gironcoli, S. Linear response approach to the calculation of the effective interaction parameters in the LDA + U method. *Phys. Rev. B: Condens. Matter Mater. Phys.* **2005**, *71*, 035105.
- (37) Juza, D.; Giegling, D.; Schäfer, H. Über die Vanadinjodide VJ₂ und VJ₃. *Z. Anorg. Allg. Chem.* **1969**, *366*, 121–129.
- (38) Berry, K. O.; Smardzewski, R. R.; McCarley, R. E. Vaporization reactions of vanadium iodides and evidence for gaseous vanadium(IV) iodide. *Inorg. Chem.* **1969**, *8*, 1994–1997.
- (39) Klemm, W.; Krose, E. Die Kristallstrukturen von ScCl₃, TiCl₃ und VCl₃. *Z. Anorg. Chem.* **1947**, *253*, 218–225.
- (40) Liu, Y.; Petrovic, C. Three-dimensional magnetic critical behavior in CrI₃. *Phys. Rev. B: Condens. Matter Mater. Phys.* **2018**, *97*, 014420.
- (41) He, J.; Ma, S.; Lyu, P.; Nachtigall, P. Unusual Dirac half-metallicity with intrinsic ferromagnetism in vanadium trihalide monolayers. *J. Mater. Chem. C* **2016**, *4*, 2518–2526.
- (42) Wang, Y.-P.; Long, M.-Q. Electronic and magnetic properties of van der Waals ferromagnetic semiconductor VI₃. *Phys. Rev. B: Condens. Matter Mater. Phys.* **2020**, *101*, 024411.
- (43) Li, Y.; Liu, Y.; Wang, C.; Wang, J.; Xu, Y.; Duan, W. Electrically tunable valleytronics in quantum anomalous Hall insulating transition metal trihalides. *Phys. Rev. B: Condens. Matter Mater. Phys.* **2018**, *98*, 201407.
- (44) Lazarević, N.; Popović, Z. V.; Hu, R.; Petrovic, C. Evidence for electron-phonon interaction in Fe_{1-x}M_xSb₂ (M = Co and Cr 0 ≤ x ≤ 0.5) single crystals. *Phys. Rev. B: Condens. Matter Mater. Phys.* **2010**, *81*, 144302.
- (45) Baum, A.; Milosavljević, A.; Lazarević, N.; Radonjić, M. M.; Nikolić, B.; Mitschek, M.; Maranloo, Z. I.; Šćepanović, M.; Grujić-Brojčin, M.; Stojilović, N.; Opel, M.; Wang, A.; Petrovic, C.; Popović, Z. V.; Hackl, R. Phonon anomalies in FeS. *Phys. Rev. B: Condens. Matter Mater. Phys.* **2018**, *97*, 054306.
- (46) Milosavljević, A.; Šolajic, A.; Pešić, J.; Liu, Y.; Petrovic, C.; Lazarević, N.; Popović, Z. V. Evidence of spin-phonon coupling in CrSiTe₃. *Phys. Rev. B: Condens. Matter Mater. Phys.* **2018**, *98*, 104306.
- (47) McCarty, K. F.; Radousky, H. B.; Hinks, D. G.; Zheng, Y.; Mitchell, A. W.; Folkerts, T. J.; Shelton, R. N. Electron-phonon coupling in superconducting Ba_{0.6}K_{0.4}BiO₃: A Raman scattering study. *Phys. Rev. B: Condens. Matter Mater. Phys.* **1989**, *40*, 2662–2665.
- (48) Proffen, T.; Page, K. L.; McLain, S. E.; Clausen, B.; Darling, T. W.; TenCate, J. A.; Lee, S.-Y.; Ustundag, E. Atomic pair distribution function analysis of materials containing crystalline and amorphous phases. *Z. Kristallogr.* **2005**, *220*, 1002–1008.
- (49) Bordet, P. Application of the pair distribution function analysis for the study of cultural heritage materials. *C. R. Phys.* **2018**, *19*, 561–574.
- (50) Bozin, E. S.; Yin, W. G.; Koch, R. J.; Abeykoon, M.; Hor, Y. S.; Zheng, H.; Lei, H. C.; Petrovic, C.; Mitchell, J. F.; Billinge, S. J. L. Local orbital degeneracy lifting as a precursor to an orbital-selective Peierls transition. *Nat. Commun.* **2019**, *10*, 3638.
- (51) Egami, T.; Billinge, S. J. L. *Underneath the Bragg Peaks: Structural Analysis of Complex Materials*; 2003; p 16.
- (52) Jin, F.; Lazarević, N.; Liu, C.; Ji, J.; Wang, Y.; He, S.; Lei, H.; Petrovic, C.; Yu, R.; Popović, Z. V.; Zhang, Q. Phonon anomalies and magnetic excitations in BaFe₂Se₂O. *Phys. Rev. B: Condens. Matter Mater. Phys.* **2019**, *99*, 144419.
- (53) Moskovits, M.; Dilella, D. Surface-enhanced Raman spectroscopy of benzene and benzene-d₆ adsorbed on silver. *J. Chem. Phys.* **1980**, *73*, 6068–6075.
- (54) Dubroka, A.; Humlíček, J.; Abrashev, M. V.; Popović, Z. V.; Sapiña, F.; Cantarero, A. Raman and infrared studies of La_{1-y}Sr_yMn_{1-x}M_xO₃ (M = Cr, Co, Cu, Zn, Sc or Ga): Oxygen disorder and local vibrational modes. *Phys. Rev. B: Condens. Matter Mater. Phys.* **2006**, *73*, 224401.
- (55) Souza Filho, A. G.; Faria, J. L. B.; Guedes, I.; Sasaki, J. M.; Freire, P. T. C.; Freire, V. N.; Mendes Filho, J.; Xavier, M. M.; Cabral, F. A. O.; de Araújo, J. H.; da Costa, J. A. P. Evidence of magnetic polaronic states in La_{0.70}Sr_{0.30}Mn_{1-x}Fe_xO₃ manganites. *Phys. Rev. B: Condens. Matter Mater. Phys.* **2003**, *67*, 052405.
- (56) Lekgoathi, M.; Kock, L. Effect of short and long range order on crystal structure interpretation: Raman and powder X-ray diffraction of LiPF₆. *Spectrochim. Acta, Part A* **2016**, *153*, 651–654.
- (57) Wolverton, C.; Zunger, A.; Lu, Z.-W. Long-versus short-range order in Ni₃V and Pd₃V alloys. *Phys. Rev. B: Condens. Matter Mater. Phys.* **1994**, *49*, 16058.
- (58) Webster, L.; Liang, L.; Yan, J.-A. Distinct spin-lattice and spin-phonon interactions in monolayer magnetic CrI₃. *Phys. Chem. Chem. Phys.* **2018**, *20*, 23546–23555.

Article

Ab Initio Study of the Electronic, Vibrational, and Mechanical Properties of the Magnesium Diboride Monolayer

Jelena Pešić ^{1,*} , Igor Popov ^{1,2} , Andrijana Šolajić ¹, Vladimir Damljanović ¹ , Kurt Hingerl ³, Milivoj Belić ⁴ and Radoš Gajić ¹

¹ Laboratory for graphene, other 2D materials and ordered nanostructures, Center for Solid State Physics and New Materials, Institute of Physics Belgrade, University of Belgrade, 11080 Belgrade, Serbia; popov@ipb.ac.rs (I.P.); solajic@ipb.ac.rs (A.Š.); damlja@ipb.ac.rs (V.D.); rgajic@ipb.ac.rs (R.G.)

² Institute for Multidisciplinary Research, University of Belgrade, Kneza Višeslava 1, 11030 Belgrade, Serbia

³ Center for Surface and Nanoanalytics, Johannes Kepler University, 4040 Linz, Austria; Kurt.Hingerl@jku.at

⁴ Science Program, Texas A&M University at Qatar, Doha P.O. Box 23874, Qatar; milivoj.belic@qatar.tamu.edu

* Correspondence: yelena@ipb.ac.rs

Received: 15 March 2019; Accepted: 1 April 2019; Published: 2 April 2019



Abstract: Magnesium diboride gained significant interest in the materials science community after the discovery of its superconductivity, with an unusually high critical temperature of 39 K. Many aspects of the electronic properties and superconductivity of bulk MgB₂ and thin sheets of MgB₂ have been determined; however, a single layer of MgB₂ has not yet been fully theoretically investigated. Here, we present a detailed study of the structural, electronic, vibrational, and elastic properties of monolayer MgB₂, based on ab initio methods. First-principles calculations reveal the importance of reduction of dimensionality on the properties of MgB₂ and thoroughly describe the properties of this novel 2D material. The presence of a negative Poisson ratio, higher density of states at the Fermi level, and a good dynamic stability under strain make the MgB₂ monolayer a prominent material, both for fundamental research and application studies.

Keywords: magnesium diboride; 2D materials; density functional theory

PACS: 71.15.Mb; 74.70.Ad

1. Introduction

Magnesium diboride was first synthesized and had its structure confirmed in 1953 [1]. An interest in its properties has grown ever since 2001, when it was discovered that MgB₂ exhibits the highest superconducting transition temperature T_c of all metallic superconductors. It is an inter-metallic s-wave compound superconductor with a quasi-two dimensional character [2] and a critical temperature of superconductive transition at $T_c = 39$ K. The experimental confirmation of the isotope effect [3] in MgB₂ indicated that it is a phonon-mediated BCS superconductor. A better definition would describe MgB₂ as self-doped semimetal with a crucial σ -bonding band that is nearly filled [4]. The basic aspects of the electronic structure and pairing is in a rather strong coupling of high frequency boron–boron stretch modes to the bonding electronic boron–boron states at the Fermi surface. The phonon-mediated mechanism with different coupling strengths between a particular phonon mode and selected electronic bands, boron σ - and π -bands [5–13], results in the presence of two superconducting gaps at the Fermi level. MgB₂ has already been fabricated in bulk, as single crystals, and as a thin film, and shows potential for practical applications.

The discovery of graphene in 2004 [14] sparked an interest in 2D materials and their properties. A variety of new properties, which distinguished graphene from graphite [14–22], inspired a search for other low-dimensional limits of layered materials and possibilities they offered. Interest in a low-dimensional limit of MgB_2 has arisen in past years, showing that it is superconductive even in a monolayer [23,24].

MgB_2 has a distinct layer structure, where boron atoms form a honeycomb layer and magnesium atoms are located above the center of the hexagons, between every boron plane. The boron layers alternate with a triangular lattice of magnesium layers. There is a noticeable structural similarity of MgB_2 to graphite-intercalated compounds (GICs), some of which also exhibit superconductivity [25–29]. Both monolayer and two-layer graphene, decorated/intercalated with atoms of alkali and alkaline earth metals, exhibit superconductivity and have been thoroughly studied using ab initio methods and isotropic and anisotropic Eliashberg theory [30–32].

Furthermore, a similarity in the electronic structure between GICs and MgB_2 exists. The peculiar and unique property of MgB_2 is a consequence of the incomplete filling of two σ bands corresponding to strongly covalent sp^2 -hybrid bonding within the graphite-like boron layers [33].

Here, we present a comprehensive study of the electronic, vibrational, and mechanical properties of MgB_2 using ab initio methods, in order to provide its detail description.

2. Computational Details

MgB_2 has a hexagonal unit cell and consists of graphite-like B_2 layers stacked with the Mg atoms in between, as shown in Figure 1. The first-principles calculations were performed within the density functional theory (DFT) formalism, using a general gradient approximation (GGA) to calculate the electronic structure. For all electronic and phonon structure, the Quantum Espresso software package [34] was used with ultra-soft pseudopotentials and a plane-wave cutoff energy of 30 Ry. All calculated structures are relaxed to their minimum energy configuration, following the internal force on atoms and stress tensor of the unit cell. We used the Monkhorst-Pack $48 \times 48 \times 48$ and $40 \times 40 \times 1$ k-meshes, for the calculations of the electronic structure of the MgB_2 bulk and MgB_2 monolayer, respectively. The phonon frequencies are calculated using Density Functional Perturbation Theory (DFPT) on the $12 \times 12 \times 12$ and $20 \times 20 \times 1$ phonon wave vector mesh for the bulk and monolayer structures, respectively. In two-dimensional systems, the van der Waals (vdW) interaction was found to play an important role on the electronic structure [35]; however, as this is study on monolayer MgB_2 , we do not treat vdW interactions, especially since, in this case, the effects are minor and including them would add additional computational costs but would not yield more accurate results.

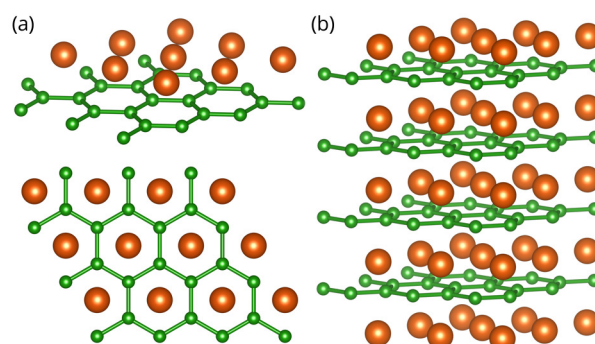


Figure 1. Crystal structure of the MgB_2 monolayer (a) and bulk MgB_2 (b), with a hexagonal unit cell. Green (orange) spheres represent Boron (Magnesium) atoms. Color online.

The crystal structure of MgB_2 and the MgB_2 monolayer are presented in Figure 1. The lattice parameters for the bulk MgB_2 are in agreement with the experimental results, $a = 3.083 \text{ \AA}$ and

$c/a = 1.142$ [9]. In order to avoid an interlayer interaction due to the periodicity and to simulate a 2D material, an artificial vacuum layer was set to be 25 Å. When the monolayer is modelled, the structure is geometrically optimized, allowing the atoms to reach a minimum potential energy state. The bond length between neighbouring atoms remained to be 1.78 Å, but the distance from the boron layer to the Mg atoms changed from $h = 1.76$ Å to $h = 1.60$ Å.

For the molecular dynamics (MD) study, the Siesta code was utilized [36]. The super-cell is built by repeating the unit cell three times in both in-plane directions, whereas the lattice vector in the perpendicular direction is 15 Å, providing a large enough vacuum space between the 2D material and its periodic replica in order to avoid their mutual interaction. The lattice parameters and the geometry of the unit cell are initially optimized using the conjugate gradient method. The Perdew-Burke-Ernzerhof form of the exchange-correlation functional [37], the double-zeta polarized basis set, and the Troulier-Martins pseudopotentials [38] were used in all MD calculations.

The second-order elastic constants were calculated using the ElaStic software package [39]. First, the direction is projected from the strain tensor and total energies for each deformation are calculated. Elastic constants are then calculated using the second derivatives of the energy curves, dependent on the parameter η . In our calculations, the maximum positive and negative amplitudes of 5% Lagrangian strain were applied, with a step of 0.1%.

For the 2D square, rectangular, or hexagonal lattices, the non-zero second-order elastic constants, in Voigt notation, are c_{11} , c_{22} , c_{12} , and c_{66} . Due to symmetry, in hexagonal structures $c_{11} = c_{22}$ and $c_{66} = \frac{1}{2}(c_{11} - c_{12})$; so, we have 2 independent elastic constants. The layer modulus, which represents the resistance of a 2D material to stretching, is given as

$$\gamma = \frac{1}{4}(c_{11} + c_{22} + 2c_{12}).$$

The 2D Young modulus Y for strains in the (10) and (01) directions, Poisson's ratio ν and the shear modulus G are obtained from the following relations,

$$Y = \frac{c_{11}^2 - c_{12}^2}{c_{11}}, \quad \nu = \frac{c_{12}}{c_{22}}, \quad G = c_{66}.$$

Units for elastic constants and those parameters are N/m.

3. Results and Discussion

In order to determine the stability of a single layer of MgB_2 , we perform MD simulations based on DFT and the super-cell approach. Besides the system with optimized (pristine) lattice parameters, we also consider a biaxially stretched system (up to 3% of tensile strain) and biaxially compressed system (up to 5% of compressive strain). The MD simulations are conducted in the range of temperatures between 50–300 K, with a step of 50 K, using the Nosé–Hoover thermostat [40].

Figure 2a shows the average distance between Mg and B atomic layers, as evolved over a time of 1 ps. Throughout the simulation time, there is no further evolution of the z-coordinate and the Mg atom shows only oscillatory movement around the equilibrium positions (as is shown in Figure 2) Importantly, the separation indicates that the Mg atoms do not leave the surface of the MgB_2 crystal. The plane in which the Mg atoms reside shifts away from the plane of the B atoms on average by 0.09 Å in a compressed crystal, while the distance between the planes decreases on average by 0.42 Å in the stretched system. This (relatively larger) shift in the latter case can be understood by analysing the details of the MgB_2 atomic structure. When the crystal is biaxially stretched, its Mg–B bond lengths increase, which is partially compensated by the nesting of the Mg atoms in the hollow sites closer to the B sublattice. Despite these atomic shifts, the MD simulations show the structural stability of the system. The stability from the MD simulations can be further quantitatively derived from the global Lindemann index, the dependence of which on temperature is shown in Figure 2b. It is calculated

for the pristine crystal, with a compressive strain of 5% and a tensile strain of 3%, from the local Lindemann indices, given by the formula

$$q_i = \frac{1}{N-1} \sum_{j \neq i} \frac{\sqrt{\langle r_{ij}^2 \rangle - \langle r_{ij} \rangle^2}}{\langle r_{ij} \rangle},$$

by averaging over all atoms. Here q_i is the local Lindemann index of atom i , N is number of atoms, r_{ij} is a separation between atoms i and j , and the angle brackets denote averaging over time (i.e., MD steps) [41]. The linear behaviour of the Lindemann indices indicate that systems are stable, at least up to room temperature.

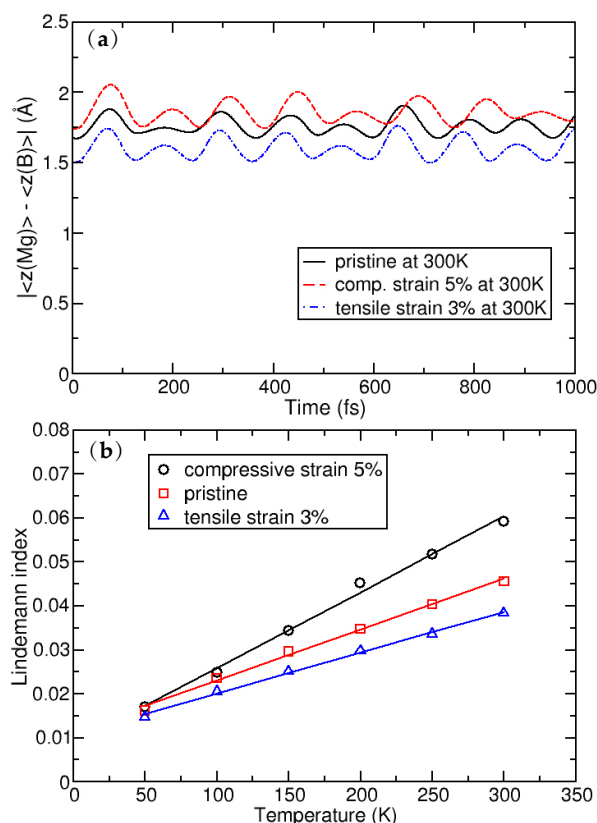


Figure 2. (a): Average distance between the Mg and B atomic layers; and (b): the dependence of the global Lindemann index as a function of temperature.

The calculated second-order elastic constants and other structural parameters for monolayer MgB_2 are given in Table 1. All elastic constants related to the bulk material (those that have 3, 4, or 5 in their subscripts), are calculated close to zero, as is expected for the monolayer. Compared to similar 2D materials, the layer modulus of MgB_2 of 30.18 N/m is relatively small (in the range of Silicene and Germanene), roughly five times smaller than that of graphene or h-BN, for example [42,43]. Similar results are obtained for the Young modulus. Compared to borophene (two-dimensional boron sheets with rectangular structures) [44], which is a hard and brittle 2D material that exhibits an extremely large Young’s modulus of 398 N/m along the a direction [45], the MgB_2 monolayer has a significantly smaller value of 63.29 N/m. The most interesting observation in the elastic properties of the MgB_2 monolayer is that the c_{12} constant is negative, which gives a negative Poisson ratio in the a and b directions, too—although, with a very small negative value of -0.05 . However, compared to 2D borophene, which has an out-of-plane negative Poisson’s ratio (that effectively holds the strong boron bonds lying along the a direction and makes the boron sheet show superior mechanical flexibility along

the b direction [46]), we obtain similar values [45]. For comparison, graphene has a Young modulus of 352.2 N/m and a Poisson ratio of 0.185 [42]. After confirming its stability and determining the elastic properties of the MgB_2 monolayer, we study its electronic properties. In Figure 3, the electronic structures of bulk MgB_2 and the MgB_2 monolayer are presented. The band structures for the bulk along the high-symmetry points Γ -K-M- Γ -A-L, and for the monolayer along Γ -K-M- Γ were calculated. The Fermi level is set to zero. The band structure of the bulk is in full agreement with previous studies [10,47–49]. The two bands crossing the Fermi level play a crucial role in the electronic properties of MgB_2 . The density of the states around E_f are predominantly related to the B atoms and their p -orbitals, whereas the Mg atom contribution is negligible in this region. Previous studies described Mg as fully ionized and showed that the electrons donated to the system are not localized on the anion but, rather, are distributed over the whole crystal [6]. A similarity to graphite can be observed, with three σ bands, corresponding to the in-plane sp_xp_y (sp^2) hybridization in the boron layer and two π -bands of boron p_z orbitals [33]. Boron $p_{x(y)}$ and p_z orbitals contribute as σ and π states. Analysing projected DOS, one concludes that the σ states are considerably involved in the total density of states at the Fermi level, while the π states have only a partial contribution. It is worth emphasizing that the bulk bands of this material at the K-point above the Fermi level present a formation similar to the Dirac cones in graphene.

In the monolayer, there is an increase in the total density of states at the Fermi level from $N(E_f)_{\text{bulk}} = 0.72$ states/eV to $N(E_f)_{\text{mono}} = 0.97$ states/eV. In the same manner as in the bulk, the monolayer Mg atoms negligibly contribute to the density of states at the Fermi level, and the main contribution comes from the B p -orbitals. The characteristic Dirac cone-like structure is still present and closer to the Fermi level. D_{g77} , as the symmetry group of the MgB_2 monolayer, hosts a Dirac-like dispersion in the vicinity of the K-point in the hexagonal Brillouin zone, if the orbital wave functions belong to the 2D representation E of the C_{3v} point group of the wave vector [50,51]. In the tight-binding case, the p_x and p_y orbitals of two boron ions give rise to one E-representation (and to two one-dimensional representations), while the s-orbitals form a basis for one E-representation and p_z -orbitals form a basis for one E-representation as well. This explains the presence of the Dirac cones at the K-point in the band structure of the MgB_2 monolayer (as shown in Figure 3b).

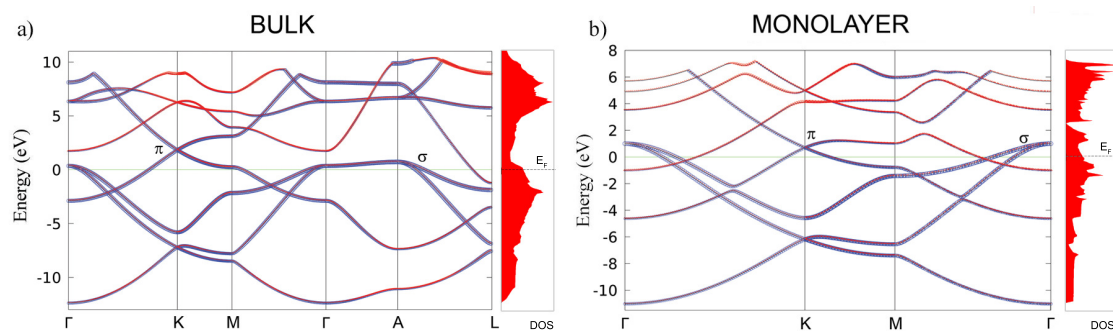


Figure 3. The electronic band structure and total density of states in bulk MgB_2 (a) and the MgB_2 monolayer (b). The blue and red colors represent the B and Mg atoms contributions to the electronic dispersion, respectively.

Table 1. The calculated elastic stiffness constants, layer modulus γ , Young’s modulus Y , Poisson’s ratio ν , and shear modulus G for the MgB_2 monolayer. All parameters are in units of N/m.

c_{11}	c_{12}	c_{66}	γ	Y	ν	G
63.4	−3.1	33.3	30.18	63.29	−0.05	33.3

Figure 4 shows the phonon dispersions for both the bulk and monolayer. For the bulk (in Figure 4a), there are four optical modes at the Γ point. Due to the light atomic mass of the B

atoms and the strong B–B coupling, the two high-frequency modes almost have a pure boron character. The in-plane stretching mode E_{2g} and the out-of-plane mode (where the atoms move in opposite directions B_{1g}) are the boron atom modes. E_{2g} is a doubly-degenerate Raman active mode and experimental studies [6,9] showed that this mode is very sensitive to structural changes and it has a strong electron-phonon coupling. The low-frequency modes (A_{2u}) and double degenerate (E_{1u}) are infrared active and they do not involve changes on in-plane bonds. In Figure 4b, the phonon dispersion of the MgB_2 monolayer is presented. In the phonon spectrum there are no imaginary frequencies, which confirms, once again, the dynamical stability of the system (also demonstrated earlier by the MD calculations).

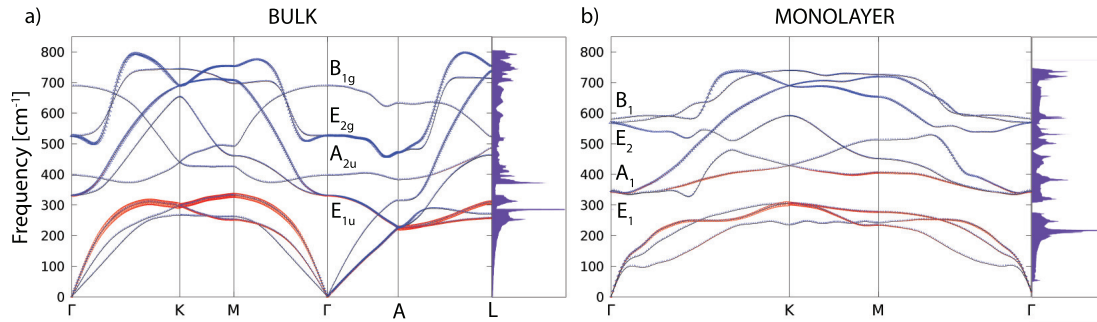


Figure 4. The phonon dispersion and the phonon density of states for the MgB_2 bulk (a) and monolayer (b). The blue and red colours represent the B and Mg atom contributions in the phonon dispersion, respectively.

At the Γ point, there are three acoustic and six optical modes (from which two pairs are doubly degenerate). The optical modes A_1 , B_1 , E_1 , and E_2 are related to the optical modes of the parent material. Two significant differences between the bulk and monolayer spectrum can be observed: The E_1 and A_1 mode become energy degenerate in the monolayer, resulting in either a slight softening (hardening) of the modes which leads to nearly equal frequencies, which opens a gap in the phonon density of states (DOS) between the acoustic and optical modes. A more significant effect concerns the softening of the B_1 mode and hardening of the E_2 mode. As in the bulk E_{2g} mode, the monolayer E_2 mode is strongly coupled to electrons, causing the superconductivity in the monolayer in a similar fashion as in the bulk. In Figure 5, the vibrational frequencies and normal coordinates for the MgB_2 monolayer are presented. The symmetry group is C_{6v} , and the acoustic modes are A_1 and E_1 . The optical modes at the Γ point are A_1 , B_1 , E_1 , and E_2 , where the infrared-active ones are A_1 and E_1 . The Raman-active modes are A_1 , E_1 , and E_2 , and B_1 is silent. In Table 2, the Raman tensor for the MgB_2 monolayer is presented [52]. Similar to graphene, the phonon eigenvectors and the normal coordinates at the Γ -point are determined by symmetry rules and, therefore, are a model independent.

Table 2. Raman tensor of the MgB_2 monolayer.

Raman Tensors	
MgB_2 -mono $Dg77 = TC_{6v}$ $O_z \parallel C_6$ $O_x \parallel \sigma_v$	$\begin{pmatrix} a & 0 & 0 \\ 0 & a & 0 \\ 0 & 0 & b \end{pmatrix} \begin{pmatrix} 0 & 0 & c \\ 0 & 0 & 0 \\ c & 0 & 0 \end{pmatrix} \begin{pmatrix} 0 & 0 & 0 \\ 0 & 0 & c \\ 0 & c & 0 \end{pmatrix} \begin{pmatrix} d & 0 & 0 \\ 0 & -d & 0 \\ 0 & 0 & 0 \end{pmatrix} \begin{pmatrix} 0 & -d & 0 \\ -d & 0 & 0 \\ 0 & 0 & 0 \end{pmatrix}$

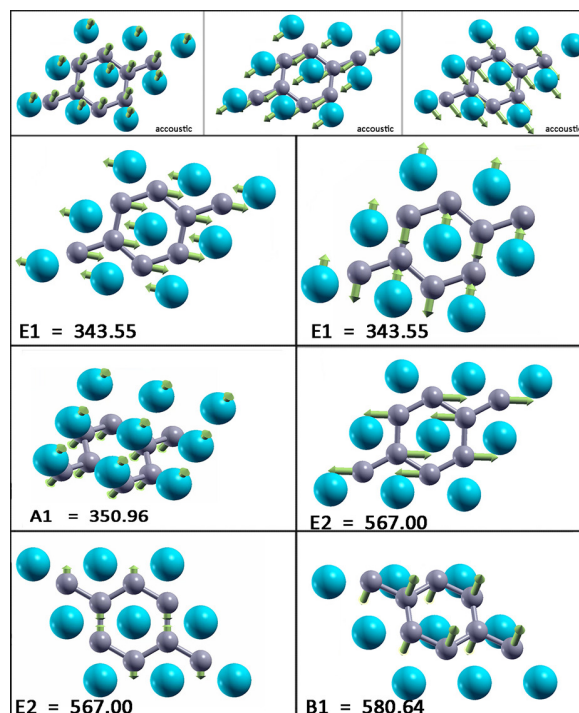


Figure 5. Vibrational frequencies (in wavenumbers) and the vibration normal coordinates at Γ for the MgB_2 monolayer.

4. Conclusions

The electronic band structure, density of states, phonon dispersion, and elastic constants have been calculated for the MgB_2 monolayer and compared to the bulk material, using first-principles calculations within the DFT framework. We demonstrated an increase of electronic density of states at the Fermi level in the monolayer (compared to the bulk) and determined its stability under various strains. These two features are crucial for the enhancement of electron–phonon coupling and they enable significant mechanical modification that increases the critical superconducting temperature. Establishing stability and offering insight into this novel 2D material, we focus on the effects of ultimate lowering of the dimensionality. The question of reduction of dimensionality to its limit, a truly atomic-scale 2D system, and the consequences of this [53–61] are highly relevant, not only to fundamental science but also to applications in nanotechnology.

Author Contributions: Conceptualization, J.P. and R.G.; Validation, K.H., M.B., R.G.; Investigation, J.P., I.P., A.Š. and V.D.; Writing—Original Draft Preparation, J.P., I.P., A.Š. and V.D.; Writing—Review & Editing, J.P.; Supervision, R.G.; Funding Acquisition, K.H., M.B. and R.G.

Funding: This research is supported by Serbian Ministry of Education, Science and Technological Development under projects OI 171005, III 45018, and III 45016 and by the Qatar National Research Fund, cycle 11, under grant number NPRP 11S-1126-170033. K.H. acknowledges the support of the European Commission under the H2020 grant TWINFUSYON.GA692034.

Acknowledgments: The DFT calculations were performed using the computational resources at Johannes Kepler University, Linz, Austria. This work was supported by the Serbian Ministry of Education, Science and Technological Development under projects OI 171005, III 45018, and III 45016.

Conflicts of Interest: The authors declare no conflict of interest.

References

1. Jones, M.E.; Marsh R.E. The preparation and structure of magnesium boride, MgB₂. *J. Am. Chem. Soc.* **1953**, *76*, 5. [[CrossRef](#)]
2. Nagamatsu, J.; Nakagawa, N.; Muranaka, T.; Zenitani, Y.; Akimitsu, J. Superconductivity at 39 K in magnesium diboride. *Nature* **2001**, *410*, 63. [[CrossRef](#)] [[PubMed](#)]
3. Bud'ko, S.L.; Lapertot, G.; Petrovic, C.; Cunningham, C.E.; Anderson, N.; Canfield, P.C. Boron Isotope Effect in Superconducting MgB₂. *Phys. Rev. Lett.* **2001**, *86*, 1877. [[CrossRef](#)] [[PubMed](#)]
4. Pickett, W. Superconductivity: 2D Physics, Unknown Mechanisms, Current Puzzles. *Emerg. Phenom. Correl. Matter Lect. Notes Autumn School Corr. Electron.* **2013**, *2013*, 45.
5. Choi, H.J.; Roundy, D.; Sun, H.; Cohen, M.L.; Steven Louie, G. The origin of the anomalous superconducting properties of MgB₂. *Nature* **2002**, *418*, 758. [[CrossRef](#)]
6. Kortus, J.; Mazin, I.I.; Belaichenko, K.D.; Antropov, V.P.; Boyer, L.L. Superconductivity of Metallic Boron in MgB₂. *Phys. Rev. Lett.* **2001**, *86*, 4656. [[CrossRef](#)]
7. An, J.M.; Pickett, W.E. Superconductivity of MgB₂: Covalent Bonds Driven Metallic. *Phys. Rev. Lett.* **2001**, *86*, 4366. [[CrossRef](#)] [[PubMed](#)]
8. Liu, A.Y.; Mazin, I.I.; Kortus, J. Beyond Eliashberg Superconductivity in MgB₂: Anharmonicity, Two-Phonon Scattering, and Multiple Gaps. *Phys. Rev. Lett.* **2001**, *87*, 087005. [[CrossRef](#)] [[PubMed](#)]
9. Kong, Y.; Dolgov, O.V.; Jepsen, O.; Andersen, O.K. Electron-phonon interaction in the normal and superconducting states of MgB₂. *Phys. Rev. B* **2001**, *64*, 020501. [[CrossRef](#)]
10. Bohnen, K.-P.; Heid, R.; Renker, B. Phonon Dispersion and Electron-Phonon Coupling in MgB₂ and AlB₂. *Phys. Rev. Lett.* **2001**, *86*, 5771. [[CrossRef](#)] [[PubMed](#)]
11. Kunc, K.; Loa, I.; Syassen, K.; Kremer, R.K.; Ahn, K. MgB₂ under pressure: phonon calculations, Raman spectroscopy, and optical reflectance. *J. Phys. Condens. Matter* **2001**, *13*, 9945. [[CrossRef](#)]
12. Choi, H.J.; Roundy, D.; Sun, H.; Cohen, M.L.; Louie, S.G. First-principles calculation of the superconducting transition in MgB₂ within the anisotropic Eliashberg formalism. *Phys. Rev. B* **2002**, *66*, 020513. [[CrossRef](#)]
13. Canfield, P.C.; Crabtree, G.W. Magnesium Diboride: Better Late than Never. *Phys. Today* **2003**, *56*, 34. [[CrossRef](#)]
14. Novoselov, K.S.; Geim, A.K.; Morozov, S.V.; Jiang, D.; Zhang, Y.; Dubonos, S.V.; Grigorieva, I.V.; Firsov, A.A. Electric Field Effect in Atomically Thin Carbon Films. *Science* **2004**, *306*, 666–669. [[CrossRef](#)]
15. Katsnelson, M.I.; Novoselov, K.S.; Geim, A.K. Chiral tunnelling and the Klein paradox in graphene. *Nat. Phys.* **2006**, *2*, 620–625. [[CrossRef](#)]
16. Katsnelson, M.I. Zitterbewegung, chirality, and minimal conductivity in graphene. *Eur. Phys. J. B* **2006**, *51*, 157–160. [[CrossRef](#)]
17. Rusin, T.M.; Zawadzki, W. Zitterbewegung of electrons in graphene in a magnetic field. *Phys. Rev. B* **2008**, *78*, 125419. [[CrossRef](#)]
18. Pisana, S.; Lazzeri, M.; Casiraghi, C.; Novoselov, K.S.; Geim, A.K.; Ferrari, A.C.; Mauri, F. Breakdown of the adiabatic Born-Oppenheimer approximation in graphene. *Nat. Mater.* **2007**, *6*, 198–201. [[CrossRef](#)] [[PubMed](#)]
19. Piscanec, S.; Lazzeri, M.; Mauri, F.; Ferrari, A.C.; Robertson, J. Kohn Anomalies and Electron-Phonon Interactions in Graphite. *Phys. Rev. Lett.* **2004**, *93*, 85503. [[CrossRef](#)]
20. Novoselov, K.S.; Jiang, Z.; Zhang, Y.; Morozov, S.V.; Stormer, H.L.; Zeitler, U.; Maan, J.C.; Boebinger, G.S.; Kim, P.; Geim, A.K. Room-temperature quantum Hall effect in graphene. *Science* **2007**, *315*, 1379. [[CrossRef](#)]
21. Zhou, S.Y.; Gweon, G.-H.; Fedorov, A.V.; First, P.N.; de Heer, W.A.; Lee, D.-H.; Guinea, F.; Castro Neto, A.H.; Lanzara, A.; et al. Substrate-induced bandgap opening in epitaxial graphene. *Nat. Mater.* **2007**, *6*, 770–775. [[CrossRef](#)]
22. Zhang, Y.; Tan, Y.; Stormer, H.L.; Kim, P. Experimental observation of the quantum Hall effect and Berry's phase in graphene. *Nature* **2005**, *438*, 201–204. [[CrossRef](#)]
23. Bekaert, J.; Aperis, A.; Partoens, B. Oppeneer, P.M.; Milošević, M.V. Evolution of multigap superconductivity in the atomically thin limit: Strain-enhanced three-gap superconductivity in monolayer MgB₂. *Phys. Rev. B* **2017**, *96*, 094510.
24. Morshedloo, T.; Roknabadi, M.R.; Behdani, M. First-principles study of the superconductivity in MgB₂ bulk and in its bilayer thin film based on electron-phonon coupling. *Physica C* **2015**, *509*. [[CrossRef](#)]

25. Calandra, M.; Profeta, G.; Mauri, F. Superconductivity in metal-coated graphene. *Phys. Status Solidi (b)* **2012**, *249*, 2544. [[CrossRef](#)]
26. Ludbrook, B.M.; Levy, G.; Nigge, P.; Zonno, M.; Schneider, M.; Dvorak, D.J.; Veenstra, C.N.; Zhdanovich, S.; Wong, D.; Dosanjh, P.; et al. Evidence for superconductivity in Li-decorated monolayer graphene. *Proc. Natl. Acad. Sci. USA* **2015**, *112*, 11795. [[CrossRef](#)] [[PubMed](#)]
27. Profeta, G.; Calandra, M.; Mauri, F. Phonon-mediated superconductivity in graphene by lithium deposition. *Nat. Phys.* **2012**, *8*, 131–134. [[CrossRef](#)]
28. Pešić, J.; Gajić, R.; Hingerl, K.; Belić, M. Strain-enhanced superconductivity in Li-doped graphene. *Europhys. Lett.* **2014**, *108*, 67005. [[CrossRef](#)]
29. Szczesniak, D.; Durajski, A.P.; Szczesniak, R. Influence of lithium doping on the thermodynamic properties of graphene based superconductors. *J. Phys-Condens. Mat.* **2014**, *26*, 255701. [[CrossRef](#)]
30. Durajski, A.; Skoczylas, K.; Szczesniak, R. Superconductivity in bilayer graphene intercalated with alkali and alkaline earth metals. *Phys. Chem. Chem. Phys.* **2019**, *21*, 5925. [[CrossRef](#)] [[PubMed](#)]
31. Zheng, J.-J.; Margine, E.R. First-principles calculations of the superconducting properties in Li-decorated monolayer graphene within the anisotropic Migdal-Eliashberg formalism. *Phys. Rev. B* **2016**, *94*, 064509. [[CrossRef](#)]
32. Margine, E.R.; Lambert, H.; Giustino, F. Electron-phonon interaction and pairing mechanism in superconducting Ca-intercalated bilayer graphene. *Sci. Rep.* **2016**, *6*, 21414. [[CrossRef](#)]
33. Mazin, I.I.; Antropov, V.P. Electronic structure, electron-phonon coupling, and multiband effects in MgB₂. *Phys. C Supercond.* **2003**, *385*, 49–65. [[CrossRef](#)]
34. Giannozzi, P.; Andreussi, O.; Brumme, T.; Bunau, O.; Buongiorno, N.M.; Calandra, M.; Car, R.; Cavazzoni, C.; Ceresoli, D.; Cococcioni, M. et al. Quantum espresso: A modular and open-source software project for quantum simulations of materials. *J. Phys. Condensed Matter* **2009**, *21*, 395502. [[CrossRef](#)] [[PubMed](#)]
35. Lu, N.; Guo, H.; Zhuo, Z.; Wang, L.; Wu, X.; Zeng, X.C. Twisted MX₂/MoS₂ heterobilayers: effect of van der Waals interaction on the electronic structure. *Nanoscale* **2017**, *9*, 19131–19138. [[CrossRef](#)] [[PubMed](#)]
36. Soler, J.M.; Artacho, E.; Gale, J.D.; García, A.; Junquera, J.; Ordejón, P.; Sánchez-Portal, D. The SIESTA method for ab initio order-N materials simulation. *J. Phys. Condens. Matter.* **2002**, *14*, 2745. [[CrossRef](#)]
37. Perdew, J.P.; Burke, K.; Ernzerhof, M. Generalized Gradient Approximation Made Simple. *Phys. Rev. Lett.* **1996**, *77*, 3865–3868. [[CrossRef](#)]
38. Troullier, N.; Martins, J.L. Efficient pseudopotentials for plane-wave calculations. *Phys. Rev. B* **1991**, *43*, 1993–2006. [[CrossRef](#)]
39. Golezorkhtabar, R.; Pavone, P.; Spitaler, J.; Puschnig, P.; Draxl, C. ElaStic: A tool for calculating second-order elastic constants from first principles. *Comput. Phys. Commun.* **2013**, *184*, 1861–1873. [[CrossRef](#)]
40. Nosé, S. A unified formulation of the constant temperature molecular dynamics methods. *J. Chem. Phys.* **1984**, *81*, 511. [[CrossRef](#)]
41. Lindemann, F.A. The calculation of molecular vibration frequencies. *Phys. Z.* **1910**, *11*, 609.
42. Andrew, R.C.; Mapasha, R.E.; Ukpong, A.M.; Chetty, N. Mechanical properties of graphene and boronitrene. *Phys. Rev. B* **2012**, *85*, 125428. [[CrossRef](#)]
43. Zhang, Z.; Yang, Y.; Penev, E.S.; Yakobson, B.I. Elasticity, Flexibility, and Ideal Strength of Borophenes. *Adv. Func. Mater.* **2017**, *27*, 1605059. [[CrossRef](#)]
44. Zhong, H.; Huang, K.; Yu, G.; Yuan, S. Electronic and mechanical properties of few-layer borophene. *Phys. Rev. B* **2018**, *98*, 054104. [[CrossRef](#)]
45. Mannix, A.J.; Zhou, X.F.; Kiraly, B.; Wood, J.D.; Alducin, D.; Myers, B.D.; Liu, X.; Fisher, B.L.; Santiago, U.; Guest, J.R.; et al. Synthesis of borophenes: Anisotropic, two-dimensional boron polymorphs. *Science* **2015**, *350*, 1513–1516. [[CrossRef](#)]
46. Wang, H.; Li, Q.; Gao, Y.; Miao, F.; Zhou, X.-F.; Wan, X.G. Strain effects on borophene: Ideal strength, negative Poisson's ratio and phonon instability. *New J. Phys.* **2016**, *18*, 073016. [[CrossRef](#)]
47. De la Pena-Seaman, O.; de Cross, R.; Heid, R.; Bohnen, K.-P. Effects of Al and C doping on the electronic structure and phonon renormalization in MgB₂. *Phys. Rev. B* **2009**, *79*, 134523. [[CrossRef](#)]
48. Ponce, S.; Margine E.R., Verdi, C.; Giustino, F. EPW: Electron-phonon coupling, transport and superconducting properties using maximally localized Wannier functions. *Comp. Phys. Commun.* **2016**, *209*, 116–133. [[CrossRef](#)]

49. Margine, E.R.; Giustino, F. Anisotropic Migdal-Eliashberg theory using Wannier functions. *Phys. Rev. B* **2013**, *87*, 024505. [[CrossRef](#)]
50. Damljanovic, V.; Gajic, R. Existence of Dirac cones in the Brillouin zone of diperiodic atomic crystals according to group theory. *J. Phys. Condens. Matter* **2016**, *28*, 085502. [[CrossRef](#)]
51. Damljanovic, V.; Gajic, R. Addendum to 'Existence of Dirac cones in the Brillouin zone of diperiodic atomic crystals according to group theory'. *J. Phys. Condens. Matter* **2016**, *28*, 439401. [[CrossRef](#)]
52. Poulet, H.; Mathieu, J.P. *Vibration Spectra and Symmetry of Crystals*; Gordon and Breach: New York, NY, USA, 1976.
53. Szalowski, K. Critical temperature of MgB₂ ultrathin superconducting films: BCS model calculations in the tight-binding approximation. *Phys. Rev. B* **2006**, *74*, 094501. [[CrossRef](#)]
54. Zhang, C.; Wang, Y.; Wang, D.; Zhang, Y.; Liu, Z.-H.; Feng, Q.-R.; Gan, Z.-Z. Suppression of superconductivity in epitaxial MgB₂ ultrathin films. *J. Appl. Phys.* **2013**, *114*, 023903. [[CrossRef](#)]
55. Ao, B.; Zhang, Z.; Tang, T.; Zhao, Y. Potential enhancement of superconductivity in MgB₂ nanosheets: First-principles calculations. *Chem. Phys. Lett.* **2014**, *591*, 185–188. [[CrossRef](#)]
56. Romero-Bermudez, A.; Garcia-Garcia, A.M. Shape resonances and shell effects in thin-film multiband superconductors. *Phys. Rev. B* **2014**, *89*, 024510. [[CrossRef](#)]
57. Romero-Bermudez, A.; Garcia-Garcia, A.M. Size effects in superconducting thin films coupled to a substrate. *Phys. Rev. B* **2014**, *89*, 064508. [[CrossRef](#)]
58. Acharya, N.; Wolak, M.A.; Cunnane, D.P.; Karasik, B.S.; Xi, X.X. MgB₂ ultrathin films fabricated by hybrid physical chemical vapor deposition and ion milling. *APL Mater.* **2016**, *4*, 086114. [[CrossRef](#)]
59. Valentinis, D.; van der Marel, D.; Berthod, C. Rise and fall of shape resonances in thin films of BCS superconductors. *Phys. Rev. B* **2016**, *94*, 054516. [[CrossRef](#)]
60. Narlikar, A.V. Small Superconductors: Introduction. In *The Oxford Handbook of Small Superconductors*, 1st ed.; Narlikar, A.V., Ed.; Oxford University Press: Oxford, UK, 2017.
61. Gariglio, S.; Scheurer, M.; Schmalian, J.; Monteiro, A.M.R.V.L.; Goswami, S.; Caviglia, A. Surface and Interface Superconductivity. In *The Oxford Handbook of Small Superconductors*, 1st ed.; Narlikar, A.V., Ed.; Oxford University Press: Oxford, UK, 2017.



© 2019 by the authors. Licensee MDPI, Basel, Switzerland. This article is an open access article distributed under the terms and conditions of the Creative Commons Attribution (CC BY) license (<http://creativecommons.org/licenses/by/4.0/>).

PAPER

Peculiar symmetry-protected electronic dispersions in two-dimensional materials

To cite this article: V Damjanovi *et al* 2020 *J. Phys.: Condens. Matter* **32** 485501

View the [article online](#) for updates and enhancements.



IOP | ebooks™

Bringing together innovative digital publishing with leading authors from the global scientific community.

Start exploring the collection—download the first chapter of every title for free.

Peculiar symmetry-protected electronic dispersions in two-dimensional materials

V Damljanović^{1,3} , N Lazic² , A Šolajić¹ , J Pešić¹ , B Nikolić²  and M Damjanović² 

¹ Institute of Physics Belgrade, University of Belgrade, Pregrevica 118, 11080 Belgrade, Serbia

² NanoLab, Faculty of Physics, University of Belgrade, PO Box 44, Belgrade 11001, Serbia

E-mail: damlja@ipb.ac.rs

Received 16 June 2020, revised 23 July 2020

Accepted for publication 30 July 2020

Published 8 September 2020



Abstract

Symmetry indicates that low energy spectra of materials could be richer than well-known Dirac, semi-Dirac, or quadratic, hosting some unusual quasiparticles. Performing the systematic study of exact forms of low energy effective Hamiltonians and dispersions in high-symmetry points with fourfold degeneracy of bands, we found new, previously unreported dispersion, which we named poppy flower (PF) after its shape. This massless fermion exists in non-magnetic two-dimensional (2D) crystals with spin-orbit coupling (SOC), which are invariant under one of the proposed ten noncentrosymmetric layer groups. We suggest real three-dimensional (3D) layered materials suitable for exfoliation, having layers that belong to these symmetry groups as candidates for realization of PF fermions. In 2D systems without spin-orbit interaction, fortune teller (FT)-like fermions were theoretically predicted, and afterward experimentally verified in the electronic structure of surface layer of silicon. Herein, we show that such fermions can also be hosted in 2D crystals with SOC, invariant under additional two noncentrosymmetric layer groups. This prediction is confirmed by density functional based calculation: layered BiIO₄, which has been synthesized already as a 3D crystal, exfoliates to stable monolayer with symmetry $pb2_1a$, and FT fermion is observed in the band structure. Analytically calculated density of states (DOS) of the PF shows semimetallic characteristic, in contrast to metallic nature of FT having non-zero DOS at the bands contact energy. We indicate possibilities for symmetry breaking patterns which correspond to the robustness of the proposed dispersions as well as to the transition from Dirac centrosymmetric semimetal to PF.

Keywords: electronic dispersions, spin-orbit coupling, symmetry, new fermions

(Some figures may appear in colour only in the online journal)

1. Introduction

Electronic dispersion essentially determines crystal properties and it is well known that it is assigned by quantum numbers of the underlying symmetry group. These are space, layer (including wallpaper) or line groups, referring respectively to dimensionality of crystals: 3D, quasi-2D (Q2D), or quasi-1D. Probably the most famous example of a low-dimensional material is graphene (there are also related single layers, such as borophene [1], borophosphene [2], graphynes

[3], etc), which hosts Dirac like (linear in quasi-momentum) dispersion in the vicinity of high symmetry Dirac points. Such shape of energy bands, besides being responsible for some intriguing phenomena, provides material realization of relativistic electron. This triggered numerous investigations of the connection between symmetry of materials and appearance of Dirac and Weyl points in their band structures. These points are attributed to existence of rotational [4], nonsymmorphic [5], mirror [6], space-time inversion [7, 8], time-reversal plus fractional translation [9], and generalized chiral symmetry [10]. There are also results on the search for Weyl and Dirac

³ Author to whom any correspondence should be addressed.

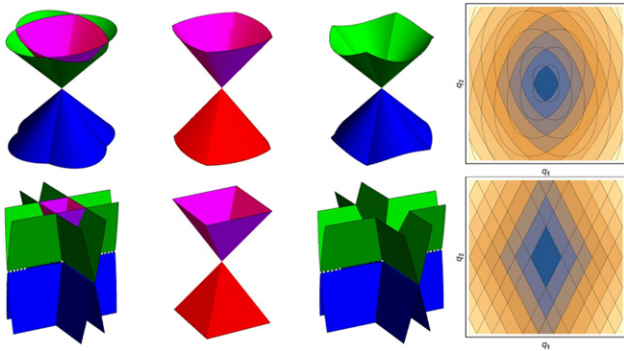


Figure 1. PF (up) and FT (bottom) dispersions (given by equations (3.1)): from left to right are all bands, bands $E_{\pm 1,+1}$, bands $E_{\pm 1,-1}$ and horizontal sections of the bands (iso-energetic lines).

points according to group theoretical criteria in Brillouin zones (BZs) of all space [11], layer [12–14] or wallpaper groups [15].

In addition, geometrical symmetries impose conditions that lead to the emergence of unconventional quasiparticles in condensed matter systems. In 3D materials, enforced by space groups, double Dirac points [16], three-component [17, 18] or hourglass fermions [19] are found, inspiring further theoretical and experimental research [20–25]. Concerning Q2D systems, besides Dirac (as in graphene [26]), there are also semi-Dirac (Dirac-like in one direction, and quadratic in the orthogonal one, as in black phosphorus [27]), quadratic (as in molybdenum disulphide [28]), and fortune teller (FT) dispersions [29], which corresponds to the coexistence of a nodal point and lines. Namely, symmetry analysis of the possible completely linear dispersions in non-magnetic, Q2D materials with negligible spin–orbit coupling (SOC) has shown that only completely massless fermions appearing in layers are Dirac and FT [29]. Recently, FT dispersion has been experimentally confirmed in a surface layer of silicon [30].

A question arises whether new types of fermions are possible in Q2D materials by inclusion of SOC? With help of layer double groups (LDGs) and time-reversal symmetry (TRS) (i.e. gray LDG), we made a quite general search for linear dispersions in the vicinity of high symmetry points (HSPs); since no reference to nonsymmorphic symmetries is made, the topological (hour-glass like) band crossing mechanisms are not *a priori* assumed, as it is usual. Indeed, it turns out that there are two peculiar types (figure 1) featuring twelve nonsymmorphic and noncentrosymmetric groups: two groups support previously predicted FT, and the remaining ones poppy flower (PF) dispersion (generalizing both FT and Dirac types).

After a brief overview of necessary group-theoretical methods, the obtained results are discussed on the basis of effective low-energy model, calculated densities of states and symmetry breaking patterns. Also, a list of material candidates supporting the new dispersions is provided. The predicted effect is justified by density functional based relaxation and band structure calculation in BiIO₄ monolayer. Synthesis of this layered 3D material was reported around a decade ago [31]. Numerical band structure con-

firms our group theoretical prediction, which may be the motivation for future laboratory synthesis of this material as monolayer.

2. Method

Symmetry determines Bloch Hamiltonian in the vicinity of high-symmetry BZ wave vector through the allowed irreducible representations (IRs) of the little group [32]. Allowed IRs of LDGs are subduced from the corresponding space groups IRs (found on Bilbao Crystallographic Server [33]), and also independently constructed by POL-Sym code [34]. Concerning LDGs with TRS, the dimensions [33, 35] of the allowed IRs (actually co-representations) are 1, 2 or 4, and for generic ones, giving bands degeneracy, this is 1 or 2. Here we focus on the band structures near quadruple points at high-symmetry momenta. Further, we do not consider generically degenerate bands, giving double degenerate Dirac dispersion (precisely, it consists of two double spinfull degenerate cones meeting at one fourfold degenerate point); this automatically excludes centrosymmetric crystals, as Kramers degeneracy in them forbids non-degenerate bands [36]. Among the remaining groups, only twelve are with special points with four-dimensional allowed (co)representation.

Analysis of all allowed IRs R of little groups $G(\mathbf{k}_0)$ of HSPs \mathbf{k}_0 in LDG lacking the inversion symmetry gives the following conditions for quadruple point: \mathbf{k}_0 is time-reversal invariant momentum, R is two-dimensional, either real or complex IR. Therefore, we consider $\hat{H}(\mathbf{k})$ being Hamiltonian of the system \hat{H}_0 (including spin–orbit) in the basis $\{|\Psi_1\rangle, |\Psi_2\rangle, |\theta\Psi_1\rangle, |\theta\Psi_2\rangle\}$, where the spinors $|\Psi_i\rangle = |\Psi_i(\mathbf{k})\rangle$ ($i = 1, 2$ counts two bands touching each other at \mathbf{k}_0 also in the absence of TRS) belong to R at \mathbf{k}_0 and θ is an anti-unitary operator of TRS, for which we used $\theta^2 = -\hat{\sigma}_0$, since spinfull case is considered. Throughout the text $\hat{\sigma}_0$ is two-by-two unit matrix, and $\hat{\sigma}_1, \hat{\sigma}_2, \hat{\sigma}_3$ are Pauli matrices. Denoting the little group elements by $\ell = (h|\mathbf{r}_{\hat{h}} + \mathbf{b})$, where h is crystallographic double point group element, while $\mathbf{r}_{\hat{h}}$ and \mathbf{b} are fractional and lattice translation, respectively, one gets the conditions imposed by time-reversal and geometrical symmetries on $\hat{H}(\mathbf{k}_0 + \mathbf{q})$ in the vicinity of \mathbf{k}_0 (therefore, the wavevector \mathbf{q} is small):

$$\hat{H}^*(\mathbf{k}_0 + \mathbf{q}) = \hat{T}^\dagger \hat{H}(\mathbf{k}_0 - \mathbf{q}) \hat{T}, \quad (2.1)$$

$$\hat{H}(\mathbf{k}_0 + \mathbf{q}) = \hat{D}^\dagger(\ell) \hat{H}(\mathbf{k}_0 + \hat{h}'\mathbf{q}) \hat{D}(\ell). \quad (2.2)$$

Here, $\hat{D} = \text{diag}(\hat{R}, \hat{R}^*)$, and \hat{h}' is an operator reduction of vector representation \hat{h} to 2D BZ, while $\hat{T} = -i\hat{\sigma}_2 \otimes \hat{\sigma}_0$ represents the action of θ on the basis of spinors.

To focus on the terms linear in \mathbf{q} , Hamiltonian is expanded in the form $\hat{H}(\mathbf{k}_0 + \mathbf{q}) \approx \sum_{i=1,2} q_i \frac{\partial \hat{H}(\mathbf{k}_0 + \mathbf{q})}{\partial q_i} \Big|_{\mathbf{q}=0}$ (energy scale is conveniently shifted such that $\hat{H}(\mathbf{k}_0) = 0$). To incorporate symmetry, the matrix elements of the Hamiltonian gradient are arranged into the four-by-eight matrix \hat{W} , which entries $w_{pq} = (w_{pq}^1 \ w_{pq}^2)$ are pairs $w_{pq}^i = \frac{\partial H_{pq}(\mathbf{k}_0 + \mathbf{q})}{\partial q_i} \Big|_{\mathbf{q}=0}$. The form

Table 1. Groups providing dispersions (3.1). Notations for layer (columns 1 and 2) and space groups (columns 4, 5 and 6) are according to [37, 38] respectively. IR notation in the eighth column is as in Bilbao Crystallographic Server [33]. Effective Hamiltonian is indicated in the last column by the nonzero parameters (and their interrelations) of (2.5). For the last four groups $a = c$ while \bar{M}_6 and \bar{M}_7 are conjugated pair of IRs.

Layer double group			Corresponding space double group				Dispersion	Nonzero v_{pq}^i	
Group	IR	Group	Plane	IR	IR				
21	$p2_12_12$	\bar{S}_5	18	$P2_12_12$	D_2^3	$z = 0$	\bar{S}_5	(3.1a)	$v_{13}^1, v_{23}^1, v_{33}^1, v_{11}^2, v_{21}^2, v_{31}^2$
25	$pba2$	\bar{S}_5	32	$Pba2$	C_{2v}^8	$z = 0$	\bar{S}_5	(3.1a)	$v_{13}^1, v_{23}^1, v_{33}^1, v_{11}^2, v_{21}^2, v_{31}^2$
28	$pm2_1b$	\bar{Y}_5, \bar{S}_5	26	$Pmc2_1$	C_{2v}^2	$y = 0$	\bar{Z}_5, \bar{U}_5	(3.1a)	$v_{11}^1, v_{21}^1, v_{31}^1, v_{10}^2, v_{20}^2, v_{30}^2$
29	$pb2_1m$	\bar{Y}_5, \bar{S}_5	26	$Pmc2_1$	C_{2v}^2	$x = 0$	\bar{Z}_5, \bar{T}_5	(3.1b)	$v_{11}^1, v_{21}^1, v_{31}^1, v_{10}^2, v_{20}^2, v_{30}^2$
30	$pb2b$	\bar{Y}_5, \bar{S}_5	27	$Pcc2$	C_{2v}^3	$x = 0$	\bar{Z}_5, \bar{T}_5	(3.1a)	$v_{11}^1, v_{21}^1, v_{31}^1, v_{10}^2, v_{20}^2, v_{30}^2$
32	$pm2_1n$	\bar{Y}_5	31	$Pmn2_1$	C_{2v}^7	$y = 0$	\bar{Z}_5	(3.1a)	$v_{13}^1, v_{23}^1, v_{33}^1, v_{10}^2, v_{20}^2, v_{30}^2$
33	$pb2_1a$	\bar{Y}_5	29	$Pca2_1$	C_{2v}^5	$y = 0$	\bar{Z}_5	(3.1b)	$v_{13}^1, v_{23}^1, v_{33}^1, v_{10}^2, v_{20}^2, v_{30}^2$
34	$pb2n$	\bar{Y}_5	30	$Pnc2$	C_{2v}^6	$x = 0$	\bar{Z}_5	(3.1a)	$v_{13}^1, v_{23}^1, v_{33}^1, v_{10}^2, v_{20}^2, v_{30}^2$
54	$p42_12$	(\bar{M}_6, \bar{M}_7)	90	$P42_12$	D_4^2	$z = 0$	(\bar{M}_6, \bar{M}_7)	(3.1a)	$\left\{ \begin{array}{l} v_{02}^1 = v_{02}^2 = v_{31}^1 = -v_{31}^2 \\ v_{10}^1 = v_{10}^2 = v_{23}^1 = -v_{23}^2 \\ v_{13}^1 = -v_{13}^2 = -v_{20}^1 = -v_{20}^2 \end{array} \right\}$
56	$p4bm$	(\bar{M}_6, \bar{M}_7)	100	$P4bm$	C_{4v}^2	$z = 0$	(\bar{M}_6, \bar{M}_7)	(3.1a)	
58	$p\bar{4}2_1m$	(\bar{M}_6, \bar{M}_7)	113	$P\bar{4}2_1m$	D_{2d}^3	$z = 0$	(\bar{M}_6, \bar{M}_7)	(3.1a)	
60	$p\bar{4}b2$	(\bar{M}_6, \bar{M}_7)	117	$P\bar{4}b2$	D_{2d}^7	$z = 0$	(\bar{M}_6, \bar{M}_7)	(3.1a)	

$$\hat{W} = \begin{pmatrix} w_{11} & w_{12} & w_{13} & w_{14} \\ w_{12}^* & w_{22} & w_{14} & w_{24} \\ w_{13}^* & w_{14}^* & -w_{11} & -w_{12}^* \\ w_{14}^* & w_{24}^* & -w_{12} & -w_{22} \end{pmatrix} \quad (2.3)$$

follows from the relation (2.1), together with $w_{pq}^i = w_{qp}^{i*}$ corresponding to the requirement that Hamiltonian \hat{H} is a Hermitian operator. Note that the form (2.3) of \hat{W} leads to the traceless Hamiltonian: it excludes the scalar term (which imposes the tilt of the bands). The geometrical symmetries are incorporated by (2.2), which is rewritten [11, 29] as an efficient fixed point condition

$$\left| \hat{W} \right\rangle = \hat{D} \otimes \hat{D}^* \otimes \hat{h}' \left| \hat{W} \right\rangle, \quad (2.4)$$

on the column vector (32×1) form $\left| \hat{W} \right\rangle$ of \hat{W} . The equation (2.4) is solved with help of the group projection operators for all of the twelve noncentrosymmetric groups hosting quadruple points at high symmetry momenta; in this way, the symmetry determines form of \hat{W} . To explicate this, it is more convenient to use another general expansion of the effective low energy Hamiltonian,

$$\hat{H}(\mathbf{q}) = \sum_{p,q=0}^3 \sum_{i=1}^2 q_i v_{pq}^i \hat{\sigma}_p \otimes \hat{\sigma}_q, \quad (2.5)$$

and find the constraints imposed by symmetry on the real coefficients v_{pq}^i (simply interrelated with w_{pq}^i).

3. Results and discussion

3.1. Symmetry adapted Hamiltonians and dispersions

Groups hosting new dispersions are listed in table 1. Besides intrinsic layer group notation (the first part), the space group

of the system obtained by periodic repetition of the layer along axis perpendicular to it (column plane) according to Bilbao Crystallographic Server is also given (second part), where the directions x , y and z are along axes of orthorhombic/tetragonal 3D primitive unit cell. On the other hand, in POLSym approach we used convention that layers are in xy -plane. Orthogonal lattice vectors \mathbf{a}_1 and \mathbf{a}_2 span primitive rectangular/square 2D unit cell, while reciprocal lattice vectors \mathbf{k}_1 and \mathbf{k}_2 satisfy $\mathbf{a}_j \cdot \mathbf{k}_l = 2\pi\delta_{jl}$ and q_1, q_2 are projections of \mathbf{q} along \mathbf{k}_1 and \mathbf{k}_2 . Relevant BZs are in figure 2.

Effective Hamiltonians allowed by symmetry group in the special points of Brillouin's zone are presented in the last column of the table 1: the nonzero real coefficients v_{pq}^i in the expansion (2.5) are specified, together with the constraints among them. The listed forms correspond to the group settings (lattice vectors and coordinate origin) and double valued irreducible co-representations obtained by POLSym code. In fact, this enabled flexibility in the choice of generators (coordinate system and translational periods), which finally results in the form of irreducible co-representations. These are chosen such to get the same form of the effective Hamiltonian whenever it is possible (for different groups). Equivalent (but different) settings (and co-representations) produce different (still equivalent with respect to dispersions) Hamiltonian forms. Clearly, the exact values of the nonzero coefficients v_{pq}^i (listed in the last column of the table 1) are material dependent. The groups' generators and their representative matrices in the allowed co-representations associated to the specified high-symmetry points are in the table 2. It should be remarked that in all the considered cases this point is fixed by the whole gray group, i.e. the little group is the gray (double) group, and the allowed co-representations of the little group are simultaneously the irreducible co-representations of the gray group. The matrices of the relevant co-representations are four-dimensional. In all the cases time-reversal corresponds to the matrix \hat{T} ; all other generators are represented by the block-diagonal

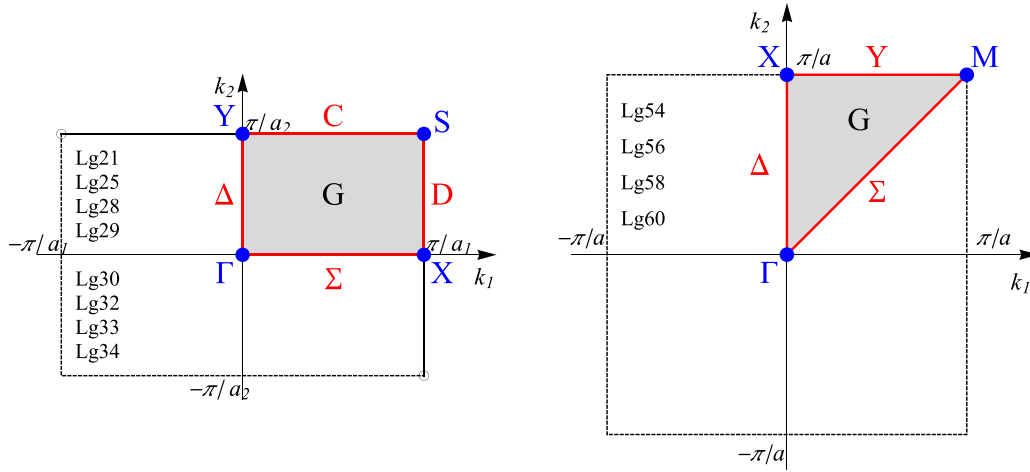


Figure 2. BZs of the groups (listed in table 1) supporting dispersions (3.1). For layer groups 28, 29, 30, 32, 33 and 34 vector k_2 is along (screw) axis of order two.

matrices $\hat{D} = \text{diag}(\hat{R}, \hat{R}^*)$, with mutually conjugated 2×2 blocks. Therefore, only this block, \hat{R} , is given in the table 2.

The described technique leads to two new types of dispersions (figure 1; crossings are taken at $E = 0$). The first one is PF, with four bands (obtained for $u, v = \pm 1$):

$$E_{v,u}(\mathbf{q}) = v\sqrt{aq_1^2 + cq_2^2 + ub|q_1q_2|}. \quad (3.1a)$$

The expression under the square root is non-negative since a, b and c are positive quantities (functions of v_{pq}^i) such that $b^2 - 4ac < 0$. For quadratic layer groups (54, 56, 58, 60) $c = a$, and above dispersion degenerates to the isotropic one $E_{v,u} = v\sqrt{aq^2 + ub|q_1q_2|}$. Two groups, 29 and 33, enforce $b^2 - 4ac = 0$, hosting thus FT dispersions (with bands counted by $u, v = \pm 1$):

$$E_{v,u}(\mathbf{q}) = v|f|q_1| + ug|q_2||, \quad (3.1b)$$

with f, g positive quantities, also functions of v_{pq}^i . Note that on the other side, the limit $b \rightarrow 0^+$ gives Dirac dispersion.

3.2. Density of states

Dispersion (3.1), differing from the well-known Dirac, semi-Dirac or quadratic, impose specific physical properties. In this context, one must take into account the range of validity of these forms, describing the realistic band structures only in the vicinity of high-symmetry point. In particular, corresponding density of states (DOS) near $E = 0$ are:

$$\rho_{\text{PF}}^{\text{SOC}} = \frac{2|E|}{\pi\sqrt{4ac - b^2}}, \quad (3.2a)$$

$$\rho_{\text{FT}}^{\text{SOC}} \approx \frac{L}{4\pi^2\sqrt{f^2 + g^2}}. \quad (3.2b)$$

Unlike to PF, but similarly to 3D nodal semimetals [39], exact calculation of DOS of FT is prevented due to the non-circular iso-energetic lines (figure 1). Thus, the last expression corresponds to realistic situations where the horizontal parts of band crossing lines are of the length L (this is an effective

range of approximation). In non-SOC case calculation of DOS gives doubled results (3.2), since each energy is spin degenerate, which is then decoupled from the orbital one. Non zero DOS of FT near $E = 0$ is in contrast to DOS of Dirac or PF dispersions being proportional to $|E|$, as well as to semi-Dirac which is proportional to $\sqrt{|E|}$. This affects many properties, to mention only charge and spin transport. Further, it can be shown that the electron effective mass, obtained from band curvatures, for all dispersions (3.1) vanishes. Let us emphasize that the higher order terms, neglected in derivation cannot change the obtained band topology (figure 1), though may distort bands slightly.

3.3. Symmetry breaking

Despite the obtained dispersions are essential, i.e. resistant to symmetry preserving perturbation, an interesting additional insight is gained by considering symmetry breaking. Herein, taking into account group-subgroup relations, we discuss the possibilities of robustness or switching between various dispersions at the same BZ-point by lowering the symmetry, e.g. due to strain. It is expected that decreasing the number of symmetry elements leads to relaxing the constraints imposed on Hamiltonians, and consequently increasing (or preserving) the number of independent parameters. In this context, taking into account the number of non-zero parameters v_{pq}^i of (2.5) given in table 1, it is meaningful to consider the transitions from FT to anisotropic PF, as well as from isotropic PF to FT, when the symmetry is lowered. Precisely, the allowed four-band model Hamiltonian diagonalizing in PF dispersion have six real independent parameters, which are reduced to three for quadratic groups; similarly, there are 4 real independent Hamiltonian parameters for FT. Before proceeding, let us take a brief look into the robustness of FT and PF.

Regarding groups 29 and 33 supporting FT dispersion, symmetry reduction in which either nonsymmorphic glide plane or screw axis (but not both) is retained causes that FT at the Y point splits into two non-degenerate conical dispersions. Opposite out-of-plane shifts of the adjacent nuclei positioned

Table 2. Allowed irreducible co-representations: for each group and corresponding HSP, the generators are listed, and the block-diagonal part \hat{R} of double valued co-representation \hat{D} representing these generators (in the same order). Here, $C_{n\hat{n}}$ is rotation for $2\pi/n$ around axis \hat{n} (which is $\hat{x}, \hat{y}, \hat{z}$, or $\hat{c} = \frac{1}{\sqrt{2}}(\hat{x} + \hat{y})$), $m_{\hat{n}}$ is vertical mirror plane which contains \hat{n} axis, m_h is horizontal mirror plane, and $S_n = C_{n\hat{z}}m_h$.

Group	HSP	Generators		\hat{R}			
21	S	$(C_{2\hat{x}} \frac{1}{2}0)$	$(C_{2\hat{y}} 0\frac{1}{2})$	$\hat{\sigma}_3$	$\hat{\sigma}_1$		
25	S	$(m_{\hat{x}} \frac{1}{2}0)$	$(m_{\hat{y}} 0\frac{1}{2})$	$\hat{\sigma}_3$	$\hat{\sigma}_1$		
28	Y	$(I 10)$	$(C_{2\hat{y}} 0\frac{1}{2})$	$m_{\hat{y}}$	$\hat{\sigma}_0$	$-\hat{\sigma}_3$	$-i\hat{\sigma}_2$
28	S	$(I 10)$	$(C_{2\hat{y}} 0\frac{1}{2})$	$m_{\hat{y}}$	$-\hat{\sigma}_0$	$-\hat{\sigma}_3$	$-i\hat{\sigma}_2$
29	Y	$(I 10)$	$(C_{2\hat{y}} 0\frac{1}{2})$	m_h	$\hat{\sigma}_0$	$-\hat{\sigma}_3$	$-i\hat{\sigma}_2$
29	S	$(I 10)$	$(C_{2\hat{y}} 0\frac{1}{2})$	m_h	$-\hat{\sigma}_0$	$-\hat{\sigma}_3$	$-i\hat{\sigma}_2$
30	Y	$(I 10)$	$(m_{\hat{y}} 0\frac{1}{2})$	$C_{2\hat{y}}$	$\hat{\sigma}_0$	$-\hat{\sigma}_3$	$-i\hat{\sigma}_2$
30	S	$(I 10)$	$(m_{\hat{y}} 0\frac{1}{2})$	$C_{2\hat{y}}$	$-\hat{\sigma}_0$	$-\hat{\sigma}_3$	$-i\hat{\sigma}_2$
32	Y	$(I 10)$	$(m_h \frac{1}{2}\frac{1}{2})$	$m_{\hat{y}}$	$\hat{\sigma}_0$	$-\hat{\sigma}_3$	$-i\hat{\sigma}_2$
33	Y	$(m_h \frac{1}{2}0)$	$(C_{2\hat{y}} 0\frac{1}{2})$		$i\hat{\sigma}_3$	$\hat{\sigma}_1$	
34	Y	$(I 10)$	$(m_h \frac{1}{2}\frac{1}{2})$	$C_{2\hat{y}}$	$\hat{\sigma}_0$	$-\hat{\sigma}_3$	$-i\hat{\sigma}_2$
54	M	$(I 10)$	$(C_{2\hat{c}} \frac{1}{2}\frac{1}{2})$	$C_{4\hat{z}}$	$-\hat{\sigma}_0$	$-i\hat{\sigma}_2$	$e^{-i\frac{3\pi}{4}} \text{diag}(1, i)$
56	M	$(I 10)$	$(m_{\hat{c}} \frac{1}{2}\frac{1}{2})$	$C_{4\hat{z}}$	$-\hat{\sigma}_0$	$-i\hat{\sigma}_2$	$e^{-i\frac{3\pi}{4}} \text{diag}(1, i)$
58	M	$(I 10)$	$(m_{\hat{c}} \frac{1}{2}\frac{1}{2})$	S_4	$-\hat{\sigma}_0$	$-i\hat{\sigma}_2$	$e^{-i\frac{3\pi}{4}} \text{diag}(1, i)$
60	M	$(I 10)$	$(C_{2\hat{c}} \frac{1}{2}\frac{1}{2})$	S_4	$-\hat{\sigma}_0$	$-i\hat{\sigma}_2$	$e^{-i\frac{3\pi}{4}} \text{diag}(1, i)$

in the mirror plane, transforms mirror into a glide plane, while doubling the lattice constant; this in turn halves primitive vector \mathbf{k}_1 of the reciprocal lattice. Group 29 reduces to 33 and the S point in 29 becomes Y point in 33. Consequently, FT in Y and S points in 29 are robust against lowering the symmetry to group 33. Similarly, concerning the PF, any homogeneous stretching along \mathbf{a}_1 or \mathbf{a}_2 axis deforms square primitive cell to rectangular, reducing the symmetries of layer groups 54 and 58 (56 and 60) to the group 21 (25) and causes PF to change from isotropic to anisotropic form, which implies direction-dependent electronic and related properties.

Since PF is a generalized form of FT, one could expect that the parameters of these dispersions can be interrelated by tuning. However, continuous transformation from FT to PF at the same point of the BZ is not possible, since neither of groups supporting FT is a subgroup of any of groups allowing PF, nor vice-versa. The expression (3.2a) for DOS of PF shows that the changing parameters such that PF approaches to FT results in a singularity at zero energy. In the other words, if opposite would hold, arbitrarily small displacements of nuclei, being sufficient to lower the symmetry, would cause a jump of (graphene-like) negligible DOS of PF to a finite and constant DOS of FT, which we found unlikely. At the same time, such obstruction from DOS does not forbid the transition between Dirac (double degenerate cones with four-fold degenerate point) and PF, nor it forbids splitting of FT and PF into two non-degenerate conical dispersions (with double degenerate point).

Following the above arguments, it is expected that transition from Dirac cone to PF may be realized by lowering the symmetry, since Dirac dispersions has less independent parameters than PF. According to [5] Dirac semimetals in time-reversal invariant two-dimensional systems with strong SOC are possible in nonsymmorphic groups with inversion symmetry. E.g. let us consider the layer group 46 ($pmmn$), hosting Dirac cones

at X , Y and S HSPs (the BZ is the same as this one given on the left panel in figure 2). It is expected that the violation of the inversion symmetry leads to Weyl points or node [5]. However, listing all subgroups, it turns out that the two of the subgroups, 32 and 21, actually host PF in the points Y and S , respectively. Indeed, in [46], using spinfull tight-binding model with four sites (with s-orbitals) per unit cell, authors show that at fillings 2, 6, system invariant under double layer group 21 is semimetal, which hosts one fourfold degenerate and four Weyl points. A plethora of such cases, where groups allowing PF from the table 1 are subgroups of symmetry groups of Dirac semimetals, indicates candidates for transitions between centrosymmetric and noncentrosymmetric crystals with protected four-fold band crossing point. Moreover, the existence of such essential fourfold degenerate point simultaneously with double degenerate Weyl points in the same system, makes that the layers from our list represent possible two-dimensional materials suitable for the study of their interplay.

3.4. Material realization

Despite the fabrication of freestanding layers is not always feasible, the above theoretical predictions required material realizations, or at least numerical simulations. To find realistic material with layer groups from table 1 we searched the list [41] of 3D layered materials, synthesis of which has been reported in the literature. In the table 3 we listed potential material candidates with symmetry groups allowing the predicted peculiar dispersions. These are laboratory fabricated 3D crystals with layered structures, which could be easily or potentially exfoliated into layers.

It is interesting to single out our group-theoretical findings indicated that dispersions (3.1) are not preserved when SOC is neglected, except for the LDG 33, which supports FT dispersion also in that case [29]. Inclusion of SOC moves FT from

Table 3. Material candidates: layered systems with symmetry groups hosting the dispersions (3.1). Layer and corresponding space groups are listed for materials given by a formula and materials project ID. Abbreviations EE and PE stand for easily and potentially exfoliable, respectively, according to [41].

Layer group	Space group	Formula	ID	EE/PE		
21	$p2_12_12$	18	$P2_12_12$	As ₂ SO ₆	mp-27230	EE
				MgMoTeO ₆	mp-1210722	EE
25	$pba2$	32	$Pba2$	Au ₂ Se ₂ O ₇	mp-28095	EE
				Re ₂ S ₂ O ₁₃ -I	mp-974650	EE
28	$pm2_1b$	26	$Pmc2_1$	TIP ₅	mp-27411	EE
				KO ₂ H ₄ F	mp-983327	PE
				NaGe ₃ P ₃	mp-1104707	PE
29	$pb2_1m$	26	$Pmc2_1$	WO ₂ Cl ₂	mp-32539	EE
32	$pm2_1n$	31	$Pmn2_1$	CuCOCl	mp-562090	EE
33	$pb2_1a$	29	$Pca2_1$	BiIO ₄	mp-1191266	PE
				KPSe ₆	mp-18625	EE
58	$p\bar{4}2_1m$	113	$P\bar{4}2_1m$	LiReO ₂ F ₄	mp-554108	EE

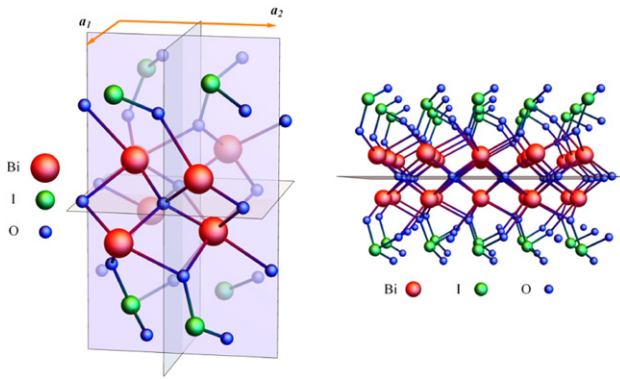


Figure 3. Crystal structure of BiIO₄ mono-layer: elementary cell (left) and a part of layer (right).

BZ corners to the Y -point. The material BiIO₄ belongs to corresponding space group 29 and has layers parallel to the $y = 0$ plane. Consequently, it should exfoliate to layer group 33 so we choose it for further DFT investigations, as an example of achievements of our theory. Since IRs from table 1 are the only extra IRs in these BZ points, the dispersions (3.1) are unavoidable for crystals with symmetry of these groups. On the other hand, the position of Fermi level cannot be determined solely by symmetry arguments, nor it can be guaranteed that no other bands cross or touch the Fermi level.

We determined crystal (figure 3) and band structure (figure 4) of BiIO₄ mono-layer configuration using DFT calculations: full relaxation and bands calculations were performed by QUANTUM ESPRESSO software package [42], full relativistic PAW pseudopotentials [43, 44], with the Perdew–Burke–Ernzerhof exchange–correlation functional [45]. The energy cutoff for electron wavefunction and charge density of 47 Ry and 476 Ry were chosen, respectively. The band structures were found in 500 k -points on selected path, and 2500 k -points for 2D band structure plots in the vicinity of HSPs.

Crystal structure of mono-layer is shown in figure 3. It belongs to rectangular lattice of the group 33, with nearly equal $a_1 = 0.566$ nm and $a_2 = 0.575$ nm. Band structure of BiIO₄

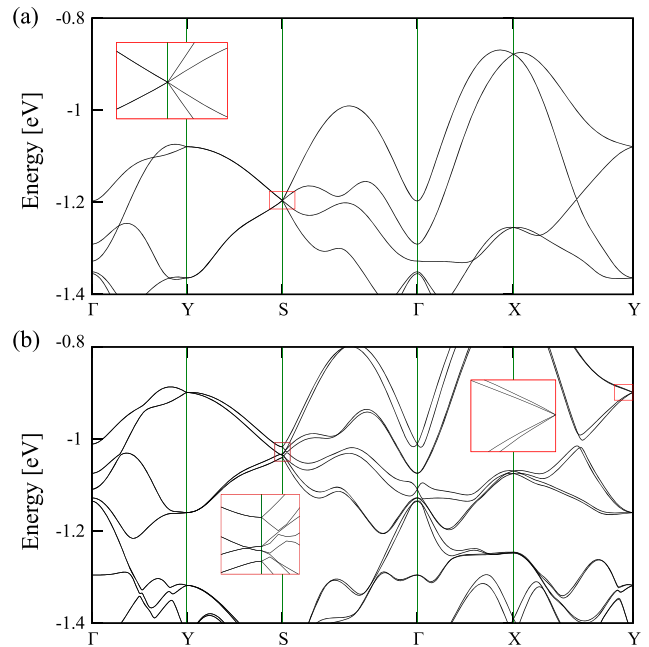


Figure 4. Band structure of BiIO₄ mono-layer without SOC (top) and with SOC (bottom), with insets showing magnified FT and split FT dispersions. The Fermi level is set to zero eV.

mono-layer with and without SOC is shown in figure 4. It turns out that the system is insulating in undoped and ungated regime. The closest to Fermi level FT state is at -0.9 eV. When SOC is neglected energy at the point S is eightfold degenerate (including spin), which gives electron filling of $8n$ that is necessary for insulating systems [40]. With inclusion of SOC the eightfold spinfull degeneracy at S is lifted, but sets of eight non-degenerate bands each, form *cat's cradle* structure along ΓX line, as predicted in reference [46]. This gives again electron filling of $8n$ [46, 47]. Our electron filling of 184, derived from DFT calculations, is indeed divisible by 8. Electron filling for DLG 33 prevents FT to be the only dispersion at the Fermi level, while for remaining groups in table 1 the filling condition necessary for Fermi surface consisting of isolated points is $\nu = 4n + 2$.

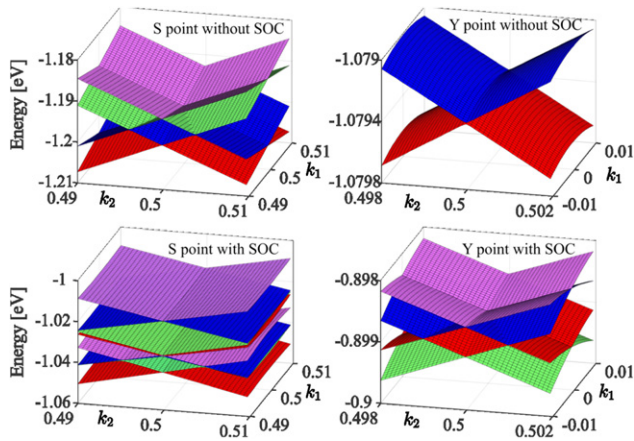


Figure 5. Band structures of BiIO₄ mono-layer without and with SOC near points *S* and *Y*. Inclusion of SOC turns FT dispersion into nodal lines in *S*, and degenerate Dirac line into FT in *Y*.

Behavior of FT states with inclusion of SOC is shown in figure 5. In non-SOC case, two pairs of Dirac lines meet at the point *S* and form the FT states. SOC splits eightfold degenerate band at *S* into four double degenerate ones. Near point *Y*, SOC splits fourfold spinfull degenerate Dirac line into one FT state. Since SOC strength is proportional to the fourth power of the atomic number [48], heavy elements in the material induced observable splitting.

4. Conclusions

Characterized by band crossings (touching) points (lines) at Fermi level from which energies disperse linearly, nodal metals/semimetals take an important role in investigations of various topological properties of crystals. Among them, symmetry-enforced ones represent a class of materials hosting such dispersions in HSPs due to increased degeneracy. In the language of group theory, while the spinless case is described by the ordinary group of geometrical transformations, the spinfull situation, when system is robust on spin-orbit perturbation, needs double groups. Additional inclusion of TRS leads to gray magnetic ordinary or double group. The increased degeneracy of energy is enabled by higher dimensional allowed irreducible (co)representations of the corresponding underlying crystal symmetry.

New fermions in 2D materials revealed by application of full gray double layer group symmetry contribute to the interesting physical phenomena of layered systems: two new types of dispersions beyond Dirac, PF and FT, accompany the fourfold degeneracy of bands in high-symmetry points. Our findings single out list of twelve nonsymmorphic and non-centrosymmetric layer groups that support such unusual linear electronic dispersions. As the method is not based on the topological mechanism (invoking nonsymmorphic symmetry), the result is general, verifying *a posteriori* the necessity of nonsymmorphic elements for the considered dispersions. Providing this list, numerical simulations aimed to find material realizations of the peculiar dispersions are facilitated, which is of a great importance to achieve corresponding physical properties. PF dispersion occurs in ten groups; in particular, there

are single isolated HSP hosting it in the groups $p2_12_12$, $pba2$ (point *S*), $pm2_1n$, $pb2n$ (*Y*), and $p42_12$, $p4bm$, $p42_1m$, $p4b2$ (*M*), while the groups $pm2_1b$ and $pb2b$ have two such points (*Y*, *S*). On the other hand, the FT type of dispersion in the group $pb2_1a$ is hosted in single (*Y*), and in the group $pb2_1m$ in two HSPs (*Y*, *S*).

Particularly interesting are groups $pb2_1a$, supporting FT dispersion both with and without SOC, as well as $pba2$ and $p4bm$, which are also wallpaper groups, preserved even when perpendicular, homogenous electric field is applied (e.g. due to gating). Moreover, coexistence of degenerate point and lines at the same energy in FT dispersion may lead to some new phenomena. FT dispersion has constant contribution to DOS, manifested as a plateau nearby zero energy in FT. This may be important in technological applications, especially when electron and/or spin transport are looked for, like materials for solar cells [49], spintronic etc. On the contrary, PF dispersion, similarly to Dirac ones, contributes by linear DOS with no states on zero energy. It has both isotropic and anisotropic forms which may be continuously transformed into each other by crystal deformations.

Our numerical calculations show that layered BiIO₄ 3D crystal, exfoliates to stable mono-layer having a symmetry group from our list. Band structure of BiIO₄ mono-layer confirms theoretical prediction, but further efforts are necessary in order to place the Fermi level at right energy.

Acknowledgments

Authors VD, AŠ and JP acknowledge funding provided by the Institute of Physics Belgrade, through the Grant by the Ministry of Education, Science and Technological Development of the Republic of Serbia. NL, BN and MD were supported by the Serbian Ministry of Education, Science and Technological Development under Project Number OI171035. DFT calculations were performed using computational resources at Johannes Kepler University, Linz, Austria.

ORCID iDs

V Damljanović <https://orcid.org/0000-0001-7517-6439>
 N Lazić <https://orcid.org/0000-0002-3634-0301>
 A Šolajić <https://orcid.org/0000-0002-0553-0858>
 J Pešić <https://orcid.org/0000-0002-8600-7187>
 B Nikolić <https://orcid.org/0000-0002-7241-3248>
 M Damljanović <https://orcid.org/0000-0003-2806-253X>

References

- [1] Gupta S, Kutana A and Yakobson B I 2018 Dirac cones and nodal line in borophene *J. Phys. Chem. Lett.* **9** 2757–62
- [2] Zhang Y, Kang J, Zheng F, Gao P-F, Zhang S-L and Wang L-W 2019 Borophosphene: a new anisotropic Dirac cone mono-layer with a high Fermi velocity and a unique self-doping feature *J. Phys. Chem. Lett.* **10** 6656–63
- [3] Zhang L Z, Wang Z F, Wang Z M, Du S X, Gao H-J and Liu F 2015 Highly anisotropic Dirac fermions in square graphynes *J. Phys. Chem. Lett.* **6** 2959–62

- [4] Fang C, Gilbert M J, Dai X and Andrei Bernevig B 2012 Multi-Weyl topological semimetals stabilized by point group symmetry *Phys. Rev. Lett.* **108** 266802
- [5] Young S M and Kane C L 2015 Dirac semimetals in two dimensions *Phys. Rev. Lett.* **115** 126803
- [6] van Miert G and Smith C M 2016 Dirac cones beyond the honeycomb lattice: a symmetry-based approach *Phys. Rev. B* **93** 035401
- [7] Wang J 2017 Antiferromagnetic Dirac semimetals in two dimensions *Phys. Rev. B* **95** 115138
- [8] Kim J, Baik S S, Jung S W, Sohn Y, Ryu S H, Choi H J, Yang B-J and Kim K S 2017 Two-dimensional Dirac fermions protected by space-time inversion symmetry in black phosphorus *Phys. Rev. Lett.* **119** 226801
- [9] Young S M and Wieder B J 2017 Filling-enforced magnetic Dirac semimetals in two dimensions *Phys. Rev. Lett.* **118** 186401
- [10] Kawarabayashi T, Aoki H and Hatsugai Y 2019 Topologically protected doubling of tilted Dirac fermions in two dimensions *Phys. Status Solidi B* **256** 1970025
- [11] Mañes J L 2012 Existence of bulk chiral fermions and crystal symmetry *Phys. Rev. B* **85** 155118
- [12] Damljanović V and Gajić R 2016 Existence of Dirac cones in the Brillouin zone of diperiodic atomic crystals according to group theory *J. Phys.: Condens. Matter* **28** 085502
- [13] Damljanović V and Gajić R 2016 Addendum to existence of Dirac cones in the Brillouin zone of diperiodic atomic crystals according to group theory *J. Phys.: Condens. Matter* **28** 439401
- [14] Park S and Yang B-J 2017 Classification of accidental band crossings and emergent semimetals in two-dimensional noncentrosymmetric systems *Phys. Rev. B* **96** 125127
- [15] Wieder B J, Bradlyn B, Wang Z, Cano J, Kim Y, Kim H-S D, Rappe A M, Kane C L and Andrei Bernevig B 2018 Wallpaper fermions and the nonsymmorphic Dirac insulator *Science* **361** 246–51
- [16] Wieder B J, Kim Y, Rappe A M and Kane C L 2016 Double Dirac semimetals in three dimensions *Phys. Rev. Lett.* **116** 186402
- [17] Bradlyn B, Cano J, Wang Z, Vergniory M G, Felser C, Cava R J and Andrei Bernevig B 2016 Beyond Dirac and Weyl fermions: unconventional quasiparticles in conventional crystals *Science* **353** aaf5037
- [18] Zhu Z, Winkler G W, Wu Qian, Ju L and Alexey A 2016 Soluyanov. Triple point topological metals *Phys. Rev. X* **6** 031003
- [19] Wang Z, Alexandradinata A, Cava R J and Andrei Bernevig B 2016 Hourglass fermions *Nature* **532** 189–94
- [20] Lv B Q *et al* 2017 Observation of three-component fermions in the topological semimetal molybdenum phosphide *Nature* **546** 627–31
- [21] Barik R K, Shinde R and Singh A K 2018 Multiple triple-point fermions in Heusler compounds *J. Phys.: Condens. Matter* **30** 375702
- [22] Yang Y *et al* 2019 Topological triply degenerate point with double Fermi arcs *Nat. Phys.* **15** 645–9
- [23] Ma J *et al* 2017 Experimental evidence of hourglass fermion in the candidate nonsymmorphic topological insulator KHgSb *Sci. Adv.* **3** e1602415
- [24] Wang S-S, Liu Y, Yu Z-M, Sheng X-L and Yang S A 2017 Hourglass Dirac chain metal in rhenium dioxide *Nat. Commun.* **8** 1844
- [25] Singh B, Ghosh B, Su C, Lin H, Agarwal A and Bansil A 2018 Topological hourglass Dirac semimetal in the nonpolar phase of Ag_2BiO_3 *Phys. Rev. Lett.* **121** 226401
- [26] Novoselov K S, Geim A K, Morozov S V, Jiang D, Zhang Y, Dubonos S V, Grigorieva I V and Firsov A A 2004 Electric field effect in atomically thin carbon films *Science* **306** 666–9
- [27] Kim J *et al* 2015 Observation of tunable band gap and anisotropic Dirac semimetal state in black phosphorus *Science* **349** 723–6
- [28] Wang Z M 2014 *MoS₂ Materials, Physics and Devices* (Berlin: Springer)
- [29] Damljanović V, Popov I and Gajić R 2017 Fortune teller fermions in two-dimensional materials *Nanoscale* **9** 19337–45
- [30] Kopciuszynski M, Krawiec M, Żurawek L and Zdyb R 2020 Experimental evidence of a new class of massless fermions *Nanoscale Horiz.* **5** 679–82
- [31] Nguyen S D, Yeon J, Kim S-H and Shiv Halasyamani P 2011 $\text{BiO}(\text{IO}_3)$: a new polar iodate that exhibits an Aurivillius-type $(\text{Bi}_2\text{O}_2)^{2+}$ layer and a large SHG response *J. Am. Chem. Soc.* **133** 12422–5
- [32] Cornwell J F 1984 *Group Theory in Physics* (New York: Academic)
- [33] Elcoro L *et al* 2017 Double crystallographic groups and their representations on the Bilbao Crystallographic Server *J. Appl. Crystallogr.* **50** 1457–77
- [34] Damljanović M and Milošević I 2015 Full symmetry implementation in condensed matter and molecular physics—modified group projector technique *Phys. Rep.* **581** 1–43
- [35] Litvin D B and Wike T R 1991 *Character Tables and Compatibility Relations of the Eighty Layer Groups and Seventeen Plane Groups* (New York: Plenum)
- [36] Dresselhaus M S, Dresselhaus G and Jorio A 2008 *Group Theory* (Berlin: Springer)
- [37] Kopsky V and Litvin D B 2002 *International Tables of Crystallography Volume E: Subperiodic Groups* (Dordrecht: Kluwer)
- [38] Hahn T 2005 *International Tables of Crystallography Volume A: Space-Group Symmetry* (Berlin: Springer)
- [39] Burkov A A, Hook M D and Leon B 2011 Topological nodal semimetals *Phys. Rev. B* **84** 235126
- [40] Watanabe H, Po H C, Zaletel M P and Vishwanath A 2016 Filling-enforced gaplessness in band structures of the 230 space groups *Phys. Rev. Lett.* **117** 096404
- [41] Mounet N *et al* 2018 Two-dimensional materials from high-throughput computational exfoliation of experimentally known compounds *Nat. Nanotechnol.* **13** 246–52
- [42] Giannozzi P *et al* 2009 QUANTUM ESPRESSO: a modular and open-source software project for quantum simulations of materials *J. Phys.: Condens. Matter* **21** 395502
- [43] Blöchl P E 1994 Projector augmented-wave method *Phys. Rev. B* **50** 17953–79
- [44] Kresse G and Joubert D 1999 From ultrasoft pseudopotentials to the projector augmented-wave method *Phys. Rev. B* **59** 1758–75
- [45] Perdew J P, Burke K and Ernzerhof M 1996 Generalized gradient approximation made simple *Phys. Rev. Lett.* **77** 3865–8
- [46] Wieder B J and Kane C L 2016 Spin-orbit semimetals in the layer groups *Phys. Rev. B* **94** 155108
- [47] Watanabe H, Po H C, Vishwanath A and Zaletel M 2015 Filling constraints for spin-orbit coupled insulators in symmorphic and nonsymmorphic crystals *Proc. Natl Acad. Sci.* **112** 14551–6
- [48] Yang S A 2016 Dirac and Weyl materials: fundamental aspects and some spintronic applications *SPIN* **06** 1640003
- [49] Boriskina S, Zhou J, Ding Z and Chen G 2018 Efficiency limits of solar energy harvesting via internal photoemission in carbon materials *Photonics* **5** 4

**RESEARCH ARTICLE**

Vacancies and spin–phonon coupling in $\text{CrSi}_{0.8}\text{Ge}_{0.1}\text{Te}_3$

Ana Milosavljević¹ | Andrijana Šolajić¹ | Bojana Višić¹ | Marko Opačić¹ |
Jelena Pešić¹ | Yu Liu² | Cedomir Petrović² | Zoran V. Popović^{1,3} |
Nenad Lazarević¹

¹Institute of Physics Belgrade, University of Belgrade, Pregrevica 118, Belgrade, 11080, Serbia

²Condensed Matter Physics and Materials Science Department, Brookhaven National Laboratory, Upton, New York, 11973-5000, USA

³Serbian Academy of Sciences and Arts, Knez Mihailova 35, Belgrade, 11000, Serbia

Correspondence

Ana Milosavljević, Institute of Physics Belgrade, University of Belgrade, Pregrevica 118, 11080 Belgrade, Serbia.
Email: ana.milosavljevic@ipb.ac.rs

Funding information

Serbian Academy of Sciences and Arts, Grant/Award Number: F-134; Slovenian Research Agency, Grant/Award Number: P1-0099; Ministry of Education, Science and Technological Development of the Republic of Serbia U.S. DOE-BES, Division of Materials Science and Engineering, Grant/Award Number: DE-SC0012704

Abstract

We report temperature-dependent Raman scattering and magnetization studies of van der Waals ferromagnetic compound $\text{CrSi}_{0.8}\text{Ge}_{0.1}\text{Te}_3$. Magnetic susceptibility measurements revealed dominant ferromagnetic interactions below T_C which shift to the lower values due to the presence of vacancies. A Raman active mode, additional to the ones predicted by symmetry in the parent compounds, has been observed. This A_g symmetry mode most likely emerges as a consequence of the atomic vacancies on Si/Ge site. Presence of the strong spin–phonon coupling at temperature around 210 K is indicated by deviations from conventional phonon self-energy temperature dependence of all analysed modes.

KEYWORDS

magnetism, phonons, raman spectroscopy, van der Waals materials

1 | INTRODUCTION

Considerable progress has been made in the field of material science through developing new materials and revealing their properties in the last decade. Namely, in the recent years, large family of van der Waals materials with inherent magnetism became the focus of experimental and theoretical research, because they seem suitable for numerous technical applications.^[1–7] The family includes $\text{Fe}_{3-x}\text{GeTe}_2$ metallic materials with high magnetic transition temperature,^[8–10] semiconductors CrXTe_3 ($X = \text{Si}, \text{Ge}, \text{Sn}$) and CrX_3 ($X = \text{Cl}, \text{Br}, \text{I}$) monolayers^[2,11–13] and heterostructures.^[14]

CrSiTe_3 and CrGeTe_3 are ferromagnetic (FM) semiconductors with band gap of 0.4 and 0.7 eV and Curie temperatures (T_C) of 32 and 61 K, respectively.^[15–18] Twinning of CrSiTe_3 single crystals along c -axes was revealed by X-ray diffraction experiment as well as Cr^{3+} ions magnetic order.^[15] Recently, through high-resolution angle-resolved photoemission spectroscopy (ARPES), it was possible to identify full electronic structure near the Fermi level. Due to spin–orbit coupling, CrSiTe_3 is a Mott-type FM insulator.^[19] Electronic structure of CrGeTe_3 single crystals was also investigated by ARPES.^[20] It was shown that the low-lying valence bands are centred around the Γ point and are mainly formed from Te 5p orbitals.

Raman scattering studies of CrSiTe_3 reveal strong spin–lattice coupling in the paramagnetic phase^[15,21] as a consequence of a short-range magnetic order in this compound. In addition to renormalization of energies and linewidths of observed Raman active modes, coupling of doubly degenerate E_g mode with magnetic continuum was found.^[21] The coupling results in an asymmetric phonon line shape up to 180 K. Besides the splitting of two low-energy E_g modes in the magnetic phase of CrGeTe_3 and unconventional behaviour of phonon properties around transition temperature, experimental results indicate spin–phonon coupling effect with magnetic quasi-elastic scattering.^[22] Pressure-dependent Raman scattering study of CrGeTe_3 showed a decrease in bond length, the deviation of Cr–Te–Cr angle, and reduction of phase transition temperature.^[23]

Change of the carrier concentration plays an important role in the physics of semiconducting materials as it can lead to surprising physical properties. Very small variations in dopant concentrations can lead to structural modifications and considerable changes in magnetic transition temperature. Here, we report a Raman scattering and magnetization studies of $\text{CrSi}_{0.8}\text{Ge}_{0.1}\text{Te}_3$. Our scanning electron microscopy (SEM) measurements reveal 10% of Ge atoms concentration and 10% of vacancies. Vacancies induced a decrease in T_C was detected within magnetic susceptibility measurements. In the Raman scattering results, we identified three A_g and four E_g symmetry modes. Additional peak of the A_g symmetry is also observed in our spectra. This mode may be traced to vacancies and possible inhomogeneous distribution of Ge atoms substitution on Si atomic site at nano-scale. Energies of modes predicted by symmetry analysis are found between the experimental values of parent compounds CrSiTe_3 and CrGeTe_3 , reported previously in Milosavljević et al.^[21] The presence of the strong spin–phonon interaction at temperature around 210 K is indicated in small deviations from conventional temperature-dependent behaviour of the observed modes energies and linewidths, including additional one.

2 | EXPERIMENT AND NUMERICAL METHOD

$\text{CrSi}_{0.8}\text{Ge}_{0.1}\text{Te}_3$ single crystals were grown as described previously.^[24] Magnetic properties were measured in a Quantum Design MPMS-XL5 system.

SEM measurements were performed using FEI HeliosNanolab 650. This microscope is equipped with an Oxford Instruments energy dispersive spectroscopy (EDS) system with an X-max SSD detector operating at 20 kV. Measurements were performed on as-cleaved samples

deposited on a graphite tape. The elemental composition EDS mapping was obtained on crystals that appeared to be uniform for several tens of microns. The maps show the presence of Cr, Ge, Te and Si.

For Raman scattering experiment, Tri Vista 557 spectrometer was used in the subtractive backscattering micro-Raman configuration. The combination of gratings was 1800/1800/2400 grooves/mm and the entrance slit of 80 μm . Solid state laser with 532-nm line was used as an excitation source. In our scattering configuration, plane of incidence is ab -plane, where $|a|=|b|$ ($\angle(a,b)=120^\circ$), with incident (scattered) light propagation direction along c -axes. Samples were cleaved in the air before being placed in vacuum. All measurements were performed in high vacuum (10^{-6} mbar) using a KONTI CryoVac continuous Helium flow cryostat with 0.5-mm thick window. Laser beam focusing was achieved using microscope objective with $\times 50$ magnification. All spectra were corrected for Bose factor.

Spin-polarized density functional theory calculations were performed in Quantum Espresso software package,^[25] based on plane waves and pseudopotentials, using Perdew–Burke–Ernzerhof (PBE) exchange–correlation functional^[26] and projector augmented wave (PAW) pseudopotentials.^[27,28] The cutoff for wavefunctions and the charge density of 85 and 425 Ry were chosen, respectively. The k -point were sampled using the Monkhorst–Pack scheme, on $8 \times 8 \times 8$ Γ centred grid used for both structures. Optimization of the lattice parameters and atomic positions in unit cell was performed until the interatomic forces were minimized down to 10^{-6} Ry/Å. Treatment of the van der Waals interactions is included using the Grimme-D2 correction, in order to obtain the lattice parameters more accurately. Phonon wave numbers were calculated within the linear response method, as implemented in PHonon part of Quantum Espresso.

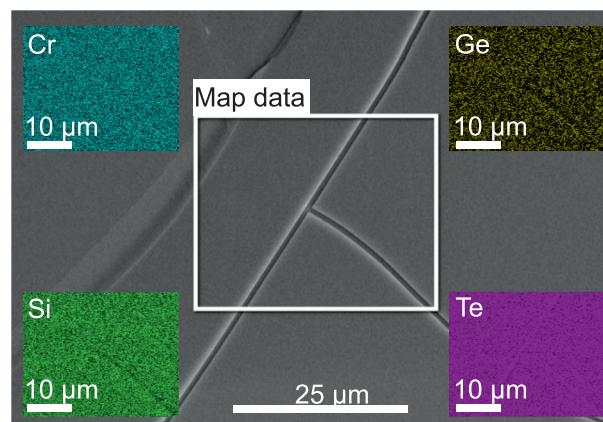


FIGURE 1 Energy dispersive spectroscopy (EDS) mapping on a $\text{CrSi}_{0.8}\text{Ge}_{0.1}\text{Te}_3$ single crystal [Colour figure can be viewed at wileyonlinelibrary.com]

3 | RESULTS AND DISCUSSION

In order to investigate uniformity and elemental composition of $\text{CrSi}_{0.8}\text{Ge}_{0.1}\text{Te}_3$ sample, SEM measurements were performed on as-cleaved crystals. EDS mapping presented in Figure 1 shows that the ratio of Cr:Si:Ge:Te (averaged over 10 measurements) is 1:0.8:0.1:3. This result reveals the presence of 10% Ge atomic vacancies in the sample.

Figure 2a,b presents the temperature dependence of zero-field cooling (ZFC) magnetic susceptibility $\chi(T) = M(T)/H$ measured in 1-kOe magnetic field applied parallel to a (a) and c (b) crystallographic axes. Curie–Weiss law $\chi = \frac{C}{T-\theta}$ fit at high temperatures yields Weiss temperatures $\theta_a = 61(2)$ K, $\theta_c = 70(2)$ K and high temperature paramagnetic moments $\mu_{\text{eff},a} = 4.14(2)\mu_B$ and $\mu_{\text{eff},c} = 3.91(2)\mu_B$ for $\text{CrSi}_{0.8}\text{Ge}_{0.1}\text{Te}_3$, consistent with dominant FM interactions below T_c and in line with the observed FM T_c and magnetic hysteresis loops.^[13,24] The approximate T_c value can be determined from the minima of the $d\chi/dT$ curves insets in Figure 2(a,b). It should be noted

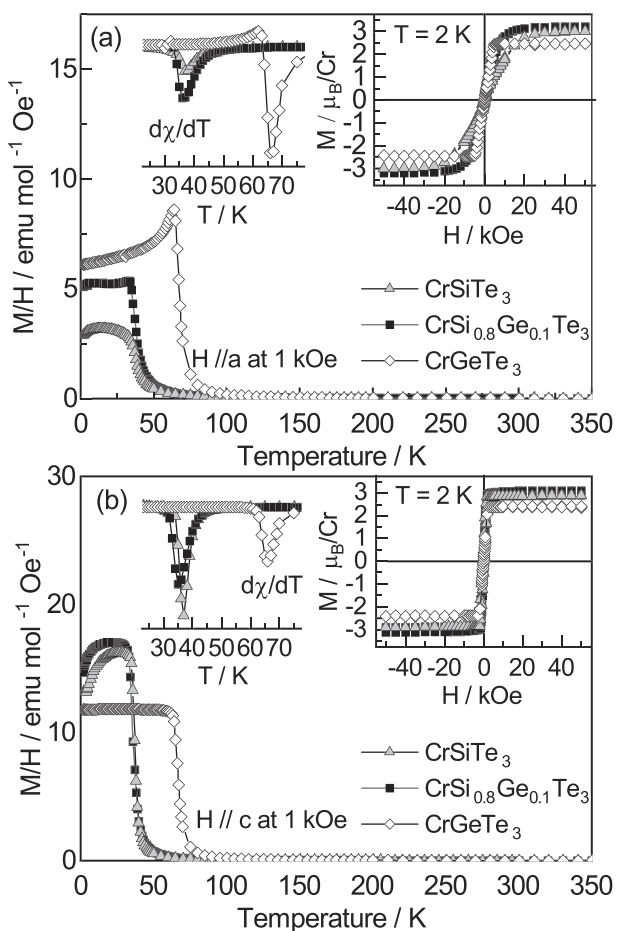


FIGURE 2 Temperature dependence of zero-field cooling (ZFC) $\chi = M/H$ for CrSiTe_3 , $\text{CrSi}_{0.8}\text{Ge}_{0.1}\text{Te}_3$ and CrGeTe_3 in 1-kOe magnetic field applied in-plane (a) and along the c -axis (b). Insets show transition temperatures of ferromagnetic orders ($d\chi/dT$) and magnetic hysteresis loops taken at 2 K

that, instead of monotonous rise, there is a weak but discernible shift to lower temperature in $d\chi/dT$ in $\text{CrSi}_{0.8}\text{Ge}_{0.1}\text{Te}_3$ when compared with CrSiTe_3 . This small reduction in FM transition temperature is likely induced by the presence of vacancies, as suggested by the EDS data. The presence of vacancies in this class of materials usually disarrange magnetic exchange due to disorder increment, which leads to the reduction of T_c .^[29]

Isostructural parent compounds CrSiTe_3 and CrGeTe_3 crystallize in the rhombohedral crystal structure, described with space group $R\bar{3}(C_{3i}^2)$.^[30] According to factor group analysis, five A_g and five double degenerate E_g symmetry modes are expected to be observed in the light scattering experiment. Detailed symmetry analysis, phonon mode distribution and selection rules for parent compounds (CrSiTe_3 and CrGeTe_3) can be found in Milosavljević et al.^[21] In our scattering configuration, the plane of incidence is ab plane, where $|a| = |b|$ ($\angle(a,b) = 120^\circ$) (inset in Figure 3), and the direction of incident (scattered) light propagation is along c -axes. According to the selection rules for this scattering configuration,^[21] all Raman active modes may be observed, having in mind that A_g symmetry modes can be detected only in parallel polarization configuration. The E_g symmetry modes are expected to appear in both the parallel and cross polarization configurations. Raman spectra of $\text{CrSi}_{0.8}\text{Ge}_{0.1}\text{Te}_3$, obtained by continuous change of the angle between polarization vectors of incident and

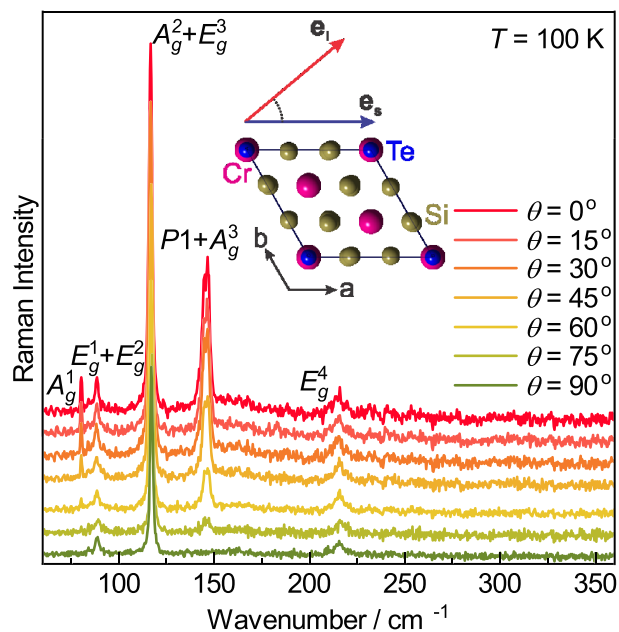


FIGURE 3 Raman spectra of $\text{CrSi}_{0.8}\text{Ge}_{0.1}\text{Te}_3$ single crystal, measured at 100 K, as a function of angle θ , between incident and scattered light polarization. Inset: schematic representation of the incident and scattered light polarization with respect to the crystal orientation [Colour figure can be viewed at wileyonlinelibrary.com]

scattered light, $\theta = \angle(\mathbf{e}_i, \mathbf{e}_s)$, ($0^\circ \leq \theta \leq 90^\circ$) at 100 K, are shown in Figure 3. It can be seen that by changing this angle, starting from $\theta = 0^\circ$, the intensities of the peaks at energies 80.2, 116.4 and 145.5 cm^{-1} continuously decrease and completely vanish for polarization angle of 90° . Therefore, these excitations obey pure A_g symmetry. On the other hand, the peaks at energies of 84.5, 88.3, 117.2 and 215.0 cm^{-1} are not influenced by change of polarization angle, so they can be identified as E_g symmetry modes.

Here, one should note that the feature observed at around 117 cm^{-1} in both scattering configurations is actually a two-peak structure comprising of 116.4 cm^{-1} A_g and 117.2 cm^{-1} E_g symmetry modes. Detailed analysis of the structure for two scattering configurations is presented in Figure A1 of Appendix. Furthermore, closer inspection of the data revealed that peak at energy of 145.5 cm^{-1} , which obeys pure A_g symmetry, is also composed of two modes, P1 (144.6 cm^{-1}) and A_g^3 (146.7 cm^{-1}), as shown in Figure A2 of Appendix.

Calculated optical phonon wavenumbers of the parent compounds, CrSiTe_3 and CrGeTe_3 , together with their experimental Raman active values as well as Raman mode energies of $\text{CrSi}_{0.8}\text{Ge}_{0.1}\text{Te}_3$, are compiled in Table 1. As expected, experimental values of $\text{CrSi}_{0.8}\text{Ge}_{0.1}\text{Te}_3$ Raman active modes are found between the values of the observed modes in parent compounds.^[21] Figure 4a shows compositional evolution of the peaks with highest

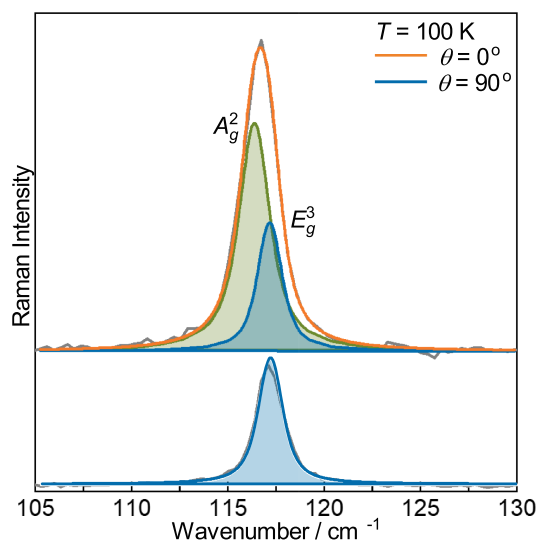


FIGURE A1 Decomposition of unresolved A_g^2 and E_g^3 symmetry modes obtained by simultaneous modelling in parallel and cross polarization configuration. Grey line represents the measured data, Voigt line of A_g^2 mode is shown by green, and blue lines represent the E_g^3 symmetry mode in parallel (upper panel) and cross (lower panel) polarization. The orange line is the superposition of these two lines [Colour figure can be viewed at wileyonlinelibrary.com]

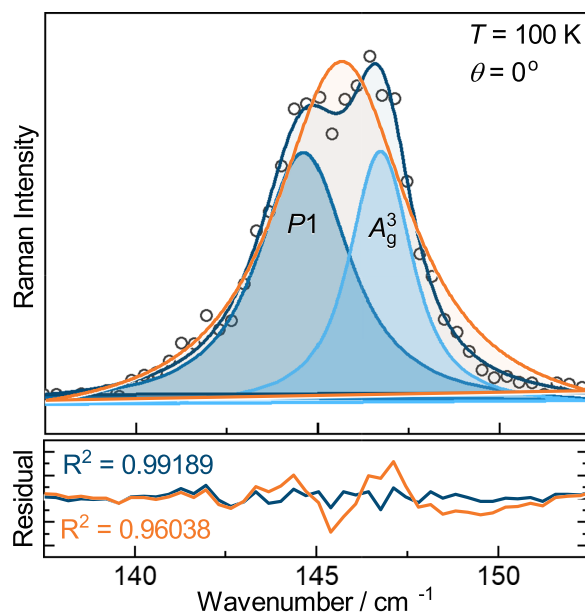


FIGURE A2 Decomposition of phonon mode in parallel scattering configuration on two A_g symmetry modes. Open circles represent the measured data and the blue one sum of two Voigt profile line shapes. Data modelled with one Voigt profile line shape (orange line) deviates significantly from measured data [Colour figure can be viewed at wileyonlinelibrary.com]

intensity, assigned as E_g^3 and A_g^3 symmetry modes in parent compounds. The E_g^3 mode energy changes almost linearly (Figure 4b), as a consequence of change in lattice parameters and “change of mass” effect. The observed energy shift is followed by doubling of the linewidth, dominantly induced by the significant crystalline disorder. The similar type of behaviour, with somewhat larger increase in the linewidth, was also observed for the A_g^3 symmetry mode. The most striking feature was the additional A_g symmetry mode (denoted as P1, see Figure A2 of the Appendix), observed in the doped sample. Generally, both the substitutional defects and vacancies may have similar impact on the Raman modes energy and linewidth. Here, the appearance of P1 peak can be understood as a consequence of the presence of vacancies on Si/Ge atomic site and their inharmonic distribution at nano-scale. The mode “splitting” is detected only for the A_g^3 but not for other observed modes, due to the fact that different nature of these vibrations results in different values of energy shifts. In the case of other modes, the difference between the shifts for corresponding domains is smaller than the spectral resolution of the instrument ($\sim 1.8 \text{ cm}^{-1}$), and therefore, the separate modes can not be resolved.

Figure 5 shows $\text{CrSi}_{0.8}\text{Ge}_{0.1}\text{Te}_3$ Raman scattering spectra measured at various temperatures. For clarity, spectra obtained for cross polarization configuration are

TABLE 1 Phonon symmetry, calculated ($T=0$ K) and experimental ($T=100$ K) Raman active phonon wavenumbers of parent compounds CrSiTe_3 and CrGeTe_3 .^[21] Experimental values for Raman active phonons of $\text{CrSi}_{0.8}\text{Ge}_{0.1}\text{Te}_3$ at 100 K are shown in the last column

Raman active modes					
Symmetry	Calculations		Experiment		
	CrSiTe_3	CrGeTe_3	CrSiTe_3	CrGeTe_3	$\text{CrSi}_{0.8}\text{Ge}_{0.1}\text{Te}_3$
A_g^1	88.2	84.2	—	—	80.2
E_g^1	93.5	82.0	88.9	83.5	84.5
E_g^2	96.9	90.8	—	—	88.3
E_g^3	118.3	114.2	118.2	112.2	117.2
A_g^2	122.0	105.9	—	—	116.4
A_g^3	148.0	134.8	147.4	137.9	146.7
A_g^4	208.7	200.3	—	—	—
E_g^4	219.5	209.6	217.2	217.5	215.0
E_g^5	357.4	229.8	—	—	—
A_g^5	508.9	290.7	—	296.6	—

Note: All values are given in cm^{-1} .

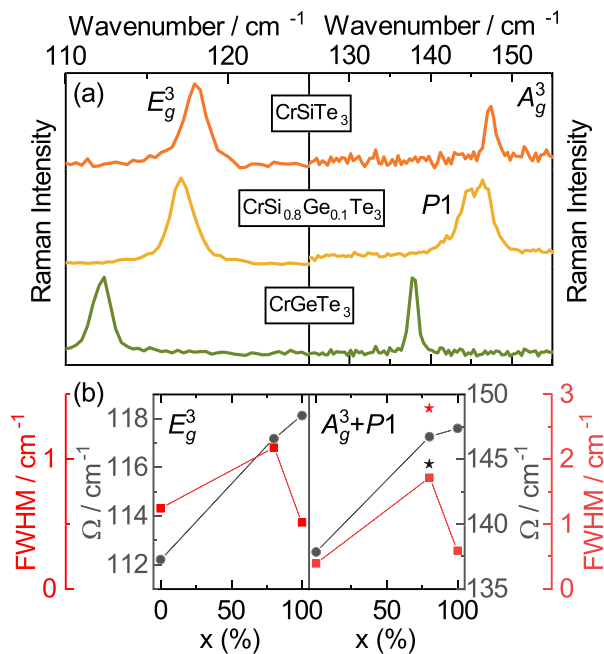


FIGURE 4 (a) Raman scattering spectra of E_g^3 and A_g^3 phonon modes of CrSiTe_3 (orange line), $\text{CrSi}_{0.8}\text{Ge}_{0.1}\text{Te}_3$ (yellow line) and CrGeTe_3 (green line) at $T=100$ K measured in cross (left panel) and parallel (right panel) scattering configuration, respectively. (b) Energy (grey line) and linewidth (red line) of these two modes with respect to the percentage of Si atoms concentration. Energy and linewidth of $P1$ mode are marked with black and red star, respectively [Colour figure can be viewed at wileyonlinelibrary.com]

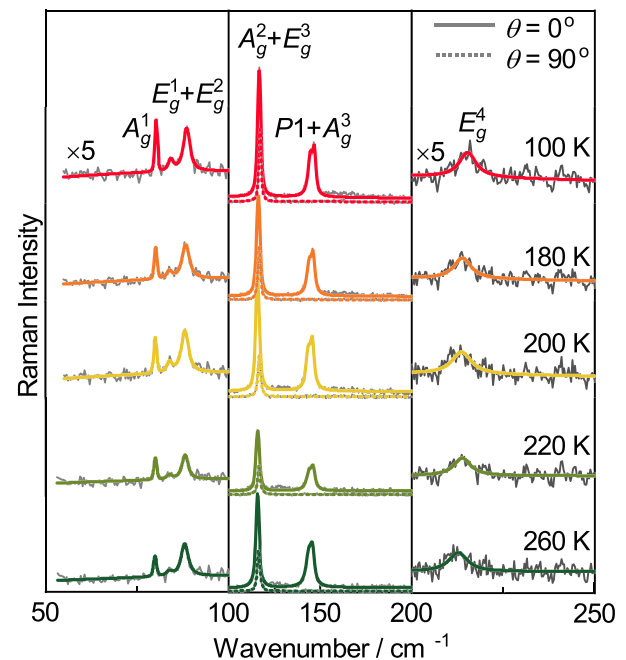


FIGURE 5 Raman spectra of $\text{CrSi}_{0.8}\text{Ge}_{0.1}\text{Te}_3$ single crystal measured at various temperatures. The spectra were analysed by using multiple Voigt peak functions and a single $\chi''_{cont} = a\Gamma\omega/(\Gamma^2 + \omega^2) + b\omega$ function, for parallel ($\theta=0^\circ$, solid coloured lines) and cross ($\theta=90^\circ$, dashed coloured lines) scattering configuration. For clarity, higher and lower energy ranges (left and right panel) are multiplied by the factor of five [Colour figure can be viewed at wileyonlinelibrary.com]

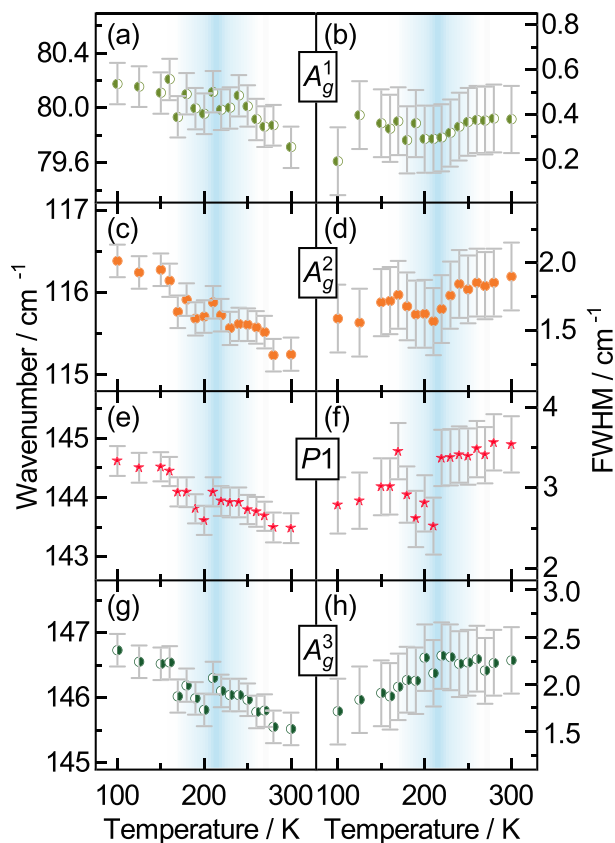


FIGURE 6 Energy and linewidth temperature dependence of A_g^1 (a,b), A_g^2 (c,d), $P1$ (e,f) and A_g^3 (g,h) Raman modes [Colour figure can be viewed at wileyonlinelibrary.com]

only shown for the mid-energy range. Temperature dependence of energies and linewidths of all the observed A_g symmetry modes, including $P1$, are presented in Figure 6. By heating the sample from 100 K to approximately 210 K, monotonous decrease in energy of all the A_g symmetry modes is present, dominantly driven by thermal expansion.^[31] In the temperature region around 210 K, these modes' energy exhibit small deviation, followed by a continuous decrease up to room temperature. In the same temperature region, deviation from expected anharmonic type of behaviour is observed for all the A_g symmetry modes linewidth. This effect is more pronounced for higher energy modes where the anharmonicity is expected to be higher. Similar response of analysed E_g symmetry modes is present and shown in Figure 7.

Concerning previously reported strong spin-phonon coupling in CrSiTe_3 ,^[15,21] which persists up to 180 K, we believe that this unconventional behaviour of energies and linewidths can be attributed to the coupling of the phonon modes to the spin system.^[32] Due to the doping and presence of vacancies, strong magnetic correlations in $\text{CrSi}_{0.8}\text{Ge}_{0.1}\text{Te}_3$ are sustained up to 210 K.

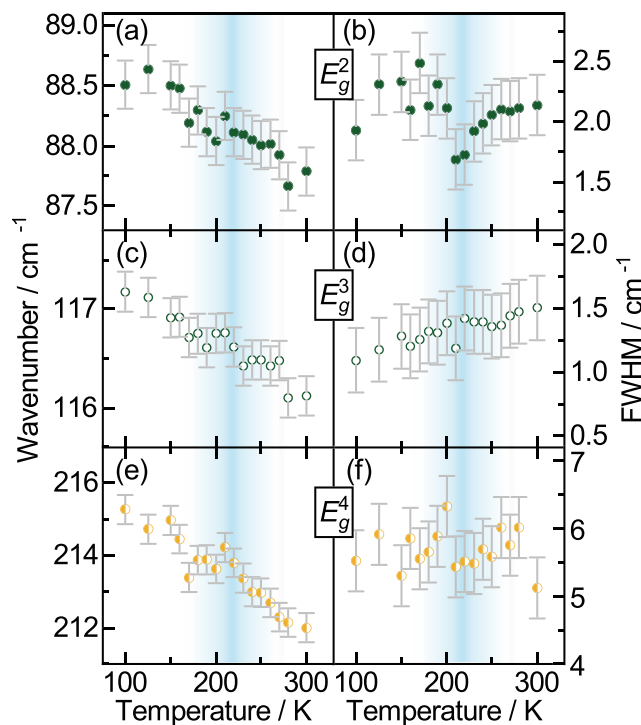


FIGURE 7 Energy and linewidth temperature dependence of E_g^2 (a,b), E_g^3 (c,d) and E_g^4 (e,f) symmetry modes [Colour figure can be viewed at wileyonlinelibrary.com]

4 | CONCLUSIONS

In summary, we presented temperature-dependent Raman scattering and magnetization studies of doped van der Waals ferromagnet $\text{CrSi}_{0.8}\text{Ge}_{0.1}\text{Te}_3$. SEM measurements revealed the presence of 10% vacancies on Si/Ge atomic site. As a consequence, magnetization measurements detected small but clear decrease in T_C . Seven out of 10 Raman active modes have been assigned in our Raman spectra. Temperature dependence of all the observed modes shows the persistence of magnetic correlations up to 210 K. In addition, the results revealed the appearance of the peak that obey pure A_g symmetry, which is attributed to the possible inhomogeneous distribution of Ge atoms and vacancies at nano-scale. This study provides an insight into the impact of doping and presence of vacancies on magnetic and lattice properties in this class of materials.

ACKNOWLEDGEMENTS

This work was supported by the Ministry of Education, Science and Technological Development of the Republic of Serbia and project no F-134 of the Serbian Academy of Sciences and Arts. DFT calculations were performed using computational resources at Johannes Kepler University, Linz, Austria. Electron microscopy was performed at Jozef Stefan Institute, Ljubljana, Slovenia,

under Slovenian Research Agency contract P1-0099 (B. V.). Work at BNL (crystal synthesis and magnetic characterization) was supported by the U.S. DOE-BES, Division of Materials Science and Engineering, under Contract No. DE-SC0012704.

ORCID

Ana Milosavljević  <https://orcid.org/0000-0002-8654-0475>

REFERENCES

- [1] F. Hellman, A. Hoffmann, Y. Tserkovnyak, G. S. Beach, E. E. Fullerton, C. Leighton, A. H. MacDonald, D. C. Ralph, D. A. Arena, H. A. Dürr, P. Fischer, *Rev. Mod. Phys.* **2017**, *89*, 025006.
- [2] N. Sivadas, M. W. Daniels, R. H. Swendsen, S. Okamoto, D. Xiao, *Phys. Rev. B* **2015**, *91*, 235425.
- [3] K. S. Novoselov, A. K. Geim, S. V. Morozov, D. Jiang, Y. Zhang, S. V. Dubonos, I. V. Grigorieva, A. A. Firsov, *Science* **2004**, *306*(5696), 666.
- [4] Q. H. Wang, K. Kalantar-Zadeh, A. Kis, J. N. Coleman, M. S. Strano, *Nat. Nanotechnol.* **2012**, *7*, 699.
- [5] G. Cheng, L. Lin, L. Zhenglu, J. Huiwen, S. Alex, X. Yang, C. Ting, B. Wei, W. Chenzhe, W. Yuan, Z. Q. Qiu, R. J. Cava, G. L. Steven, X. Jing, Z. Xiang, *Nature* **2017**, *546*, 265.
- [6] B. Huang Bevin, G. Clark, E. Navarro-Moratalla, D. R. Klein, R. Cheng, K. L. Seyler, D. Zhong, E. Schmidgall, M. A. McGuire, D. H. Cobden, W. Yao, *Nature* **2017**, *546*, 270.
- [7] K. S. Burch, D. Mandrus, J.-G. Park, *Nature* **2018**, *563*(7729), 47.
- [8] J.-X. Zhu, M. Janoschek, D. Chaves, S. J. C. Cezar, T. Durakiewicz, F. Ronning, Y. Sassa, M. Mansson, B. L. Scott, N. Wakeham, E. D. Bauer, J. D. Thompson, *Phys. Rev. B* **2016**, *93*, 144404.
- [9] B. Chen, J. H. Yang, H. D. Wang, M. Imai, H. Ohta, C. Michioka, K. Yoshimura, M. H. Fang, *J. Phys. Soc. Japan* **2013**, *82*(12), 124711.
- [10] A. Milosavljević, A. Šolajić, S. Djurdjic-Mijin, J. Pešić, B. Višić, Y. Liu, C. Petrovic, N. Lazarević, Z. V. Popović, *Phys. Rev. B* **2019**, *99*, 214304.
- [11] M. A. McGuire, H. Dixit, V. R. Cooper, B. C. Sales, *Chem. Mat.* **2015**, *27*(2), 612.
- [12] H. L. Zhuang, Y. Xie, P. R. C. Kent, P. Ganesh, *Phys. Rev. B* **2015**, *92*, 035407.
- [13] G. T. Lin, H. L. Zhuang, X. Luo, B. J. Liu, F. C. Chen, J. Yan, Y. Sun, J. Zhou, W. J. Lu, P. Tong, Z. G. Sheng, *Phys. Rev. B* **2017**, *95*, 245212.
- [14] M. Gibertini, M. Koperski, A. F. Morpurgo, K. S. Novoselov, *Nat. Nanotech.* **2019**, *14*(5), 408.
- [15] L. D. Casto, A. J. Clune, M. O. Yokosuk, J. L. Musfeldt, T. J. Williams, H. L. Zhuang, M.-W. Lin, K. Xiao, R. G. Hennig, B. C. Sales, J.-Q. Yan, D. Mandrus, *APL Mat.* **2015**, *3*(4), 041515.
- [16] X. Zhang, Y. Zhao, Q. Song, S. Jia, J. Shi, W. Han, *JJpn. J. Appl. Phys.* **2016**, *55*(3), 033001.
- [17] B. Siberchicot, S. Jobic, V. Carreaux, P. Gressier, G. Ouvrard, *Phys. J. Chem.* **1996**, *100*(14), 5863.
- [18] V. Carreaux, F. Moussa, M. Spiessner, *EPL* **1995**, *29*(3), 251.
- [19] J. Zhang, X. Cai, W. Xia, A. Liang, J. Huang, C. Wang, L. Yang, H. Yuan, Y. Chen, S. Zhang, Y. Guo, *Phys. Rev. Lett.* **2019**, *123*, 047203.
- [20] Y. F. Li, W. Wang, W. Guo, C. Y. Gu, H. Y. Sun, L. He, J. Zhou, Z. B. Gu, Y. F. Nie, X. Q. Pan, *Phys. Rev. B* **2018**, *98*, 125127.
- [21] A. Milosavljević, A. Šolajić, J. Pešić, Y. Liu, C. Petrovic, N. Lazarević, Z. V. Popović, *Phys. Rev. B* **2018**, *98*, 104306.
- [22] Y. Tian, M. J. Gray, H. Ji, R. J. Cava, K. S. Burch, *2D Mater.* **2016**, *3*(2), 025035.
- [23] Y. Sun, R. C. Xiao, G. T. Lin., R. R. Zhang, L. S. Ling, Z. W. Ma, X. Luo, W. J. Lu, Y. P. Sun, Z. G. Sheng, *Appl. Phys. Lett.* **2018**, *112*(7), 072409.
- [24] Y. Liu, C. Petrovic, *Phys. Rev. Mater.* **2019**, *3*, 014001.
- [25] P. Giannozzi, S. Baroni, N. Bonini, M. Calandra, R. Car, C. Cavazzoni, D. Ceresoli, G. L. Chiarotti, M. Cococcioni, I. Dabo, A. Dal Corso, *J. Phys. Condens. Matter.* **2009**, *21*(39), 395502.
- [26] J. P. Perdew, K. Burke, M. Ernzerhof, *Phys. Rev. Lett.* **1996**, *77*, 3865.
- [27] P. E. Blöchl, *Phys. Rev. B* **1994**, *50*, 17953.
- [28] G. Kresse, D. Joubert, *Phys. Rev. B* **1999**, *59*, 1758.
- [29] F. A. May, S. Calder, C. Cantoni, H. Cao, M. A. McGuire, *Phys. Rev. B* **2016**, *93*, 014411.
- [30] R. E. Marsh, *J. Solid State Chem.* **1988**, *77*(1), 190.
- [31] M. Opačić, N. Lazarević, M. Šćepanović, H. Ryu, H. Lei, C. Petrovic, Z. V. Popović, *J. Phys. Condens. Matter.*, *48*(27), 485701.
- [32] F. Feng, N. Lazarević, C. Liu, J. Ji, Y. Wang, S. He, H. Lei, C. Petrovic, R. Yu, Z. V. Popović, Q. Zhang, *Phys. Rev. B* **2019**, *99*, 144419.

How to cite this article: Milosavljević A, Šolajić A, Višić B, et al. Vacancies and spin-phonon coupling in CrSi_{0.8}Ge_{0.1}Te₃. *J Raman Spectrosc.* 2020;1–8. <https://doi.org/10.1002/jrs.5962>

APPENDIX: A DECOMPOSITION OF UNRESOLVED MODES

Analysing the spectra of CrSi_{0.8}Ge_{0.1}Te₃ single crystal, in different polarization configurations (Figure 3), in the energy range around 117 cm⁻¹, becomes clear that lower energy part completely disappears in cross polarization configuration, whereas higher energy part persists. Enlarged part of this energy region is shown in Figure A1, in parallel and cross polarization configuration at temperature of 100 K. After simultaneous modelling of these spectra becomes clear that they consist of the A_g² and E_g³ modes, at energies 116.4 and 117.2 cm⁻¹, respectively. This is completely supported with theoretical calculations presented in Table 1.

On the other hand, existence of $P1$ is not predicted by theoretical calculations, as Raman active peak. Only closer inspection and detailed analysis, presented in

Figure A2, shows that much better agreement with experimental results gives modelling as a superposition of two Voigt lines.

Evidence of spin-phonon coupling in CrSiTe₃A. Milosavljević,¹ A. Šolajić,¹ J. Pešić,¹ Yu Liu (刘育),² C. Petrovic,² N. Lazarević,^{1,*} and Z. V. Popović^{1,3}¹*Center for Solid State Physics and New Materials, Institute of Physics Belgrade, University of Belgrade, Pregrevica 118, 11080 Belgrade, Serbia*²*Condensed Matter Physics and Materials Science Department, Brookhaven National Laboratory, Upton, New York 11973-5000, USA*³*Serbian Academy of Sciences and Arts, Knez Mihailova 35, 11000 Belgrade, Serbia*

(Received 12 July 2018; published 18 September 2018)

We present Raman scattering results on the layered semiconducting ferromagnetic compound CrSiTe₃. Four Raman-active modes, predicted by symmetry, are observed and assigned. The experimental results are supported by density functional theory calculations. The self-energies of the A_g^3 and the E_g^3 symmetry modes exhibit unconventional temperature evolution around 180 K. In addition, the doubly degenerate E_g^3 mode shows a clear change of asymmetry in the same temperature region. The observed behavior is consistent with the presence of the previously reported short-range magnetic order and strong spin-phonon coupling.

DOI: [10.1103/PhysRevB.98.104306](https://doi.org/10.1103/PhysRevB.98.104306)**I. INTRODUCTION**

Trichalcogenides CrXTe₃ ($X = \text{Si, Ge}$) belong to a rare class of quasi-two-dimensional semiconducting materials with a ferromagnetic order, band gaps of 0.4 eV for Si and 0.7 eV for Ge compounds, and Curie temperatures (T_C) of 32 and 61 K, respectively [1–6]. Because of their layered structure, due to van der Waals bonding, they can be exfoliated to mono- and few-layer nanosheets, which, together with their semiconducting and magnetic properties, make an ideal combination for applications in optoelectronics and nanospintronics [7–11]. This was further supported by the observation of giant resistivity modulation of CrGeTe₃-based devices [12].

From an x-ray diffraction study [1], it was revealed that CrSiTe₃ crystals are twinned along c axes, the thermal expansion is negative at low temperatures, and the thermal conductivity shows strong magnon-phonon scattering effects. A very small single-ion anisotropy favoring magnetic order along c axes and spin waves was found in CrSiTe₃ by elastic and inelastic neutron scattering [13]. Spin-wave measurements suggest the absence of three-dimensional correlations above T_C , whereas in-plane dynamic correlations are present up to 300 K. First-principles calculations suggested the possibility of graphenelike mechanical exfoliation for CrXTe₃ ($X = \text{Si, Ge}$) single crystals with conserved semiconducting and ferromagnetic properties [14]. The exfoliation of CrSiTe₃ bulk to mono- and few-layer two-dimensional crystals onto a Si/SiO₂ substrate has been achieved [15] with a resistivity between 80 and 120 K, depending on the number of layers. Critical exponents for CrSiTe₃ were also determined from theoretical analysis [16].

Spin-phonon coupling in CrGeTe₃ was investigated in Raman scattering experiments [17]. Splitting of the two lowest-energy E_g modes in the ferromagnetic phase has been observed and ascribed to time-reversal symmetry breaking by

the spin ordering. Furthermore, the significant renormalization of the three higher-energy modes' self-energies below T_C provided additional evidence of spin-phonon coupling [17]. The external pressure-induced effect on lattice dynamics and magnetization in CrGeTe₃ has also been studied [18].

The Raman spectrum of CrSiTe₃ single crystals was reported in Ref. [1], where three Raman-active modes have been observed. Similar results have also been presented in Ref. [15] for ultrathin nanosheets of CrSiTe₃. Here, we report a Raman scattering study of CrSiTe₃ single crystals, with the main focus on phonon properties in the temperature range between 100 and 300 K. Our experimental results are qualitatively different from those previously reported [1,15] but consistent with the results obtained for CrGeTe₃ [17,18]. Furthermore, our data reveal the asymmetry of the E_g^3 mode, which is suppressed at higher temperatures. The A_g^3 and E_g^3 symmetry modes exhibit nonanharmonic self-energy temperature dependence in the region around 180 K, related to the strong spin-lattice interaction due to short-range magnetic order [1]. Energies and symmetries of the observed Raman-active modes are in good agreement with theoretical calculations.

II. EXPERIMENT AND NUMERICAL METHOD

Single crystals of CrSiTe₃ and CrGeTe₃ were grown as described previously [19]. For a Raman scattering experiment, a Tri Vista 557 spectrometer was used in the backscattering micro-Raman configuration with a 1800/1800/2400 grooves/mm diffraction grating combination. A coherent Verdi G solid-state laser with a 532-nm line was used as the excitation source. The direction of the incident (scattered) light coincides with a crystallographic c axis. Right before being placed in the vacuum, the samples were cleaved in the air. All measurements were performed in a high vacuum (10^{-6} mbar) using a KONTI CryoVac continuous-flow cryostat with a 0.5-mm-thick window. Laser-beam focusing was achieved through a microscope objective with $\times 50$ magnification, a spot size of approximately 8 μm , and a power

*nenadl@ipb.ac.rs

TABLE I. Calculated and experimental crystallographic lattice parameters for CrSiTe₃ ($|a| = |b|$), bond lengths, interlayer distance (d), and van der Waals (vdW) gap.

CrSiTe ₃	Calculation (Å)	Experiment (Å) [20]
a	6.87	6.76
c	19.81	20.67
Si-Si	2.27	2.27
Si-Te	2.52	2.51
Cr-Te	2.77	2.78
d	6.86	6.91
vdW gap	3.42	3.42

<2 mW on the surface of a sample. All spectra were corrected for the Bose factor.

Density functional theory calculations were performed in the Quantum Espresso software package [21], using the PBE exchange-correlation functional [22], PAW pseudopotentials [23,24], and energy cutoffs for wave functions and the charge density of 85 and 425 Ry, respectively. For k -point sampling, the Monkhorst-Pack scheme was used, with a Γ -centered $8 \times 8 \times 8$ grid. Optimization of the atomic positions in the unit cell was performed until the interatomic forces were minimized down to 10^{-6} Ry/Å. In order to obtain the parameters accurately, treatment of the van der Waals interactions was included using the Grimme-D2 correction [25]. Phonon frequencies were calculated at the Γ point

TABLE II. (a) Type of atoms, Wyckoff positions, each site's contribution to the phonons at the Γ point, and corresponding Raman tensors for the $R\bar{3}$ space group of CrSiTe₃. (b) Phonon symmetry, calculated optical phonon frequencies at 0 K, and experimental values for Raman-active (at 100 K) and infrared (IR)-active (at 110 K) [1] CrSiTe₃ phonons.

(a) Space group $R\bar{3}$ (No. 148)					
Atom(s) (Wyckoff positions)			Irreducible representations		
Cr, Si (6c)			$A_g + E_g + A_u + E_u$		
Te (18f)			$3A_g + 3E_g + 3A_u + 3E_u$		
(b) Raman tensors					
$A_g = \begin{pmatrix} a & 0 & 0 \\ 0 & b & 0 \\ 0 & 0 & c \end{pmatrix}$		$E_g^1 = \begin{pmatrix} c & d & e \\ d & -c & f \\ e & f & 0 \end{pmatrix}$		$E_g^2 = \begin{pmatrix} d & -c & -f \\ -c & -d & e \\ -f & e & 0 \end{pmatrix}$	
Raman active			IR active [1]		
Symmetry	Calc. (cm ⁻¹)	Expt. (cm ⁻¹)	Symmetry	Calc. (cm ⁻¹)	Expt. (cm ⁻¹)
A_g^1	88.2	–	A_u^1	91.8	91.0
E_g^1	93.5	88.9	E_u^1	93.7	–
E_g^2	96.9	–	A_u^2	116.8	–
E_g^3	118.3	118.2	E_u^2	117.1	–
A_g^2	122.0	–	A_u^3	202.4	–
A_g^3	148.0	147.4	E_u^3	206.2	207.9
A_g^4	208.7	–	A_u^4	243.7	–
E_g^4	219.5	217.2	E_u^4	365.8	370.4
E_g^5	357.4	–			
A_g^5	508.8	–			

within the linear response method implemented in Quantum Espresso. Calculated crystallographic properties obtained by relaxing the structures are in good agreement with x-ray diffraction measurements [20]. A comparison between our, calculated, and experimental results is presented in Table I.

III. RESULTS AND DISCUSSION

A. Polarization dependence

CrSiTe₃ crystallizes in the rhombohedral crystal structure, described by $R\bar{3}$ (C_{3i}^2) [26]. Wyckoff positions of atoms, together with each site's contribution to phonons at the Γ point and corresponding Raman tensors, are listed in Table II. The phonon mode distribution obtained by factor-group analysis for the $R\bar{3}$ space group is as follows:

$$\Gamma_{\text{Raman}} = 5A_g + 5E_g,$$

$$\Gamma_{\text{IR}} = 4A_u + 4E_u,$$

$$\Gamma_{\text{Acoustic}} = A_u + E_u.$$

Since the plane of incidence is ab , where $|a| = |b|$ [$\angle(a, b) = 120^\circ$], and the direction of light propagation is along c axes, from the selection rules, it is possible to observe all Raman-active modes, i.e., five A_g modes and five doubly degenerate E_g modes. According to the Raman tensors presented in Table II, A_g symmetry modes are observable only in the parallel polarization configuration, whereas E_g symmetry

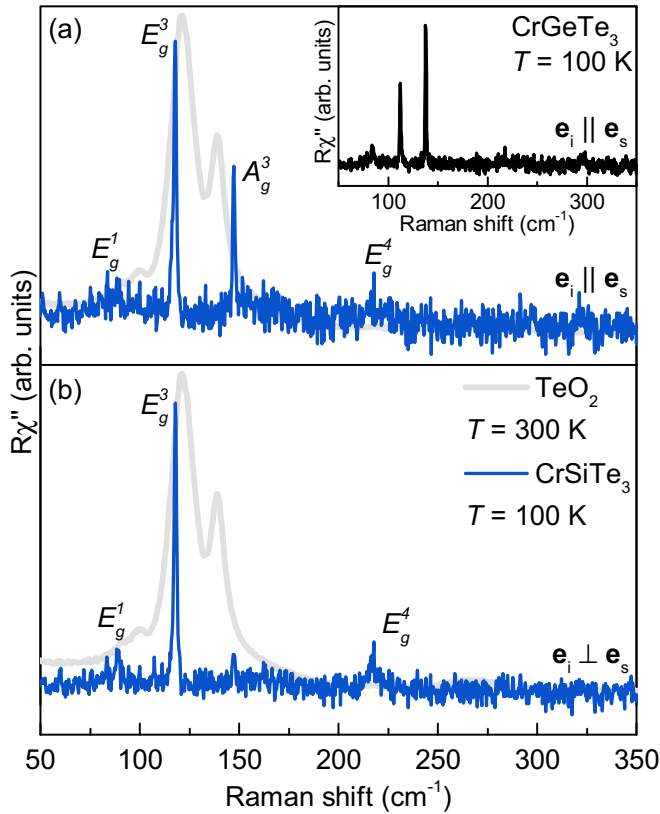


FIG. 1. Raman spectra of CrSiTe₃ single crystals measured at 100 K in (a) parallel and (b) cross polarization configurations. The gray line represents the TeO₂ spectrum measured at 300 K. Inset: Raman spectrum of CrGeTe₃ in the parallel polarization configuration measured at 100 K.

modes can be expected to appear for both in-parallel and cross polarization configurations.

The Raman spectra of CrSiTe₃ for two main linear polarization configurations, at 100 K, are shown in Fig. 1. Four peaks can be observed in the spectra, at energies of 88.9, 118.2, 147.4, and 217.2 cm⁻¹. Since only the peak at 147.4 cm⁻¹ vanishes in the cross polarization configuration, it corresponds to the A_g symmetry mode. The other three modes appear in both parallel and cross polarization configurations and, thereby, can be assigned as E_g symmetry modes (Fig. 1).

In order to exclude the possibility that any of the observed features originate from the TeO₂ [17,27], its Raman spectrum is also presented in Fig. 1. It can be noted that no TeO₂ contribution is present in our CrSiTe₃ data. Furthermore, the observed CrSiTe₃ Raman spectra are also consistent with the CrGeTe₃ Raman spectra (see inset in Fig. 1), isostructural to CrSiTe₃. Five Raman-active modes have been observed for CrGeTe₃, two A_g modes, at 137.9 and 296.6 cm⁻¹, and three E_g modes, at 83.5, 112.2, and 217.5 cm⁻¹, in agreement with the previously published data [17,18]. The main difference in the spectra of CrSiTe₃ and CrGeTe₃ arises from the change in mass and lattice parameter effects that cause the peaks to shift.

Calculated and observed Raman-active phonon energies are compiled in Table II, together with the experimental energies of the infrared (IR)-active phonons [1], and are found to be in good agreement. Displacement patterns of the A_g

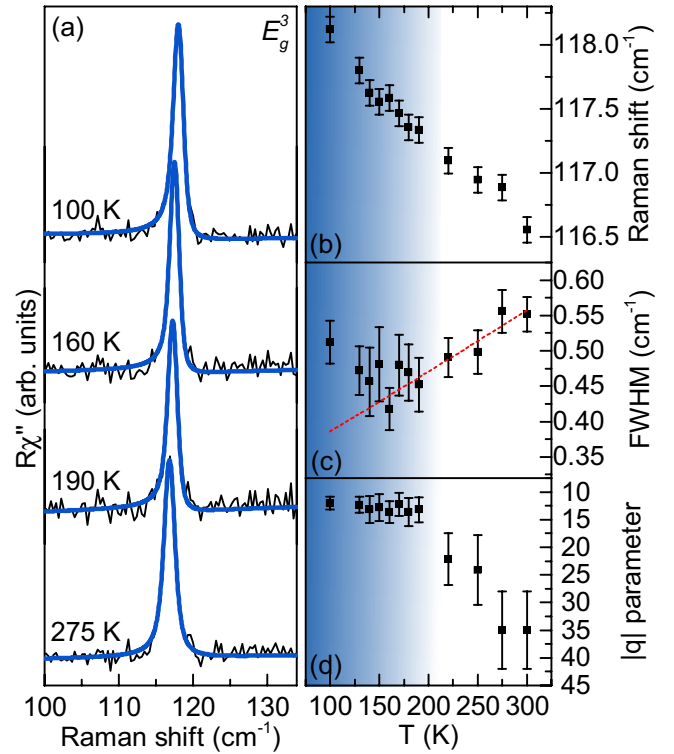


FIG. 2. (a) The E_g^3 mode Raman spectra of CrSiTe₃ at four temperatures measured in the cross polarization configuration. Blue lines represent line shapes obtained as a convolution of the Fano line shape and Gaussian, calculated to fit the experimental data. Temperature dependence of (b) the energy, (c) the line width, and (d) the Fano parameter q of the E_g^3 mode. The dashed red line represents standard anharmonic behavior [28,29]. All the parameters show a change in tendency around 180 K.

and E_g symmetry modes are presented in Fig. 4, in the Appendix.

B. Temperature dependence

After proper assignment of all the observed CrSiTe₃ Raman-active modes we proceeded with temperature evolution of their properties, focusing on the most prominent ones, E_g³ and A_g³. Figure 2(a) shows the spectral region of the doubly degenerate E_g³ mode at an energy of 118.2 cm⁻¹, at four temperatures. Closer inspection of the 100 K spectra revealed clear asymmetry of the peak on the low-energy side. The presence of defects may result in the appearance of the mode asymmetry [30], however, they would also contribute to the mode line width and, possibly, the appearance of phonons from the edge of the Brillouin zone in the Raman spectra [29]. The very narrow lines and absence of additional features in the Raman spectra of CrSiTe₃ do not support this scenario. The asymmetry may also arise when the phonon is coupled to a continuum [31]. Such a coupling of the E_g³ phonon mode would result in a line shape given by the convolution of a Fano function and a Gaussian, the latter representing the resolution of the spectrometer [29]. Comparison between the Fano line shape convoluted with a Gaussian, the Voigt line shape, and the experimental data at 100 K is presented in Fig. 5, in the

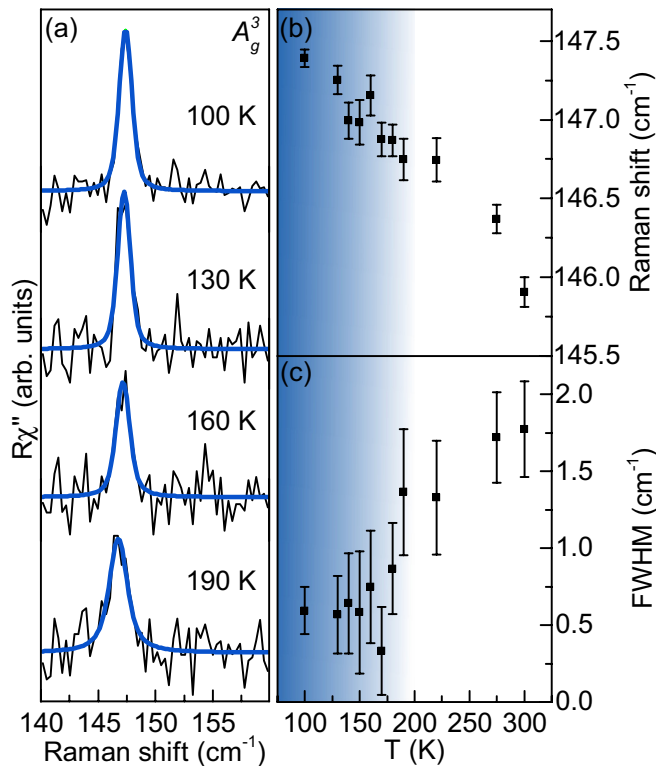


FIG. 3. (a) A_g^3 mode Raman spectra of CrSiTe_3 at four temperatures measured in the parallel polarization configuration. Blue lines represent Voigt line shapes. (b) Energy and (c) line-width temperature dependence of the A_g^3 mode.

Appendix, with the former yielding better agreement with the experimental data. Furthermore, it fully captures the E_g^3 mode line shape at all temperatures under investigation [Figs. 2(a) and 6].

Upon cooling of the sample, the E_g^3 mode energy hardens [Fig. 2(b)] with a very small discontinuity in the temperature range around 180 K. Down to the same temperature, the line width monotonically narrows in line with the standard anharmonic behavior [dashed red line in Fig. 2(c)]. Upon further cooling, the line width increased, deviating from the expected anharmonic tendency. This indicates activation of an additional scattering mechanism, e.g., spin-phonon interaction. Figure 2(d) shows the evolution of the Fano parameter, $|q|$. Whereas in the region below 180 K, it increases slightly but continuously, at higher temperatures it promptly goes to lower values and the mode recovers a symmetric line shape. We believe that the observed behavior of the E_g^3 mode can be traced back to the short-range magnetic correlations, which, according to Ref. [1], persist up to 150 K, and the strong spin-phonon coupling in CrSiTe_3 . Similar behavior of the energy and line width, which differs from the conventional anharmonic, as well as the E_g mode Fano-type line shape, was recently reported in $\alpha\text{-RuCl}_3$ and was interpreted as a consequence of the spin-phonon interaction [32].

Unlike the E_g^3 mode, no pronounced asymmetry was observed for the A_g^3 mode. As can be seen from Figs. 3(b) and 3(c) both the energy and the line width of the A_g^3 mode showed

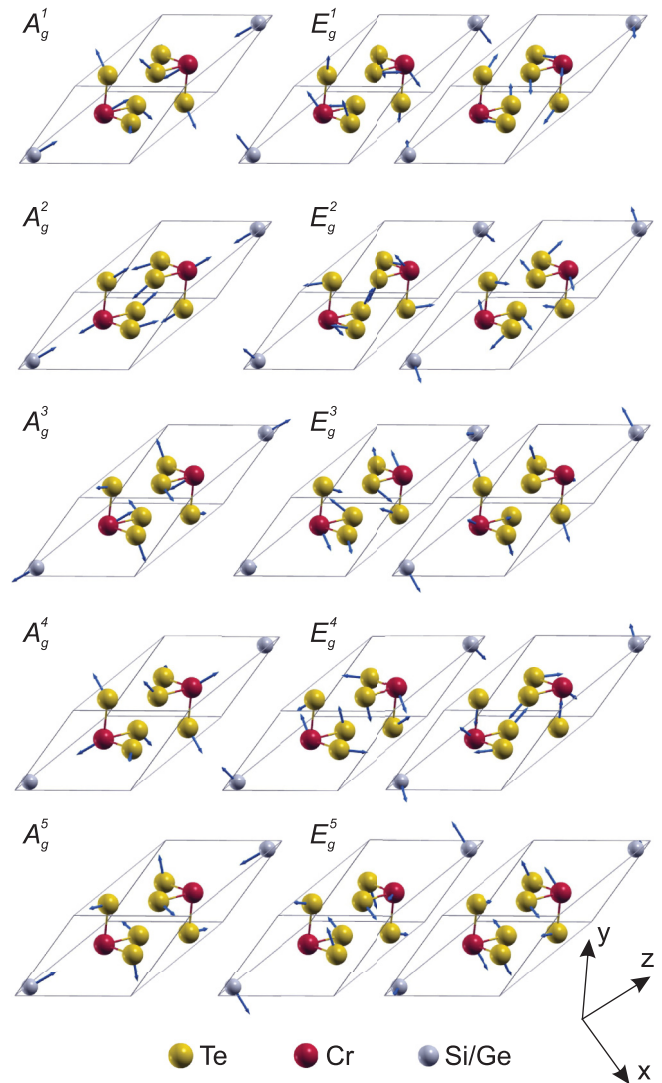


FIG. 4. Unit cell of a CrSiTe_3 single crystal (solid lines) with the displacement patterns of the A_g and E_g symmetry modes. Arrow lengths are proportional to the square root of the interatomic forces.

a similar change in tendency in the same temperature region as the E_g^3 mode, most likely due to the spin-phonon coupling.

IV. CONCLUSION

The lattice dynamics of CrSiTe_3 , a compound isostructural to CrGeTe_3 , is presented. An A_g and three E_g modes were observed and assigned. The experimental results are well supported by theoretical calculations. The temperature dependences of the energies and line widths of the A_g^3 and E_g^3 modes deviate from the conventional anharmonic model in the temperature range around 180 K. In addition, the E_g^3 mode shows clear Fano resonance at lower temperatures. This can be related to the previously reported short-range magnetic correlations at temperatures up to 150 K [1] and the strong spin-phonon coupling.

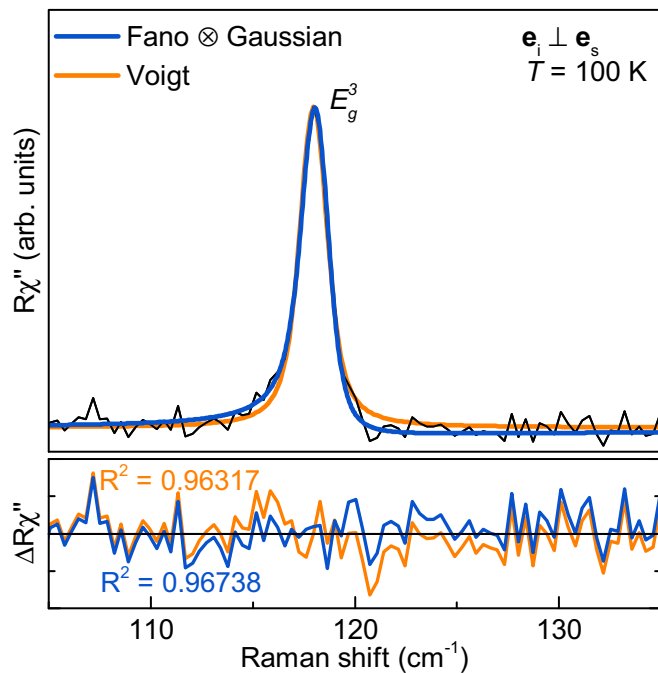


FIG. 5. Analysis of the E_g^3 asymmetry. Measured data are shown as the black line. The solid blue line represents the line shape obtained as a convolution of the Fano line shape and a Gaussian, whereas the orange line represents a Voigt line shape, both calculated to fit the experimental data. The Voigt profile deviates from the experimental data at the peak flanks.

ACKNOWLEDGMENTS

The work was supported by the Serbian Ministry of Education, Science and Technological Development under Projects III45018 and OI171005. DFT calculations were performed using computational resources at Johannes Kepler University, Linz, Austria. Work at Brookhaven is supported by the U.S. DOE under Contract No. DE-SC0012704.

A.M. and N.L. conceived and performed the experiment, analyzed and discussed data, and wrote the paper; A.S. and J.P. calculated phonon energies, analyzed and discussed data, and wrote the paper; Y.L. and C.P. synthesized and characterized the samples; Z.V.P. analyzed and discussed data and wrote the paper. All authors commented on the manuscript.

APPENDIX

1. Eigenvectors of Raman-active modes

Figure 4 summarizes the A_g and E_g symmetry mode displacement patterns of a CrSiTe₃ single crystal ($R\bar{3}$ space group). Arrow lengths are proportional to the square root of the interatomic forces.

2. Asymmetry of the E_g^3 line

The peak at 118.2 cm^{-1} , which we assigned as the E_g^3 symmetry mode, at low temperatures shows a significant asymmetry towards lower energies. The possibility of additional defect-induced features in Raman spectra can be excluded, since the modes are very narrow, suggesting high crystallinity

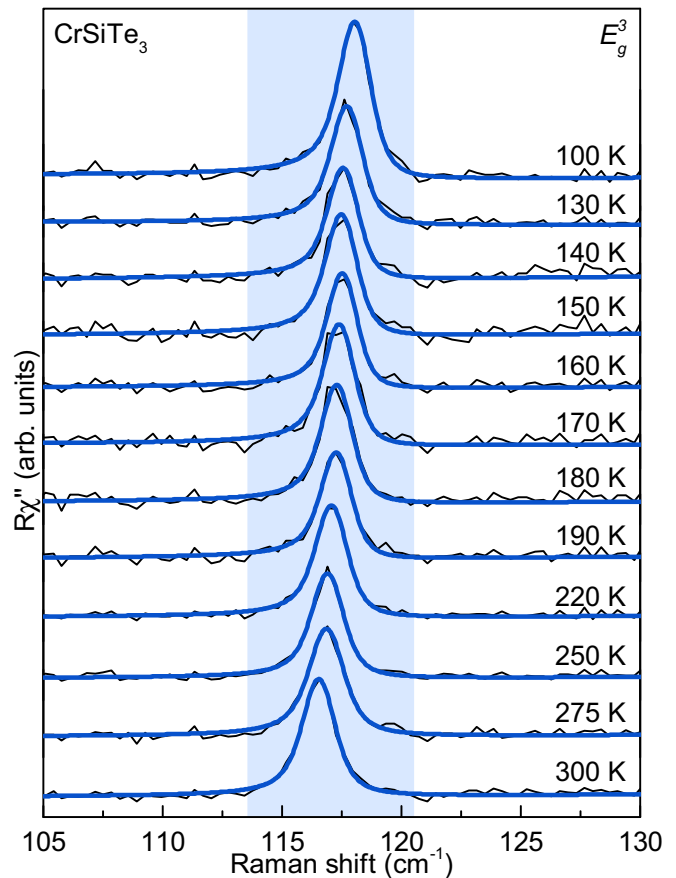


FIG. 6. The E_g^3 mode Raman spectra of CrSiTe₃ at all temperatures measured in the cross polarization configuration. Blue lines represent calculated spectra obtained as the convolution of the Fano line shape and Gaussian.

of the sample. Also, the theoretical calculations do not predict additional Raman-active modes in this energy region. On the other hand, coupling of the phonon mode to a continuum may result in an asymmetric line shape described with the Fano function. Due to the finite resolution of the spectrometer it has to be convoluted with a Gaussian ($\Gamma_G = 1 \text{ cm}^{-1}$). In Fig. 5 we present a comparison of the line obtained as a convolution of the Fano line shape and a Gaussian (blue line) and a Voigt line shape (orange line) fitted to the experimental data. Whereas the Voigt line shape deviates at the peak flanks, excellent agreement has been achieved for convolution of the Fano line shape and a Gaussian.

3. E_g^3 mode temperature dependence

Figure 6 shows Raman spectra of CrSiTe₃ in the region of the E_g^3 mode in the cross polarization configuration at various temperatures. Solid blue lines represent the convolution of the Fano line shape and Gaussian fitted to the experimental data. The asymmetry is the most pronounced below 190 K. Above this temperature, the asymmetry is decreasing, and at high temperatures the peak recovers the fully symmetric line shape.

- [1] L. D. Casto, A. J. Clune, M. O. Yokosuk, J. L. Musfeldt, T. J. Williams, H. L. Zhuang, M.-W. Lin, K. Xiao, R. G. Hennig, B. C. Sales, J.-Q. Yan, and D. Mandrus, Strong spin-lattice coupling in CrSiTe₃, *APL Mater.* **3**, 041515 (2015).
- [2] X. Zhang, Y. Zhao, Q. Song, S. Jia, J. Shi, and W. Han, Magnetic anisotropy of the single-crystalline ferromagnetic insulator Cr₂Ge₂Te₆, *Jpn. J. Appl. Phys.* **55**, 033001 (2016).
- [3] T. Leineweber and H. Kronmüller, Micromagnetic examination of exchange coupled ferromagnetic nanolayers, *J. Magn. Magn. Mater.* **176**, 145 (1997).
- [4] G. Ouvrard, E. Sandre, and R. Brec, Synthesis and crystal structure of a new layered phase: The chromium hexatellurosilicate Cr₂Si₂Te₆, *J. Solid State Chem.* **73**, 27 (1988).
- [5] B. Siberchicot, S. Jobic, V. Carteaux, P. Gressier, and G. Ouvrard, Band structure calculations of ferromagnetic chromium tellurides CrSiTe₃ and CrGeTe₃, *J. Phys. Chem.* **100**, 5863 (1996).
- [6] V. Carteaux, F. Moussa, and M. Spiesser, 2D Ising-like ferromagnetic behaviour for the lamellar Cr₂Si₂Te₆ compound: A neutron scattering investigation, *Europhys. Lett.* **29**, 251 (1995).
- [7] N. Sivasdas, M. W. Daniels, R. H. Swendsen, S. Okamoto, and D. Xiao, Magnetic ground state of semiconducting transition-metal trichalcogenide monolayers, *Phys. Rev. B* **91**, 235425 (2015).
- [8] K. S. Novoselov, A. K. Geim, S. V. Morozov, D. Jiang, Y. Zhang, S. V. Dubonos, I. V. Grigorieva, and A. A. Firsov, Electric field effect in atomically thin carbon films, *Science* **306**, 666 (2004).
- [9] Q. H. Wang, K. Kalantar-Zadeh, A. Kis, J. N. Coleman, and M. S. Strano, Electronics and optoelectronics of two-dimensional transition metal dichalcogenides, *Nat. Nanotechnol.* **7**, 699 (2012), review Article.
- [10] C. Gong, L. Li, Z. Li, H. Ji, A. Stern, Y. Xia, T. Cao, W. Bao, C. Wang, Y. Wang, Z. Q. Qiu, R. J. Cava, S. G. Louie, J. Xia, and X. Zhang, Discovery of intrinsic ferromagnetism in two-dimensional van der Waals crystals, *Nature* **546**, 265 (2017).
- [11] B. Huang, G. Clark, E. Navarro-Moratalla, D. R. Klein, R. Cheng, K. L. Seyler, D. Zhong, E. Schmidgall, M. A. McGuire, D. H. Cobden, W. Yao, D. Xiao, P. Jarillo-Herrero, and X. Xu, Layer-dependent ferromagnetism in a van der Waals crystal down to the monolayer limit, *Nature* **546**, 270 (2017).
- [12] W. Xing, Y. Chen, P. M. Odenthal, X. Zhang, W. Yuan, T. Su, Q. Song, T. Wang, J. Zhong, S. Jia, X. C. Xie, Y. Li, and W. Han, Electric field effect in multilayer Cr₂Ge₂Te₆: A ferromagnetic 2D material, *2D Mater.* **4**, 024009 (2017).
- [13] T. J. Williams, A. A. Aczel, M. D. Lumsden, S. E. Nagler, M. B. Stone, J.-Q. Yan, and D. Mandrus, Magnetic correlations in the quasi-two-dimensional semiconducting ferromagnet CrSiTe₃, *Phys. Rev. B* **92**, 144404 (2015).
- [14] X. Li and J. Yang, CrXTe₃ (X = Si, Ge) nanosheets: Two dimensional intrinsic ferromagnetic semiconductors, *J. Mater. Chem. C* **2**, 7071 (2014).
- [15] M.-W. Lin, H. L. Zhuang, J. Yan, T. Z. Ward, A. A. Puretzy, C. M. Rouleau, Z. Gai, L. Liang, V. Meunier, B. G. Sumpter, P. Ganesh, P. R. C. Kent, D. B. Geohegan, D. G. Mandrus, and K. Xiao, Ultrathin nanosheets of CrSiTe₃: A semiconducting two-dimensional ferromagnetic material, *J. Mater. Chem. C* **4**, 315 (2016).
- [16] B. Liu, Y. Zou, S. Zhou, L. Zhang, Z. Wang, H. Li, Z. Qu, and Y. Zhang, Critical behavior of the van der Waals bonded high T_C ferromagnet Fe₃GeTe₂, *Sci. Rep.* **7**, 6184 (2017).
- [17] Y. Tian, M. J. Gray, H. Ji, R. J. Cava, and K. S. Burch, Magnetoelastic coupling in a potential ferromagnetic 2D atomic crystal, *2D Mater.* **3**, 025035 (2016).
- [18] Y. Sun, R. C. Xiao, G. T. Lin, R. R. Zhang, L. S. Ling, Z. W. Ma, X. Luo, W. J. Lu, Y. P. Sun, and Z. G. Sheng, Effects of hydrostatic pressure on spin-lattice coupling in two-dimensional ferromagnetic Cr₂Ge₂Te₆, *Appl. Phys. Lett.* **112**, 072409 (2018).
- [19] Y. Liu and C. Petrovic, Critical behavior of quasi-two-dimensional semiconducting ferromagnet Cr₂Ge₂Te₆, *Phys. Rev. B* **96**, 054406 (2017).
- [20] G. T. Lin, H. L. Zhuang, X. Luo, B. J. Liu, F. C. Chen, J. Yan, Y. Sun, J. Zhou, W. J. Lu, P. Tong, Z. G. Sheng, Z. Qu, W. H. Song, X. B. Zhu, and Y. P. Sun, Tricritical behavior of the two-dimensional intrinsically ferromagnetic semiconductor CrGeTe₃, *Phys. Rev. B* **95**, 245212 (2017).
- [21] P. Giannozzi, S. Baroni, N. Bonini, M. Calandra, R. Car, C. Cavazzoni, D. Ceresoli, G. L. Chiarotti, M. Cococcioni, I. Dabo, A. D. Corso, S. de Gironcoli, S. Fabris, G. Fratesi, R. Gebauer, U. Gerstmann, C. Gougoussis, A. Kokalj, M. Lazzeri, L. Martin-Samos, N. Marzari, F. Mauri, R. Mazzarello, S. Paolini, A. Pasquarello, L. Paulatto, C. Sbraccia, S. Scandolo, G. Sclauzero, A. P. Seitsonen, A. Smogunov, P. Umari, and R. M. Wentzcovitch, Quantum espresso: A modular and open-source software project for quantum simulations of materials, *J. Phys.: Condens. Matter* **21**, 395502 (2009).
- [22] J. P. Perdew, K. Burke, and M. Ernzerhof, Generalized Gradient Approximation Made Simple, *Phys. Rev. Lett.* **77**, 3865 (1996).
- [23] P. E. Blöchl, Projector augmented-wave method, *Phys. Rev. B* **50**, 17953 (1994).
- [24] G. Kresse and D. Joubert, From ultrasoft pseudopotentials to the projector augmented-wave method, *Phys. Rev. B* **59**, 1758 (1999).
- [25] G. Stefan, Semiempirical GGA-type density functional constructed with a long-range dispersion correction, *J. Comput. Chem.* **27**, 1787 (2006).
- [26] R. E. Marsh, The crystal structure of Cr₂Si₂Te₆: Corrigendum, *J. Solid State Chem.* **77**, 190 (1988).
- [27] N. Lazarević, E. S. Bozin, M. Šćepanović, M. Opačić, Hechang Lei, C. Petrovic, and Z. V. Popović, Probing IrTe₂ crystal symmetry by polarized Raman scattering, *Phys. Rev. B* **89**, 224301 (2014).
- [28] M. Opačić, N. Lazarević, M. Šćepanović, H. Ryu, H. Lei, C. Petrovic, and Z. V. Popović, Evidence of superconductivity-induced phonon spectra renormalization in alkali-doped iron selenides, *J. Phys.: Condens. Matter* **27**, 485701 (2015).
- [29] A. Baum, A. Milosavljević, N. Lazarević, M. M. Radonjić, B. Nikolić, M. Mitschek, Z. Inanloo Maranloo, M. Šćepanović, M. Grujić-Brojčin, N. Stojilović, M. Opel, Aifeng Wang, C. Petrovic, Z. V. Popović, and R. Hackl, Phonon anomalies in FeS, *Phys. Rev. B* **97**, 054306 (2018).
- [30] N. Lazarević, M. Radonjić, M. Šćepanović, Hechang Lei, D. Tanasković, C. Petrovic, and Z. V. Popović, Lattice dynamics of KNi₂Se₂, *Phys. Rev. B* **87**, 144305 (2013).

- [31] N. Lazarević, Z. V. Popović, Rongwei Hu, and C. Petrovic, Evidence for electron-phonon interaction in Fe_{1-x}M_xSb₂ ($M =$ Co and Cr; $0 \leq x \leq 0.5$) single crystals, *Phys. Rev. B* **81**, 144302 (2010).
- [32] L. J. Sandilands, Y. Tian, K. W. Plumb, Y.-J. Kim, and K. S. Burch, Scattering Continuum and Possible Fractionalized Excitations in α -RuCl₃, *Phys. Rev. Lett.* **114**, 147201 (2015).

Lattice dynamics and phase transition in CrI₃ single crystals

S. Djurdjic-Mijin,¹ A. Šolajić,¹ J. Pešić,¹ M. Šćepanović,¹ Y. Liu (刘育),² A. Baum,^{3,4} C. Petrovic,²
N. Lazarević,¹ and Z. V. Popović^{1,5}

¹Center for Solid State Physics and New Materials, Institute of Physics Belgrade, University of Belgrade,
Pregrevica 118, 11080 Belgrade, Serbia

²Condensed Matter Physics and Materials Science Department, Brookhaven National Laboratory, Upton, New York 11973-5000, USA

³Walther Meissner Institut, Bayerische Akademie der Wissenschaften, 85748 Garching, Germany

⁴Fakultät für Physik E23, Technische Universität München, 85748 Garching, Germany

⁵Serbian Academy of Sciences and Arts, Knez Mihailova 35, 11000 Belgrade, Serbia



(Received 9 July 2018; published 18 September 2018)

The vibrational properties of CrI₃ single crystals were investigated using Raman spectroscopy and were analyzed with respect to the changes of the crystal structure. All but one mode are observed for both the low-temperature $R\bar{3}$ and the high-temperature $C2/m$ phase. For all observed modes the energies and symmetries are in good agreement with DFT calculations. The symmetry of a single layer was identified as $p\bar{3}1/m$. In contrast to previous studies we observe the transition from the $R\bar{3}$ to the $C2/m$ phase at 180 K and find no evidence for coexistence of both phases over a wide temperature range.

DOI: [10.1103/PhysRevB.98.104307](https://doi.org/10.1103/PhysRevB.98.104307)

I. INTRODUCTION

Two-dimensional layered materials have gained attention due to their unique properties, the potential for a wide spectrum of applications, and the opportunity for the development of functional van der Waals heterostructures. CrI₃ is a member of the chromium-trihalide family which are ferromagnetic semiconductors [1]. Recently they have received significant attention as candidates for the study of magnetic monolayers. The experimental realization of CrI₃ ferromagnetic monolayers [1] motivated further efforts towards their understanding. CrI₃ features electric field controlled magnetism [2] as well as a strong magnetic anisotropy [3,4]. With the main absorption peaks lying in the visible part of the spectrum, it is a great candidate for low-dimensional semiconductor spintronics [5]. In its ground state, CrI₃ is a ferromagnetic semiconductor with a Curie temperature of 61 K [1,6] and a band gap of 1.2 eV [6]. It was demonstrated that the magnetic properties of CrI₃ mono- and bilayers can be controlled by electrostatic doping [2]. Upon cooling, CrI₃ undergoes a phase transition around 220 K from the high-temperature monoclinic ($C2/m$) to the low-temperature rhombohedral ($R\bar{3}$) phase [3,7]. Although the structural phase transition is reported to be first order, it was suggested that the phases may coexist over a wide temperature range [3]. Raman spectroscopy can be of use here due to its capability to simultaneously probe both phases in a phase-separated system [8–10].

A recent theoretical study predicted the energies of all Raman active modes in the low-temperature and high-temperature structure of CrI₃ suggesting a near degeneracy between the A_g and B_g modes in the monoclinic ($C2/m$) structure. Their energies match the energies of E_g modes in the rhombohedral ($R\bar{3}$) structure [7].

In this article we present an experimental and theoretical Raman scattering study of CrI₃ lattice dynamics. In both phases all but one of the respective modes predicted by

symmetry were observed. The energies for all modes are in good agreement with the theoretical predictions for the assumed crystal symmetry. Our data suggest that the first-order transition occurs at $T_s \approx 180$ K without evidence for phase coexistence over a wide temperature range.

II. EXPERIMENT AND NUMERICAL METHOD

The preparation of the single crystal CrI₃ sample used in this study is described elsewhere [11]. The Raman scattering experiment was performed using a Tri Vista 557 spectrometer in backscattering micro-Raman configuration with a 1800/1800/2400 grooves/mm diffraction grating combination. The 532 nm line of a Coherent Verdi G solid state laser was used for excitation. The direction of the incident light coincides with the crystallographic c axis. The sample was oriented so that its principal axis of the $R\bar{3}$ phase coincides with the x axis of the laboratory system. A KONTI CryoVac continuous helium flow cryostat with a 0.5-mm-thick window was used for measurements at all temperatures under high vacuum (10^{-6} mbar). The sample was cleaved in air before being placed into the cryostat. The obtained Raman spectra were corrected by the Bose factor and analyzed quantitatively by fitting Voigt profiles to the data whereby the Gaussian width $\Gamma_{\text{Gauss}} = 1 \text{ cm}^{-1}$ reflects the resolution of the spectrometer.

The spin polarized density functional theory (DFT) calculations have been performed in the Quantum Espresso (QE) software package [12] using the Perdew-Burke-Ernzerhof (PBE) exchange-correlation functional [13] and PAW pseudopotentials [14,15]. The energy cutoffs for the wave functions and the charge density were set to be 85 and 425 Ry, respectively, after convergence tests. For k -point sampling, the Monkhorst-Pack scheme was used with a $8 \times 8 \times 8$ grid centered around the Γ point. Optimization of the atomic positions in the unit cell was performed until the interatomic forces

were smaller than 10^{-6} Ry/Å. To treat the van der Waals (vdW) interactions a Grimme-D2 correction [16] is used in order to include long-ranged forces between the layers, which are not properly captured within LDA or GGA functionals. This way, the parameters are obtained more accurately, especially the interlayer distances. Phonon frequencies were calculated at the Γ point using the linear response method implemented in QE. The phonon energies are compiled in Table III together with the experimental values. The eigenvectors of the Raman active modes for both the low- and high-temperature phase are depicted in Fig. 5 of the Appendix.

III. RESULTS AND DISCUSSION

CrI₃ adopts a rhombohedral $R\bar{3}$ (C_{3i}^2) crystal structure at low temperatures and a monoclinic $C2/m$ (C_{2h}^3) crystal structure at room temperature [3], as shown in Fig. 1. The main difference between the high- and low-temperature crystallographic space groups arises from different stacking sequences with the CrI₃ layers being almost identical. In the rhombohedral structure the Cr atoms in one layer are placed above the center of a hole in the Cr honeycomb net of the two adjacent layers. When crossing the structural phase transition at T_s to the monoclinic structure the layers are displaced along the a direction so that every fourth layer is at the same place as the first one. The interatomic distances, mainly the interlayer distance, and the vdW gap, are slightly changed by the structural transition. The crystallographic parameters for both phases are presented in Table I. The numerically obtained values are in good agreement with reported x-ray diffraction data [11].

The vibrational properties of layered materials are typically dominated by the properties of the single layers composing the crystal. The symmetry of a single layer can be described by one of the 80 dipericodic space groups (DG) obtained by

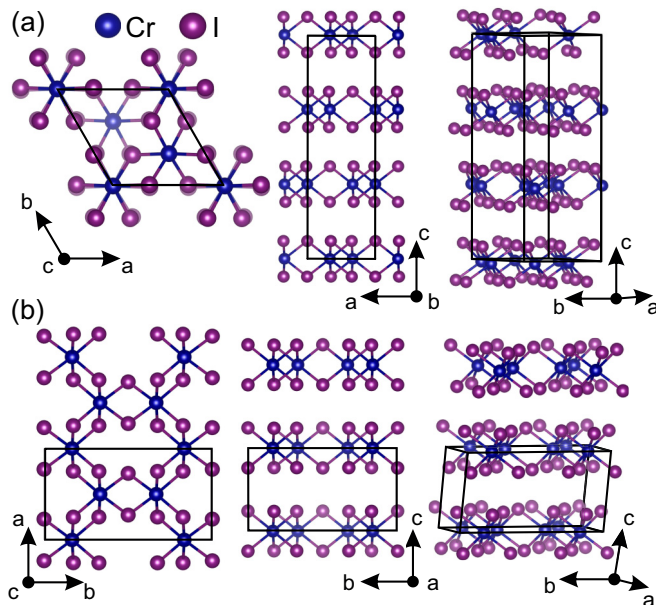


FIG. 1. Schematic representation of (a) the low-temperature $R\bar{3}$ and (b) the high-temperature $C2/m$ crystal structure of CrI₃. Black lines represent unit cells.

TABLE I. Calculated and experimental [11] parameters of the crystallographic unit cell for the low-temperature $R\bar{3}$ and high-temperature $C2/m$ phase of CrI₃.

T (K)	Space group $R\bar{3}$		Space group $C2/m$	
	Calc.	Expt. [11]	Calc.	Expt. [11]
a (Å)	6.87	6.85	6.866	6.6866
b (Å)	6.87	6.85	11.886	11.856
c (Å)	19.81	19.85	6.984	6.966
α (deg)	90	90	90	90
β (deg)	90	90	108.51	108.68
γ (deg)	120	120	90	90

lifting translational invariance in the direction perpendicular to the layer [17]. In the case of CrI₃, the symmetry analysis revealed that the single layer structure is fully captured by the $p\bar{3}1/m$ (D_{3d}^1) dipericodic space group DG71, rather than by $R\bar{3}2/m$ as proposed in Ref. [7].

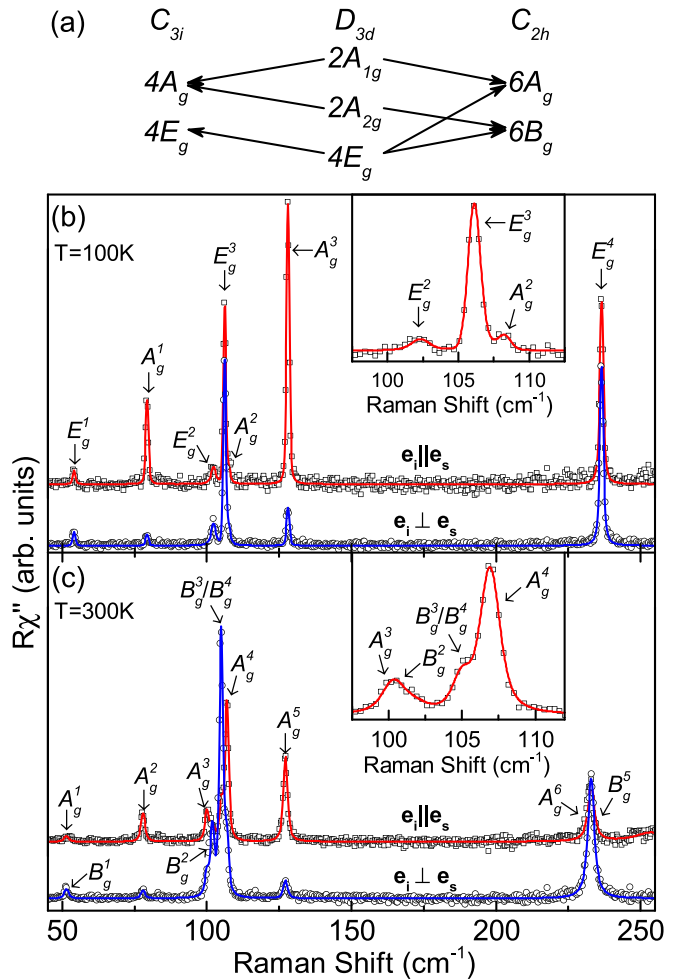


FIG. 2. (a) Compatibility relations for the CrI₃ layer and the crystal symmetries. Raman spectra of (b) the low-temperature $R\bar{3}$ and (c) the high-temperature $C2/m$ crystal structure measured in parallel (open squares) and crossed (open circles) polarization configurations at 100 and 300 K, respectively. Red and blue solid lines represent fits of Voigt profiles to the experimental data.

TABLE II. Wyckoff positions of the two types of atoms and their contributions to the Γ -point phonons for the $R\bar{3}$ and $C2/m$ as well as the $p\bar{3}1/m$ diperiodic space group. The second row shows the Raman tensors for the corresponding space groups.

Space group $R\bar{3}$		Diperiodic space group $p\bar{3}1/m$		Space group: $C2/m$	
Atoms	Irreducible representations	Atoms	Irreducible representations	Atoms	Irreducible representations
Cr (6c)	$A_g + A_u + E_g + E_u$	Cr (2c)	$A_{2g} + A_{2u} + E_g + E_u$	Cr (4g)	$A_g + A_u + 2B_g + 2B_u$
I (18f)	$3A_g + 3A_u + 3E_g + 3E_u$	I (6k)	$2A_{1g} + A_{1u} + A_{2g} + 2A_{2u} + 3E_g + 3E_u$	I (4i)	$2A_g + 2A_u + B_g + B_u$
	$A_g = \begin{pmatrix} a & & \\ & a & \\ & & b \end{pmatrix}$		$A_{1g} = \begin{pmatrix} a & & \\ & a & \\ & & b \end{pmatrix}$		$A_g = \begin{pmatrix} a & d \\ & c \\ d & b \end{pmatrix}$
	${}^1E_g = \begin{pmatrix} c & d & e \\ d & -c & f \\ e & f & \end{pmatrix}$		${}^1E_g = \begin{pmatrix} c & & \\ -c & d & \\ d & & \end{pmatrix}$		$B_g = \begin{pmatrix} e & \\ & f \\ e & f \end{pmatrix}$
	${}^2E_g = \begin{pmatrix} d & -c & -f \\ -c & -d & e \\ -f & e & \end{pmatrix}$		${}^2E_g = \begin{pmatrix} & -c & -d \\ -c & & \\ -d & e & \end{pmatrix}$		

According to the factor group analysis (FGA) for a single CrI_3 layer, six modes ($2A_{1g} + 4E_g$) are expected to be observed in the Raman scattering experiment (see Table II). By stacking the layers the symmetry is reduced and, depending on the stacking sequence, FGA yields a total of eight Raman active modes ($4A_g + 4E_g$) for the $R\bar{3}$ and 12 Raman active modes ($6A_g + 6B_g$) for the $C2/m$ crystal symmetry. The correlation between layer and crystal symmetries for both cases is shown in Fig. 2(a) [18,19].

Figure 2(b) shows the CrI_3 single crystal Raman spectra measured at 100 K in two scattering channels. According to the selection rules for the rhombohedral crystal structure (Table II) the A_g modes can be observed only in the parallel polarization configuration, whereas the E_g modes appear in both parallel and crossed polarization configurations. Based on the selection rules the peaks at about 78, 108, and 128 cm^{-1} were identified as A_g symmetry modes, whereas the peaks at about 54, 102, 106, and 235 cm^{-1} are assigned as E_g symmetry. The weak observation of the most pronounced A_g modes in crossed polarizations [Fig. 2(b)] is attributed to

the leakage due to a slight sample misalignment and/or the presence of defects in the crystal. The energies of all observed modes are compiled in Table III together with the energies predicted by our calculations and by Ref. [7], and are found to be in good agreement for the E_g modes. The discrepancy is slightly larger for the low energy A_g modes. Our calculations in general agree with those from Ref. [7]. The A_g^4 mode of the rhombohedral phase, predicted by calculation to appear at about 195 cm^{-1} , was not observed in the experiment, most likely due to its low intensity.

When the symmetry is lowered in the high-temperature monoclinic $C2/m$ phase [Fig. 2(c)] the E_g modes split into an A_g and a B_g mode each, whereas the rhombohedral A_g^2 and A_g^4 modes are predicted to switch to the monoclinic B_g symmetry. The correspondence of the phonon modes across the phase transition is indicated by the arrows in Table III. The selection rules for $C2/m$ (see Table II) predict that A_g and B_g modes can be observed in both parallel and crossed polarization configurations. Additionally, the sample forms three types of domains which are rotated with respect to each other. We

TABLE III. Phonon symmetries and phonon energies for the low-temperature $R\bar{3}$ and high-temperature $C2/m$ phase of CrI_3 . The experimental values were determined at 100 and 300 K, respectively. All calculations were performed at zero temperature. Arrows indicate the correspondence of the phonon modes across the phase transition.

Space group $R\bar{3}$				Space group $C2/m$			
Symm.	Expt. (cm^{-1})	Calc. (cm^{-1})	Calc. (cm^{-1}) [7]	Symm.	Expt. (cm^{-1})	Calc. (cm^{-1})	Calc. [7] (cm^{-1})
E_g^1	54.1	59.7	53	B_g^1	52.0	57.0	52
				A_g^1	53.6	59.8	51
A_g^1	73.33	89.6	79	A_g^2	78.6	88.4	79
E_g^2	102.3	99.8	98	A_g^3	101.8	101.9	99
				B_g^2	102.4	101.8	99
E_g^3	106.2	112.2	102	B_g^3	106.4 ^a	108.9	101
				A_g^4	108.3	109.3	102
A_g^2	108.3	98.8	88	B_g^4	106.4 ^a	97.8	86
A_g^3	128.1	131.1	125	A_g^5	128.2	131.7	125
A_g^4	–	195.2	195	B_g^5	–	198.8	195
E_g^4	236.6	234.4	225	A_g^6	234.6	220.1	224
				B_g^6	235.5	221.1	225

^aObserved as two peak structure.

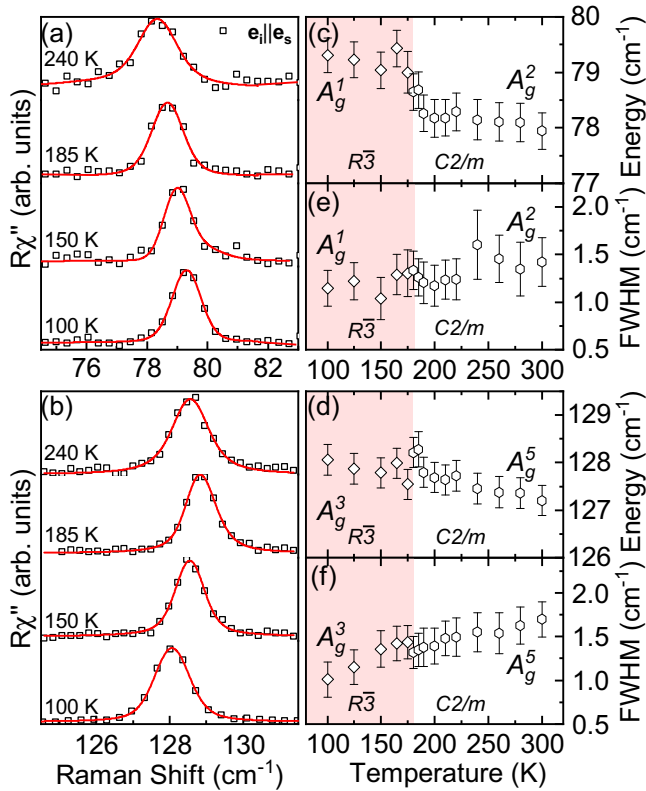


FIG. 3. Temperature dependence of the A_g^1 and A_g^3 phonon modes of the rhombohedral structure and the corresponding A_g^2 and A_g^5 modes of the monoclinic structure, respectively. (a) and (b) Raman spectra at temperatures as indicated. The spectra are shifted for clarity. Solid red lines represent Voigt profiles fitted to the data. (c) and (d) and (e) and (f) Temperature dependence of the phonon energies and linewidths, respectively. Both modes show an abrupt change in energy at the phase transition at 180 K.

therefore identify the phonons in the $C2/m$ phase in relation to the calculations and find again good agreement of the energies. The B_g^3 and B_g^4 modes overlap and therefore cannot be resolved separately. As can be seen from the temperature dependence shown below [Fig. 4(b)] the peak at 106 cm^{-1} broadens and gains spectral weight in the monoclinic phase in line with the expectation that two modes overlap. The missing rhombohedral A_g^4 mode corresponds to the monoclinic B_g^5 mode, which is likewise absent in the spectra.

The temperature dependence of the observed phonons is shown in Figs. 3 and 4. In the low-temperature rhombohedral phase all four E_g modes as well as A_g^1 and A_g^2 soften upon warming, whereas A_g^3 hardens up to $T \approx 180\text{ K}$ before softening again. Crossing the first-order phase transition from $R\bar{3}$ to $C2/m$ crystal symmetry is reflected in the spectra as a symmetry change and/or renormalization for the non-degenerate modes and lifting of the degeneracy of the E_g modes as shown in Table II. In our samples, this transition is observed at $T_s \approx 180\text{ K}$. The splitting of the E_g phonons into A_g and B_g modes at the phase transition is sharp (Fig. 4). The rhombohedral A_g^1 and A_g^3 phonons show a jump in energy and a small discontinuity in the linewidth at T_s (Fig. 3). Our spectra were taken during warming in multiple runs after

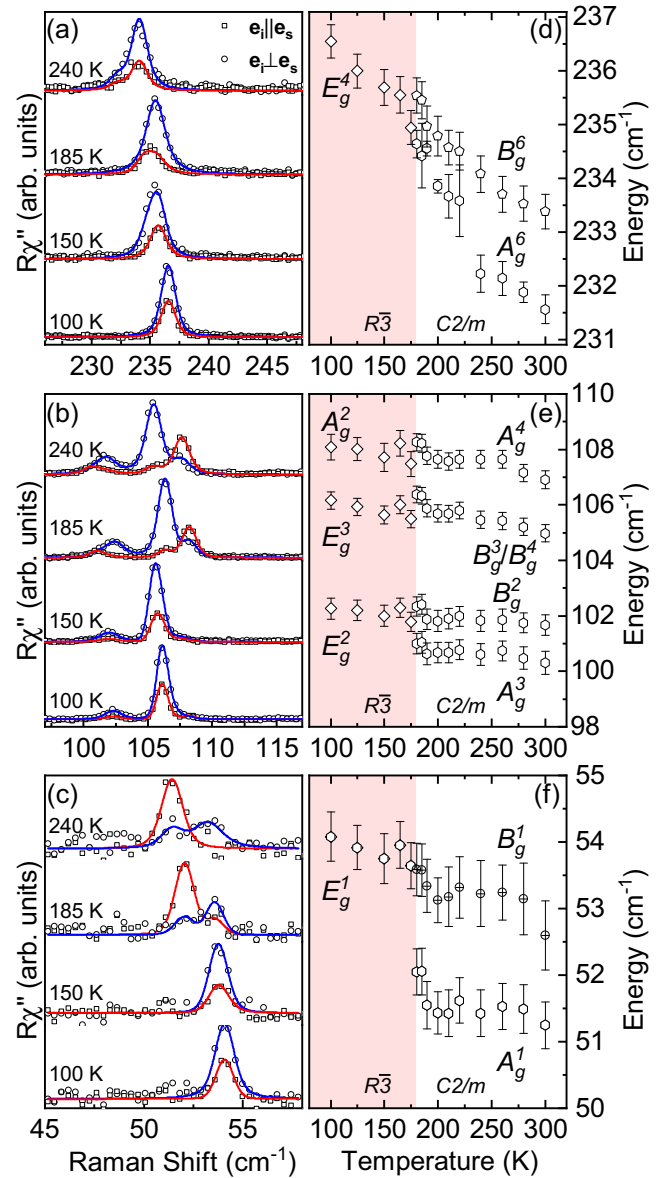


FIG. 4. Temperature dependence of the rhombohedral A_g^4 and E_g modes. (a)–(c) Raman spectra in parallel (open squares) and crossed (open circles) light polarizations at temperatures as indicated. The spectra are shifted for clarity. Blue and red solid lines are fits of Voigt profiles to the data. Two spectra were analyzed simultaneously in two scattering channels with the integrated intensity as the only independent parameter. (d)–(f) Phonon energies obtained from the Voigt profiles. Each E_g mode splits into an A_g and a B_g mode above 180 K.

cooling to 100 K each time. We found that the temperature dependence for the phonon modes obtained this way was smooth in each phase. McGuire *et al.* [3,20] reported T_s in the range of 220 K, a coexistence of both phases and a large thermal hysteresis. However, they also noted that the first and second warming cycle showed identical behavior and only found a shift of the transition temperature to higher values for cooling cycles. We therefore consider the difference between the reported transition around 220 K and our $T_s \approx 180\text{ K}$ significant. To some extent this difference may be attributed

to local heating by the laser. More importantly, we find no signs of phase coexistence in the observed temperature range. The spectra for the low-temperature and high-temperature phases are distinctly different (Fig. 2) and the E_g modes exhibit a clearly resolved splitting which occurs abruptly at T_S . We performed measurements in small temperature steps (see Figs. 3 and 4). This limits the maximum temperature interval where the phase coexistence could occur in our samples to approximately 5 K, much less than the roughly 30 to 80 K reported earlier [3,20]. We cannot exclude the possibility that a small fraction of the low-temperature phase could still

coexist with the high-temperature phase over a wider temperature range, whereby weak peaks corresponding to the remains of the low-temperature $R\bar{3}$ phase might be hidden under the strong peaks of the $C2/m$ phase.

IV. CONCLUSION

We studied the lattice dynamics in single crystalline CrI_3 using Raman spectroscopy supported by numerical calculations. For both the low-temperature $R\bar{3}$ and the high-temperature $C2/m$ phase, all except one of the predicted

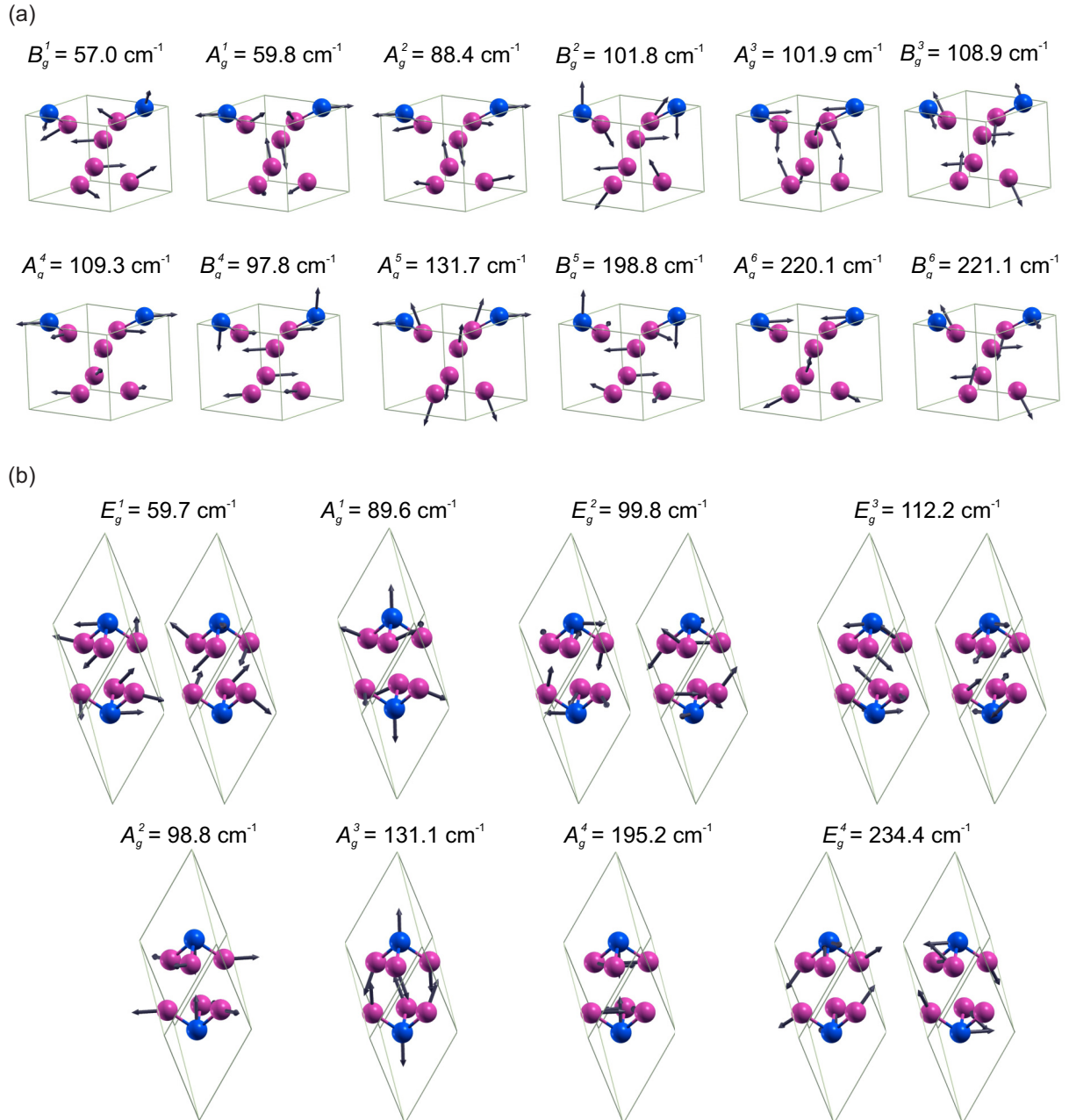


FIG. 5. Raman-active phonons in CrI_3 for (a) the monoclinic phase hosting A_g and B_g modes and for (b) the rhombohedral phase hosting A_g and E_g modes. Blue and violet spheres denote Cr and I atoms, respectively. Solid lines represent primitive unit cells. Arrow lengths are proportional to the square root of the interatomic forces. The given energies are calculated for zero temperature.

phonon modes were identified and the calculated and experimental phonon energies were found to be in good agreement. We determined that the symmetry of the single CrI₃ layers is $p\bar{3}1/m$. Abrupt changes to the spectra were found at the first-order phase transition which was located at $T_s \approx 180$ K, lower than in previous studies. In contrast to the prior reports we found no sign of phase coexistence over temperature ranges exceeding 5 K.

ACKNOWLEDGMENTS

The work was supported by the Serbian Ministry of Education, Science and Technological Development under Projects No. III45018 and No. OI171005. DFT calculations were performed using computational resources at Johannes Kepler University, Linz, Austria. Work at Brookhaven is supported by the U.S. DOE under Contract No. DE-SC0012704.

S.Dj.M. and N.L. conceived the experiment, performed the experiment, analyzed and discussed the data, and wrote the paper. A.Š. and J.P. calculated the phonon energies, analyzed and discussed the data, and wrote the paper. Y.L. and C.P. synthesized and characterized the samples. M.Š. performed the experiment and analyzed and discussed the data. A.B. and Z.V.P. analyzed and discussed the data and wrote the paper. All authors commented on the manuscript.

APPENDIX: EIGENVECTORS

In addition to the phonon energies we also calculated the phonon eigenvectors which are shown in Fig. 5(a) for the high-temperature monoclinic phase and in Fig. 5(b) for the low-temperature rhombohedral phase. The energies, as given, are calculated for zero temperature. The relative displacement of the atoms is denoted by the length of the arrows.

-
- [1] E. Navarro-Moratalla, B. Huang, G. Clark *et al.*, Layer-dependent ferromagnetism in a van der Waals crystal down to the monolayer limit, *Nature (London)* **546**, 270 (2017).
- [2] S. Jiang, L. Li, Z. Wang, K. F. Mak, and J. Shan, Controlling magnetism in 2D CrI₃ by electrostatic doping, *Nat. Nanotechnol.* **13**, 549 (2018).
- [3] M. A. McGuire, H. Dixit, V. R. Cooper, and B. C. Sales, Coupling of crystal structure and magnetism in the layered, ferromagnetic insulator CrI₃, *Chem. Mater.* **27**, 612 (2015).
- [4] J. L. Ladno and J. Fernández-Rossier, On the origin of magnetic anisotropy in two dimensional CrI₃, *2D Mater.* **4**, 035002 (2017).
- [5] W.-B. Zhang, Q. Qu, P. Zhu, and C.-H. Lam, Robust intrinsic ferromagnetism and half semiconductivity in stable two-dimensional single-layer chromium trihalides, *J. Mater. Chem. C* **3**, 12457 (2015).
- [6] J. F. Dillon, Jr. and C. E. Olson, Magnetization, resonance, and optical properties of the ferromagnet CrI₃, *J. Appl. Phys.* **36**, 1259 (1965).
- [7] D. T. Larson and E. Kaxiras, Raman Spectrum of CrI₃: An *ab initio* study, *Phys. Rev. B* **98**, 085406 (2018).
- [8] N. Lazarević, M. Abeykoon, P. W. Stephens, H. Lei, E. S. Bozin, C. Petrovic, and Z. V. Popović, Vacancy-induced nanoscale phase separation in K_xFe_{2-y}Se₂ single crystals evidenced by Raman scattering and powder x-ray diffraction, *Phys. Rev. B* **86**, 054503 (2012).
- [9] H. Ryu, M. Abeykoon, K. Wang, H. Lei, N. Lazarevic, J. B. Warren, E. S. Bozin, Z. V. Popovic, and C. Petrovic, Insulating and metallic spin glass in Ni-doped K_xFe_{2-y}Se₂ single crystals, *Phys. Rev. B* **91**, 184503 (2015).
- [10] H. Ryu, K. Wang, M. Opacic, N. Lazarevic, J. B. Warren, Z. V. Popovic, E. S. Bozin, and C. Petrovic, Sustained phase separation and spin glass in Co-doped K_xFe_{2-y}Se₂ single crystals, *Phys. Rev. B* **92**, 174522 (2015).
- [11] Y. Liu and C. Petrovic, Three-dimensional magnetic critical behavior in CrI₃, *Phys. Rev. B* **97**, 014420 (2018).
- [12] P. Giannozzi, S. Baroni, N. Bonini, M. Calandra, R. Car, C. Cavazzoni, D. Ceresoli, G. L. Chiarotti, M. Cococcioni, I. Dabo, A. D. Corso, S. de Gironcoli, S. Fabris, G. Fratesi, R. Gebauer, U. Gerstmann, C. Gougoussis, A. Kokalj, M. Lazzeri, L. Martin-Samos, N. Marzari, F. Mauri, R. Mazzarello, S. Paolini, A. Pasquarello, L. Paulatto, C. Sbraccia, S. Scandolo, G. Sclauzero, A. P. Seitsonen, A. Smogunov, P. Umari, and R. M. Wentzcovitch, Quantum espresso: A modular and open-source software project for quantum simulations of materials, *J. Phys. Condens. Matter* **21**, 395502 (2009).
- [13] J. P. Perdew, K. Burke, and M. Ernzerhof, Generalized Gradient Approximation Made Simple, *Phys. Rev. Lett.* **77**, 3865 (1996).
- [14] P. E. Blöchl, Projector augmented-wave method, *Phys. Rev. B* **50**, 17953 (1994).
- [15] G. Kresse and D. Joubert, From ultrasoft pseudopotentials to the projector augmented-wave method, *Phys. Rev. B* **59**, 1758 (1999).
- [16] S. Grimme, Semiempirical GGA-type density functional constructed with a long-range dispersion correction, *J. Comput. Chem.* **27**, 1787 (2006).
- [17] E. A. Wood, The 80 diperiodic groups in three dimensions, *Bell Syst. Tech. J.* **43**, 541 (1964).
- [18] W. G. Fateley, N. T. McDevitt, and F. F. Bentley, Infrared and raman selection rules for lattice vibrations: The correlation method, *Appl. Spectrosc.* **25**, 155 (1971).
- [19] N. Lazarević, Z. V. Popović, R. Hu, and C. Petrovic, Evidence of coupling between phonons and charge-density waves in ErTe₃, *Phys. Rev. B* **83**, 024302 (2011).
- [20] M. A. McGuire, G. Clark, S. KC, W. M. Chance, G. E. Jellison, V. R. Cooper, X. Xu, and B. C. Sales, Magnetic behavior and spin-lattice coupling in cleavable van der Waals layered CrCl₃ crystals, *Phys. Rev. Mater.* **1**, 014001 (2017).

Lattice dynamics and phase transitions in $\text{Fe}_{3-x}\text{GeTe}_2$

A. Milosavljević,¹ A. Šolajić,¹ S. Djurdjić-Mijin,¹ J. Pešić,¹ B. Višić,¹ Yu Liu (刘育),² C. Petrovic,²
N. Lazarević,¹ and Z. V. Popović^{1,3}

¹Center for Solid State Physics and New Materials, Institute of Physics Belgrade,

University of Belgrade, Pregrevica 118, 11080 Belgrade, Serbia

²Condensed Matter Physics and Materials Science Department, Brookhaven National Laboratory, Upton, New York 11973-5000, USA

³Serbian Academy of Sciences and Arts, Knez Mihailova 35, 11000 Belgrade, Serbia



(Received 23 April 2019; published 17 June 2019)

We present Raman spectroscopy measurements of the van der Waals bonded ferromagnet $\text{Fe}_{3-x}\text{GeTe}_2$, together with lattice dynamics. Four out of eight Raman active modes are observed and assigned, in agreement with numerical calculations. The energies and linewidths of the observed modes display an unconventional temperature dependence at about 150 and 220 K, followed by the nonmonotonic evolution of the Raman continuum. Whereas the former can be related to the magnetic phase transition, the origin of the latter anomaly remains an open question.

DOI: [10.1103/PhysRevB.99.214304](https://doi.org/10.1103/PhysRevB.99.214304)

I. INTRODUCTION

A novel class of magnetism hosting van der Waals bonded materials has recently become of great interest, since the materials are suitable candidates for numbers of technical applications [1–5]. Whereas CrXTe_3 ($X = \text{Si, Ge, Sn}$) and CrX_3 ($X = \text{Cl, Br, I}$) classes maintain low phase transition temperatures [1,6–9] even in a monolayer regime [10], $\text{Fe}_{3-x}\text{GeTe}_2$ has a high bulk transition temperature, between 220 and 230 K [11,12], making it a promising applicant.

The $\text{Fe}_{3-x}\text{GeTe}_2$ crystal structure consists of Fe_{3-x}Ge sublayers stacked between two sheets of Te atoms, and a van der Waals gap between neighboring Te layers [13,14]. Although the structure contains two different types of Fe atoms, it is revealed that vacancies take place only in the Fe2 sites [13,15].

Neutron diffraction, thermodynamic and transport measurements, and Mössbauer spectroscopy were used to analyze the magnetic and functional properties of $\text{Fe}_{3-x}\text{GeTe}_2$, with an Fe atom deficiency of $x \approx 0.1$ and $T_C = 225$ K. It is revealed that at a temperature of 1.5 K, magnetic moments of $1.95(5)\mu_B$ and $1.56(4)\mu_B$ are directed along the easy magnetic c axes [16]. In chemical vapor transport (CVT) grown Fe_3GeTe_2 single crystals, besides the ferromagnetic (FM)-paramagnetic (PM) transition at a temperature of 214 K, FM layers order antiferromagnetically at 152 K [17]. Close to a ferromagnetic transition temperature of 230 K, a possible Kondo lattice behavior, i.e., coupling of traveling electrons and periodically localized spins, is indicated at $T_K = 190 \pm 20$ K, which is in good agreement with theoretical predictions of 222 K [18].

Lattice parameters, as well as the magnetic transition temperature, vary with Fe ion concentration. Lattice parameters a and c follow the opposite trend, whereas the Curie temperature T_C decreases with an increase of Fe ion concentration [15]. For flux-grown crystals, the critical behavior was investigated by bulk dc magnetization around the ferromagnetic phase transition temperature of 152 K [13]. The anomalous Hall effect was also studied, where a significant amount of defects produces bad metallic behavior [19].

Theoretical calculations predict a dynamical stability of Fe_3GeTe_2 single-layer, uniaxial magnetocrystalline anisotropy that originates from spin-orbit coupling [20]. Recently, anomalous Hall effect measurements on single-crystalline metallic Fe_3GeTe_2 nanoflakes with different thicknesses are reported, with a T_C near 200 K and strong perpendicular magnetic anisotropy [21].

We report $\text{Fe}_{3-x}\text{GeTe}_2$ single-crystal lattice dynamic calculations, together with Raman spectroscopy measurements. Four out of eight Raman active modes were observed and assigned. Phonon energies are in a good agreement with theoretical predictions. Analyzed phonon energies and linewidths reveal fingerprint of a ferromagnetic phase transition at a temperature around 150 K. Moreover, discontinuities in the phonon properties are found at temperatures around 220 K. Consistently, in the same temperature range, the Raman continuum displays nonmonotonic behavior.

II. EXPERIMENT AND NUMERICAL METHOD

$\text{Fe}_{3-x}\text{GeTe}_2$ single crystals were grown by the self-flux method as previously described [13]. Samples for scanning electron microscopy (SEM) were cleaved and deposited on graphite tape. Energy dispersive spectroscopy (EDS) maps were collected using a FEI Helios NanoLab 650 instrument equipped with an Oxford Instruments EDS system, equipped with an X-max SSD detector operating at 20 kV. The surface of the as-cleaved $\text{Fe}_{3-x}\text{GeTe}_2$ crystal appears to be uniform for several tens of microns in both directions, as shown in Fig. 4 of Appendix A. Additionally, the elemental composition maps of Fe, Ge, and Te show a distinctive homogeneity of all the three elements (Fig. 5 of Appendix A).

For Raman scattering experiments, a Tri Vista 557 spectrometer was used in the backscattering micro-Raman configuration. As an excitation source, a solid state laser with a 532 nm line was used. In our scattering configuration, the plane of incidence is the ab plane, where $|a| = |b|$ ($\angle(a, b) = 120^\circ$), with the incident (scattered) light propagation direction

TABLE I. Top panel: The type of atoms, Wyckoff positions, each site's contribution to the phonons in the Γ point, and corresponding Raman tensors for the $P6_3/mmc$ space group of $\text{Fe}_{3-x}\text{GeTe}_2$. Bottom panel: Phonon symmetry, calculated optical Raman active phonon frequencies (in cm^{-1}) for the magnetic (M) phase, and experimental values for Raman active phonons at 80 K.

Space group $P6_3/mmc$ (No. 194)		
Fe1 (4e)		$A_{1g} + E_{1g} + E_{2g} + A_{2u} + E_{1u}$
Fe2 (2c)		$E_{2g} + A_{2u} + E_{1u}$
Ge (2d)		$E_{2g} + A_{2u} + E_{1u}$
Te (2c)		$A_{1g} + E_{1g} + E_{2g} + A_{2u} + E_{1u}$
Raman tensors		
$A_{1g} = \begin{pmatrix} a & 0 & 0 \\ 0 & a & 0 \\ 0 & 0 & b \end{pmatrix}$	$E_{1g} = \begin{pmatrix} 0 & 0 & -c \\ 0 & 0 & c \\ -c & c & 0 \end{pmatrix}$	$E_{2g} = \begin{pmatrix} d & -d & 0 \\ -d & -d & 0 \\ 0 & 0 & 0 \end{pmatrix}$
Raman active modes		
Symmetry	Calculations (M)	Experiment (M)
E_{2g}^1	50.2	
E_{1g}^1	70.3	
E_{2g}^2	122.2	89.2
A_{1g}^1	137.2	121.1
E_{1g}^2	209.5	
E_{2g}^3	228.6	214.8
A_{1g}^2	233.4	239.6
E_{2g}^4	334.3	

along the c axes. Samples were cleaved in the air, right before being placed in the vacuum. All the measurements were performed in the high vacuum (10^{-6} mbar) using a KONTI CryoVac continuous helium flow cryostat with a 0.5 mm thick window. To achieve laser beam focusing, a microscope objective with $\times 50$ magnification was used. A Bose factor correction of all spectra was performed. More details can be found in Appendix C.

Density functional theory (DFT) calculations were performed with the QUANTUM ESPRESSO (QE) software package [22]. We used the projector augmented-wave (PAW) pseudopotentials [23,24] with the Perdew-Burke-Ernzerhof (PBE) exchange-correlation functional [25]. The electron wave function and charge density cutoffs of 64 and 782 Ry were chosen, respectively. The k points were sampled using the Monkhorst-Pack scheme, with an $8 \times 8 \times 4$ Γ -centered grid. Both magnetic and nonmagnetic calculations were performed, using the experimentally obtained lattice parameters and the calculated values obtained by relaxing the theoretically proposed structure. In order to obtain the lattice parameters accurately, a treatment of the van der Waals interactions is introduced. The van der Waals interaction was included in all calculations using the Grimme-D2 correction [26]. Phonon frequencies in the Γ point are calculated within the linear response method implemented in QE.

III. RESULTS AND DISCUSSION

$\text{Fe}_{3-x}\text{GeTe}_2$ crystallizes in a hexagonal crystal structure, described with the $P6_3/mmc$ (D_{6h}^4) space group. The atom type, site symmetry, each site's contribution to the phonons

in the Γ point, and corresponding Raman tensors for the $P6_3/mmc$ space group are presented in Table I.

Calculated displacement patterns of Raman active modes, which can be observed in our scattering configuration, are presented in Fig. 1(a). Since the Raman tensor of the E_{1g} mode contains only the z component (Table I), by selection rules, it cannot be detected when measuring from the ab plane in the backscattering configuration. Whereas A_{1g} modes include vibrations of Fe and Te ions along the c axis, E_{2g} modes include in-plane vibrations of all four atoms. The Raman spectra of $\text{Fe}_{3-x}\text{GeTe}_2$ in the magnetic phase (M), at 80 K, and nonmagnetic phase (NM), at 280 K, in a parallel scattering configuration ($\mathbf{e}_i \parallel \mathbf{e}_s$), are presented in Fig. 1 (b). As it can be seen, four peaks at 89.2, 121.1, 214.8, and 239.6 cm^{-1} can be clearly observed at 80 K. According to numerical calculations (see Table I), peaks at 89.2 and 239.6 cm^{-1} correspond to two out of four E_{2g} modes, whereas peaks at 121.1 and 239.6 cm^{-1} can be assigned as two A_{1g} symmetry modes. One should note that numerical calculations performed by using experimentally obtained lattice parameters in the magnetic phase yield a better agreement with experimental values. This is not surprising since the calculations are performed for the stoichiometric compound as opposed to the nonstoichiometry of the sample. Furthermore, it is known that lattice parameters strongly depend on the Fe atom deficiency [15]. All calculated Raman and infrared phonon frequencies, for the magnetic and nonmagnetic phase of $\text{Fe}_{3-x}\text{GeTe}_2$, using relaxed and experimental lattice parameters, together with experimentally observed Raman active modes, are summarized in Table II of Appendix D.

After assigning all observed modes we focused on their temperature evolution. Having in mind finite instrumental

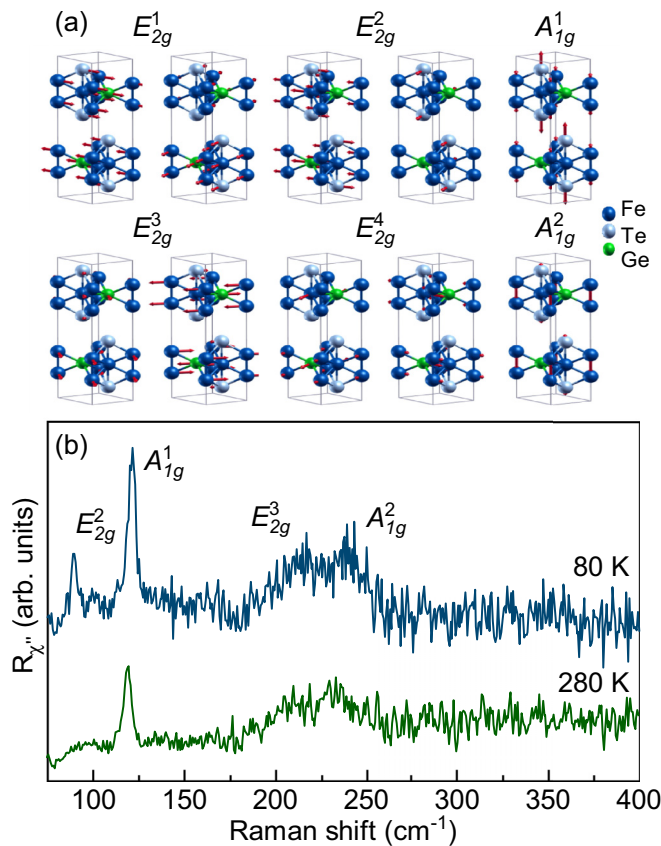


FIG. 1. (a) Displacement patterns of A_{1g} and E_{2g} symmetry modes. (b) Raman spectra of $\text{Fe}_{3-x}\text{GeTe}_2$ single crystal measured at different temperatures in a parallel polarization configuration.

broadening, the Voigt line shape was used for the data analysis [27,28]. The modeling procedure is described in detail in Appendix B and presented in Fig. 6. Figure 2 shows the temperature evolution of the energy and linewidth of the A_{1g}^1 , E_{2g}^3 , and A_{1g}^2 modes between 80 and 300 K. Upon heating the sample, both the energy and linewidth of A_{1g}^1 and A_{1g}^2 symmetry modes exhibit a small but sudden discontinuity at about 150 K [Figs. 2(a) and 2(e)]. An apparent discontinuity in energy of all analyzed Raman modes is again present at temperatures around 220 K. In the same temperature range the linewidths of these Raman modes show a clear deviation from the standard anharmonic behavior [27–31].

Apart from the anomalies in the phonon spectra, a closer inspection of the temperature-dependent Raman spectra measured in the parallel polarization configuration reveals a pronounced evolution of the Raman continuum [Fig. 3(a)]. For the analysis we have used a simple model including a damped Lorentzian and linear term, $\chi''_{\text{cont}} \propto a\Gamma\omega/(\omega^2 + \Gamma^2) + b\omega$ [32], where a , b , and Γ are temperature-dependent parameters. Figure 3(b) summarizes the results of the analysis with the linear term omitted (most likely originating from a luminescence). At approximately the same temperatures, where phonon properties exhibit discontinuities, the continuum temperature dependence manifests nonmonotonic behavior. The maximum positions of the curve were obtained by integrating

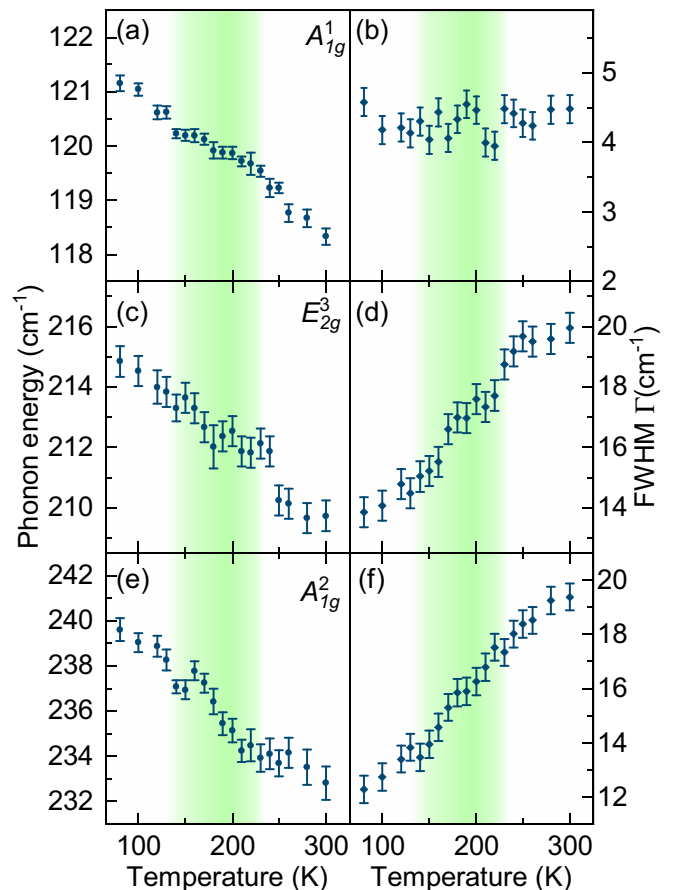


FIG. 2. Energy and linewidth temperature dependence of A_{1g}^1 [(a) and (b)], E_{2g}^3 [(c) and (d)], and A_{1g}^2 [(e) and (f)] phonon modes in $\text{Fe}_{3-x}\text{GeTe}_2$.

those shown in Fig. 3(b). The inset of Fig. 3(b) shows the temperature evolution of their displacements. This analysis confirms the presence of discontinuities in the electronic continuum at temperatures around 150 and 220 K, which leaves a trace in the phonon behavior around these temperatures (Fig. 2). While we do not have evidence for the Kondo effect in the $\text{Fe}_{3-x}\text{GeTe}_2$ crystals we measured, a modification of the electronic background at FM ordering due to localization or the Kondo effect cannot be excluded.

The temperature evolutions of the phonon self-energies and the continuum observed in the Raman spectra of $\text{Fe}_{3-x}\text{GeTe}_2$ suggest the presence of phase transition(s). Magnetization measurements of the samples were performed as described in Ref. [13], revealing a FM-PM transition at 150 K. Thus, the discontinuity in the observed phonon properties around this temperature can be traced back to the weak to moderate spin-phonon coupling. The question remains open regarding the anomaly observed at about 220 K. As previously reported, the Curie temperature of the $\text{Fe}_{3-x}\text{GeTe}_2$ single crystals grown by the CVT method is between 220 and 230 K [11,12,14], varying with the vacancy concentration, i.e., a decrease in the vacancy content will result an increment of T_C [15]. On the other hand, the $\text{Fe}_{3-x}\text{GeTe}_2$ crystals grown by the self-flux method usually have a lower Curie temperature, since the

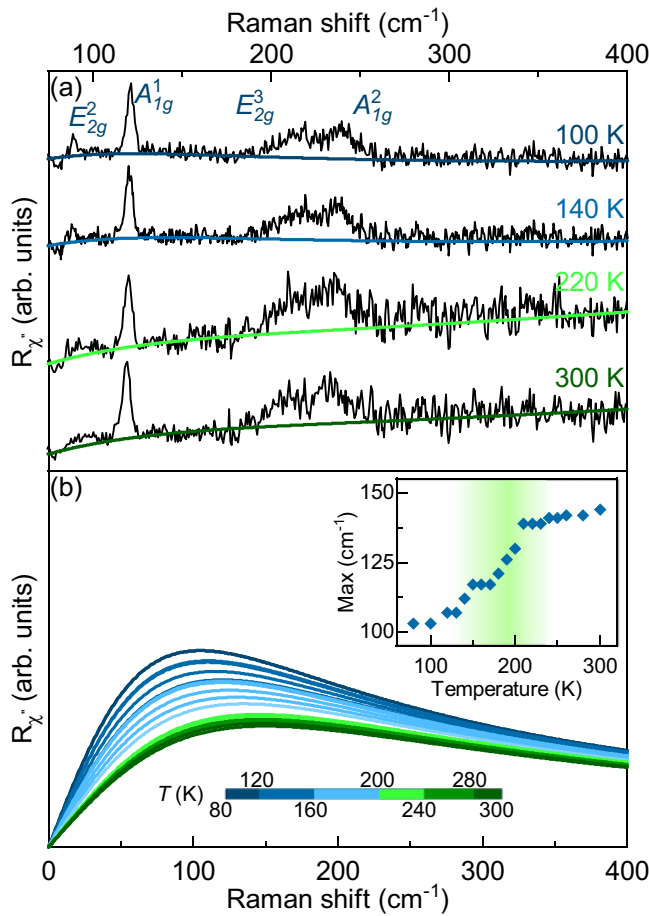


FIG. 3. (a) Raman spectra of $\text{Fe}_{3-x}\text{GeTe}_2$ at four temperatures measured in a parallel polarization configuration. Solid lines represent the theoretical fit to the experimental data. (b) Temperature evolution of the electronic continuum after omitting the linear term. Inset: Displacement of the maximum of fitted curves.

vacancy content is higher [13,15]. Crystals used in the Raman scattering experiment presented here were grown by the self-flux method with a Fe vacancy content of $x \approx 0.36$ [13]. This is in good agreement with our EDS results of $x = 0.4 \pm 0.1$, giving rise to the FM-PM transition at 150 K. Nevertheless,

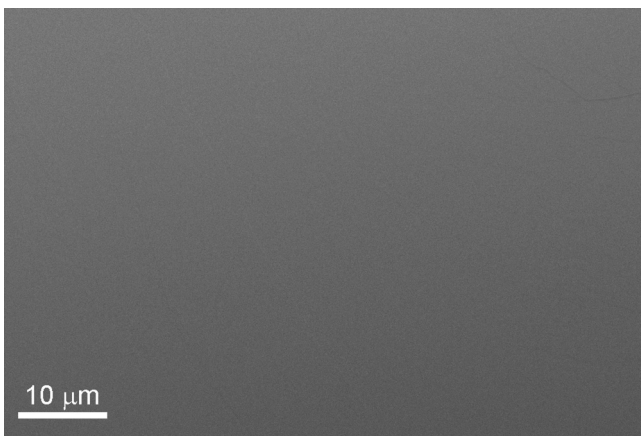


FIG. 4. SEM image of a $\text{Fe}_{3-x}\text{GeTe}_2$ single crystal.

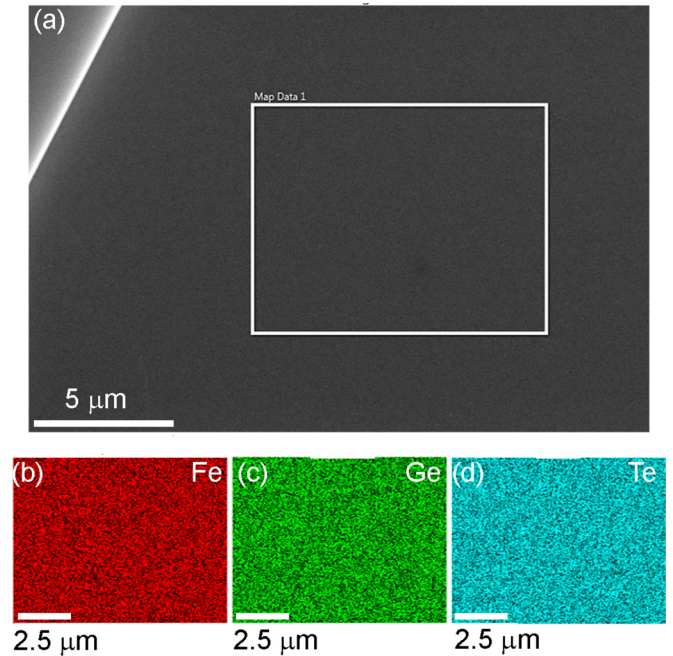


FIG. 5. EDS mapping on a $\text{Fe}_{3-x}\text{GeTe}_2$ single crystal. (a) Secondary electron image of the crystal with the mapping performed within the rectangle. (b)–(d) Associated EDS maps for Fe, Ge, and Te, respectively.

an inhomogeneous distribution of vacancies may result in the formation of vacancy depleted “islands” which in turn would result in an anomaly at 220 K similar to the one observed in our Raman data. However, the EDS data (see Fig. 5) do not support this possibility. At this point we can only speculate that while the long-range order temperature is shifted to a lower temperature by the introduction of vacancies, short-range correlations may develop at 220 K.

IV. CONCLUSION

We have studied the lattice dynamics of flux-grown $\text{Fe}_{3-x}\text{GeTe}_2$ single crystals by means of Raman spectroscopy and DFT. Four out of eight Raman active modes, two A_{1g} and two E_{2g} , have been observed and assigned. DFT calculations are in good agreement with experimental results. The temperature dependence of the A_{1g}^1 , E_{2g}^3 , and A_{1g}^2 mode properties reveals a clear fingerprint of spin-phonon coupling, at a temperature of around 150 K. Furthermore, the anomalous behavior in the energies and linewidths of the observed phonon modes is present in the Raman spectra at temperatures around 220 K with the discontinuity also present in the electronic continuum. Its origin still remains an open question, and requires further analysis.

ACKNOWLEDGMENTS

The work was supported by the Serbian Ministry of Education, Science and Technological Development under Projects No. III45018 and No. OI171005. DFT calculations were performed using computational resources at Johannes Kepler University, Linz, Austria. Materials synthesis was supported

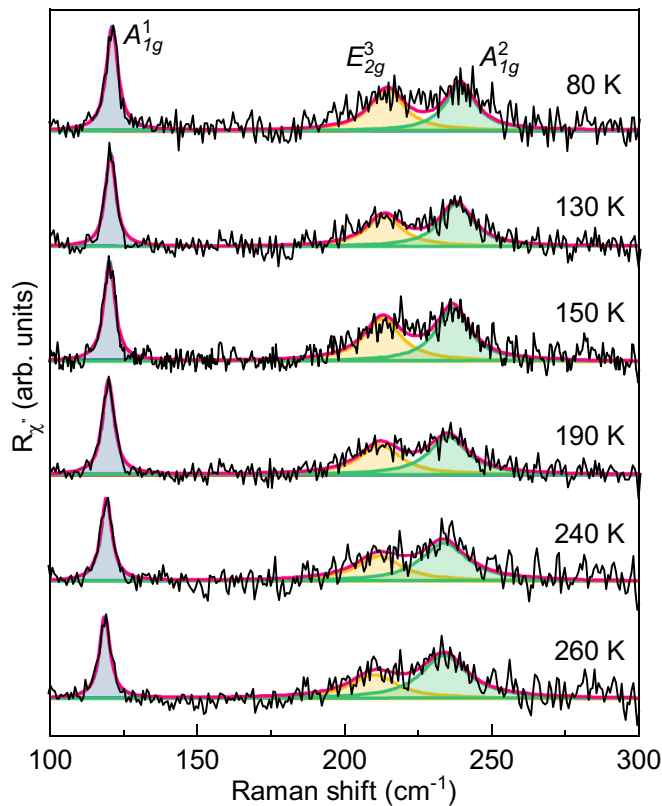


FIG. 6. Modeled Raman spectra of $\text{Fe}_{3-x}\text{GeTe}_2$ single crystal, after subtracting continuum contributions, obtained at various temperatures. For experimental data modeling, the Voigt line shape was used.

by the US Department of Energy, Office of Basic Energy Sciences as part of the Computation Material Science Program (Y.L. and C.P.). Electron microscopy was performed at Jozef Stefan Institute, Ljubljana, Slovenia under Slovenian Research Agency Contract No. P1-0099 (B.V.). This work has received funding from the European Union's Horizon 2020 research and innovation program under the Marie Skłodowska-Curie Grant Agreement No. 645658 (DAFNEOX Project).

APPENDIX A: ELECTRON MICROSCOPY

In order to examine the uniformity of $\text{Fe}_{3-x}\text{GeTe}_2$, Scanning electron microscopy (SEM) was performed on as-cleaved crystals. It can be seen from Fig. 4 that the crystals maintain uniformity for several tens of microns. Furthermore, the elemental composition was obtained using EDS mapping, as shown in Fig. 5. The atomic percentage, averaged over ten measurements, is 47%, 17%, and 36% ($\pm 2\%$) for Fe, Ge, and Te, respectively, with the vacancy content $x = 0.4 \pm 0.1$. The maps associated with the selected elements appear homogeneous, as they are all present uniformly with no apparent islands or vacancies.

APPENDIX B: DATA MODELING

In order to obtain the temperature dependence of the energies and linewidths of the observed $\text{Fe}_{3-x}\text{GeTe}_2$ phonon modes, the Raman continuum, shown in colored lines in

TABLE II. Top panel: Comparison of calculated energies of Raman active phonons using relaxed (R) and experimental [non-relaxed (NR)] lattice parameters for the magnetic (M) and nonmagnetic phase (NM), given in cm^{-1} . Obtained experimental values in the magnetic phase at a temperature of 80 K are given in the last column. Bottom panel: Comparison of calculated energies of infrared optical phonons of $\text{Fe}_{3-x}\text{GeTe}_2$.

Raman active modes					
Sym.	Calculations				Experiment (M)
	NM-R	M-R	NM-NR	M-NR	
E_{2g}^1	28.4	49.6	33.9	50.2	
E_{1g}^1	79.2	70.2	71.7	70.3	
E_{2g}^2	115.5	121.0	100.0	122.2	89.2
A_{1g}^1	151.7	139.2	131.7	137.2	121.1
E_{1g}^2	225.5	206.0	194.3	209.5	
E_{2g}^3	238.0	232.6	204.9	228.6	214.8
A_{1g}^2	272.0	262.6	235.7	233.4	239.6
E_{2g}^4	362.0	337.6	315.4	334.7	
Infrared active modes					
A_{2u}^1	70.7	96.6	73.5	92.7	
E_{1u}^1	112.5	121.2	89.4	121.6	
A_{2u}^2	206.0	162.5	183.1	153.7	
E_{1u}^2	226.4	233.6	192.1	231.3	
A_{2u}^3	271.8	248.6	240.8	241.0	
E_{1u}^3	361.1	336.6	314.7	334.7	

Fig. 3(a), was subtracted for simplicity from the raw Raman susceptibility data (black line). The spectra obtained after the subtraction procedure are presented in Fig. 6 (black line) for various temperatures. Because of the finite resolution of the spectrometer and the fact that line shapes of all the observed phonons are symmetric, the Voigt line shape ($\Gamma_G = 0.8 \text{ cm}^{-1}$) was used for data modeling. Blue, yellow, and green lines in Fig. 6 represent fitting curves for A_{1g}^1 , E_{2g}^3 , and A_{1g}^2 phonon modes, respectively, whereas the overall spectral shape is shown in the red line.

APPENDIX C: EXPERIMENTAL DETAILS

Before being placed in a vacuum and being cleaved, the sample was glued to a copper plate with GE varnish in order to achieve good thermal conductivity and prevent strain effects. Silver paste, as a material with high thermal conductivity, was used to attach the copper plate with the sample to the cryostat. The laser beam spot, focused through an Olympus long-range objective of $\times 50$ magnification, was approximately $6 \mu\text{m}$ in size, with a power less than 1 mW at the sample surface. A TriVista 557 triple spectrometer was used in the subtractive mode, with a diffraction grating combination of 1800/1800/2400 grooves/mm and the entrance and second intermediate slit set to $80 \mu\text{m}$, in order to enhance stray light rejection and attain good resolution.

APPENDIX D: CALCULATIONS

In Table II the results of DFT calculations are presented for magnetic (M) and nonmagnetic (NM) relaxed and experimental lattice parameters. For comparison, the

experimental results are shown in the last column. Since the lattice parameters strongly depend on the Fe atom deficiency, the best agreement with experimental results gives the magnetic nonrelaxed solution.

- [1] N. Sivadas, M. W. Daniels, R. H. Swendsen, S. Okamoto, and D. Xiao, Magnetic ground state of semiconducting transition-metal trichalcogenide monolayers, *Phys. Rev. B* **91**, 235425 (2015).
- [2] K. S. Novoselov, A. K. Geim, S. V. Morozov, D. Jiang, Y. Zhang, S. V. Dubonos, I. V. Grigorieva, and A. A. Firsov, Electric field effect in atomically thin carbon films, *Science* **306**, 666 (2004).
- [3] Q. H. Wang, K. Kalantar-Zadeh, A. Kis, J. N. Coleman, and M. S. Strano, Electronics and optoelectronics of two-dimensional transition metal dichalcogenides, *Nat. Nanotechnol.* **7**, 699 (2012).
- [4] C. Gong, L. Li, Z. Li, H. Ji, A. Stern, Y. Xia, T. Cao, W. Bao, C. Wang, Y. Wang, Z. Q. Qiu, R. J. Cava, S. G. Louie, J. Xia, and X. Zhang, Discovery of intrinsic ferromagnetism in two-dimensional van der Waals crystals, *Nature (London)* **546**, 265 (2017).
- [5] B. Huang, G. Clark, E. Navarro-Moratalla, D. R. Klein, R. Cheng, K. L. Seyler, D. Zhong, E. Schmidgall, M. A. McGuire, D. H. Cobden, W. Yao, D. Xiao, P. Jarillo-Herrero, and X. Xu, Layer-dependent ferromagnetism in a van der Waals crystal down to the monolayer limit, *Nature (London)* **546**, 270 (2017).
- [6] M. A. McGuire, H. Dixit, V. R. Cooper, and B. C. Sales, Coupling of crystal structure and magnetism in the layered, ferromagnetic insulator CrI₃, *Chem. Mater.* **27**, 612 (2015).
- [7] H. L. Zhuang, Y. Xie, P. R. C. Kent, and P. Ganesh, Computational discovery of ferromagnetic semiconducting single-layer CrSnTe₃, *Phys. Rev. B* **92**, 035407 (2015).
- [8] G. T. Lin, H. L. Zhuang, X. Luo, B. J. Liu, F. C. Chen, J. Yan, Y. Sun, J. Zhou, W. J. Lu, P. Tong, Z. G. Sheng, Z. Qu, W. H. Song, X. B. Zhu, and Y. P. Sun, Tricritical behavior of the two-dimensional intrinsically ferromagnetic semiconductor CrGeTe₃, *Phys. Rev. B* **95**, 245212 (2017).
- [9] L. D. Casto, A. J. Clune, M. O. Yokosuk, J. L. Musfeldt, T. J. Williams, H. L. Zhuang, M.-W. Lin, K. Xiao, R. G. Hennig, B. C. Sales, J.-Q. Yan, and D. Mandrus, Strong spin-lattice coupling in CrSiTe₃, *APL Mater.* **3**, 041515 (2015).
- [10] M.-W. Lin, H. L. Zhuang, J. Yan, T. Z. Ward, A. A. Puretzyk, C. M. Rouleau, Z. Gai, L. Liang, V. Meunier, B. G. Sumpter, P. Ganesh, P. R. C. Kent, D. B. Geohegan, D. G. Mandrus, and K. Xiao, Ultrathin nanosheets of CrSiTe₃: A semiconducting two-dimensional ferromagnetic material, *J. Mater. Chem. C* **4**, 315 (2016).
- [11] J.-X. Zhu, M. Janoschek, D. S. Chaves, J. C. Cezar, T. Durakiewicz, F. Ronning, Y. Sassa, M. Mansson, B. L. Scott, N. Wakeham, E. D. Bauer, and J. D. Thompson, Electronic correlation and magnetism in the ferromagnetic metal Fe₃GeTe₂, *Phys. Rev. B* **93**, 144404 (2016).
- [12] B. Chen, J. H. Yang, H. D. Wang, M. Imai, H. Ohta, C. Michioka, K. Yoshimura, and M. H. Fang, Magnetic properties of layered itinerant electron ferromagnet Fe₃GeTe₂, *J. Phys. Soc. Jpn.* **82**, 124711 (2013).
- [13] Y. Liu, V. N. Ivanovski, and C. Petrovic, Critical behavior of the van der Waals bonded ferromagnet Fe_{3-x}GeTe₂, *Phys. Rev. B* **96**, 144429 (2017).
- [14] H.-J. Deiseroth, K. Aleksandrov, C. Reiner, L. Kienle, and R. K. Kremer, Fe₃GeTe₂ and Ni₃GeTe₂ - Two new layered transition-metal compounds: Crystal structures, HRTEM investigations, and magnetic and electrical properties, *Eur. J. Inorg. Chem.* **2006**, 1561 (2006).
- [15] A. F. May, S. Calder, C. Cantoni, H. Cao, and M. A. McGuire, Magnetic structure and phase stability of the van der Waals bonded ferromagnet Fe_{3-x}GeTe₂, *Phys. Rev. B* **93**, 014411 (2016).
- [16] V. Yu. Verchenko, A. A. Tsirlin, A. V. Sobolev, I. A. Presniakov, and A. V. Shevelkov, Ferromagnetic order, strong magnetocrystalline anisotropy, and magnetocaloric effect in the layered telluride Fe_{3-δ}GeTe₂, *Inorg. Chem.* **54**, 8598 (2015).
- [17] J. Yi, H. Zhuang, Q. Zou, Z. Wu, G. Cao, S. Tang, S. A. Calder, P. R. C. Kent, D. Mandrus, and Z. Gai, Competing antiferromagnetism in a quasi-2D itinerant ferromagnet: Fe₃GeTe₂, *2D Mater.* **4**, 011005 (2016).
- [18] Y. Zhang, H. Lu, X. Zhu, S. Tan, W. Feng, Q. Liu, W. Zhang, Q. Chen, Y. Liu, X. Luo, D. Xie, L. Luo, Z. Zhang, and X. Lai, Emergence of Kondo lattice behavior in a van der Waals itinerant ferromagnet, Fe₃GeTe₂, *Sci. Adv.* **4**, eaao6791 (2018).
- [19] Y. Liu, E. Stavitski, K. Attenkofer, and C. Petrovic, Anomalous Hall effect in the van der Waals bonded ferromagnet Fe_{3-x}GeTe₂, *Phys. Rev. B* **97**, 165415 (2018).
- [20] H. L. Zhuang, P. R. C. Kent, and R. G. Hennig, Strong anisotropy and magnetostriction in the two-dimensional Stoner ferromagnet Fe₃GeTe₂, *Phys. Rev. B* **93**, 134407 (2016).
- [21] C. Tan, J. Lee, S.-G. Jung, T. Park, S. Albarakati, J. Partridge, M. R. Field, D. G. McCulloch, L. Wang, and C. Lee, Hard magnetic properties in nanoflake van der Waals Fe₃GeTe₂, *Nat. Commun.* **9**, 1554 (2018).
- [22] P. Giannozzi *et al.*, QUANTUM ESPRESSO: A modular and open-source software project for quantum simulations of materials, *J. Phys.: Condens. Matter* **21**, 395502 (2009).
- [23] P. E. Blöchl, Projector augmented-wave method, *Phys. Rev. B* **50**, 17953 (1994).
- [24] G. Kresse and D. Joubert, From ultrasoft pseudopotentials to the projector augmented-wave method, *Phys. Rev. B* **59**, 1758 (1999).
- [25] J. P. Perdew, K. Burke, and M. Ernzerhof, Generalized Gradient Approximation Made Simple, *Phys. Rev. Lett.* **77**, 3865 (1996).
- [26] S. Grimme, Semiempirical GGA-type density functional constructed with a long-range dispersion correction, *J. Comput. Chem.* **27**, 1787 (2006).
- [27] A. Milosavljević, A. Šolajić, J. Pešić, Y. Liu, C. Petrovic, N. Lazarević, and Z. V. Popović, Evidence of spin-phonon coupling in CrSiTe₃, *Phys. Rev. B* **98**, 104306 (2018).
- [28] A. Baum, A. Milosavljević, N. Lazarević, M. M. Radonjić, B. Nikolić, M. Mitschek, Z. I. Maranloo, M. Šćepanović, M. Grujić-Brojčin, N. Stojilović, M. Opel, A. Wang,

- C. Petrovic, Z. V. Popović, and R. Hackl, Phonon anomalies in FeS, *Phys. Rev. B* **97**, 054306 (2018).
- [29] M. Opačić, N. Lazarević, M. M. Radonjić, M. Šćepanović, H. Ryu, A. Wang, D. Tanasković, C. Petrovic, and Z. V. Popović, Raman spectroscopy of $K_xK_{2-y}Se_2$ single crystals near the ferromagnet–paramagnet transition, *J. Phys.: Condens. Matter* **28**, 485401 (2016).
- [30] Z. V. Popović, N. Lazarević, S. Bogdanović, M. M. Radonjić, D. Tanasković, R. Hu, H. Lei, and C. Petrovic, Signatures of the spin-phonon coupling in $Fe_{1+y}Te_{1-x}Se_x$ alloys, *Solid State Commun.* **193**, 51 (2014).
- [31] Z. V. Popović, M. Šćepanović, N. Lazarević, M. Opačić, M. M. Radonjić, D. Tanasković, H. Lei, and C. Petrovic, Lattice dynamics of $BaFe_2X_3$ ($X = S, Se$) compounds, *Phys. Rev. B* **91**, 064303 (2015).
- [32] T. P. Devereaux and R. Hackl, Inelastic light scattering from correlated electrons, *Rev. Mod. Phys.* **79**, 175 (2007).



Ab-initio calculations of electronic and vibrational properties of Sr and Yb intercalated graphene

Andrijana Šolajić¹ · Jelena Pešić¹ · Radoš Gajić¹

Received: 14 October 2017 / Accepted: 14 June 2018
© Springer Science+Business Media, LLC, part of Springer Nature 2018

Abstract

Since the 1960s, Graphite intercalation compounds (GIC) have been extensively studied, showing many new properties and exotic physics. This inspired many to investigate a single or few-layer intercalated graphene. Intercalated graphene has many extraordinary properties and it is different compared to pristine graphene or bulk GICs, with great spectra of characteristics induced by various intercalants. This method opens new possibilities for research and applications in electronics and photonics. Here we present the results of a DFT study on electronic and vibrational properties of the graphene doped with Sr and Yb adatoms, taking into account that only their corresponding bulk compounds have been investigated so far. The calculations were performed in Quantum Espresso software package.

Keywords Graphene · DFT · Electronic properties · 2D materials

1 Introduction

Since the experimental discovery in Novoselov et al. (2004), graphene has been attracting enormous attention. The relativistic behaviour of the low-energy excitations (the so-called *Dirac fermions*) leads to many interesting effects and the linear electronic dispersion of graphene in the vicinity of the K-point mimics the physics of the massless fermions in quantum electrodynamics, at speed 300 times smaller than the speed of light. Therefore, many unusual properties can be observed in graphene, such are the Klein paradox (Katsnelson et al. 2006) or the anomalous integer quantum Hall effect (Gusynin and Sharapov 2005; Neto et al. 2006) which can be observed at room temperatures (Novoselov et al. 2007).

This article is part of the Topical Collection on Focus on Optics and Bio-photonics, Photonica 2017.

Guest Edited by Jelena Radovanovic, Aleksandar Krmpot, Marina Lekic, Trevor Benson, Mauro Pereira, Marian Marciniak.

✉ Andrijana Šolajić
solajic@ipb.ac.rs

¹ Laboratory for Graphene, Other 2D Materials and Ordered Nanostructures, Center for Solid State Physics and New Materials, Institute of Physics Belgrade, University of Belgrade, Pregrevica 118, Belgrade 11080, Serbia

Graphene has excellent thermal conductivity, high electron mobility (Bolotin et al. 2008) and transparency, and at the same time it is one of the strongest materials known (Lee et al. 2008), about 200 times stronger than structural steel, yet very flexible and stretchable. With all its unique properties, graphene has various potential applications in almost all research fields, especially in electronics and optoelectronics (Ferrari 2015; Blake et al. 2008; Todorović et al. 2015). With high electrical and optical conductivity, it is promising candidate for applications in energy storage (Bonaccorso et al. 2015), detectors (Sassi et al. 2017; Liu et al. 2014), or even for the flexible touch screen technology (Ahn and Hong 2014; Bae et al. 2010). Ultra-thin graphitic films are also well researched for applications in photonics with high transparency and electrical conductivity (Matković et al. 2016).

Already extraordinary characteristics of graphene can be tailored and enhanced in many ways—by various types of disorders, controlling the type of edges (Peres et al. 2006; Wakabayashi et al. 1996, 2009), number of layers, by doping, applying the strain (Levy et al. 2010; Choi et al. 2010; Settnes et al. 2016; Masir et al. 2013), etc. Among them, doping graphene is an excellent way to make graphene suitable for various applications (Sharma and Ahn 2013; Wang et al. 2010; Qu et al. 2010; Jeong et al. 2011; Cui et al. 2011). Especially interesting is intercalation of various species in a few layer graphene (or doping a single layer graphene with adatoms), in a similar manner to the graphite intercalation compounds (GIC). This provides very high level of doping and leads to many interesting effects that are not present in pristine graphene, offering a new way to design various materials with magnetic, highly conductive or superconducting properties. Doping via adsorption is also very convenient, as the graphene can host various adatoms or small molecules while preserving its own structure, and at the same time drastically change its electronic properties. By covering the graphene sheet with the layer of adatoms, significant structural changes are avoided, as the dopant atoms are not fitted in the graphene lattice instead of the carbon atoms. However, adsorbed atoms can strongly affect the electronic properties of graphene, dominantly through the p_z orbitals. Therefore, it is an excellent tool for tuning the properties of graphene in a wide range and obtain new effects. GIC have been extensively researched since the 1960s (Rüdrorf 1959; Enoki et al. 2003; Dresselhaus and Dresselhaus 2002), but the interest for them has significantly raised with discovery of the superconductivity in some of the alkali or alkaline earth metal intercalated graphite structures, among which are CaC_6 and YbC_6 (Weller et al. 2005) with relatively high critical temperatures of $T_c = 11.5$ K and $T_c = 6.5$ K. As research of 2D materials has raised in the last decade, the superconductivity in GIC imposed a question of investigating the monolayer graphene doped with alkali and alkaline earth metal adatoms, searching for the atomically thin superconductors. The electrical characteristics of the doped graphene depend strongly on the species of the used adatom. Reports on related structures suggest the occurrence of superconductivity in some of them, usually with alkali or alkaline earth metals doping, similar to the GICs. The explanation for the emergence of the superconductivity in the alkali doped graphene lies in the electron-phonon coupling that arises from the new intercalant-derived band and the graphene π -bands at the Fermi level. Among first researched doped graphene structures was Li decorated graphene (Profeta et al. 2012; Pešić et al. 2015), which is superconducting with the critical temperature of $T = 5.9$ K. It can also be enhanced by applying the strain (Pešić et al. 2014). The experimental evidence of superconductivity in the Li doped graphene (Ludbrook 2015) inspired many to search for other 2D superconducting structures (Calandra et al. 2012; Penev et al. 2016; Shimada et al. 2017; Saito et al. 2016). Graphene doped with the Ca atoms is also reported to be superconducting as the doped monolayer (Profeta et al. 2012) and bilayer intercalated graphene (Mazin and Balatsky 2010; Margine et al. 2016), there are also reports for a

few-layer potassium doped graphene (Xue et al. 2012). Among other similar structures, the heavily n-doped graphene was also predicted to be superconducting (Margine and Giustino 2014), the combination of biaxial strain with charge doping, which leads to the superconductor with T_c estimated to be up to 30 K (Si et al. 2013), or the hole-doped graphene which was predicted to be a high T_c superconductor, with a critical temperature in range 60–80 K (Durajski 2015). However, many possible structures based on doped graphene with potential superconducting properties are not considered yet.

In this paper we studied the electronic and vibrational properties of Sr and Yb doped graphene using the density functional theory approach. We were motivated by the fact that both structures are known as superconductors in their corresponding bulk compounds, YbC_6 with critical temperature of $T_c = 6.5$ K (Weller et al. 2005) and SrC_6 with up to $T_c = 3.03$ K (Calandra and Mauri 2006). We are first to report the results for a monolayer graphene doped with those adatoms.

2 Computational details

All calculations were performed using the Quantum Espresso software package (Giannozzi et al. 2009), based on the plane waves and pseudopotentials. We used norm-conserving pseudopotentials (Perdew and Zunger 1981) and LDA exchange-correlation functional. The plane wave energy cutoff is 120 Ry for SrC_6 -mono and 160 Ry for YbC_6 -mono. The unit cell for both structures is modelled as $\sqrt{3} \times \sqrt{3}R30^\circ$ supercell of the graphene unit cell, with adatoms positioned in the H-site. This is the favorable adsorption site for both adatoms, according to the DFT study (Nakada and Ishii 2011). The value of the hexagonal cell parameter a is 4.26\AA taken theoretically, as there are no experimental realization of those structures. The top and side view of the structures are shown in Fig. 1. In order to avoid interactions between layers, the hexagonal cell parameter c of the unit cell was chosen to be sufficiently large, $c = 11.4\text{\AA}$ for SrC_6 -mono and 11.3\AA for YbC_6 -mono. Prior to any calculations, the ionic positions in systems are fully relaxed to their minimum energy configuration, using the Broyden-Fletcher-Goldfarb-Shanno (BFGS) algorithm. Obtained vertical distance between graphene layer and the adsorbed atom is $h = 2.22\text{\AA}$ for SrC_6 -mono and $h = 2.25\text{\AA}$ for YbC_6 -mono. Phonon properties are obtained with the Density

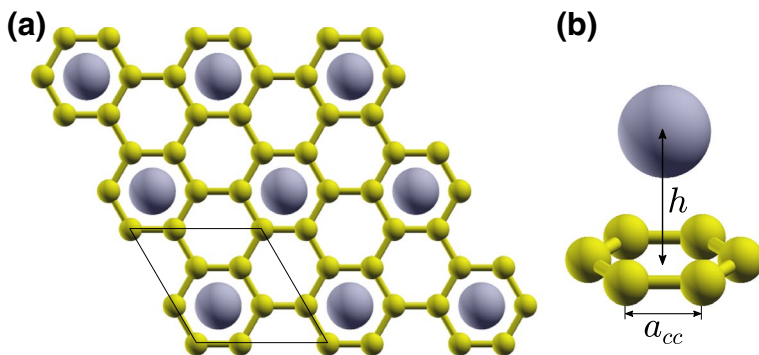


Fig. 1 **a** Top view of the graphene structure with the adatoms adsorbed in the H-site. Unit cell is marked with the black line, **b** side view of the one hexagon with the adatom above

Functional Perturbation Theory (DFPT) implemented in the PHonon part of the Quantum Espresso software.

3 Results and discussion

As we said in Sect. 2, the unit cell for our H-site doped structures is enlarged compared to the pristine graphene. Due to the increase in the size of the primitive cell in direct space, basis vector lengths in reciprocal space are reduced. As a consequence, the K-point of the Brillouin zone of graphene is folded to the Γ point of the Brillouin zone of H-site doped graphene. Brillouin zones of the graphene unit cell and the H-site doped graphene are shown in Fig. 2.

3.1 Electronic properties

Electronic dispersions along Γ -M-K- Γ high symmetry points for SrC₆-mono and YbC₆-mono are shown in Fig. 3. Fermi level is set to zero in all figures. Folding the π and π^* bands of graphene from K-point to Γ -point, the inner and outer carbon π and π^* bands are obtained, crossing at the Γ point. For both structures, lower bands from the σ bonds in the valence band are almost unaffected, as expected, and they are not shown in figures. The Fermi level is shifted up in both structures. By deposition of adatoms on top of graphene, new interlayer band derived from the Yb or Sr adatoms is formed around the Fermi level, showing a nearly free-electron-like dispersion. They are placed at 2.2 and 1.5 eV below the Fermi level in the YbC₆-mono and SrC₆-mono, respectively, being partially occupied. The density of states on Fermi level is also raised. The carbon π bands are not affected by the presence of the adatoms. Previously unoccupied π^* bands now intersect the new up-shifted Fermi level and are strongly hybridized with the new band derived from the adsorbed atoms. In YbC₆-mono, 4*f* orbitals coming from the Yb atoms form a set of flat non-dispersive bands, similar to the bulk YbC₆ (Csányi et al. 2005). Those flat bands are characteristic for most lanthanides. They are localized at 0.7 eV below the Fermi level with the corresponding peak clearly observed in the density of states. As reported for the bulk YbC₆, calculations with the Hubbard+U corrections do not give significant changes and result only in slightly shifting down those bands, so the same is expected for the monolayer. The Dirac points from graphene are folded to the Γ point in the H-site doped graphene, and

Fig. 2 Brillouin zones of graphene (black) and the H-site doped graphene (red). (Color figure online)

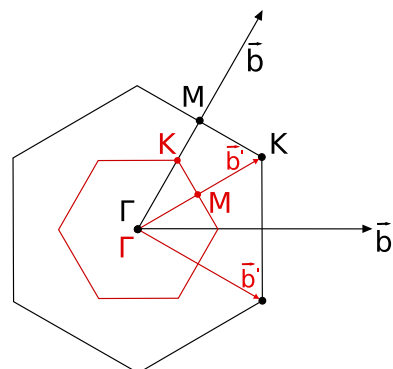
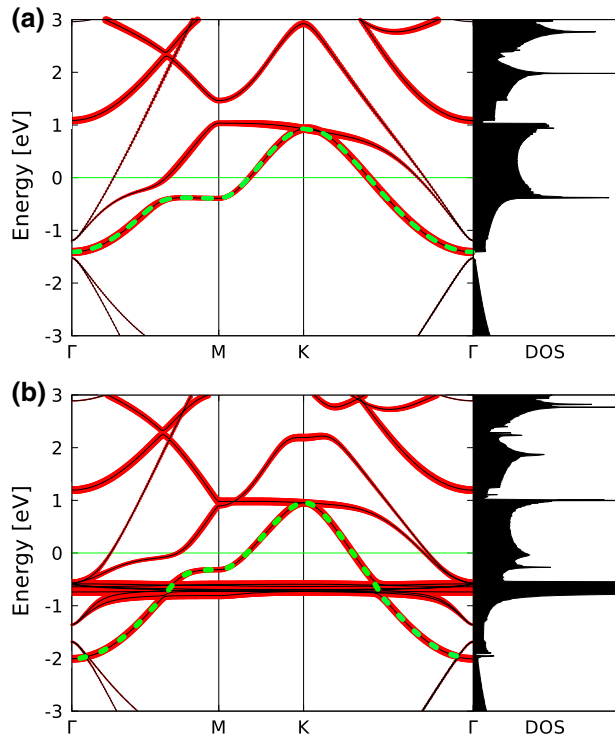


Fig. 3 Electronic dispersions of **a** SrC₆-mono and **b** YbC₆-mono. Thickness of the red lines is proportional to the Sr/Yb character and the interlayer band is marked in green dotted line. (Color figure online)



they are now below the Fermi level. Due to the adatom presence, the symmetry is broken and a gap is opened. In the SrC₆, interlayer band is placed between the π and π^* and a very small gap can be observed in the density of states, while in the YbC₆-mono, the new interlayer band intersect the π band and the gap is closed.

3.2 Phonon properties

The symmetry group of graphene with adatoms adsorbed in the H-site is $Dg77 = T' C_{6v}$, which is a subgroup of the diperiodic group of graphene, $Dg80 = TD_{6h}$ (Damljanović et al. 2014). In order to connect the phonon modes of the H-site doped graphene with the corresponding phonon modes of graphene, the corresponding irreducible representation of group $Dg77$ of graphene to its subgroup $Dg80$ (Damljanović et al. 2014). The modes from the Γ point, ΓE_{2g} and ΓB_{1g} correspond to ΓE_2 and ΓB_1 . For the modes of graphene in the K point, KA'_1 corresponds to the modes A_1 and B_2 , KA'_2 to A_2 and B_1 , KE' and KE'' to E_1 and E_2 (Altmann and Herzig 1994; Damljanović and Gajić 2012). The modes A_1 and E_1 are both infrared and Raman active, while E_2 modes are only Raman active. The symmetry classification of optical modes and Raman tensors for H-site doped graphene are given in Table 1. The displacement patterns of the SrC₆-mono and YbC₆-mono, in the Γ point are shown in Fig. 4. Those modes have displacement patterns similar to those of graphene phonons at Γ and K points, which happens due to the Brillouin zone folding. As the K point of graphene is folded to the Γ point of the new Brillouin zone in the H-site doped graphene, the phonon modes in graphene at the Γ and K points correspond to the Γ modes in the H-site doped

Table 1 Raman tensors and symmetry classification of optical modes

Raman tensors			
Graphene	A_{1g}	E_{1g}	E_{2g}
$Dg80 = TD_{6h}$	$\begin{pmatrix} a & 0 & 0 \\ 0 & a & 0 \\ 0 & 0 & b \end{pmatrix}$	$\begin{pmatrix} 0 & 0 & 0 \\ 0 & 0 & c \\ 0 & c & 0 \end{pmatrix}$	$\begin{pmatrix} 0 & 0 & -c \\ 0 & 0 & 0 \\ c & 0 & 0 \end{pmatrix}$
$O_z \parallel C_6$		$\begin{pmatrix} 0 & 0 & -c \\ 0 & 0 & 0 \\ c & 0 & 0 \end{pmatrix}$	$\begin{pmatrix} d & 0 & 0 \\ 0 & -d & 0 \\ 0 & 0 & 0 \end{pmatrix}$
$O_x \parallel C_2$			$\begin{pmatrix} 0 & -d & 0 \\ -d & 0 & 0 \\ 0 & 0 & 0 \end{pmatrix}$
$A\alpha$	A_1	E_1	E_2
$Dg77 = TC_{6v}$	$\begin{pmatrix} a & 0 & 0 \\ 0 & a & 0 \\ 0 & 0 & b \end{pmatrix}$	$\begin{pmatrix} 0 & 0 & c \\ 0 & 0 & 0 \\ c & 0 & 0 \end{pmatrix}$	$\begin{pmatrix} 0 & 0 & 0 \\ 0 & -d & 0 \\ 0 & 0 & 0 \end{pmatrix}$
$O_z \parallel C_6$		$\begin{pmatrix} 0 & 0 & c \\ 0 & 0 & 0 \\ c & 0 & 0 \end{pmatrix}$	$\begin{pmatrix} 0 & -d & 0 \\ -d & 0 & 0 \\ 0 & 0 & 0 \end{pmatrix}$
$O_x \parallel \sigma_v$			$\begin{pmatrix} 0 & -d & 0 \\ -d & 0 & 0 \\ 0 & 0 & 0 \end{pmatrix}$
Optical modes			
$A\alpha$	$\Gamma_{\text{opt}} = 2A_1 + A_2 + 2B_1 + B_2 + 3E_1 + 3E_2$		

structures. This is valid for all H-site doped graphene structures as the unit cell is the type. As the Kohn anomaly is present in graphene at Γ and K points in E_{2g} and KA'_1 modes, we expect it to be present in the H-site doped graphene structures for the modes related to these two. Modes with Kohn anomaly can not be calculated precisely using the density functional theory as the DFT is based on the adiabatic Born-Oppenheimer approximation which is in this case broken. Comparing the calculated phonon modes for graphene at K and Γ point, with the corresponding phonon modes at the Γ point of the SrC_6 and YbC_6 monolayers, we can observe small differences in the corresponding frequencies. Some of these are lower than in pristine graphene and some frequencies are split. For example, frequencies of E_2 mode in Sr and Yb doped graphene are 1470 cm^{-1} and 1488 cm^{-1} , respectively, while the frequency of E_{2g} in pristine graphene is 1550 cm^{-1} ; Frequency of E' mode in graphene is 1200 cm^{-1} , and corresponding modes in doped graphene are E_2 at 1180 cm^{-1} and E_1 at 1200 cm^{-1} ; E'' mode in graphene is at 580 cm^{-1} , and corresponding modes in doped graphene are E_2 at 495 cm^{-1} and E_1 at 510 cm^{-1} for SrC_6 -mono and E_2 at 477 cm^{-1} and E_1 at 500 cm^{-1} for YbC_6 -mono. This can be ascribed to the adatoms impact, and in general, it depends on the type of the adatom.

4 Conclusion

Using the density functional theory approach, we calculated the electronic and phonon properties of the Sr and Yb doped graphene, in a similar manner to the GICs. Their corresponding bulk compounds have been studied so far and we are first to investigate the monolayer graphene doped with those adatoms. The electronic and phonon properties are of essential interest for electron-phonon coupling as well as the guidelines for experimental research. From the electronic band structure calculations, we can observe a new adatom-derived interlayer band crossing the Fermi level in both structures, which hybridize strongly with the carbon p_z orbitals. Density of states on the Fermi level is also raised. Those results can be indicating a possible superconductivity and can be inspiring for further research of those structures. Displacement patterns calculated in the Γ point are similar to those in the K and Γ point of the pristine graphene, as a consequence of the zone folding effect, but due to the adatoms impact we can observe some differences in frequencies and the splitting of

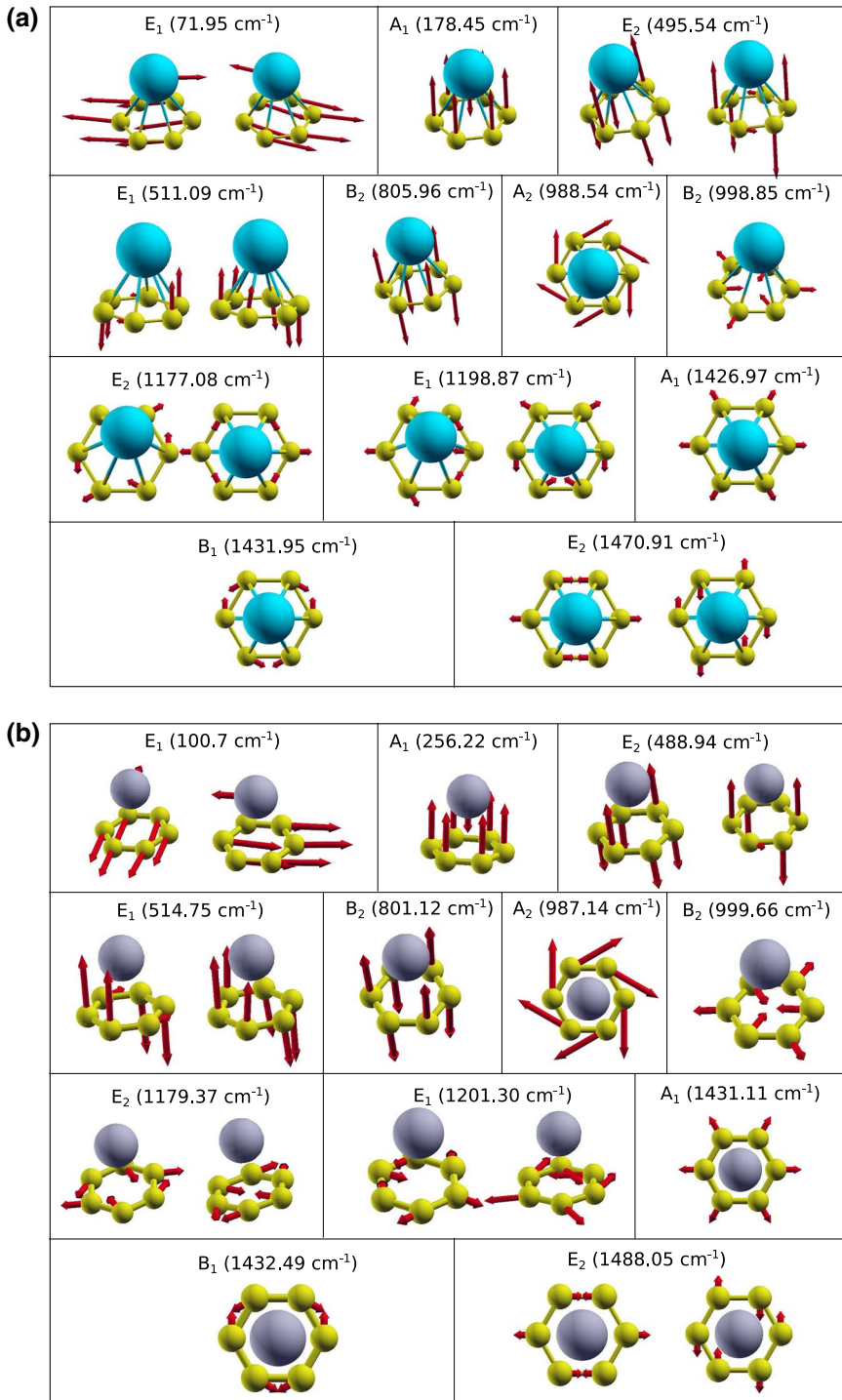


Fig. 4 Displacement patterns of **a** SrC₆-mono and **b** YbC₆-mono. Acoustic modes ($\omega = 0$) are not shown in pictures

some modes. The results obtained in this paper are important base for further theoretical and experimental research of those two structures, as well for future research of similar structures of graphene doped with other metal adatoms.

Acknowledgements This work is supported by the Serbian MPNTR through Project OI 171005 and by Qatar National Research Foundation through Project NPRP 7-665-1-12.

References

- Ahn, J.H., Hong, B.H.: Graphene for displays that bend. *Nat. Nanotechnol.* **9**(10), 737–738 (2014)
- Altmann, S., Herzog, P.: *Point-Group Theory Tables*. Oxford Science Publications, Clarendon Press, Oxford (1994)
- Bae, S., Kim, H., Lee, Y., Xu, X., Park, J.S., Zheng, Y., Balakrishnan, J., Lei, T., Kim, H.R., Song, Y.I., et al.: Roll-to-roll production of 30-inch graphene films for transparent electrodes. *Nat. Nanotechnol.* **5**(8), 574–578 (2010)
- Blake, P., Brimicombe, P.D., Nair, R.R., Booth, T.J., Jiang, D., Schedin, F., Ponomarenko, L.A., Morozov, S.V., Gleeson, H.F., Hill, E.W., Geim, A.K., Novoselov, K.S.: Graphene-based liquid crystal device. *Nano Lett.* **8**(6), 1704–1708 (2008)
- Bolotin, K., Sikes, K., Jiang, Z., Klima, M., Fudenberg, G., Hone, J., Kim, P., Stormer, H.: Ultrahigh electron mobility in suspended graphene. *Solid State Commun.* **146**(9), 351–355 (2008)
- Bonaccorso, F., Colombo, L., Yu, G., Stoller, M., Tozzini, V., Ferrari, A.C., Ruoff, R.S., Pellegrini, V.: Graphene, related two-dimensional crystals, and hybrid systems for energy conversion and storage. *Science* **347**(6217), 1246501 (2015)
- Calandra, M., Mauri, F.: Possibility of superconductivity in graphite intercalated with alkaline earths investigated with density functional theory. *Phys. Rev. B* **74**, 094507 (2006)
- Calandra, M., Profeta, G., Mauri, F.: Superconductivity in metal-coated graphene. *Physica Status Solidi (B)* **249**(12), 2544–2548 (2012)
- Choi, S.M., Jhi, S.H., Son, Y.W.: Effects of strain on electronic properties of graphene. *Phys. Rev. B* **81**, 081407 (2010)
- Csányi, G., Littlewood, P., Nevidomskyy, A.H., Pickard, C.J., Simons, B.: The role of the interlayer state in the electronic structure of superconducting graphite intercalated compounds. *Nat. Phys.* **1**(1), 42–45 (2005)
- Cui, T., Lv, R., Huang, Z.H., Zhu, H., Zhang, J., Li, Z., Jia, Y., Kang, F., Wang, K., Wu, D.: Synthesis of nitrogen-doped carbon thin films and their applications in solar cells. *Carbon* **49**(15), 5022–5028 (2011)
- Damljanović, V., Kostić R., Gajić R.: Characters of graphenes symmetry group dg80. *Physica Scr.* **2014**(T162), 014022 (2014)
- Damljanović, V., Gajić, R.: Phonon eigenvectors of graphene at high-symmetry points of the brillouin zone. *Physica Scr.* **2012**(T149), 014067 (2012)
- Dresselhaus, M.S., Dresselhaus, G.: Intercalation compounds of graphite. *Adv. Phys.* **51**(1), 1–186 (2002)
- Durajski, A.P.: Influence of hole doping on the superconducting state in graphane. *Supercond. Sci. Technol.* **28**(3), 035002 (2015)
- Enoki, T., Suzuki, M., Endo, M.: *Graphite Intercalation Compounds and Applications*, pp. 1–456. Oxford University Press, Oxford (2003)
- Ferrari, A.C., et al.: Science and technology roadmap for graphene, related two-dimensional crystals, and hybrid systems. *Nanoscale* **7**, 4598–4810 (2015)
- Giannozzi, P., et al.: Quantum espresso: a modular and open-source software project for quantum simulations of materials. *J. Phys. Condens. Matter* **21**(39), 395–502 (2009)
- Gusynin, V.P., Sharapov, S.G.: Unconventional integer quantum hall effect in graphane. *Phys. Rev. Lett.* **95**, 146801 (2005)
- Jeong, H.M., Lee, J.W., Shin, W.H., Choi, Y.J., Shin, H.J., Kang, J.K., Choi, J.W.: Nitrogen-doped graphene for high-performance ultracapacitors and the importance of nitrogen-doped sites at basal planes. *Nano Lett.* **11**(6), 2472–2477 (2011)
- Katsnelson, M., Novoselov, K., Geim, A.: Chiral tunnelling and the klein paradox in graphene. *Nat. Phys.* **2**(9), 620–625 (2006)

- Lee, C., Wei, X., Kysar, J.W., Hone, J.: Measurement of the elastic properties and intrinsic strength of monolayer graphene. *Science* **321**(5887), 385–388 (2008)
- Levy, N., Burke, S.A., Meaker, K.L., Panlasigui, M., Zettl, A., Guinea, F., Neto, A.H.C., Crommie, M.F.: Strain-induced pseudo-magnetic fields greater than 300 tesla in graphene nanobubbles. *Science* **329**(5991), 544–547 (2010)
- Liu, C.H., Chang, Y.C., Norris, T.B., Zhong, Z.: Graphene photodetectors with ultra-broadband and high responsivity at room temperature. *Nat. Nanotechnol.* **9**(4), 273–278 (2014)
- Ludbrook, B.M., et al.: Evidence for superconductivity in li-decorated monolayer graphene. *Proc. Nat. Acad. Sci.* **112**(38), 11795–11799 (2015)
- Margine, E.R., Giustino, F.: Two-gap superconductivity in heavily *n*-doped graphene: Ab initio migdal-elishberg theory. *Phys. Rev. B* **90**, 014518 (2014)
- Margine, E., Lambert, H., Giustino, F.: Electron-phonon interaction and pairing mechanism in superconducting ca-intercalated bilayer graphene. *Sci. Rep.* **6**, 21414 (2016)
- Masir, M.R., Moldovan, D., Peeters, F.: Pseudo magnetic field in strained graphene: revisited. *Solid State Commun.* **175**, 76–82 (2013)
- Matković, A., Milošević, I., Milićević, M., Tomašević-Ilić, T., Pešić, J., Musić, M., Spasenović, M., Jovanović, D., Vasić, B., Deeks, C., Panajotović, R., Belić, M.R., Gajić, R.: Enhanced sheet conductivity of Langmuir-Blodgett assembled graphene thin films by chemical doping. *2D Mater.* **3**(1), 015002 (2016)
- Mazin, I., Balatsky, A.: Superconductivity in Ca-intercalated bilayer graphene. *Philos. Mag. Lett.* **90**(10), 731–738 (2010)
- Nakada, K., Ishii, A.: DFT calculation for adatom adsorption on graphene. In: Gong, J.R. (ed.) *Graphene Simulation*. InTech, Rijeka, Croatia (2011)
- Neto, A.H.C., Guinea, F., Peres, N.M.R.: Edge and surface states in the quantum hall effect in graphene. *Phys. Rev. B* **73**, 205408 (2006)
- Novoselov, K.S., Geim, A.K., Morozov, S.V., Jiang, D., Zhang, Y., Dubonos, S.V., Grigorieva, I.V., Firsov, A.A.: Electric field effect in atomically thin carbon films. *Science* **306**(5696), 666–669 (2004)
- Novoselov, K.S., Jiang, Z., Zhang, Y., Morozov, S.V., Stormer, H.L., Zeitler, U., Maan, J.C., Boebinger, G.S., Kim, P., Geim, A.K.: Room-temperature quantum hall effect in graphene. *Science* **315**(5817), 1379–1379 (2007)
- Penev, E.S., Kutana, A., Yakobson, B.I.: Can two-dimensional boron superconduct? *Nano Lett.* **16**(4), 2522–2526 (2016)
- Perdew, J.P., Zunger, A.: Self-interaction correction to density-functional approximations for many-electron systems. *Phys. Rev. B* **23**, 5048–5079 (1981)
- Peres, N.M.R., Neto, A.H.C., Guinea, F.: Conductance quantization in mesoscopic graphene. *Phys. Rev. B* **73**, 195411 (2006)
- Pešić, J., Gajić, R., Hingerl, K., Belić, M.: Strain-enhanced superconductivity in li-doped graphene. *EPL (Europhys. Lett.)* **108**(6), 67005 (2014)
- Pešić, J., Damljanović, V., Gajić, R., Hingerl, K., Belić, M.: Density functional theory study of phonons in graphene doped with Li, Ca and Ba. *EPL (Europhys. Lett.)* **112**(6), 67006 (2015)
- Profeta, G., Calandra, M., Mauri, F.: Phonon-mediated superconductivity in graphene by lithium deposition. *Nat. Phys.* **8**(2), 131–134 (2012)
- Qu, L., Liu, Y., Baek, J.B., Dai, L.: Nitrogen-doped graphene as efficient metal-free electrocatalyst for oxygen reduction in fuel cells. *ACS Nano* **4**(3), 1321–1326 (2010)
- Rüddorf, W.: *Graphite Intercalation Compounds*. *Advances in Inorganic Chemistry and Radiochemistry*, pp. 223–266. Academic Press, Cambridge (1959)
- Saito, Y., Nojima, T., Iwasa, Y.: Highly crystalline 2d superconductors. *Nat. Rev. Mater.* **2**, 16094 (2016)
- Sassi, U., Parret, R., Nanot, S., Bruna, M., Borini, S., De Fazio, D., Zhao, Z., Lidorikis, E., Koppens, F., Ferrari, A., et al.: Graphene-based mid-infrared room-temperature pyroelectric bolometers with ultra-high temperature coefficient of resistance. *Nature Commun.* **8**, 14311 (2017)
- Settnes, M., Power, S.R., Jauho, A.P.: Pseudomagnetic fields and triaxial strain in graphene. *Phys. Rev. B* **93**, 035456 (2016)
- Sharma, B.K., Ahn, J.H.: Graphene based field effect transistors: efforts made towards flexible electronics. *Solid-State Electron.* **89**(Supplement C), 177–188 (2013)
- Shimada, N.H., Minamitani, E., Watanabe, S.: Theoretical prediction of phonon-mediated superconductivity with $T_c = 25\text{K}$ in Li-intercalated hexagonal boron nitride bilayer. *Appl. Phys. Express* **10**(9), 093101 (2017)
- Si, C., Liu, Z., Duan, W., Liu, F.: First-principles calculations on the effect of doping and biaxial tensile strain on electron-phonon coupling in graphene. *Phys. Rev. Lett.* **111**, 196802 (2013)

- Todorović, D., Matković, A., Milićević, M., Jovanović, D., Gajić, R., Salom, I., Spasenović, M.: Multilayer graphene condenser microphone. *2D Mater* **2**(4), 045013 (2015)
- Wakabayashi, K., Fujita, M., Kusakabe, K., Nakada, K.: Magnetic structure of graphite ribbon. *Czech J. Phys.* **46**(4), 1865–1866 (1996)
- Wakabayashi, K., Takane, Y., Yamamoto, M., Sigrist, M.: Edge effect on electronic transport properties of graphene nanoribbons and presence of perfectly conducting channel. *Carbon* **47**(1), 124–137 (2009)
- Wang, Y., Shao, Y., Matson, D.W., Li, J., Lin, Y.: Nitrogen-doped graphene and its application in electrochemical biosensing. *ACS Nano* **4**(4), 1790–1798 (2010)
- Weller, T.E., Ellerby, M., Saxena, S.S., Smith, R.P., Skipper, N.T.: Superconductivity in the intercalated graphite compounds C_6Yb and C_6Ca . *Nat. Phys.* **1**(1), 39–41 (2005)
- Xue, M., Chen, G., Yang, H., Zhu, Y., Wang, D., He, J., Cao, T.: Superconductivity in potassium-doped few-layer graphene. *J. Am. Chem. Soc.* **134**(15), 6536–6539 (2012)



Optical and mechanical properties and electron–phonon interaction in graphene doped with metal atoms

Andrijana Šolajić¹ · Jelena Pešić¹ · Radoš Gajić¹

Received: 31 October 2019 / Accepted: 5 March 2020
© Springer Science+Business Media, LLC, part of Springer Nature 2020

Abstract

Graphene, the first experimentally realized 2D material with outstanding mechanical and electrical properties as well an excellent optical transparency, is predicted to have many applications in various scientific fields. Furthermore, there are numerous ways for modifications of pure graphene that allow precise tuning of its properties or observation of some new effects, including the applied strain, various types of controlled defects, exposure to electrical or magnetic field, or doping. It is known that graphene with alkali metal atoms adsorbed on its surface becomes superconducting with due to enhanced electron–phonon coupling. The question remains what happens with optical and mechanical properties of such structures, can we preserve or enhance these superb properties while making graphene superconducting at the same time. Here we investigate structures based on graphene doped with several metal atoms—Sr, and some transition metal atoms such are Y and Sc. Using the density functional theory, we analyze the optical and elastic properties of those structures, discussing the influence of adsorbed atoms on these properties and calculate the electron–phonon coupling related properties.

Keywords Graphene · DFT · Superconductivity · Electron–phonon interaction · Optical properties · 2D materials

1 Introduction

Since the experimental discovery in 2004, graphene has been attracting enormous attention, not only as the first experimentally realised 2D material as the large scale samples, but mostly for its many unique properties. With this wide spectra of effects, graphene was also predicted to be suitable for various applications (Ferrari 2015; Blake et al. 2008; Todorović et al. 2015; Bonaccorso et al. 2015; Sassi et al. 2017; Liu et al. 2014). Monolayer graphene

This article is part of the Topical Collection on Advanced Photonics Meets Machine Learning.

Guest edited by Goran Gligoric, Jelena Radovanovic and Aleksandra Maluckov.

✉ Andrijana Šolajić
solajic@ipb.ac.rs

¹ Institute of Physics Belgrade, University of Belgrade, Pregrevica 118, Belgrade 11080, Serbia

formed on various metal surfaces was also extensively researched (Wintterlin and Bocquet 2009; Aizawa et al. 1990a, b; Taleb and Farías 2016) along with intercalation of these supported graphene systems (Gall et al. 1997; Shikin et al. 1998; Farías et al. 1999). Up to today, a couple of thousands papers about graphene are published and it is very well-known today how special graphene is and how its characteristics can be tailored to be suitable for even more suitable use. But in the long list of graphene's remarkable properties (Katsnelson et al. 2006; Gusynin and Sharapov 2005; Castro Neto et al. 2006; Lee et al. 2008), there is one notable effect missing, the superconductivity, which is absent in pristine graphene. Among many attempts to make graphene superconducting, a successful idea came from the so-called Graphite intercalation compounds (GICs). GICs are composed from graphite layers, with metallic atoms nested between. They were extensively studied since the 1960s, but with discovery of the superconductivity in some of the GICs (CaC_6 with $T_c = 11.5\text{K}$ and YbC_6 with $T_c = 6.5\text{K}$), an interest in those structures has raised again. The origin of superconductivity in GICs was debated for a long time, but most suggested was that the pairing mediated by electron–phonon interactions as the mechanism (Mazin 2005; Calandra and Mauri 2005), which was later confirmed by experimental data. As it can be observed, in all superconducting GICs there is an intercalant Fermi surface at the Fermi level, and those electrons are strongly coupled to the phonons. As reported in several studies, similar effects are present when going down to the thinnest limit, case of monolayer graphene doped with alkali adatoms in a similar manner to GICs. The electron–phonon coupling constant, λ ,

$$\lambda = \frac{N(0)D^2}{M\omega_{ph}^2}, \quad (1)$$

is proportional to the density of states at the Fermi level and the deformational potential D , and inversely proportional to effective atomic mass M and the frequency of the phonon involved ω_{ph} . As the DOS on the Fermi level in graphene is zero and slowly growing in its vicinity, the superconductivity in pristine graphene can not be observed, similar to pristine bulk graphite. However, the situation is changed upon doping with metallic adatoms, similar as in GICs. In the presence of adatoms, new electronic band is formed, the number of carriers is enlarged and, if the interlayer band occurs at the Fermi level, the electron–phonon coupling λ is enhanced and the coupling to carbon out-of-plane vibrations is promoted. Besides DOS, electron–phonon coupling constant also depends on the deformation potential D , which is inversely related to the distance between the graphene and adatoms. Hence for occurrence of the superconductivity it is favourable for adatoms to be closer to the graphene plane. On the other hand, it was shown that too small distance would result in a complete charge transfer between the graphene and the adatoms, so the interlayer band would be completely empty, as is the case with the bulk LiC_6 where the strong confinement along the z axis leads to interlayer band to be completely unoccupied and the superconductivity is suppressed. In contrary, in the LiC_6 monolayer, the quantum confinement is removed, resulting in partially occupied interlayer band and superconductivity with T_c up to 8K.

Motivated by these results, we wanted to explore graphene doped with Sr atoms and also with some transition metal atoms such as Sc and Y. Besides the electron–phonon properties crucial for the superconductivity, we were interested to investigate mechanical and optical properties also in order to study effects of added adatoms, questioning can we obtain superconducting material and preserve this superb graphene's properties, which would be of great significance for many applications. Using the density functional theory, we analyse the electron–phonon interaction properties and predict the critical temperature in the framework of the

electron–phonon coupling theory. We analyse the mechanical and optical properties of these structures and discuss the influence of adatoms on these properties.

2 Computational details

All calculations were performed in the Quantum Espresso software package (Giannozzi et al. 2009), in the LDA approximation, which is proven to be suitable for graphene systems and often is used. We used norm-conserving pseudopotentials, with the energy cutoff for wavefunctions of 120 Ry, obtained with respect to the convergence test. The unit cell for all doped graphene structures is modelled as $\sqrt{3} \times \sqrt{3}R30^\circ$ supercell of graphene unit cell, with adatoms positioned above the centres of carbon hexagons, the so-called H-site, as it is the most favourable site for all three atoms, according to the DFT study (Nakada and Ishii 2011). In order to avoid the interactions due to periodicity and to simulate a 2D system, the hexagonal c parameter was set to be sufficiently large, more than $c = 10 \text{ \AA}$. Prior to any further calculations, the structures were relaxed to their minimum energy configuration, using the BFGS algorithm. The dielectric function was calculated within the framework of the random-phase approximation (RPA), as implemented in `epsilon.x` code of QE, on the uniform k -point grid composed of 4096 k -points. The second-order elastic constants were calculated using the `ElaStic` code. First, the strain type and strength is chosen, and for each deformation, total energies are calculated. From the second derivatives of energy curves, elastic constants are calculated. Here we used amplitudes of 7% positive and negative Lagrangian strain.

The grid for electron–phonon coupling was used up to $48 \times 48 \times 1$ electronic k -mesh and $12 \times 12 \times 1$ phonon-momentum mesh using the Monkhorst pack. The electron–phonon coupling parameter λ and the critical temperature T_c are obtained with the isotropic Eliashberg theory. The Eliashberg function is defined as

$$\alpha^2 F(\omega) = \frac{1}{N(0)N_k N_q} \sum_{nk,mq,\nu} |g_{nk,mk+q}^\nu|^2 \times \delta(\epsilon_{nk}) \delta(\epsilon_{mk+q}) \delta(\omega - \omega_q^\nu) \quad (2)$$

where $N(0)$ is total density of states per spin, N_k and N_q are the total numbers of k and q points. $g_{nk,mk+q}^\nu$ is the electron–phonon matrix element, and electron eigenvalues and the band indexes are labelled with n and m , the wavevectors \mathbf{k} and $\mathbf{k} + \mathbf{q}$, the phonon frequencies with the mode number ν and the wavevector \mathbf{q} . From previous equation, the electron–phonon coupling coefficient is given as

$$\lambda(\omega) = 2 \int_0^\omega \frac{\alpha^2 F(\omega')}{\omega'} d\omega' \quad (3)$$

The total electron phonon coupling is obtained for $\omega \rightarrow \infty$. The superconducting critical temperature is estimated using the Allen–Dynes formula,

$$T_c = \frac{\omega_{log}}{1.2} \exp \left[\frac{-1.04(1 + \lambda)}{\lambda(1 - 0.62\mu^*) - \mu^*} \right] \quad (4)$$

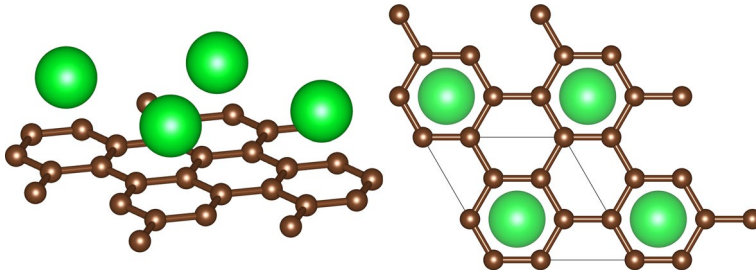


Fig. 1 The structure of graphene with atoms adsorbed on H-site. On the right, top view of structure is shown, with unit cell marked with black line

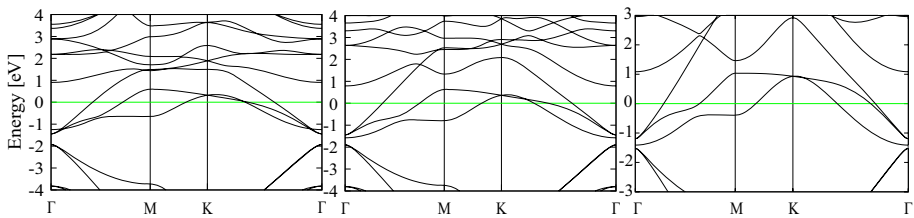


Fig. 2 Electronic structure of ScC_6 , YC_6 and SrC_6 along Γ -M-K- Γ direction. Fermi level is centered on 0 eV

where μ^* is the screened Coulomb pseudopotential and

$$\omega_{\log} = \exp \left[\frac{2}{\lambda} \int \frac{d\omega}{\omega} \alpha^2 F(\omega) \log \omega \right] \quad (5)$$

is the phonon frequencies logarithmic average.

3 Results and Discussion

The atomic structure of SrC_6 monolayer is consisted of graphene sheet covered with Sr adatoms positioned in the H-site, as shown in Fig. 1. Upon relaxing the systems, obtained distance between the graphene sheet and the adatom are $h = 2.22 \text{ \AA}$ for SrC_6 , $h = 2.04 \text{ \AA}$ for YC_6 , and $h = 1.76 \text{ \AA}$ for ScC_6 . Comparing to, for example the bulk SrC_6 compound, where this distance is 2.475 \AA , Sr atoms are closer to the graphene plane, more nested in the centres of carbon hexagons.

The electronic structure of SrC_6 monolayer is discussed in details in our previous work (Šolajić et al. 2018). We have shown the interlayer band that is forming due to the presence of Sr atoms, positioned near the Fermi level, partially occupied. Carbon π^* bands are strongly hybridized with new adatom-derived bands and also the DOS on Fermi level is significantly raised. Very similar are monolayers of ScC_6 and YC_6 , without almost any qualitative difference or significant difference in position of the Fermi level. Electronic structure of all three systems are shown in Fig. 2.

Motivated with those results, we proceeded to calculate the phonon dispersion and electron phonon coupling. In Fig. 3 the phonon dispersion of SrC_6 and phonon density of states for all structures are shown. The adatom contribution to phonon modes is marked

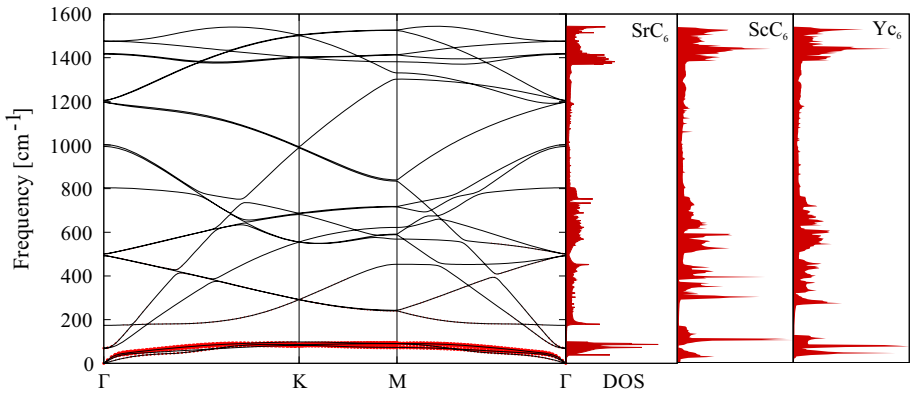


Fig. 3 Phonon dispersion for SrC₆-mono and phonon density of states for all three structures

with red circles. The phonon dispersions do not show any negative modes and they suggest that systems are dynamically stable. Similar to other metal doped graphene structures, we can observe three distinguished regions. Lowest region belongs to adatom modes, in the middle region are positioned carbon out-of-plane modes, and highest modes are C–C stretching modes. Since the phonon dispersions show minor differences for all three structures, presented is only SrC₆. First two modes with lowest energies (degenerated one at $\approx 70 \text{ cm}^{-1}$ and one at $\approx 175 \text{ cm}^{-1}$) are related to pristine graphene’s acoustic modes. That can be also seen in Fig 4. of our previous study (Šolajić et al. 2018), for the lowest mode at 70 cm^{-1} , the in plane displacements of carbon atoms are like TA and LA modes, with the adatom oscillating in opposite direction, and analogue case for the mode at 175 cm^{-1} , related to ZA graphene mode. This splitting of ZA-like mode from the lower two is similar to the case where graphene layer is formed on metal substrates, and the gap at the Γ point is introduced due to interaction of graphene with substrate [The shift of ZA mode is seen at 48 cm^{-1} in graphene on Cu(111) substrate (Taleb and Fariás 2016) and at 282 cm^{-1} for graphene on transition-metal carbides TaC(111), HfC(111) and TiC(111) (Aizawa et al. 1990b)]. We can consider that the splitting of the ZA-like mode can be described in a similar way, representing the interaction between the graphene and adsorbed metal atoms. The formed gap depends on the strength of the graphene-substrate coupling and as given in the following models. For free-standing pristine graphene, the dispersion of the acoustic ZA mode in the vicinity of the Γ point is given by Taleb et al. (2015):

$$\omega_{ZA}^{free}(\mathbf{q}) = \sqrt{\frac{\kappa}{\rho_{2D}} \mathbf{q}^2}, \tag{6}$$

where $\rho_{2D} = 7.6 \times 10^{-8} \text{ g/cm}^2$ is the two-dimensional mass density of graphene. Coupling to the substrate introduces a gap at a frequency ω_0 at the Γ point and the dispersion relation is given by Amorim and Guinea (2013)

$$\omega_{ZA}^{free}(\mathbf{q}) = \sqrt{\frac{\kappa}{\rho_{2D}} \mathbf{q}^4 + \omega_0^2}, \tag{7}$$

where $\omega_0 = \sqrt{g/\rho_{2D}}$ and g is the coupling strength between graphene and substrate. Following this model, we can approximate the similar interaction of graphene with adsorbed

metal layer and determine the $g = 0.739 \times 10^{19} \text{ N/m}^3$. This value is significantly smaller than for graphene on various substrates [from $g = 5.7 \times 10^{19} \text{ N/m}^3$ for graphene on Cu (Taleb et al. 2015), to the order of 2×10^{21} for the (111) surface of transition metal carbides (Amorim and Guinea 2013)], as somewhat expecting given that the graphene is covered with not so dense placed Sr metal atoms and not suspended on a real surface.

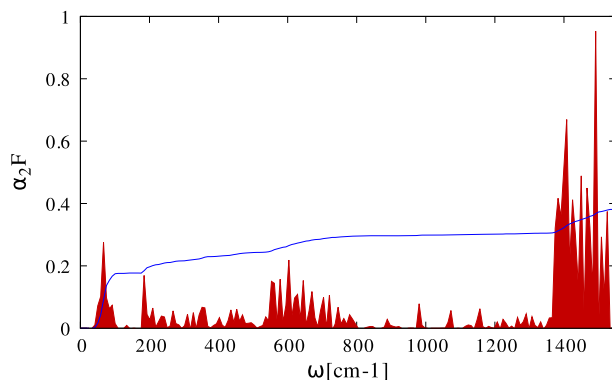
The right side of Fig. 3 shows the phonon DOS for doped graphene structures. For all three structures, the phonon DOS is largest in the adatom region, as well in carbon in-plane modes area. As it can be seen in Eliashberg function, presented in Fig. 4, those modes also have significant contribution in electron–phonon coupling. The choice of adatom does not affect the phonon density of states and, in every of three systems, largest peaks are in low energy region and the highest ones with some minor difference in positions of peaks.

In the Eliashberg function calculated for SrC₆ monolayer, shown in Fig. 4, three distinguished peaks are present as expected, one from the lowest adatom-related modes, one wide and narrow in the middle-energy region, and the highest peak at 1400–1500 cm⁻¹ related to the carbon in-plane modes. Although the C–C stretching modes are strongly coupled with electronic states at Fermi level, the λ parameter is enhanced most in the low energy region related to adatoms (≈ 0.18), given that it depends on the phonon energy inversely, so the low-energy modes have largest contribution to electron–phonon coupling constant. Comparing this to bulk SrC₆ compound (Calandra and Mauri 2006), we can observe slightly softened Sr_z phonon mode, giving a larger peak in Eliashberg function. However, in the middle region, the contribution of carbon out-of-plane modes is significantly smaller and the contribution to electron–phonon coupling is drastically lowered than in bulk. Very similar case is reported with CaC₆ (Calandra and Mauri 2006; Profeta et al. 2012) where the carbon out-of-plane vibrations are similar in bulk and the monolayer case but overall contribution to λ is decreased in the monolayer. This is also an opposite to the LiC₆ where the removal of confinement gives a rise to the λ .

Overall electron–phonon coupling constant in SrC₆-monolayer is $\lambda = 0.38$, with $\omega_{log} = 280.9 \text{ cm}^{-1}$. The superconducting transition temperature, estimated using the Allen–Dynes formula with $\mu^* = 0.112$ is $T_c = 0.9 \text{ K}$, lower than in its bulk counterpart (3K). Both other structures have very similar electronic and phonon structure and enhanced electron–phonon coupling is expected, with critical temperatures in similar range. Further calculations of electron–phonon coupling parameter are needed to be confirmed.

Interested to see what happens with mechanical properties that are superb in graphene, we calculated the elastic constants of our doped structures and compare them

Fig. 4 Eliashberg function with integrated electron–phonon coupling parameter for SrC₆-mono



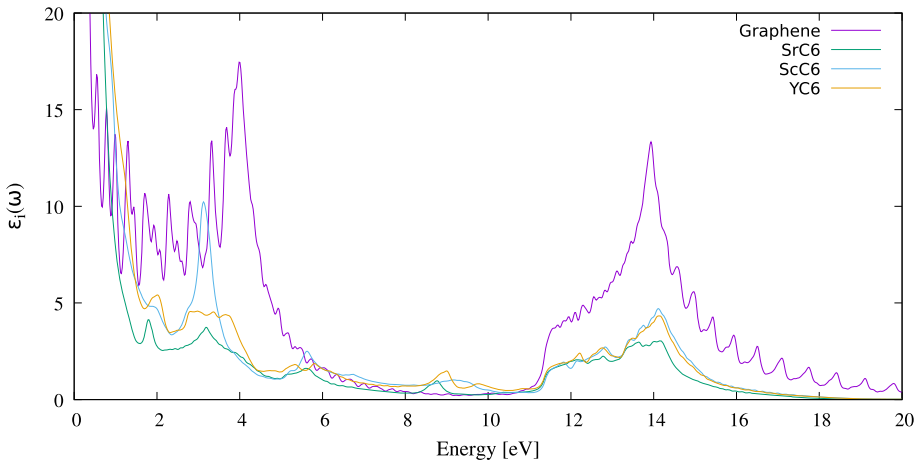


Fig. 5 Eliashberg function with integrated electron–phonon coupling parameter for SrC6-mono

with pristine graphene, which are shown in Table 1. 2D hexagonal, square and rectangular lattices have 4 non-zero second-order elastic constants, c_{11} , c_{12} , c_{22} and c_{66} , where due to symmetry, in case of hexagonal lattice, only two elastic constants are independent because $c_{11} = c_{22}$ and $c_{66} = \frac{1}{2}(c_{11} - c_{22})$. In this case, the Young modulus and Poisson's ratio are defined according to Wei and Peng (2014) as $Y = \frac{c_{11}^2 - c_{12}^2}{c_{11}}$ and $\nu = \frac{c_{21}}{c_{11}}$. Obtained results for elastic properties of pristine graphene are overall in good agreement with previous experimental and theoretical studies. Calculated elastic constants c_{11} and c_{12} are both larger than in literature (estimated to be around 350 and 60 N/m, respectively), so the Young Modulus is also larger (experimentally measured to 342 N/m in Politano et al. 2012 and 340 N/m in Lee et al. 2008). The Poisson's ratio is however accurately obtained to 0.19, presumably due to both c_{11} and c_{12} similarly overestimated. Pristine graphene has extraordinary large values of elastic constants and also can be stretched up to roundly 20%. It is clearly observable that upon doping, elastic constants drop to almost half of the pristine graphene ones, as it is somewhat expected due to added adatoms on top of graphene surface. Still, that leaves these parameters very high in comparison to many other similar 2D materials. Moreover, parameters such as Young modulus remains exceptionally good. The elastic constants and Young modulus of doped graphene structures are in range of hBN and slightly larger than SiC (Andrew et al. 2012; Zhang et al. 2017), and still much larger than many other 2D structures, such as MgB₂ (Pešić et al. 2019) or silicene (Zhang et al. 2017). This possibility to

Table 1 The calculated elastic constants, Young's modulus Y , Poisson's ratio ν and the shear modulus G , for pristine graphene, ScC₆, YC₆ and SrC₆ monolayers

	c_{11}	c_{12}	c_{66}	Y	ν	G
Graphene	462.3	79.6	191.4	448.6	0.19	94.67
ScC ₆	244.8	37.2	103.8	239.2	0.15	103.83
SrC ₆	205.9	33.3	86.3	200.5	0.16	86.26
YC ₆	239.7	38.2	100.8	233.6	0.16	100.77

All parameters are given in units of N/m, except the Poisson's ratio which is dimensionless

strain graphene can be also exploited for tuning superconducting properties, as previously was shown that certain types of strain can enhance the superconducting critical temperature significantly. Pešić et al. (2014).

Calculated imaginary part of dielectric function for our doped structures and pristine graphene, for the electric field vector perpendicular to the c axis, is shown in Fig. 5. Dielectric function of pristine graphene is discussed before (Marinopoulos et al. 2004) and we will not discuss it in details. Our calculations are in agreement with previous theoretical as well experimental studies, showing clear peaks at 4 eV and 14 eV, originating from $\pi \rightarrow \pi^*$ and $\sigma \rightarrow \sigma^*$ interband transitions. The singularity at zero frequency is present and shows metallicity of the system. Upon doping, two small differences can be observed. First, the first peak which is in pristine graphene at 4 eV is shifted to around 3 eV and it is lower intensity in all structures. The second peak at 14 eV does not change position in energy, but drops to much lower intensity in all three structures. These lower intensities and changes in positions of the peaks can be related to Fermi level shift and an adatom influence on π^* bands. Varying the type of dopants however does not make any significant changes in position or intensity of these peaks, except in case of ScC_6 monolayer where intensity of first peak is slightly smaller than in pristine graphene. Moreover, none of the changes in dielectric function induced by adatoms is crucial for the quality of the optical properties and they remain superb as in pristine graphene.

4 Conclusions

In this work we investigated the electron–phonon coupling and possibility of superconductivity in graphene doped with Sr, Y and Sc adatoms, as well their mechanical and optical properties. The bulk SrC_6 which is superconducting with $T_c = 3\text{K}$, was studied theoretically as well experimentally. Moreover, previously studied electronic properties predict the monolayer as good candidate for occurrence of superconductivity. Here we expanded our research by doping with transition metals such as Sc and Y. The phonon dispersion of systems show they are dynamically stable, with no negative frequencies present. Using the isotropic Eliashberg theory, we calculated the total electron–phonon coupling parameter of SrC_6 monolayer, $\lambda = 0.38$. As in bulk SrC_6 compound, superconductivity is occurring, but with lower T_c , which is estimated as $T_c = 0.9\text{K}$ using the Allen–Dynes formula with $\mu^* = 0.112$. Other two discussed structures have similar electronic structure and density of states, as well the phonon dispersion too and have potential to have superconducting properties with similar critical temperatures, and need further investigation. Our calculations of elastic constants and mechanical properties show that upon doping graphene, elastic constants and other parameters like Young modulus, drop by half of pristine graphene's, which is still extraordinary good in comparison to many similar structures. Calculated imaginary parts of dielectric constants show no significant changes other than lower intensities of the peaks and slightly shifting in energy. This makes those structures an excellent candidates for potential applications.

Acknowledgements The authors acknowledge funding provided by the Institute of Physics Belgrade, through the grant by the Ministry of Education, Science, and Technological Development of the Republic of Serbia. DFT calculations were performed using computational resources at Johannes Kepler University, Linz, Austria.

References

- Aizawa, T., Souda, R., Otani, S., Ishizawa, Y., Oshima, C.: Anomalous bond of monolayer graphite on transition-metal carbide surfaces. *Phys. Rev. Lett.* **64**, 768–771 (1990a). <https://doi.org/10.1103/PhysRevLett.64.768>
- Aizawa, T., Souda, R., Otani, S., Ishizawa, Y., Oshima, C.: Bond softening in monolayer graphite formed on transition-metal carbide surfaces. *Phys. Rev. B* **42**, 11469–11478 (1990b). <https://doi.org/10.1103/PhysRevB.42.11469>
- Amorim, B., Guinea, F.: Flexural mode of graphene on a substrate. *Phys. Rev. B* **88**(11), 115418–115425 (2013)
- Andrew, R.C., Mapasha, R.E., Ukpong, A.M., Chetty, N.: Mechanical properties of graphene and boron-*nitrene*. *Phys. Rev. B* **85**, 125428–125437 (2012). <https://doi.org/10.1103/PhysRevB.85.125428>
- Blake, P., Brimicombe, P.D., Nair, R.R., Booth, T.J., Jiang, D., Schedin, F., Ponomarenko, L.A., Morozov, S.V., Gleeson, H.F., Hill, E.W., Geim, A.K., Novoselov, K.S.: Graphene-based liquid crystal device. *Nano Lett.* **8**(6), 1704–1708 (2008). <https://doi.org/10.1021/nl080649i>
- Bonaccorso, F., Colombo, L., Yu, G., Stoller, M., Tozzini, V., Ferrari, A.C., Ruoff, R.S., Pellegrini, V.: Graphene, related two-dimensional crystals, and hybrid systems for energy conversion and storage. *Science* (2015). <https://doi.org/10.1126/science.1246501>
- Calandra, M., Mauri, F.: Theoretical explanation of superconductivity in c_6 Ca. *Phys. Rev. Lett.* **95**, 237002–237006 (2005). <https://doi.org/10.1103/PhysRevLett.95.237002>
- Calandra, M., Mauri, F.: Possibility of superconductivity in graphite intercalated with alkaline earths investigated with density functional theory. *Phys. Rev. B* **74**, 094507–094515 (2006). <https://doi.org/10.1103/PhysRevB.74.094507>
- Castro Neto, A.H., Guinea, F., Peres, N.M.R.: Edge and surface states in the quantum hall effect in graphene. *Phys. Rev. B* **73**, 205408–205416 (2006). <https://doi.org/10.1103/PhysRevB.73.205408>
- Fariás, D., Shikin, A.M., Rieder, K.H., Dedkov, Y.S.: Synthesis of a weakly bonded graphite monolayer on ni(111) by intercalation of silver. *J. Phys. Condens. Matter* **11**(43), 8453–8458 (1999). <https://doi.org/10.1088/0953-8984/11/43/308>
- Ferrari, A.C., et al.: Science and technology roadmap for graphene, related two-dimensional crystals, and hybrid systems. *Nanoscale* **7**, 4598–4810 (2015). <https://doi.org/10.1039/C4NR01600A>
- Gall, N.R., Rut'kov, E.V., Tontogode, A.Y.: Two dimensional graphite films on metals and their intercalation. *Int. J. Mod. Phys. B* **11**(16), 1865–1911 (1997). <https://doi.org/10.1142/S0217979297000976>
- Giannozzi, P., et al.: Quantum espresso: a modular and open-source software project for quantum simulations of materials. *J. Phys. Condens. Matter* **21**(39), 395502–395521 (2009)
- Gusynin, V.P., Sharapov, S.G.: Unconventional integer quantum hall effect in graphene. *Phys. Rev. Lett.* **95**, 146801–146805 (2005). <https://doi.org/10.1103/PhysRevLett.95.146801>
- Katsnelson, M., Novoselov, K., Geim, A.: Chiral tunnelling and the klein paradox in graphene. *Nat. Phys.* **2**(9), 620–625 (2006). <https://doi.org/10.1038/nphys384>
- Lee, C., Wei, X., Kysar, J.W., Hone, J.: Measurement of the elastic properties and intrinsic strength of monolayer graphene. *Science* **321**(5887), 385–388 (2008). <https://doi.org/10.1126/science.1157996>
- Liu, C.H., Chang, Y.C., Norris, T.B., Zhong, Z.: Graphene photodetectors with ultra-broadband and high responsivity at room temperature. *Nat. Nanotechnol.* **9**(4), 273–278 (2014)
- Marinopoulos, A.G., Reining, L., Rubio, A., Olevano, V.: Ab initio study of the optical absorption and wave-vector-dependent dielectric response of graphite. *Phys. Rev. B* **69**, 245419–245431 (2004). <https://doi.org/10.1103/PhysRevB.69.245419>
- Mazin, I.I.: Intercalant-driven superconductivity in YbC_6 and CaC_6 . *Phys. Rev. Lett.* **95**, 227001–227005 (2005). <https://doi.org/10.1103/PhysRevLett.95.227001>
- Nakada, K., Ishii, A.: DFT calculation for adatom adsorption on graphene. In: Gong, J.R. (ed.) *Graphene Simulation*. InTech, Rijeka, Croatia (2011)
- Pešić, J., Gajić, R., Hingerl, K., Belić, M.: Strain-enhanced superconductivity in li-doped graphene. *Europhys. Lett.: EPL* **108**(6), 67005–67011 (2014)
- Pešić, J., Popov, I., Šolajić, A., Damljanović, V., Hingerl, K., Belić, M., Gajić, R.: Ab initio study of the electronic, vibrational, and mechanical properties of the magnesium diboride monolayer. *Condens. Matter* (2019). <https://doi.org/10.3390/condmat4020037>
- Politano, A., Marino, A.R., Campi, D., Fariás, D., Miranda, R., Chiarello, G.: Elastic properties of a macroscopic graphene sample from phonon dispersion measurements. *Carbon* **50**(13), 4903–4910 (2012). <https://doi.org/10.1016/j.carbon.2012.06.019>
- Profeta, G., Calandra, M., Mauri, F.: Phonon-mediated superconductivity in graphene by lithium deposition. *Nat. Phys.* **8**(2), 131–134 (2012)

- Sassi, U., Parret, R., Nanot, S., Bruna, M., Borini, S., De Fazio, D., Zhao, Z., Lidorikis, E., Koppens, F., Ferrari, A., et al.: Graphene-based mid-infrared room-temperature pyroelectric bolometers with ultra-high temperature coefficient of resistance. *Nat. Commun.* **8**, 14311–14321 (2017)
- Shikin, A.M., Fariás, D., Rieder, K.H.: Phonon stiffening induced by copper intercalation in monolayer graphite on ni(111). *Europhys. Lett.: EPL* **44**(1), 44–49 (1998). <https://doi.org/10.1209/epl/1998-00432-x>
- Šolajić, A., Pešić, J., Gajić, R.: Ab-initio calculations of electronic and vibrational properties of sr and yb intercalated graphene. *Opt. Quantum Electron.* **50**(7), 276–286 (2018). <https://doi.org/10.1007/s11082-018-1541-x>
- Taleb, A.A., Fariás, D.: Phonon dynamics of graphene on metals. *J. Phys. Condens. Matter* **28**(10), 103005–103024 (2016). <https://doi.org/10.1088/0953-8984/28/10/103005>
- Taleb, A.A., Yu, H.K., Anemone, G., Fariás, D., Wodtke, A.M.: Helium diffraction and acoustic phonons of graphene grown on copper foil. *Carbon* **95**, 731–737 (2015). <https://doi.org/10.1016/j.carbon.2015.08.110>
- Todorović, D., Matković, A., Miličević, M., Jovanović, D., Gajić, R., Salom, I., Spasenović, M.: Multilayer graphene condenser microphone. *2D Mater.* **2**(4), 045013–045019 (2015)
- Wei, Q., Peng, X.: Superior mechanical flexibility of phosphorene and few-layer black phosphorus. *Appl. Phys. Lett.* **104**(25), 251915–251920 (2014). <https://doi.org/10.1063/1.4885215>
- Winterlin, J., Bocquet, M.L.: Graphene on metal surfaces. *Surface Science* **603**(10), 1841–1852 (2009). <https://doi.org/10.1016/j.susc.2008.08.037>. (Special Issue of Surface Science dedicated to Prof. Dr. Dr. h.c. mult. Gerhard Ertl, Nobel-Laureate in Chemistry 2007)
- Zhang, Z., Yang, Y., Penev, E.S., Yakobson, B.I.: Elasticity, flexibility, and ideal strength of borophenes. *Adv. Funct. Mater.* **27**(9), 1605059–1605066 (2017). <https://doi.org/10.1002/adfm.201605059>

Publisher's Note Springer Nature remains neutral with regard to jurisdictional claims in published maps and institutional affiliations.